The Design and Use of Heterogeneous and Homogeneous Catalysts for the Activation of Small Molecules

by

Thomas Charles Draper

A thesis presented for the degree of

Doctor of Philosophy

School of Life Sciences

University of Sussex

2016

Declaration

I hereby declare that this thesis has not been, and will not be, submitted in whole or in part to another University for the award of any other degree.

Signed:.....

Thomas Charles Draper

For my wife, Sammy.

"Evans boldly put 50 atm of ethylene in a cell with 25 atm of oxygen. The apparatus subsequently blew up, but luckily not before he obtained the spectra shown in figure 8." †

† A. J. Merer, R. S. Mulliken, *Chem. Rev.*, 1969, **69**, 639-656

University of Sussex

Thomas Charles Draper

Submitted for the degree of Doctor of Philosophy

The Design and Use of Heterogeneous and Homogeneous Catalysts for the Activation of Small Molecules

Abstract

This thesis presents research conducted on the activation of small molecules. The traditional gases are considered by reacting them with sterically hindered metal complexes. Additionally, the complete oxidation of siloxanes, and partial oxidation of methane, is investigated using photoactive titania. The work approaches the field from both a heterogeneous and homogeneous viewpoint, focusing on nanophotocatalysts, whilst also investigating the design and synthesis of possible model molecular systems.

Siloxanes are present in biogas, posing a risk to equipment that uses biogas as an energy source. The study on their removal using photocatalytic titania nanofibres is presented, both in the laboratory and in an industrial setting. Removal is achieved by complete oxidation of the siloxanes to silica, reducing their vapour pressure and thereby effectively removing them from the gas stream. The synthesis of titania nanofibres was designed and developed, using an adapted novel electrospinning method. The catalytic performance of the nanocatalysts was evaluated for the removal of siloxane. Doping of the nanofibres with silver, tungsten and cobalt is also reported, with 1 % WO_3 doping showing a three-fold increase in activity, compared to pristine titania nanofibres.

Titania, as an efficient photocatalyst, is then investigated to determine its ability to partially oxidise methane, to form a more valuable feedstock chemical. Tungsten trioxide, iron(III) oxide and uranium dioxide are also investigated as alternative photocatalysts. Conversion of methane was monitored by GC-MS and FTIR. Titania showed the most activity, generating carbon dioxide. However, no partial oxidation products were detected. The use of perfluorocarbons as a phase is also investigated, in an attempt to improve solubility and selectivity. These experiments demonstrated the photocatalytic oxidation of ethanol to acetaldehyde.

In order to tailor the electronic property and catalytic activity, molecular catalysts were also synthesised. Consequently, the use of triptycene as a ligand for transition metals was studied for the first time. The synthesis, isolation and full characterisation of a novel triptycene precursor is reported, including the single crystal X-ray structure. This precursor is ligated to a number of metal centres, including iron, cobalt and chromium for the first time. Many of the synthesised species are new examples of the rare low-spin state in a tetrahedral geometry. Of these novel complexes, the cobalt triptycene species was shown to successfully activate dioxygen.

The catalytic performance of molecular catalysts was also investigated in the activation of oxygen and water. New molecular mimics of a previously reported heterogeneous cobalt oxide catalyst have been synthesised, using a number of phosphate ligands with a cobalt metal centre. The resulting complexes are fully characterised, with a single crystal X-ray structure reported. In-depth analysis of the complexes is reported, including electronic absorption, variable temperature magnetic studies and cyclic voltammetry.

Acknowledgements

This PhD and accompanying thesis could not have been achieved without the help and support of many people. Chief amongst these is my wife, Sammy. After agreeing to be dragged to Brighton, she has been an amazing source of strength as we built our lives on the seafront. I don't know where I would be without her continuous love, support and supply of coffee. It is with great pride that I dedicate this thesis to her.

My parents have also always been there for me. Their unwavering encouragement has been phenomenal, always willing to jump in whenever and wherever necessary to move a dining table or washing machine. I am proud to call them my parents, and I hope that they enjoy this as some light bedtime reading.

A large cheer goes to the Nanolab — both old and new. Fangward, the entity previous composed of Fang and Adward, have been a continuous source of frustration and laughs. They shall be missed. As will the old-hats Ali and Brnyia, to whom a tip of the hat goes. Last, but certainly not least, is my pseudo-Irish friend Giacomo. Giac has defined Brighton, and it is hard to imagine my time at Sussex without him, and his seemingly continuous supply of boardgames.

As is always the way, the Nano-torch must pass from old to new. The responsibility falls to Dan, Emmanuel and Munirah to keep up the traditions of those who paved the way. Your primary duties are to maintain the postcard wall, and to keep longing for a fully constructed XPS.

Honorary members of the Nanolab are also worthy of mention, especially Matt 'fire-alarm' Molloy, who I raised since he was a wee baby. Vicki Greenacre, the provider of baked treats, who helped with single crystal structures. Matt Leech, who is the ears of the department. JK, whose drive to be here inspires us all. Katy Kirzynowski, whose washing up was always appreciated. And a special thanks to Chris Inman, for his help with CV.

Over the years, many undergraduates have passed through my labs, both under my instruction and not. I would like to first thanks those students who worked closest to me, Jone-him 'Crispy' Tsang, Rob 'coffee-break' Ziolek, Reilly Moule, Martin Horman and Richard Dixey. There have been many students who have helped make my time in the basement labs bearable, both with their friendship and distractions. I say thank you to (in no particular order) Edward Hills, Charlie

Readman, Sam Pearce, Thomas Samuels, Anna ‘firestarter’ Crosby, Josh Fellowes, Pete McNulty, Ben Fry, Charles Creissen, Christy Tuohy and Declan Rowlands.

Formally, I would like to thank Dr Alaa Abdul-Sada for his help with MS, and Dr Mark Roe for his help with single crystal XRD. I would also like to do a shout out for the unsung heroes of the Chemistry department, Alex Burns, Paul Andrews and Barry Jackson. Whenever the water-cooling failed, you were there. Whenever a magpie broke into the lab, you were there. Whenever a high-voltage power supply needed constructing, you were there. The unsung heroes of the Nanolab (*i.e.* the teaching lab) are also owed a massive thanks. Mick Henry and Fran Chick were always able, if slowly less willing, to lend any and all equipment necessary. And Chris Dadswell’s willingness to share his knowledge, and access, of GC’s is greatly appreciated.

None of this would have been possible if not for the opportunity given to me by my supervisors, Dr John Turner and Dr Qiao Chen. Their guidance and support over the past four years have helped shape this document and my future, thank you. Finally, I thank Innovate UK and PpTek Ltd for the three years of funding that helped keep me fed and watered.

Contents

List of Figures

List of Schemes

List of Tables

Abbreviations

ATR	Attenuated total reflectance
BEHP	Bis(2-ethylhexyl) phosphate
BET	Brunauer-Emmett-Teller
Bu	Butyl
CV	Cyclic voltammetry
D3	Hexamethylcyclotrisiloxane
D4	Octamethylcyclotetrasiloxane
D5	Decamethylcyclopentasiloxane
D6	Dodecamethylcyclohexasiloxane
DBP	Dibutyl phosphate
DCE	Dichloroethane
DMF	Dimethylformamide
DOS	Density of States
DPP	Diphenyl phosphate
e^-	Electron
E_F	Fermi level
E_g	Band gap
EDX	Energy-dispersive X-ray spectroscopy
EI	Electron ionisation
ESI	Electrospray ionisation
Et	Ethyl
FID	Flame ionised detection
FTIR	Fourier transform-infrared spectroscopy
FTO	Fluorine-doped tin oxide
GC	Gas chromatography
h^+	Hole
HMBC	Heteronuclear multiple-bond correlation
HOMO	Highest occupied molecular orbital
HSQC	Heteronuclear single quantum coherence
ICSD	Inorganic crystal structure database
IUPAC	International Union of Pure and Applied Chemistry
$\boldsymbol{k}$	Wave vector
k	Rate constant
L2	Hexamethyldisiloxane
L3	Octomethyltrisiloxane
L4	Decamethyltetrasiloxane

LCAO	Linear combination of atomic orbitals
LMCT	Ligand-metal charge-transfer
LUMO	Lowest unoccupied molecular orbital
m^*	Effective mass
M^+	Molecular ion
m_e	Mass of an electron
Me	Methyl
MMO	Methane monooxygenase
MS	Mass spectrometry
MvK	Mars-van Krevelen
NHE	Normal hydrogen electrode
NMR	Nuclear magnetic resonance
nor	1-norbornyl
OCM	Oxidative coupling of methane
P25	Commercial nanoparticulate TiO_2
PCET	Proton-coupled electron transfer
PDMS	Polydimethylsiloxane
pFMeCy	Perfluoromethylcyclohexane
Ph	Phenyl
Phos	Phosphate
PMMA	Poly(methyl methacrylate)
pXRD	Powder X-ray diffraction
Py	Pyridine
RHE	Reversible hydrogen electrode
SEM	Scanning eletron microscopy
SHE	Standard hydrogen electrode
SSA	Steady state approximation
TEM	Transmission electron microscopy
THF	Tetrahydrofuran
TOF	Turnover frequency
TON	Turnover number
Trip	Triptycene
TTiP	Titanium tetraisopropoxide
UV	Ultraviolet light
UV_A	Ultraviolet light (315 nm to 400 nm)
UV-Vis	UV-Visible spectroscopy
VOC	Volatile organic compound
VT	Variable Temperature
XPS	X-ray photoelectron spectroscopy
XRD	Single crystal X-ray diffraction

Chapter 1

Introduction

This work was funded by Innovate UK, formally the Technology Strategy Board, with grant titled: *A Green Approach to Biogas Purification with Nanomaterials*. It was funded and conducted in collaboration with PpTek Ltd, which is now part of Parker Hannifin Corporation.

1.1 An Efficient Photocatalyst: Titanium Dioxide

Titanium dioxide, also known as titania, is a brilliant white metal oxide semiconductor. The white colour is due to the size of its band gap, which results in the reflection of all visible light, and the absorption of ultraviolet (UV) light. It is a highly stable compound, which has led to its large use in industry as a pigment in a wide range of applications, from household paint to tattoo ink. It is also safe, as demonstrated by its use as a food dye, having the e-number E171,[1] and as a sun screen due to its absorption of all UV light.

The use of titanium dioxide, TiO_2, as a pigment was observed to produce paints that began to flake and peel on extended exposure to light. Subsequent investigations into this problem revealed that TiO_2 was acting as a photocatalyst, degrading the paint.[2] It was not until the 1970s, when the reality of the global oil crisis was beginning to become apparent, that the scientific community took interest in the phenomenon, with a paper by Fujishima and Honda on the TiO_2 mediated photolysis of water becoming seminal.[3] Since then TiO_2 has been used in many commercial applications, including water purification,[4] self-cleaning glass,[5] hydrogen production[6] and volatile organic compound (VOC) degradation.[7]

There are three common phases of TiO_2, anatase, rutile and brookite. The crystal geometries of these are displayed in figure 1.1. Both anatase and rutile are tetragonal, and brookite is orthorhombic. All three polymorphs are witnessed in nature, however brookite is less common. There is a large amount of research that suggests that the resulting polymorph from solution-formed TiO_2 depends on the chemistry of the reactants and precursors used.[8–11] The large variation in reported

synthetic experimental procedures however, means that a direct comparison is very difficult to conclusively conduct.[12]

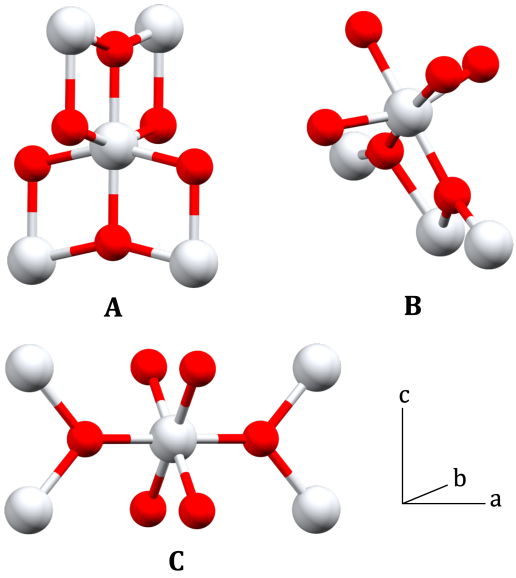

Figure 1.1. The crystal structure unit cells of (a) anatase,[13] (b) brookite[14] and (c) rutile.[15] The abc cell axes are labelled, and each structure is positioned accordingly. Anatase and rutile are tetragonal, whilst brookite is orthorhombic.

Rutile is the most stable form of macro-sized TiO_2 thermodynamically, with both anatase and brookite being kinetically stable. On heating either of these above ~500 °C they slowly convert to the thermodynamically stable rutile. The most thermodynamically stable form of TiO_2 varies with particle size. While rutile is the most stable form generally, when the particle size is between 11 nm and 35 nm brookite becomes more stable. When the particle size is reduced further to below 11 nm, anatase becomes the most stable.[16] As the particle size decreases, the surface energy becomes increasingly important to the overall free energy of the particle; the change in thermodynamic stability order is caused by this surface energy variation.

The use of titanium dioxide as a photocatalyst is prolific in academia, and this thesis. Therefore, a brief summary of the quantum electronics behind photocatalysts is presented, in order to provide a thorough background.

1.2 The Electronic Structure of Photocatalysts

1.2.1 Band Structure

A single atom has one set of orbitals. Using the linear combination of atomic orbitals, when two atoms form a chemical bond, they reach an equilibrium state between the atoms which is described

by the constructive and destructive interference of electrons. This forms both a bonding (low energy) and anti-bonding (high energy) orbital. As the number of atoms in a cluster increases, so do the number of bonding and anti-bonding orbitals. The number of bonding and anti-bonding orbitals is always equal to the number of atoms present, resulting in a large number of bonding and anti-bonding orbitals at similar energies. This causes the energy difference between the various anti-bonding and bond orbitals to reduce until an effective continuum of energy levels exists, called bands. This is the principle behind the linear combination of atomic orbitals (LCAO), shown graphically in figure 1.2. The lowest unoccupied band is known as the conduction band and the highest occupied band is known as the valence band. These bands are demonstrated graphically in figure 1.3.

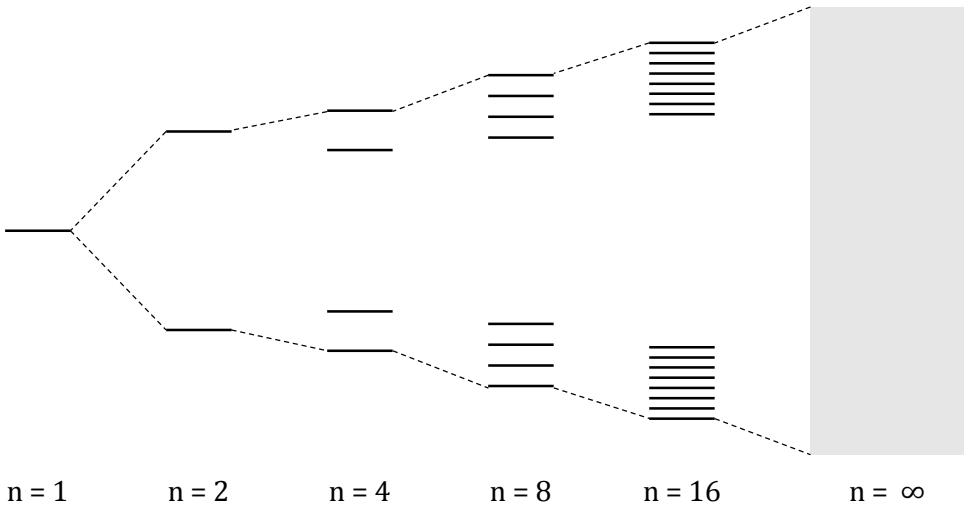

Figure 1.2. A simple graphical representation of the linear combination of atomic orbitals.

The density of states (DOS) is the distribution of orbitals as a function of energy. This distribution can include energy levels, the occupation of which is forbidden. This distribution of energy levels can also be represented as wave vector, $\boldsymbol{k}$. When the forbidden energy levels extend through all wave vectors, the forbidden region is known as the band gap. The band gap is direct when the promotion of an electron from the top of the valence band (valence band maximum) to the bottom of the conduction band (conduction band minimum) conserves crystal momentum, $\Delta \boldsymbol{k} = 0$. When crystal momentum is not conserved, $\Delta \boldsymbol{k} \neq 0$, the band gap is indirect.

As materials are reduced in size towards the nanoscale range, their electronic properties begin to differ. Known as quantum size effects, this is because the number of atoms in the crystal lattice becomes small, relative to macroscale bulk materials. This results in quantised, non-continuous

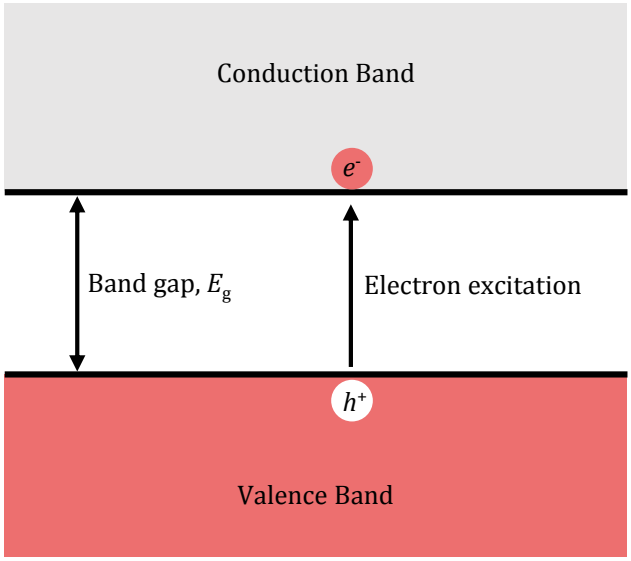

Figure 1.3. A graphical representation of the band gap of a semiconductor. The electron, e^-, has been excited to the conduction band from the valence band by absorbing the band gap energy, E_g, leaving a hole, h^+, in the valence band.

energy levels that electrons can reside in. As a result, the electronic structure of nanomaterials become a function of their size.

A simple, analytically tractable model for the quantisation of energy levels is the particle-in-a-box. In this model, a particle is placed in a one-dimensional region of space of width x. The potential along x is defined by $V(x)$. The box is defined as $0 < x < L_x$. When $x \leqslant 0$ or $x \geqslant L_x$, $V(x) = \infty$; else $V(x) = 0$. This results in zero probability that the particle will exist outside of the box. A graphical representation of this box can be seen in figure 1.4.

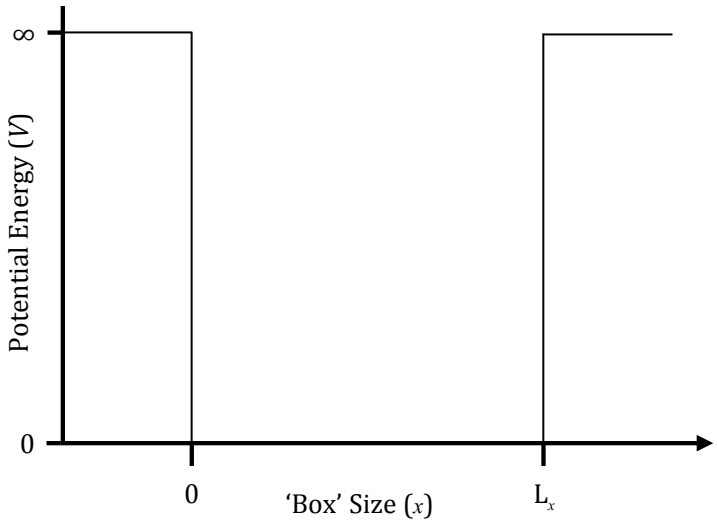

Figure 1.4. A schematic showing the particle-in-a-box. The box is defined by its edges at $x = 0, L_x$, inside which $V = 0$. Outside of this area the potential energy rises instantly to infinity.

The Schrödinger equation can be used to determine the available energies available to the particle trapped inside the box. In its general case, the time-independent Schrödinger equation is written as

$$\hat{H}\Psi = E\Psi, \tag{1.1}$$

where $\hat{H}$ is the Hamiltonian operator, Ψ is the wavefunction of the particle and E is the total energy of the particle. When postulating a time-independent one-dimensional particle, the Hamiltonian is defined as

$$\hat{H} = -\frac{\hbar^2}{2m}\frac{d^2}{dx^2} + V(x). \tag{1.2}$$

This can be solved with the general solution

$$\Psi(x) = A\sin(kx) + B\cos(kx) \qquad \text{when} \qquad E = \frac{k^2\hbar^2}{2m} \tag{1.3}$$

where A and B are constants. As previously stated $\Psi(0) = 0$, therefore $\Psi(0) = B$, as $\sin(0) = 0$ and $\cos(0) = 1$. As previously stated however, there is zero probability of the particle existing at $x = 0$, therefore $\Psi(0) = 0 = B$. This means, in this example, the wavefunction can be simplified to

$$\Psi(x) = A\sin(kx). \tag{1.4}$$

At the other limit $\Psi(L_x) = 0$, therefore $A\sin(kL_x) = 0$. A cannot be equal to zero, as then $\Psi(x) = 0$, implying that the particle is nowhere. As such, kL_x only satisfies all conditions when $\sin(kL_x) = 0$. This occurs when $kL_x = n\pi$, where n is a positive, non-zero integer. When input back into equation (1.4), it yields

$$\Psi(x) = A\sin\left(\frac{n\pi x}{L_x}\right) \qquad n = 1, 2, 3, ... \tag{1.5}$$

As k is related to n by $kL_x = n\pi$, it can be substituted into the energy component of equation (1.3), giving

$$E_n = \frac{n^2h^2}{8mL_x^2} \qquad n = 1, 2, 3, ... \tag{1.6}$$

As before, the n in equation (1.6) is limited to positive, non-zero integers. From this it can be concluded that, in order to satisfy the boundary conditions set above, the particle trapped in the box can only possess certain wavefunctions, and therefore only occupy certain discrete, quantised energy levels. Some of these wavefunctions are displayed in figure 1.5.

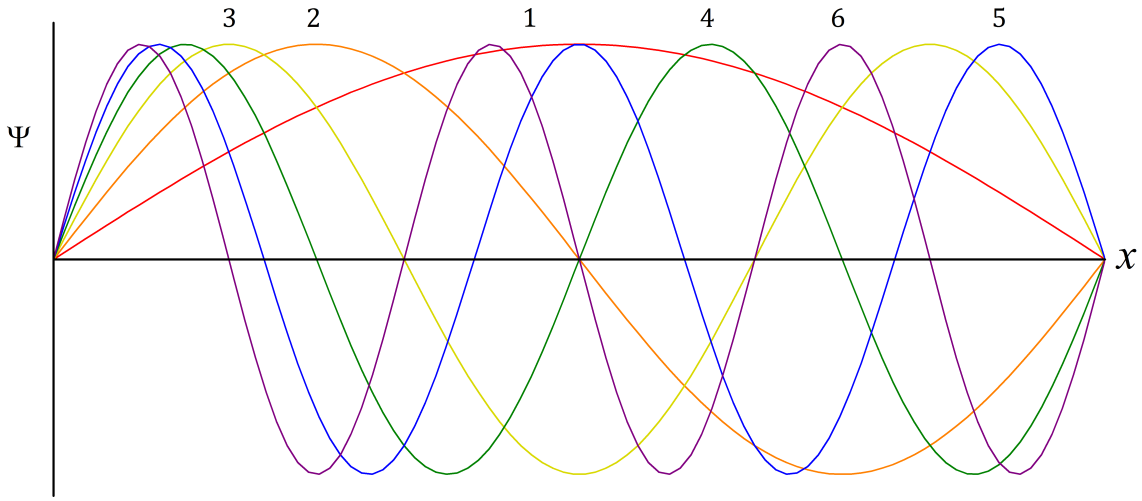

Figure 1.5. Discrete wavefunctions that are permitted in the particle-in-a-box model. The wavefunctions are standing waves, with labelled values of n from 1 to 6.

The particle-in-a-box model can also be extended to both two and three dimensional environments. In two dimensions, the potential along the new y-axis is defined as $V(y)$, with the new dimension defined as $0 < y < L_y$. As with to x, when $y \leqslant 0$ or $y \geqslant L_y$, $V(y) = \infty$; else $V(y) = 0$. As such, the time-independent two-dimensional Hamiltonian operator is defined as

$$\hat{H} = -\frac{\hbar^2}{2m}\left(\frac{d^2}{dx^2} + \frac{d^2}{dy^2}\right) + V(x, y). \tag{1.7}$$

Once solved, we obtain an equation for energy levels that is very similar to the one dimensional equivalent above, equation (1.6).

$$E_{n_1 n_2} = \frac{h^2}{8m}\left(\frac{n_1^2}{L_x^2} + \frac{n_2^2}{L_y^2}\right) \qquad n = 1, 2, 3, \ldots \tag{1.8}$$

The three dimensional particle-in-a-box can be treated in the same manner. The resulting equation has three n values, due to the additional new z-axis.

$$E_{n_1 n_2 n_3} = \frac{h^2}{8m}\left(\frac{n_1^2}{L_x^2} + \frac{n_2^2}{L_y^2} + \frac{n_3^2}{L_z^2}\right) \qquad n = 1, 2, 3, \ldots \tag{1.9}$$

From equations (1.6), (1.8) and (1.9) it can be seen that $E \propto 1/(L_x^2+L_y^2+L_z^2)$, resulting in a large

increase in energy levels as the box is reduced in size. Another consequence of box size reduction is an increase in the spacing of the energy levels.

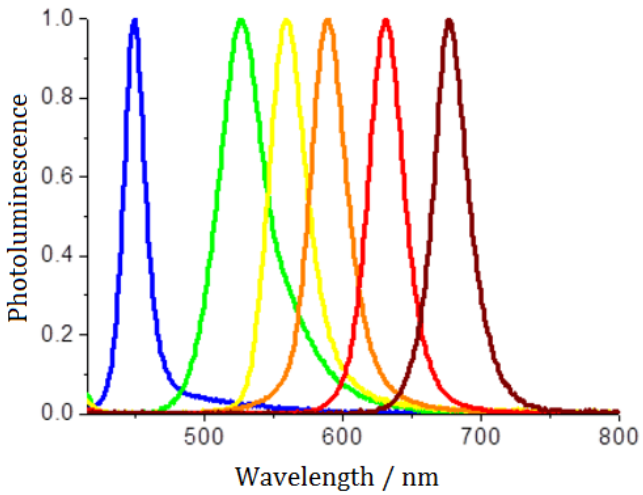

Figure 1.6. Example photoluminescence spectra of CdSe quantum dots. Sizes range from 2 nm (blue) to 5 nm (red). Graph adapted from Yuan and Krüger.[17]

These quantum size effects can be observed experimentally. Quantum dots are semiconductors with tunable photoluminescence, a typical example being CdSe nanoparticles with diameters ~4 nm. By varying the diameter of the quantum dot the band gap can be tuned, giving fluorescence at different wavelengths, and therefore different colours for the same material.[18] This occurs because of the change in ΔE_{2-1}, caused by variation of L. Example photoluminescence spectra for CdSe quantum dots, of a range of diameters, are shown in figure 1.6.[17]

1.2.2 Surface Area to Volume Ratio Effects

The surface area to volume ratio is much higher for nanomaterials than bulk materials. This is important because most chemical reactions occur on the surface of materials, not in the bulk. Surfaces contain a substantially higher proportion of unsaturated sites, due to them being at the end of a repeating unit, and so are much more reactive than the bulk.

As the dimensions of materials increases out of the nano-range and into bulk, the ratio of surface to volume decreases drastically. The surface area increases quadratically, whilst the volume increases cubically. This is shown graphically in figure 1.7, where the changes in surface area and volume for a spherical particle of varying diameter are shown. The result of this is that the ratio of surface area to volume drops off exponentially, according to L^{-1}. Consequently, to maximise the availability of reactive unsaturated sites, the surface area to volume ratio should be maximised by minimising particle size.

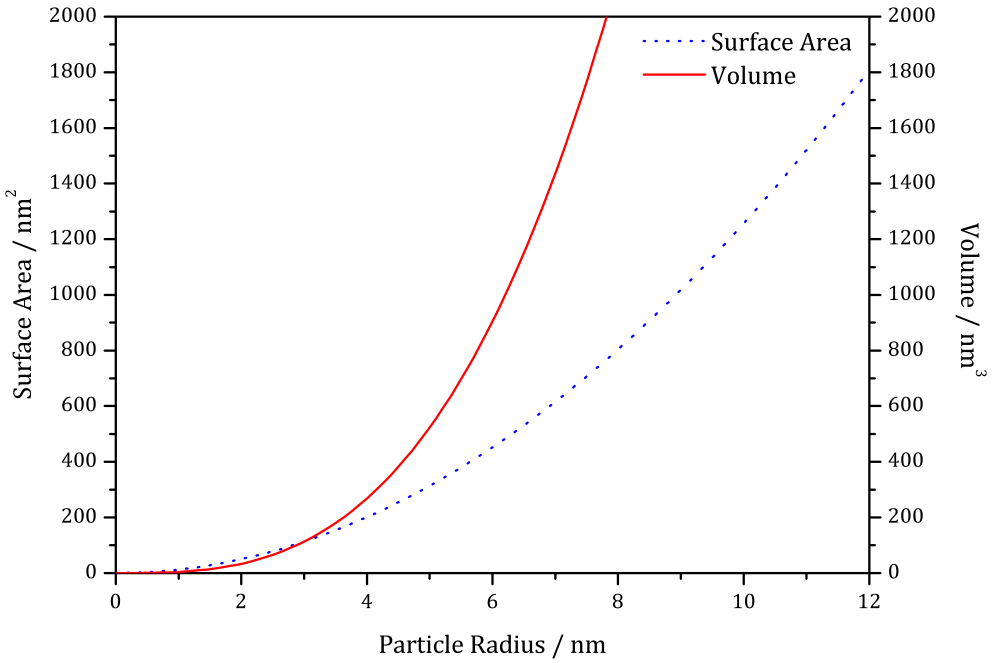

Figure 1.7. A comparison of the change in surface area and volume with particle diameter, for a spherical particle. The blue dotted line, representing the surface area, increases to the second power. Whereas the red solid line, representing the volume, increases to the third power.

An additional effect of minimising surface area is the consequential depression of the materials melting point. This phenomenon is not observed in bulk materials. Due to the reduced number of neighbouring atoms on the surface *i.e.* around half as many as in the bulk, each atom can form around half as many bonds. The reduced number of bonds holding the atom to the bulk reduces the required thermal energy to free the atom from the bulk. As the ratio of surface-to-bulk atoms increases, the average energy required throughout the particle decreases, resulting in depression of the melting point. This phenomenon can be observed with gold nanoparticles, shown in figure 1.8, where the reduction in particle size causes an exponential decrease in melting point; from 1064 °C in the bulk, to below 500 °C when the particles are only 2 nm across.[19]

1.2.3 Fermi Level and Energy

The Fermi level, E_F, is the thermodynamic work required to add one electron to the system. This can also be considered to be a hypothetical energy level, that has a 50 % chance of being occupied at any moment in time. As this energy level is hypothetical, it can exist in the forbidden region. If the Fermi level lies in the valence or conduction band then the material will be a conductor, as the electrons will be free to move around. Comparatively, if the Fermi level lies within the band gap, where the DOS is zero and occupation is forbidden, then the material will be either an insulator

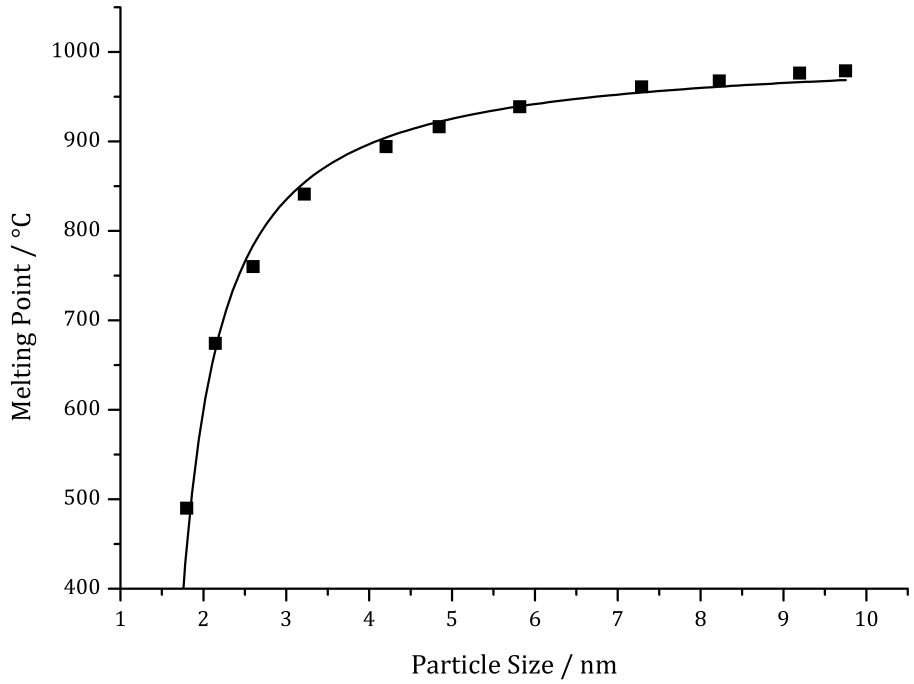

Figure 1.8. The variation of the melting point of gold with particle size. For comparison, the melting point of bulk gold is 1064 °C.[19] The source data is adapted from Schmid and Corain.[19]

or a semiconductor. The distinction between the two depends on the size of the band gap and the location of the Fermi level. If the band gap is large (>~4 eV) and the Fermi level is centrally placed then the material will be an insulator, while if the band gap is small (<~4 eV) or if the Fermi level is sufficiently close to a band then the material will be a semiconductor. This is demonstrated graphically in figure 1.9.

The Fermi energy of a compound is the energy difference between the highest-occupied and lowest-occupied energy level of a compound at absolute zero. At 0 K there is a sharp reduction in state occupation probability from 1 to 0, as such the Fermi energy can also be considered the Fermi level at absolute zero.

The thermal energy available at room temperature can be sufficient to promote some electrons from the valence band to the conduction band of a semiconductor. This promotion leads to conductivity in the semiconductor, which is proportional to the number of promoted electrons, and therefore the temperature of the material. Promoted electrons will eventually relax to their ground state, however at a set temperature there will be an equilibrium between electrons being promoted and electrons relaxing, leading to a steady number of excited electrons, called the carrier concentration. The relationship between temperature and the number of excited electrons can be explained using statistics. Specifically, the Fermi-Dirac distribution[20,21] shown in equation (1.10), where $\bar{n}_i$ is the average number of electrons in state i; ϵ_i is the energy level of state i; E_F is the Fermi level;

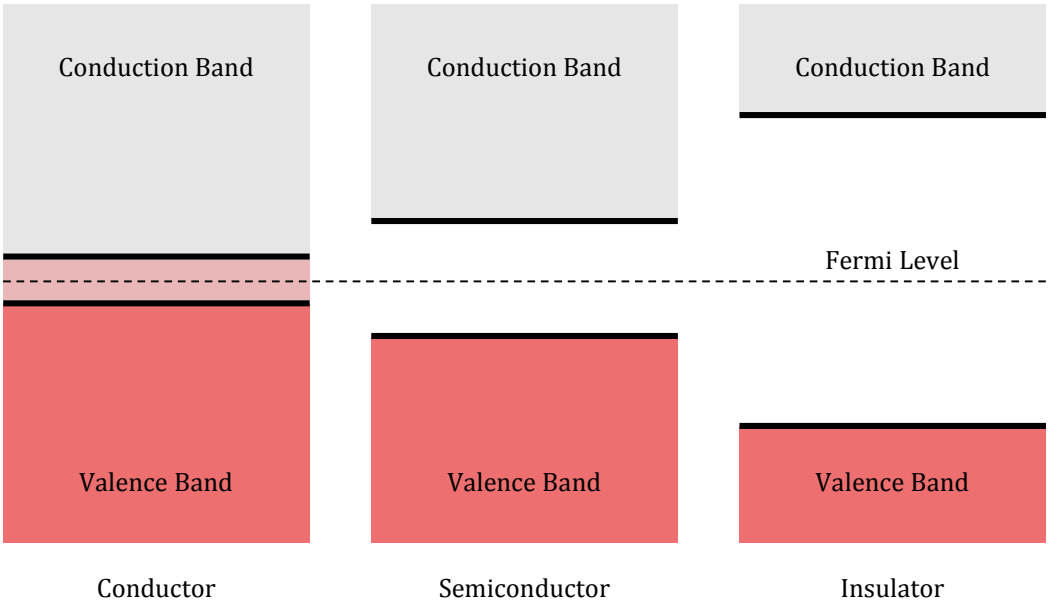

Figure 1.9. A graphical representation of the band gaps of conductors, semiconductors and insulators, with the location of the Fermi level labelled. The overlap of the conduction and valence band in the conductor is visible.

k_B is the Boltzmann constant; and T is the absolute temperature. This shows that the number of excited electrons is proportional to $e^{1/-T}$, indicating that as temperature increases, the excited population will increase, before levelling out and reaching a steady state.

$$\bar{n}_i = \frac{1}{e^{(\epsilon_i - E_F)/k_B T} + 1} \propto e^{\frac{1}{-T}} \tag{1.10}$$

1.2.4 Charge Carriers

The previously mentioned carrier concentration is the number of species available to carry a charge. In an typical semiconductor, where the Fermi energy is at the top of the valence band and the Fermi level lies in the middle of the band gap, electrons can be promoted to the conduction band in a number of ways. Thermal excitation has been mentioned already, two alternatives are to apply a voltage bias or to use photonic energy. The use of photons is preferable, as there is an unlimited and free source of photons readily available, namely the Sun. When a photon of sufficient energy ($\geqslant E_g$) strikes the surface of a semiconductor the photon is absorbed, and the energy promotes an electron to the conduction band. The newly formed electrical vacancy in the valence band is known as a hole, h^+, whilst for the promoted electron the notation e^- is used. Together the hole and electron are known as an exciton, a loosely bound electron-hole pair quasiparticle.

Both holes and electrons are capable of being charge carriers, however for this to occur they

need to have mobility through the crystal lattice. If this mobility is not sufficiently high enough then the electron will relax back to the valence band, recombining with the hole and preventing any conductivity. The energy lost through recombination is emitted either as thermal energy, or photonic energy through fluorescence. Increasing the mobility of charge carriers leads to a decrease in the electron-hole recombination, and therefore an increase in both conductivity and photoactivity. This can be achieved by increasing crystal purity and crystallinity.

The likelihood of an electron-hole pair recombining can be increased by the presence of impurities, such as acceptor centres and donor centres, which can act as carrier traps. The acceptor centres contain a positive charge, and so attract and hold electrons, reducing their mobility until they recombine with a hole; and vice versa for donor centres and holes. These carrier traps can be introduced accidentally or intentionally, generally by doping with additional elements.

The mobility of an electron is generally greater than that of a hole. This is because carrier mobility is inversely proportional to both the recombination rate and the carrier's effective mass, m^*. The recombination rate is the same for both the electron and the hole, therefore the difference in mobility is caused by the differences in effective mass. The effective mass is the mass that the carrier appears to have when responding to external forces, such as voltage bias. It is often very different from the actual mass of an electron, m_e, because of the curvature of the bottom of the conduction band and top of the valance band (which are normally not as flat as depicted in figure 1.3). Some typical examples of electron and hole mobility, and effective masses can be seen in table 1.1.[22–26]

Table 1.1. Typical values for carrier effective masses and mobilities.[22–26]

Material	Electron Effective Mass / e_m	Hole Effective Mass / e_m	Electron Mobility / $cm^2\ V^{-1}\ s^{-1}$	Hole Mobility / $cm^2\ V^{-1}\ s^{-1}$
Si	1.09	1.15	1400	450
ZnO	0.29	1.21	2000	20
Ge	0.55	0.37	3900	1900

1.2.5 Imperfections: Dopants and Vacancies

In order to increase both the light absorption range and photoactivity of a semiconductor, such as TiO_2, it is possible to add dopants to the crystal lattice. The effect of the dopant depends on both the element that is used and the dopant concentration. When a comparatively electron-rich element is added to TiO_2 the Fermi level is moved up, increasing the number of electrons in the

conduction band which increases conductivity. Conversely, addition of a comparatively electron-deficient element causes the Fermi level to move down. Both cases can lead to the introduction of interstitial energy levels in the forbidden band gap. These levels act as 'stepping stones' for the electrons, meaning that they can absorb multiple photons of energy $<E_g$ to reach the conduction band.

The coordination number of the dopant is also important. In titania, substituting some of the Ti^{4+} lattice atoms with M^{n+}, where n<4, can lead to an increase in oxygen vacancies. Example dopants include Co^{2+}, Ni^{2+} and Zn^{2+}.[27] Rutile is the least dense of the polymorphs, and therefore the most able to accommodate additional oxygen vacancies. This leads to an effect where doping with a low-coordinating cation can lead to the rutile phase being more stable than normal. This in turn lowers the temperature required to convert from the kinetically stable anatase to the thermodynamically stable rutile. The opposite is also true, doping with an element such as phosphorus can lead to a large decrease in oxygen vacancies. This decrease causes a drop in the thermodynamic stability of rutile, consequently increasing the temperature required for a phase change by up to 300 °C.[28]

The creation of oxygen vacancies is also credited with an increase in photoactivity in titania. They act as important adsorption points and active sites for catalysis, whilst simultaneously creating Ti^{3+} centres.[29] These Ti^{3+} centres can act as dopants independently. As such, the introduction and resulting properties of oxygen vacancies in TiO_2 has been investigated thoroughly.[30–32] It has been revealed that the number of oxygen vacancies can directly affect the charge carriers,[33] electronic structure,[30] and surface properties[34] (though not the hydrophilicity[35]) of TiO_2. Successful attempts have been made to 'fill in' the oxygen vacancies, to prevent their reoxidation by atmospheric oxygen. An example was reported by Ihara *et al.*, who successfully doped with nitrogen, forming $N_O^{\times}$ and preventing reoxidation.[36]

Vacancies, interstitial atoms, and other crystal lattice defects can be displayed using Kröger-Vink notation.[37] Where, for lattice site A_B^C, A is the atom or a vacancy (*e.g.* Ti or V), situated in position B (*e.g.* Ti or i for interstitial), with C describing the electrical properties. These electrical properties are shown with $^{\bullet}$ or $'$ to cumulatively demonstrate a positive or negative charge respectively, or an $^{\times}$ to show a neutral charge. For example, V_O'' is a vacancy at an oxygen lattice site with a double negative charge. Holes are displayed as $h^{\bullet}$ or h^{+}, and electrons are displayed as e' or e^{-}.

The formation of oxygen vacancies in TiO_2 is displayed using Kröger-Vink notation in scheme 1.1(a), where a lattice oxygen is lost forming a vacancy and dioxygen. The formation of oxygen

vacancies with interstitial titanium atoms and free electrons is shown in scheme 1.1(b) and (c). The formation of titanium vacancies, and the corresponding number of holes, is shown in scheme 1.1(d). Scheme 1.1(e) shows electron-hole recombination, resulting in mutual elimination. All of these reactions are reversible.[38]

$$O_O^{\times} \rightleftharpoons V_O'' + 2\,e^- + 0.5\,O_2 \quad \text{(a)}$$

$$Ti_{Ti} + 2\,O_O \rightleftharpoons Ti_i^{\bullet\bullet\bullet} + 3\,e^- + O_2 \quad \text{(b)}$$

$$Ti_{Ti} + 2\,O_O \rightleftharpoons Ti_i^{\bullet\bullet\bullet\bullet} + 4\,e^- + O_2 \quad \text{(c)}$$

$$O_2 \rightleftharpoons 2\,O_O + V_{Ti}'''' + 4\,h^{\bullet} \quad \text{(d)}$$

$$e^- + h^{\bullet} \rightleftharpoons nil \quad \text{(e)}$$

Scheme 1.1. The formation of oxygen and titanium vacancies & interstitials, and recombination of electron-holes, using Kröger-Vink notation.[38] Schemes (a)-(c) show free electron formation through creation of oxygen vacancies and titanium interstitials, scheme (d) shows the formation of free holes, and scheme (e) shows electron-hole recombination.

1.2.6 The Bands of Titania

The band gaps of rutile and brookite are both direct, whereas the band gap of anatase is indirect. This refers to the change in the value of crystal momentum, the $\boldsymbol{k}$-vector. When there is a change in $\boldsymbol{k}$-vector, electron excitation is hindered because simultaneous phonon absorption is required in addition to the photon, in order to conserve crystal momentum (photons cannot carry crystal momentum). This leads to a more facile electron excitation in brookite and rutile, compared to anatase. Literature suggests that anatase, however, is the more active photocatalyst,[39,40] having slower electron-hole recombination due to the change in $\boldsymbol{k}$-vector.[41] In an attempt to utilise this, many commercial suppliers provide a product with a mixture of anatase and rutile. The principle behind them is that the electrons are promoted in the rutile phase, before transferring to the anatase phase to slow down recombination. There is also very recent evidence that the valence band of anatase is lower than in rutile, resulting in holes transferring from anatase to rutile.[42] One such commercial product is Aeroxide® P25, a nanoparticulate powder of approximately 75 % anatase and 10 % rutile, with the remaining 15 % being amorphous.[43] P25 features heavily in this thesis.

The conduction band of TiO_2 consists of the empty 3d orbitals of titanium(IV). The bottom of the conduction band is, specifically, the triply degenerate t_{2g} orbital set. The valence band of TiO_2 is made up of the filled 2p orbitals of the oxygen dianion. It is possible for the orbitals of doped elements to interact and hybridise with the orbitals of TiO_2. For instance, it was reported

by Asashi *et al*. that when doping with nitrogen, the nitrogen 2p orbital hybridises with the oxygen 2p orbital due to their closeness in energy.[44] This resulted in a widening of the valence band, and consequent narrowing of the band gap. This band gap narrowing had the effect of moving the absorption cut-off from 400 nm to 500 nm, increasing the efficiency and versatility of the catalyst.

1.3 Photocatalysts for Water Splitting

One of the major research directions for TiO_2, and semiconductors in general, is the use of them in photovoltaics as a renewable energy source. However due to the diurnal nature of sunlight, the produced energy needs to be stored for use at night. The most common forms of energy storage, unfortunately, have a very low energy density compared to liquid hydrocarbons. For example, batteries at ~0.5 MJ kg^{-1}, super capacitors at ~0.01 MJ kg^{-1} and flywheels at ~0.5 MJ kg^{-1}; compared to 48 MJ kg^{-1} for diesel.[45] This low energy density hinders the desirability to switch from hydrocarbons to solar energy.

An elegant chemical solution to this problem is the creation and use of dihydrogen, which has an energy density of 142 MJ kg^{-1}.[46] The main hydrogen forming reaction is the splitting of water. This is shown in scheme 1.2, where (a) and (b) are the cathodic and anodic half-reactions respectively, and (c) is the combined final reaction. The splitting of water is obviously not spontaneous, and a theoretical energy input of 1.23 V is required. Though in practice an overpotential is also needed to account for kinetic effects and to surpass the activation barrier.[47] Generally this overpotential takes a value of 0.25 V to 1.20 V.[48–50]

$$2\,H^+ + 2\,e^- \longrightarrow H_2 \quad \text{(a)}$$

$$2H_2O \longrightarrow O_2 + 4\,H^+ + 4\,e^- \quad \text{(b)}$$

$$H_2O \longrightarrow H_2 + {}^1/_2\,O_2 \quad \text{(c)}$$

Scheme 1.2. The cathodic (a) and anodic (b) half reactions of the water splitting reaction. The combined overall reaction is shown in (c).

This required energy input is often reduced by using a catalyst. These catalysts work by providing an alternative pathway for the oxidation step (scheme 1.2(b)). Any water splitting system requires this step, which necessitates the coupling of a four-electron–four-proton transfer. This is considered to be the primary hindrance to the large scale uptake of hydrogen energy storage,[51] as the accompanying two-electron reduction proceeds readily.

1.3.1 Cobalt Oxide as a Catalyst

A reported catalyst that has achieved a remarkably low overpotential is the cobalt catalyst by Kanan and Nocera.[52] The catalyst is primarily comprised of amorphous cobalt(III) oxide, with the addition of phosphate as a major constituent.[53] The phosphate is responsible for proton mobility, and can be replaced with similar compounds, such as methylphosphonate.[54] The catalytic film is synthesised by low voltage electrolysis of a phosphate buffer solution containing Co^{2+} cations, resulting in the electrodeposition of cobalt oxide and phosphate on the anode. The anode can be any conductive material, such as titanium or fluorine-doped tin oxide (FTO). If the potential is greater than ~1.3 V, then oxygen is evolved from the anode at an increasing rate, according to the film thickness that has been deposited. Once this film has formed, there is no longer a requirement for cobalt cations in the solution — the catalytic evolution of oxygen can be conducted with the preformed cobalt oxide thin film and a phosphate buffer solution.

The catalyst forms by the oxidation of the aqueous cobalt(II) ions to cobalt(III). The cobalt(II) ion is known to be highly labile and prone to substitution in aqueous environments, whereas the cobalt(III) ion is comparatively inert.[i] As the cobalt is reduced at the anode it becomes less soluble, depositing onto the anode. It has been noted that the film only forms on oxidation to cobalt(II).[45] As the water oxidation reaction requires the transfer of four electrons, there is obviously a change in oxidation of the cobalt metal in the film. It is believed that during the catalytic cycle the cobalt centre goes through the +2, +3 and +4 oxidation states.[56]

This leads to both an issue of stability and the solution of self-repair. When the catalyst is in the +2 oxidation state, it can resolvate into the solution as cobalt phosphate — dissolving the film. However, as the reaction conditions for oxygen evolution are the same as for the film-forming reaction, the cobalt phosphate is simply reoxidised under the applied potential and redeposited onto the surface, along with the phosphate. This leads to a dynamic equilibrium between cobalt(II) in solution and cobalt(III) in the film, resulting in continuous catalyst repair. This behaviour has been monitored and confirmed with the use of radioactive ^{57}Co and ^{32}P.[53] The mechanism is considered *self-repair* of the catalyst, as opposed to *repair* of the catalyst, because it exists as an equilibrium on the catalytic cycle, not off it. For this reason, some consider the catalyst to be unique.[57]

The mechanism of the reaction, as previously mentioned, cycles through three oxidation states of cobalt.[45,53,56,57] A proposed catalytic cycle is shown in scheme 1.3. Using cobalt(III) as the

[i] This is because octahedral Co^{2+} is d^7, resulting in occupation of the e_g orbital. In Co^{3+} the e_g orbital is unoccupied, increasing the crystal field stabilisation energy.[55]

start point, the catalyst is first oxidised to cobalt(IV) by proton-coupled electron transfer (PCET), where an electron and proton are both transferred away from the metal centre by a concerted means, though not by a radical pathway. The proton carrier is the phosphate buffer. The formed cobalt(IV) oxo species then undergoes reduction to cobalt(II) with the elimination of dioxygen, in what is currently considered to be both an irreversible process and the rate limiting step.[56] The cobalt(II) is then reoxidised back the the starting cobalt(III) species. An alternative pathway via aqueous cobalt(II) is also possible, which is the *self-repair* route, allowing for the continuous renewal of the catalytic film.

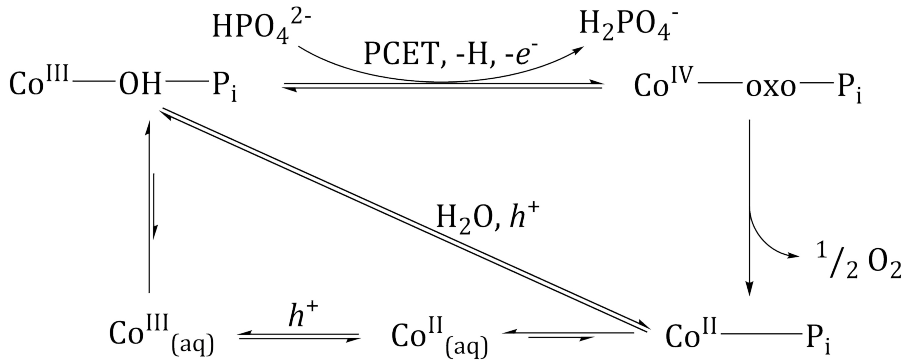

Scheme 1.3. The proposed catalytic cycle for the cobalt oxygen evolving catalyst reported by Nocera.[52] Scheme adapted from Kanan *et al*. and Surendranath *et al*.[45,56] P_i indicates the inorganic phosphate group.

It is important to note that it is probable the active sites of the cobalt catalyst do not completely cover the surface of the film. Solid state catalysts tend to have active sites located at imperfections on the surface, such as edges, steps, corners and kinks.[58] These imperfections cause breaks in the regularity of the crystal lattice, leading to unsaturated sites. It is at these unsaturated sites that heterogeneous catalysis takes place.

1.3.2 Molecular Mimics

The study of large heterogeneous catalysts, such as the previously mentioned cobalt oxide catalyst, is difficult. This is mainly because there are limited analytical techniques that can be used *in situ* to monitor the reaction sites during catalysis. For this reason, molecular mimics of larger catalysts is becoming increasingly common.[59] In this thesis, new homogeneous molecular models of the heterogeneous cobalt oxide catalyst are synthesised, with the aim to reproduce the catalytic environment with coordination complexes. A recent success in this field is the synthesis by Karunadasa *et al*. of the organometallic mimic of molybdenum disulfide,[60] a promising heterogeneous catalyst

to replace platinum for hydrogen generation.

Another difficulty that arises from the attempted study of solid state catalysts, is that the majority of the catalyst material is in the bulk, which is not where the catalytic activity occurs. This prevents the use of techniques such as powder X-ray diffraction (pXRD) for gaining insight on the active sites. There is the additional problem that a large portion of the surface is inactive — the imperfections at edges *etc*. only make up a small amount of the surface. This leads to very little data being available for the the actual site of catalytic activity.

By using molecular mimics solution phase analytical techniques can be used. These techniques, which are unavailable for heterogeneous catalysts, include solution-phase multinuclear nuclear magnetic resonance (NMR), *in situ* Fourier transform-infrared spectroscopy (FTIR) and electronic absorption information via UV-visible spectra. There is the additional bonus that, if the active site can be recreated along with its activity, a vastly increased proportion of the material would be catalytically active as the entire compound would essentially be composed of active sites.

The model complex of a good surface mimic should have the same, or similar, coordination environment, sterics and electronic configuration as the catalyst in question. These features can be managed with some control by varying the properties of the coordinating ligands. Many features can be governed, for example variance in chelation can change the coordination number, an increase in the size of the ligands leads to an increase in the steric bulk of the environment, and modification of ligand functional groups can change the electronic configuration.

As previously discussed, the cobalt metal centre in Nocera's oxygen evolving catalyst undergoes transitions between cobalt(II), cobalt(III) and cobalt(IV). Any molecular mimic needs to be able to support cobalt in these unusually high oxidation states. There is some precedence for this, specifically the work of Theopold's lab,[61] who reported the successful synthesis, and characterisation via single crystal X-ray diffraction (XRD), of an alkyl cobalt(IV) species.[ii] The cobalt(IV) centre was stabilised using four 1-norbornyl (nor) ligands as large bulky protection to prevent other molecules reaching the reactive metal centre, whilst the highly electron donating properties of norboryl partially stabilise the electron deficient cobalt. The stabilising effects of a tetrakis(1-norboryl) ligand arrangement is so great, that cobalt(V) has also been isolated in the form $[Co(nor)_4][BF_4]$.[63]

A common ligand for organometallic surface mimics is tris(*tert*-butoxy)silanol.[64] This ligand has many advantages, having large *tert*-butoxy fragments helps the ligand dissolve in hydrocarbon solvents, whilst also acting as a convenient handle for NMR analysis. The silyl ether helps simulate

[ii] It should be noted however, that the complex in question was first synthesised, though not fully characterised or explored, by Bower and Tennent.[62]

bonding to silica, a common catalyst support in industry. The O−^{t}Bu motif can undergo secondary coordination to the metal centre via the oxygen atom, enabling complete coordination. The *tert*-butoxy group is also a strong electron donator, which will both help activate the metal centre and stabilise higher oxidation states. Finally, the large body of *tert*-butyl groups saturates the molecules sterics, preventing premature reactions with undesired substrates. For these reasons, initial studies in chapter 5 begin with this ligand.

1.4 Homogeneous Catalysis of Other Small Molecules

Water is only one of several small molecules that have been of recent interest to scientists. Small molecules such as O_2, N_2 and CH_4, are also appealing targets for synthetic chemists. Whilst being essential for terrestrial biological activity, many of them are also implicated in global warming and ozone depletion due to the large industrial generation of small molecules, such as CO_2. Despite this, they are useful in many carbon-neutral energy supply schemes because of the large amount of energy that can be stored in their bonds. Consequently much research has been conducted on maximising our use of small molecules, with the process considered the current prime challenge for chemists, by some.[65] Some of the work in this thesis looks at the design and synthesis of new homogeneous catalysts, with the aim to activate one or more of these gases.

Many small molecules are inert at standard temperature and pressure, and therefore require activation. Even O_2 is relatively unreactive in its triplet ground state, being sluggish to react with common singlet state molecules due to the conservation of spin quantum numbers, requiring activation energy to initiate reactions, often via singlet oxygen.[66] In order to provide the required energy the substrate is normally adsorbed to the surface of a heterogeneous catalyst, whilst a homogeneous catalyst usually coordinates the substrate to the metal centre. Once coordinated it is able to undergo a variety of transformations, leading to the formation and release of the product. For the activation of small molecules the use of large bulky ligands is normally required, in order to minimise the available space around the metal centre and prevent the coordination of undesired compounds. The ligands are normally flexible, in order to accommodate the change in metal oxidation which will occur, for this reason chelation is common. The use of electron-donating or electron-withdrawing motifs on the ligands can also be used to fine tune the electronics of the catalyst, as can the use of π-bonding.

A typical example of a dioxygen activation catalyst is the cobalt(II) species N,N′-ethylenebis-

(3-*tert*-butylsalicylideniminato)cobalt, **1**. This complex is stable at room temperature under air, however reacts with pure dioxygen in the presence of pyridine to form the octahedral cobalt(III) complex, **2**, shown in scheme 1.4.[67] The binding causes a reduction of the bond order of dioxygen, seen in the elongation of the O−O bond from 1.21 Å to 1.35 Å. The angle between cobalt and the bound dioxygen is 116.4° in the crystal structure, indicating that the oxygen is binding through one of its lone pairs.

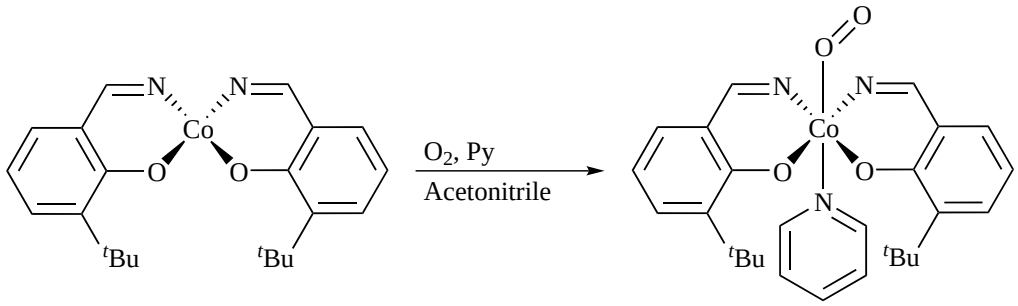

1 **2**

Scheme 1.4. The activation of O_2 by complex **1**.[67]

Binding of carbon dioxide typically requires a nucleophillic metal centre and a coordination vacancy. Carbon dioxide is weakly electrophillic, and will bind to metals in a variety of manners. A common method is η^1, where the carbon atom forms a sigma bond to the metal centre. This bond is reinforced through back-bonding from the d_{z^2} orbital on the metal to the π^* orbitals on the CO_2, which align. The η^1 bind mode is not robust however, and is only one of nine recognised binding modes for CO_2.[68] An example of the activation of CO_2 is shown in scheme 1.5, wherein complex **3** is placed under a partial pressure of CO_2, after which X-ray suitable crystals of coordinated complex **4** are collected.[69] The O−C−O bond angle in the crystal structure is 126°, which indicates that there is a substantial amount of π-back-bonding into the CO_2 π^* orbital. This is also shown in the C−O bond elongation from 1.16 Å to 1.25 Å.

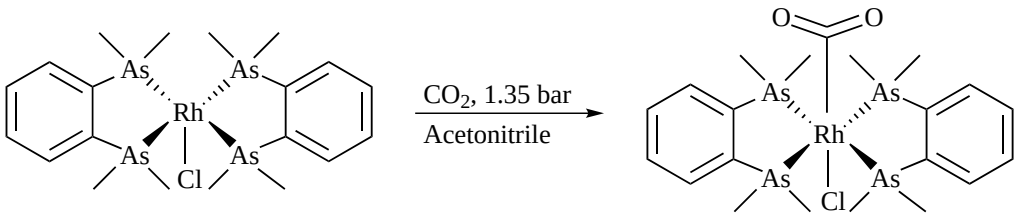

3 **4**

Scheme 1.5. The activation of CO_2 by complex **3**.[69]

The activation of carbon monoxide has been exploited on an industrial scale for many decades, the famous example being the Monsanto process for the synthesis of acetic acid from methanol and

carbon monoxide.[70] Due to its polar nature and available π^* orbitals, carbon monoxide is relatively active for a small molecule, for instance it is infamous for having a higher binding coefficient with haemoglobin than oxygen. For this reason there are numerous academic texts committed to the field.[71,72] One example complex for the activation of CO is the rhodium complex **5**. Shown in figure 1.10, complex **5** has an eightfold increase in activity for carbonylation over the original Monsanto catalyst.[73] This gain in activity is due to an increase in electron donation to the metal centre, combined with an optimisation of the steric environment of the catalyst.[74]

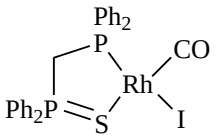

5

Figure 1.10. A rhodium complex capable of using carbon monoxide to form acetic acid from methanol. It is eight times more active than the original Monsanto catalyst.[73]

The activation of dinitrogen is an impressive feat. Nitrogen is incredibly inert, having a bond order of three and a bond strength of 940 kJ mol^{-1}.[75] Compared to carbon monoxide, with whom it is isoelectric, it is more difficult to activate because it has no dipole, is a weaker σ-donor and a poorer π-acceptor.[76] Despite this, there are numerous examples of activated dinitrogen with many transition metals.[77–79] The degree of nitrogen activation depends on the amount of back-bonding into the π^* orbitals of nitrogen; this can be measured, as with other small molecules, by observing the N−N bond length in the coordinated complex. As one may expect, there are numerous binding modes for N_2. The most common however is μ-η^1:η^1, involving a bimetallic complex. An example of this type of binding is shown in scheme 1.6, where the mononuclear niobium complex **6** reacts with N_2 and sodium triethylborohydride to form the bimetallic complex **7**.[80] The N−N bond length in the activated complex **7** is 1.34 Å, compared to 1.10 Å for free nitrogen. This large bond elongation means that complex **6** is classed as a strong activator of N_2.[76]

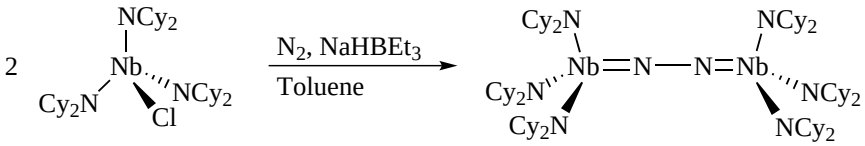

6 **7**

Scheme 1.6. The activation of N_2 by complex **6**.[80]

1.5 Aims of the Research Work

This thesis presents research conducted on the catalytic activation of small molecules, with relevance to industrial chemistry. It was sponsored by Innovate UK in collaboration with PpTek Ltd. The work focuses both on the use of heterogeneous photocatalysts for the full and partial oxidation of siloxane and methane, as well as the the design and synthesis of novel model systems and homogeneous catalysts. Chapter 1 provides background information on the topics that have been studied. This includes the electronic structure of photocatalytic semiconductors, details on water-splitting, and an introduction to small molecule activation using homogeneous catalysts.

The first family of small molecules is addressed in chapter 2, the siloxanes. These can be straight chain or cyclic, with typical masses from 160 g mol^{-1} to 460 g mol^{-1}. The standard siloxane used in this work is hexamethyldisiloxane, L2, which is a good model for all siloxanes. Siloxanes are present in biogas, and as such pose a risk to the equipment that uses biogas as an energy source. Current techniques for the removal of siloxanes are very energetically demanding, and environmentally unfriendly. Therefore a new approach was devised, using photocatalytic titania nanofibres to fully oxidise the siloxanes to silica, effectively removing them from the gas stream. This new technology was tested in an industrial setting, with promising results. Attempts to improve the activity of the catalytic nanofibres are also made by doping. The optimal dopant was found to increase activity three-fold.

The ideas developed in oxidising siloxanes were then applied to methane, and discussed in chapter 3. Methane is a valuable source of energy for the world's population, however much is lost due to inefficient and costly storage and transport of the gas. Therefore, there is a market for the activation of methane to other chemicals, and a description of the current techniques for this is presented. Previous studies have tried to partially oxidise methane using photocatalysts in the presence of oxygen, however a large amount of CO_2 is always formed. Therefore, it was envisioned that removal of the oxygen could prevent the formation of CO_2. Instead, this work uses hydroxyl radicals to oxidise methane, formed from the photoactivity of TiO_2 with water. Methane oxidation was seen to occur, and the formation of carbon dioxide was monitored.

In order to allow for better control of the electronics and catalytic properties of the catalysts, investigations were conducted on the homogeneous catalysis of small molecules. Therefore, the synthesis and use of triptycene as a ligand for organometallic complexes is reported in chapter 4. Starting with the synthesis, isolation and full characterisation of a novel triptycene precursor, the

chapter goes on to describe the synthesis of a variety of triptycene ligated metal centres. This marks the first time triptycene has been used as a σ-bound ligand for a transition metal. The novel complexes are characterised, with single crystal X-ray structures recorded. The activity of a number of small molecules with these complexes is then reported, with the successful activation of dioxygen with a cobalt triptycene complex, forming a new oxygen-bound tetrahedral cobalt complex. This is the first step on a new catalytic cycle.

A number of homogeneous catalysts were then designed and synthesised, using the heterogeneous cobalt oxide system developed by Nocera as a model.[52] The aim was to allow for the easy tuning of the electrical and catalytic properties, and allow for the use of solution-phase *in situ* analytical techniques. This in turn should provide a better understanding of the original heterogeneous catalyst. Reported in chapter 5, the work involved the synthesis of new ligands and complexes, which were fully characterised, including a crystal structure. A thorough exploration of their electrochemistry was undertaken, including electronic absorption, variable temperature magnetic studies and cyclic voltammetry. The new information on these novel molecular mimics can be used to further understand the catalytic water-splitting ability of cobalt oxide.

All experimental procedures are reported in chapter 6. The chapter begins with general remarks about synthesising air sensitive compounds. Specific experimental conditions for all reactions are then provided, along with characterisation data.

Chapter 2

Photocatalytic Nanofibres for Biogas Purification

Titanium dioxide is a well-known photocatalyst, and has been reported to generate hydroxyl radicals from water when illuminated with UV_A radiation.[81] This chapter explores the use of photocatalytic titania nanofibres to generate these radicals, using them to fully oxidise the siloxanes in biogas to silica.

2.1 Economics of Biogas

Siloxanes are small molecules often found in biogas, they originate primarily from old cosmetic products which have been sent to landfill. Their activation, and subsequent oxidation to silica, is investigated as an improved means of removing them from the gas stream.

2.1.1 The Energy Crisis

In 2012, the world's current energy consumption was an average of 426 TW h each day.[82] Currently 81.7 % of this comes from the non-renewable resources known as fossil fuels,[83] such as coal, oil and gas. A breakdown of energy sources is shown in table 2.1. These sources of energy were historically easy to access, easy to transport, and easy to obtain energy from; humanity has had millennia learning how best to use the heat and light created from burning fossil fuels.[84]

There are a number of problems however with the continued, and increasing, use of fossil fuels. These energy sources are produced over millions of years by the high temperature and pressure present in the Earth's crust. However, over the past century, the rate that these fuels have been extracted has increased drastically, which leads to the first issue: peak oil.

Peak oil is an event that was famously described by Marrion King Hubbert in 1956.[85] He used

Table 2.1. Sources of energy across the globe, averaged per day, for 2012.[82]

Fuel Source	Consumption / TW h d^{-1}	Percentage / %
Coal	123.6	29.0
Crude Oil	134.0	31.4
Natural Gas	90.6	21.3
Nuclear	20.5	4.8
Renewables[(a)]	57.4	13.5
Total	426.1	100.0

(a) In this table, renewable energy sources include hydro, biofuel, geothermal, solar, wind & heat.

an analytical model[iii] describing the extraction rate, and subsequent decline, of US oil reserves. Shown in figure 2.1, he successfully predicted that the highest extraction rate of US oil would occur in approximately 1970, and that falling reserve levels, and the increased difficulty in reaching those reserves, would cause an ensuing slow-down of oil extraction. Hubbert's prediction was accurate until recent years, when the advent of hydraulic fracturing caused a temporary respite for the petroleum industry.

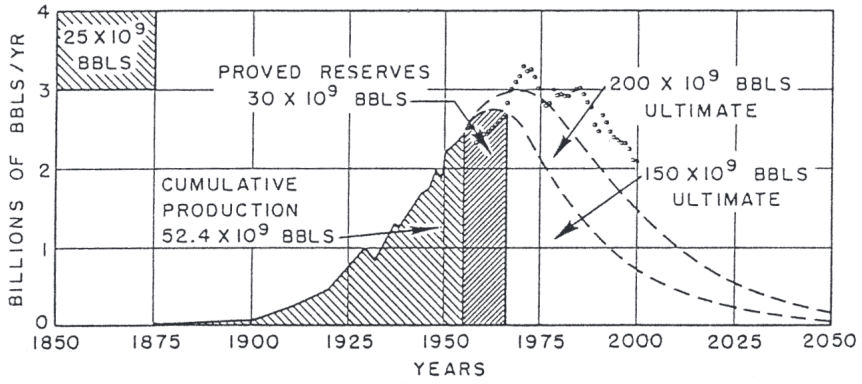

Figure 2.1. Hubbert's graph estimating US oil production, peaking in 1970 for his higher estimate. The small circles show actual production for 1956 through to 2000.[87]

Hubbert's model can be applied to global oil reserves. The result of this modelling depends on many factors, including but not limited to, estimations of future oil discoveries and the cost of extracting and refining deep and non-conventional reserves. The main themes however, all point to the same eventual conclusion: that oil is a finite resource, and will at some point run dry. This is the crux of peak oil.

The second issue with our continued use of fossil fuels is more contested; that of climate change. Fossil fuels are made up of a large variety of hydrocarbons; including alkanes, cycloalka-

[iii]The analytical model used by Hubbert was the logistic equation, first described by Verhulst in 1845 with relation to population studies.[86]

nes and aromatics. When a fossil fuel is fully combusted its components are oxidised, as shown in scheme 2.1. As the major components of fuel are hydrocarbons, the major components of exhaust gases are carbon dioxide and water. Carbon monoxide can also be formed when combustion is incomplete, as well as a large variety of other gases (nitrous and sulphurous oxides) and particulates (carbon). These components cause a multitude of problems, the main measure of their global impact, however, is carbon dioxide.

$$C_xH_y + (x + y/4)\,O_2 \longrightarrow x\,CO_2 + y/2\,H_2O$$

Scheme 2.1. The complete combustion of a general hydrocarbon. Incomplete combustion occurs when there is a substoichiometric amount of oxygen.

Carbon dioxide, once released, is mostly found in the troposphere and stratosphere (from ground level up to approximately 50 km).[88] At these altitudes the gas is exposed to the black body radiation of the Earth, which contains a proportionally large amount of infrared. Carbon dioxide molecules absorb this radiation (which would otherwise be emitted to space) and then emit it, warming the Earth's atmosphere and surface. This phenomenon is known as global warming, and gives carbon dioxide its label as a greenhouse gas.

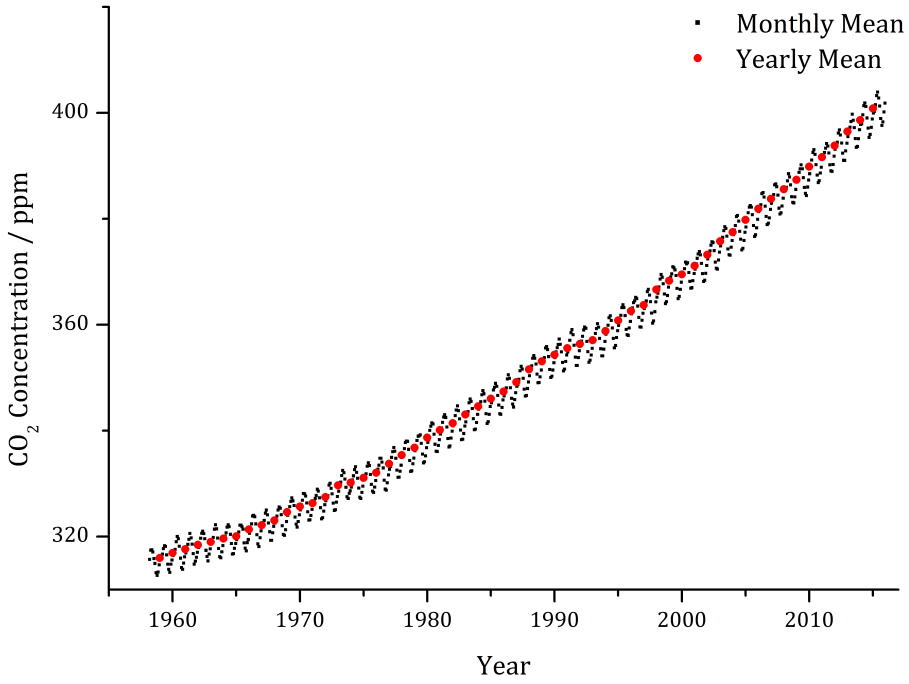

Figure 2.2. Atmospheric CO_2 concentration. The data has been collected continuously at the Mauna Loa Observatory, Hawaii since 1958.[89–91] The black dots shows the seasonal monthly rise and fall of CO_2 levels. The red dots shows the annual mean.

The level of greenhouse gases, specifically carbon dioxide, has been rising exponentially in recent years. By measuring historic values, it has been shown that the rise started suddenly in

approximately 1850. This coincides with when humans started burning fossil fuels *en masse* — the start of the industrial revolution. Direct measurements have been taken continuously since 1958 at the Mauna Loa Observatory in Hawaii, plotted in what is known as the Keeling curve, shown in figure 2.2.[89–91] The Keeling curve shows the unmistakable increase of carbon dioxide, along with the seasonal rise and fall in levels.

The rise in anthropogenic carbon dioxide emissions, and other greenhouse gases, is causing a rise in global temperature. This global warming has many major consequences, including melting of the ice caps, and the subsequent increase in sea levels and decrease in salinity; disruption of established oceanic and atmospheric currents, and the subsequent prevalence in extreme weather incidents; and agricultural and political instability, leading to ensuing environmental mass-migration.

2.1.2 Renewable Energy

In order to meet the world's energy requirements, it is clear that alternative sources of energy are required. Ideally this energy should come from renewable sources, such as wind or sunlight, instead of non-renewable sources like coal or uranium. Current sources of renewable energy account for only 13.5 % of the world's energy consumption, which is broken down in table 2.2.

Table 2.2. Global production values for renewable energy sources in 2011.[92]

Source	Production Capacity / GW	Total Production / 10^9 L
Hydro	970	–
Solar PV	70	–
Solar thermal	234	–
Wind	238	–
Biomass	72	–
Ethanol	–	86.1
Biodiesel	–	21.4

Biogas is a source of renewable energy formed from the anaerobic degradation of organic matter. The source of this organic matter can be very varied, examples range from standard landfill sites to specific food waste digesters. A particular type of bacteria, methanogens, break down the organic waste as an energy source. The primary by-products of their efforts are methane and carbon dioxide, produced in approximately equal quantities. This flammable gas mixture is generally then used as fuel in an internal combustion engine, which is used to generate electricity. This is a renewable and carbon-neutral energy source, because using the biogas both satisfies energy demands and prevents the gas being released to the atmosphere as the more-harmful methane.

There are however, some practical issues with the use of biogas. It is a mix of methane and carbon dioxide, one of which is not flammable; additionally it is often saturated with water vapour. Both of these properties hinder its energy density and efficiency in an engine. A more pressing issue however, is that biogas is not a clean mixture of two compounds. It is made up of a multitude of components, and every biogas site has a different mix of components due to varying biogas sources (food waste, landfill, sewage treatment etc.). A typical chemical compositional make-up of biogas is shown in table 2.3.

Table 2.3. The chemical composition of typical biogas.[93–95] The typical chemical composition of biogas is shown, along with values for a select few compounds of interest. Actual values vary significantly between sites, due to the non-consistent make up of feedstock.

Compound	Concentration / mg m^{-3}	Concentration / %
Methane	365 000	55.6
Carbon Dioxide	668 000	37.1
Oxygen	12 900	0.99
Total Non-Methane Organic Compounds	2500	<0.1
Ethane	294	<0.1
Limonene	210	<0.1
Toluene	60.8	<0.1
α-Pinene	47.1	<0.1
Propane	25.2	<0.1
Isopentane	12	<0.1
Styrene	9.27	<0.1
Chlorobenzene	5.7	<0.1
Total Siloxane Compounds	60	<0.1
Decamethylcyclopentasiloxane (D5)	9	<0.1
Octamethylcyclotetrasiloxane (D4)	4	<0.1

2.1.2.1 Siloxanes

One component which is prevalent in biogas is the family of siloxanes. These chemicals are made up of alternating silicon and oxygen atoms, with methyl groups capping the silicon atoms. They end up in the landfills through their use in domestic and commercial products, such as shampoo, lubricants and lipstick. The naming convention for linear and cyclic siloxanes, used in literature and throughout this document, is shown in figure 2.3. They are only present at concentrations in the low parts per million, but they cause significant damage to combustion engines and boilers. The siloxanes enter combustion chamber as part of the biogas mix, and when combusted in the engine's cylinders, form carbon dioxide, water and silicon dioxide. As a nanocrystalline solid, the

silicon dioxide is not removed from the chamber with the exhaust gases. This gradual build up is the equivalent of adding sand to the fuel mix. As well as causing excessive wear to engines, it can form large deposits in boilers; both of which increase running and maintenance costs, leading to early equipment failure.

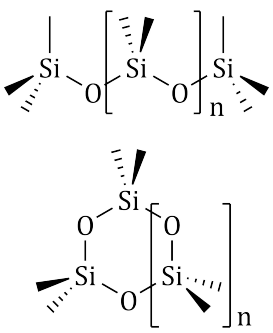

n=0 L2 Hexamethyldisiloxane
n=1 L3 Octamethyltrisiloxane
n=2 L4 Decamethyltetrasiloxane
n=...

n=1 D3 Hexamethylcyclotrisiloxane
n=2 D4 Octamethylcyclotetrasiloxane
n=3 D5 Decamethylcyclopentasiloxane
n=...

Figure 2.3. The naming convention of the siloxane family. Linear siloxanes are denoted L, with the following number representing the number of silicon atoms present. Cyclic siloxanes are denoted D, with the following number representing the total number of Si−O motifs present.

Siloxanes are synthesised from the condensation of two silanols, which are in turn synthesised by the hydrolysis of the appropriate silyl chloride. An example reaction scheme for this process can be seen in scheme 2.2.

$$R_3SiCl + H_2O \longrightarrow R_3SiOH + HCl \quad (a)$$

$$2\,R_3SiOH \longrightarrow R_3SiOSiR_3 + H_2O \quad (b)$$

$$n\,R_2Si(OH)_2 \longrightarrow H(R_2SiO)_nOH + (n-1)\,H_2O \quad (c)$$

$$n\,R_2Si(OH)_2 \longrightarrow (R_2SiO)_n + n\,H_2O \quad (d)$$

Scheme 2.2. The synthesis of siloxanes. Where (a) shows the formation of silanol by hydrolysis of a silyl chloride, (b) shows the condensation of two silanols to form a disiloxane, (c) shows the condensation of disilanols to form a linear siloxane, and (d) shows the condensation of disilanols to form a cyclic siloxane.

2.2 Current Techniques for the Removal of Siloxanes from Biogas

The issue of impurities in biogas has been evident since the latter half of the 1990's.[96] Consequently, research has already been undertaken in the field of biogas purification, with some papers specifically investigating siloxane removal. Here, these treatment options are split into seven categories: removal at the source, removal through membranes, biological degradation, cryogenic condensation, absorption, adsorption and catalytic decomposition.

2.2.1 Treatment at the Source

The siloxanes in biogas come from silicone compounds in the source of the biogas, generally landfill sites, sewage sites or biodigesters. It has recently been shown that reducing the siloxane content in the biogas source reduces the siloxane content in the biogas itself. Work done by Dewil *et al*. in 2008 investigated this with the the addition of peroxides to the landfill sites.[97] From a variety of peroxides, they discovered that dimethyldioxirane yielded the best results, with siloxane reductions of up to 85 % for D4, and 50 % for D5; they did not investigate the effect on linear siloxanes.

Dewil hypothesised that the siloxanes were being partially or fully oxidised to silicones and silica in the landfill, which have lower vapour pressures than their comparative siloxanes. One of the detrimental effects of this approach however, is that the peroxides also break down some synthetic polymers, to which the siloxanes can be bound. If this occurs, and the released siloxane is not itself decomposed, then additional siloxanes can be released. Due to this side effect, it would be advantageous to apply this 'pre-treatment' before digestion of the waste begins, giving any released siloxanes the ability to disperse before being trapped and becoming part of the resulting biogas.

2.2.2 Purification through Membranes

A rarely seen technique for removing siloxanes is the use of semipermeable membranes. Membranes are however, in use to remove the carbon dioxide from biogas, to produce biomethane, on a pilot plant scale.[98] Work to selectively remove siloxanes using semipermeable membranes was first published in 2006 by M. Ajhar *et al*., who continued their work, publishing again in 2012.[99,100] Ajhar discovered that the use of polydimethylsiloxane (PDMS) as a semipermeable membrane could drastically reduce the quantity of siloxanes in biogas. By using a PDMS membrane with a thickness of 50 µm and a surface area of just 10 cm^2 they were able to remove 90 % of L4 and D5 from the biogas. The removal of more volatile siloxanes is not as effective however, with removal rates dropping as low as 40 % for L2.

This technique has the added advantage that, due to the high water permeability of PDMS, siloxanes and water are both removed from the gas stream, lowering the relative humidity of the biogas. This not only aids combustion, but also any further purification processes. An elegant set up for this approach could be the use of the engine exhaust as the sweep gas. The exhaust could then, once contaminated with unwanted siloxanes and VOCs, be flamed to avoid the release of unwanted compounds into the atmosphere.

Unfortunately, PDMS is also partially permeable to methane. As a result, methane levels can drop as much as 7 %, which is too great a loss to be commercially feasible. This field shows potential, and further research into highly selective membranes could be promising.

2.2.3 Biological Degradation

A new form of siloxane removal has appeared in recent years, the biological degradation pathway. This method relies on either the aerobic or the anaerobic respiration of bacteria. Accettola *et al*. investigated the biological consumption of D3 under aerobic conditions in 2008.[101] It was discovered that some bacteria (predominantly *Pseudomonas*) consume D3. The bacteria degrade the siloxane to dimethylsilanediol. Unfortunately, the process is slow and inefficient, with an optimised removal of only 20 %.

Research into the biological consumption of D4 was published a few months later by M. Deshusses.[102] Anaerobic and aerobic conditions were studied, however initial results were disappointing. It was proposed that the main cause of the low conversion could be the slow mass-transport taking place as the D4 vapour passes into the aqueous phase. This hypothesis was supported by kinetic analysis. In an attempt to increase this rate, an additional non-miscible solvent was added (octadecenol). After the addition of this 'interphase', the maximum D4 removal was 43 %, with a 20 minute bed retention time. Whilst this is still low compared to other currently available techniques, its low cost and environmentally friendly nature make it an attractive possibility for the future.

2.2.4 Cryogenic Condensation

The idea of cooling down biogas, in an attempt to condense unwanted components from the biogas, was first considered in the early 1990's.[103] It has been shown that cooling the gas to 5 °C is insufficient, removing 27 % of the larger siloxanes (D5) and 12 % of the more volatile silicon compounds (trimethylsilanol).[104] When the temperature is decreased to −30 °C, it has been reported that 50 % of the siloxanes were condensed out.[105] Unfortunately, specific siloxanes were not specified. Theoretically, when the temperature is further lowered to −70 °C, L4, D4 and D5 can be reduced to below 1 mg m^{-3}. However, L2, L3 and D3 are too volatile to be condensed out of the gas stream.[106] This could be compensated for by increasing the pressure of the system, although the added complexity and cost should also be noted.

This method is currently in commercial use due to its additional ability to reduce the water

content of the biogas.[107] This is beneficial as, mentioned above, the effectiveness of other types of siloxane removal technologies can be decreased by high water loadings. A downside to cryogenic cooling, caused by the desirable water removal, is that large efforts have to be made to reduce and clear the inevitable icing of the equipment.

2.2.5 Absorption into Media

Another method proposed for the removal of siloxanes is their absorption into the bulk of another compound, typically a high boiling point solvent. This is achieved either by bubbling the gas through a Drechsel bottle, filled with an appropriate solvent; by passing the biogas through a counter-current tray tower; or by passing the gas through a column packed with Raschig rings (used to increase contact between liquid and vapour phases). In the counter-current tray tower and Raschig rings methods, the solvent runs down the column counter-current to the gas flow, thus maximising interaction and siloxane diffusion.

Work done by D. Schneider in 2001 concentrated on the use of alkali solutions as the liquid phase.[108] Sodium hydroxide solutions used showed promise, removing large quantities of L2, L3, L4, D3, D4 and 30 % of D5. A problem with the use of this base, however, is the precipitation of sodium carbonate due to the large amount of carbon dioxide in biogas. This solid builds up and regularly clogs the reaction unit.[96] Elevated temperatures were also required, generally 60 °C. The use of pure water for this system would be highly advantageous, due to the low cost and environmentally friendly nature of water; unfortunately the use of pure water showed no decrease in siloxane concentrations.[108]

The use of acidic liquids was investigated in 2001 by M. Niessner *et al.*[104] They reported that the use of concentrated sulphuric acid (97 wt%) could quantitatively remove both L2 and D5 at a temperature of 60 °C. At room temperature the removal rate fell to 60 %. The use of ultrasound in an attempt to reduce the required temperature was unsuccessful. A negative side effect of this treatment is the highly corrosive nature of sulphuric acid. Rapidly corroding the media chamber, the biogas would also pick up sulphuric acid vapours and carry them to the engine where they were combusted, leading to an additional detrimental effect on the combustion chamber. They were able to reproduce the quantitative siloxane removal using half-concentrated sulphuric acid (48 wt%), however this did not reduce the corrosion.

In an attempt to abate the corrosive nature of this technique, the use of nitric acid was also investigated. It was discovered that concentrated nitric acid (68 wt%) at 60 °C will also quantitatively

remove all siloxanes from the gas stream. Whilst nitric acid is known to dissolve iron, it does not in the bulk as chemical passivation takes place, protecting the iron with an oxide surface layer.

It was noted by E. Wheless and J. Pierce in 2004 that a pilot plant was using Selexol™ as their liquid for the absorptive removal of siloxanes.[109] Using a tray tower system, they report the removal of 99 % of all siloxanes, as well as hydrogen sulfide and VOCs. Selexol is a mixture of dimethyl ethers of polyethylene glycol made by UOP LLC for the removal of acidic gases from gas streams.

The process of siloxane absorption is promising and is already showing impressive results. It does however have the drawback that, whilst siloxanes can diffuse into the solvent, they can also diffuse out. Due to the continuously fluctuating concentrations of siloxanes in biogas, the siloxanes can actually vaporise out of the liquid, adding to the total siloxane concentration in the gas stream. This can be abated by using chemical absorption (such as acid) where the siloxanes are converted to a less volatile substance, instead of physical absorption (such as Selexol) where the siloxanes diffuse into the liquid.

2.2.6 Adsorption onto Media

By far the most common form of siloxane removal is their adsorption onto the surface of a medium. The process involves passing the biogas through a mesh or bed of the adsorptive compound. The siloxanes are adsorbed, remaining behind while the cleaned biogas exits. Many different compounds have been investigated for possible use as the adsorbent. In 2001, R. Niessner reported the use of two different types of polymer beads, 13X molecular sieves, silica gel, powdered graphite (surface area ~100 $m^2\,g^{-1}$) and activated carbon.[104] Of these, only silica gel and activated carbon did not show significant breakthrough at a loading of 4 $mg_{siloxane}/g_{adsorbent}$.

Niessner also tested the effectiveness of silica gel with moist siloxane vapour; this is important because biogas is generally saturated with water vapour, and silica gel is known to have a high affinity for water. The breakthrough level dropped from 100 $mg_{siloxane}/g_{adsorbent}$ for dry gas, to 5 $mg_{siloxane}/g_{adsorbent}$ for gas at 50 % relative humidity. It is suggested that this drastic drop is caused by the water competing for sites on the silica. An advantage for silica however, is its ease of regeneration; 20 minutes at 250 °C under a gas flow of 200 mL min^{-1} removes 95 % of the adsorbed siloxanes

Interestingly, R. Niessner[104] also reports on a sewage treatment plant in Munich, Germany that combines the gas treatment techniques of silica gel with cryogenic condensation. In their system,

the biogas is passed over a bed of silica gel at a temperature of −50 °C and a pressure of 5 bar. Under these conditions, it has been determined that 98 % of siloxanes are removed, along with all water and VOCs with boiling points greater than 130 °C. The silica gel bed is periodically regenerated by blowing through hot air.

Further work into different adsorptive mediums has been conducted by T. Matsui *et al*. and K. Oshita *et al*.[110,111] They looked into the siloxane adsorptive properties of 22 different activated carbons, 13X and 8 Å molecular sieves, a hydrophobic zeolite and silica gel. The activated carbons varied by surface area, pore volume, pH, and pore size distribution. Their results showed minimal siloxane adsorption whilst using 8 Å molecular sieves or the zeolite, 8 % adsorption by 13X molecular sieves, 10 % by silica gel, and 5 % to 19 % by the activated carbons. The poor performance of the 8 Å molecular sieves is caused by the large diameter of siloxane molecules — the smallest siloxane, L2, has a diameter circa 7.5 Å. By comparing the performance of the different activated carbons to their properties, Matsui and Oshita were able to determine that to maximise siloxane adsorption, it is necessary to maximise the surface area, pore volume and pH of the activated carbon.

The most effective variation of activated carbon examined by Matsui was subsequently tested using real biogas.[110] Its effectiveness was ascertained by monitoring the levels of D4 and D5, which were 3 mg m^{-3} and 15 mg m^{-3} respectively at the inlet. Unfortunately, no gas flow rate was reported. The activated carbon worked well, removing all siloxanes for 1500 hours (~62.5 days) of continuous operation. After this point the levels of both D4 and D5 in the gas output steadily rose. Whilst these are promising results, once the activated carbon is saturated, removal of the siloxanes from the media requires extremely high temperatures and is therefore very costly, discouraging commercial regeneration. As a result, the necessary continuous replacement of the activated carbon filters results in high operating costs.

A less common adsorbent in use is vermiculite, a magnesium aluminium iron silicate formed naturally and mined. Studies published in 2010 indicate that it is useful as a pre-filter for the biogas.[112] It has been shown that siloxane levels can be brought down to a steady state of ~1.5 mg m^{-3}, from an initial concentration of ~30 mg m^{-3}. Whilst this study only looked at D4, D5 and D6, it is possible that similar results would be found with linear siloxanes. This material, like activated carbon, is not regenerated once saturated with siloxanes. However, it is only one-tenth the price of activated carbon, and so has great potential as a pre-adsorbent, before final treatment with another process, *e.g*. activated carbon.

PpTek Ltd currently uses an externally sourced polyamide resin as the adsorbent in their commercial siloxane removal products.[113,114] By passing biogas through beds of ~1 mm diameter polyamide beads, PpTek are able to quantitatively remove all siloxanes. The media does not last long however, requiring regular regeneration (~12 hours). The regeneration period depends on the level of siloxane contamination in the biogas stream. Regeneration occurs by passing hot air (120 °C) over the catalyst bed.[115] By running two catalytic beds in tandem, they alternate between one bed being regenerated whilst the other processes biogas, providing seamless siloxane removal.[116] There are two major downsides to this technique. The first is the large energy cost associated with heating large volumes of air for regeneration purposes. The second is the medium itself has poor thermal stability, and therefore requires replacement periodically (typically every 3–5 years).

2.2.7 Catalytic Decomposition

A different approach to the problem involves the catalytic decomposition of the siloxanes, as well as potentially many of the VOCs. Research published by W. Urban *et al*. in 2009 proposed a three-stage biogas purification system.[117] The biogas is first passed over an aluminium oxide catalyst at an elevated temperature of 300 °C. The siloxanes are catalytically decomposed to microcrystalline silica, which remains on the surface of the alumina. This gradual build up destroys the microporosity of the catalyst, which they suggest to be irreparable. Alumina, however, is cheap so the cost of replacement is not excessive. In their experiments, they spiked biogas with 300 ppm of siloxanes, considerably higher than standard biogas. Using 250 g of alumina, they managed complete removal of all siloxanes from the 'enriched' biogas for 10 hours at a flow rate of 1115 $L\,h^{-1}$ (~18.5 $L\,min^{-1}$). After this time the removal efficiency steadily declines, reaching 20 % at 40 hours. Whilst 10 hours may not seem impressive, it is worth noting the abnormally high siloxane levels, combined with the high flow rate, is putting a disproportionate load on the catalyst.

Once the siloxanes are removed, the biogas is passed over a V_2O_5/TiO_2 catalyst, again at 300 °C, to decompose the majority of the heteroatom-containing VOCs into gaseous HCl, HF and SO_2. The methane content is not affected. Because this stage does not produce any precipitate, the dual metal catalyst does not degrade from a loss of active surface area. The final stage involves the passing of the biogas over alkalised alumina (such as $Na_2O \cdot Al_2O_3$) which adsorbs the acidic gases, leaving clean biogas. This can be regenerated using a reducing gas containing carbon monoxide and hydrogen.[118] Whilst this system was successful at removing all siloxanes and many unwanted VOCs, the high temperatures and nature of the multistage process makes it an expensive option.

2.3 Overview of Nanomaterials and Their Characterisation

2.3.1 Nanostructures

A nanomaterial is a substance that has been designed and synthesised with small structures on the nano scale (~10^{-9} m). They are generally classified by their dimensions, starting unconventionally, at zero-dimension (0D). The structures that make up zero-dimension nanomaterials are less than 100 nm in all three dimensions, examples include quantum dots and nanoparticulates. One-dimensional (1D) nanomaterials have structures with one macro-sized dimension and two nano-sized dimensions, such as nanorods or nanotubes. Two-dimensional (2D) nanomaterials have two macro-scale dimensions and one nano-sized dimension, a typical example being thin films or monolayers.

Nanomaterials are designed to take advantage of their properties, which often vary from those observed in the bulk. This disparity is caused by two factors. Firstly, the relative surface area of nanomaterials is much higher than in the bulk. As the the volume of the material shrinks, the available surface area is reduced much slower; this can be seen in figure 1.7 and is discussed in section 1.2.2. Quantum effects are the second factor, which also become more incipient as the structural dimensions are reduced. One such effect is the fluorescence variance of quantum dots, discussed in section 1.2.1. Other examples include the use of nanostructures as wave-guides, possible due to visible light having a wavelength of comparable size.[119] One recent use of quantum wave-guides is the development of a new ultra-thin magnifying lens for light microscopes.[120]

2.3.1.1 Nanofibres

This work focuses heavily on the use of nanofibres. These are one-dimensional nanostructures with diameters generally in the range of 10 nm to 500 nm, and of no fixed length. They are of considerable interest because, whilst maintaining an incredibly high surface area to weight ratio, they are also mechanically strong.[121] Some of their potential uses include sensors,[122,123] membranes,[124,125] drug delivery,[126,127] fuel cells[128,129] and spacecraft.[130,131] Nanofibres are of interest here because of their high surface area. This gives them an extended surface for chemical activities to take place, be it adsorption or catalysis, therefore increasing efficiency and rates.

2.3.2 Characterisation

Due to the small size of the nanomaterials, specific characterisation techniques are required. For this work, characterisation of the synthesised nanomaterials was conducted using a combination of powder X-ray diffraction (pXRD), scanning electron microscopy (SEM), energy-dispersive X-ray spectroscopy (EDX) and diffuse reflectance UV-visible spectroscopy.

2.3.2.1 Powder X-ray Diffraction

Powder X-ray diffraction (pXRD) is a common technique in material chemistry for the analysis of inorganic compounds. X-rays are directed at the sample along a known variable angle, θ, these X-rays diffract inside the lattice spacing of the compound before leaving at angle 2θ. As the incident angle θ is varied, the X-ray detector is rotated, in order to always measure at an angle of 2θ. This is demonstrated in figure 2.4. On exiting the sample there is constructive and destructive interference between the X-rays, due to the varied heights of the planes delaying some radiation. This leads to regions of high and low (zero) intensity of X-rays being detected as 2θ is scanned, leading to peaks in the recorded diffraction pattern. The value of 2θ for peaks varies between compounds, which is used to identify the material.

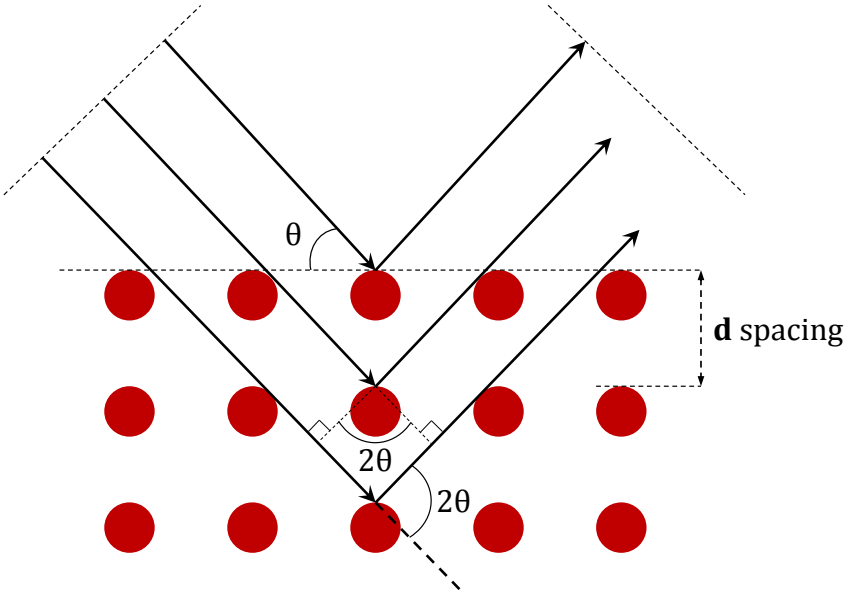

Figure 2.4. A schematic showing the path of the incident and diffracted X-rays. Note the delay caused by some paths entering further into the the lattice than others. Angles θ and 2θ are shown, along with the d spacing.

2.3.2.2 Scanning Electron Microscopy

A scanning electron microscope (SEM) is used to obtain vital information on the surface morphology of the nanomaterial. A tungsten filament is heated, generating an electron beam which is accelerated to 30 keV. An ultra-high vacuum is required for SEM, this both extends the mean free path of the electrons, as well as reducing oxidation of the filament. The high energy electron beam is then focused using a system of lenses, before being passed through the scanning coils. These direct the electron beam towards the sample, repeatedly scanning the location along the x and y axes in a raster fashion.

When the electron beam strikes the sample there are several possible consequences. The classical outcome is that the incident high energy electrons will be scattered elastically. These elastic high energy electrons are known as back-scattered-electrons, and are generally not used for imaging because they contain information from deep within the sample. Secondary electrons are formed by the inelastic scattering of the incident electron beam — some of the incident electron's energy is transferred to a core K electron, which is emitted as a secondary electron. The secondary electrons have much less kinetic energy, approximately 50 eV, and so can be used to gain topological information. Their low energy allows them to be redirected towards the detector by attracting them to an electrical grid. The newly formed core electron vacancy is quickly filled by the relaxation of a higher energy electron. The difference in energy is then emitted, either as X-rays (see section 2.3.2.3) or by emission of an additional electron known as an Auger electron.[132–134]

2.3.2.3 Energy-Dispersive X-ray Spectroscopy

Energy-dispersive X-ray spectroscopy (EDX) was conducted in the SEM imaging chamber using X-ray fluorescence. Core electrons are removed from the atom using a high energy electron beam. Higher energy electrons then relax down to fill the core level vacancy, emitting X-rays in the process. The energy level difference is unique to each element, and therefore the frequency of the emitted X-rays can be used to determine the elements present in the sample. A greater intensity of emitted X-rays at a specific frequency is indicative of a larger amount of that element.

2.3.2.4 Diffuse Reflectance UV-Visible Spectroscopy

The band gap, E_g, of semiconductors is of great importance for their activity. It is therefore important to be able to measure and monitor the band gap of any synthesised nanomaterials. As valence electrons require a certain amount of energy to cross the band gap to the conduction band,

the absorbed wavelengths in UV-visible spectroscopy (UV-Vis) can be used to measure this minimum energy. This method of band gap determination was first developed in 1968 by Tauc.[135] It allows for the direct correlation between the band gap of a substrate and its absorption coefficient, α. Tauc's formula is shown in equation (2.1), where h is the Planck constant; ν is the frequency of light; A is the proportionality constant of the system, often taken as unity; and n is a constant, whose value depends on the type of transition. The value of n is 0.5 for direct allowed transitions, 1.5 for direct forbidden transitions, 2 for indirect allowed transitions and 3 for indirect forbidden transitions.[136]

$$\alpha h\nu = A(h\nu - E_g)^n \tag{2.1}$$

The band gap is obtained from equation (2.1) by plotting $h\nu$ against $(\alpha h\nu)^2$, forming a Tauc plot. The Tauc plot displays a linear section, which is extrapolated to the x-axis, the intercept of which is the value of the band gap for the substrate. An example of this for P25 is shown in figure 2.5, where the red line shows a linear fit, the x-axis intercept of which gives a band gap of 3.08 eV.

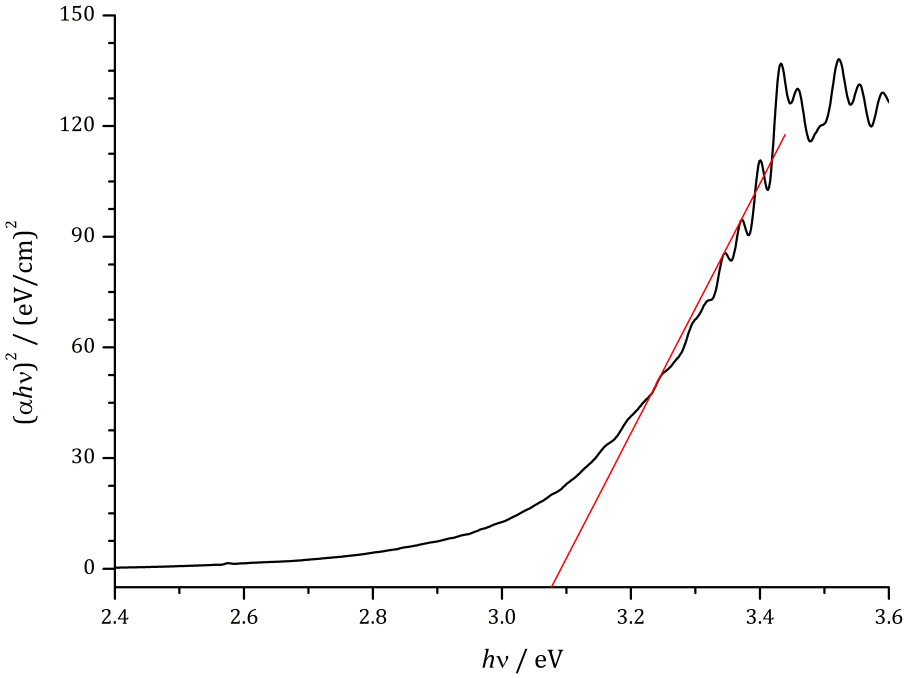

Figure 2.5. A Tauc plot of P25. The x-axis intercept gives a band gap of 3.08 eV.

Traditional techniques for measuring the UV-Visible spectrum of a sample, *i.e.* directly by transmission, directly provide the absorption coefficient of said sample. However, these techniques are limited to gaseous, liquid, solvated and thin film solids. For solid samples, such as

powders or nanomaterials, a technique was developed by Kumar *et al*. using diffuse reflectance UV-Vis.[137] This model is shown in equation (2.2), where t is the film thickness, R_{max} is the maximum reflectance intensity, R_{min} is the minimum reflectance intensity, and R is the reflectance at the current wavelength, recorded as $R = I/I_0$.

$$2\alpha t = \ln\left(\frac{R_{\text{max}} - R_{\text{min}}}{R - R_{\text{min}}}\right) \tag{2.2}$$

It can be seen that α is proportional to the natural log function, and so Kumar *et al*. successfully proposed plotting $h\nu$ against $\ln[h\nu(R_{\text{max}} - R_{\text{min}})/(R - R_{\text{min}})]$. This allows a Tauc plot to be taken from a diffuse reflectance UV-Vis spectrum.

The diffuse nature of the reflected incident light, caused by scattering, means that the intensity is too weak to be detected at a single point. Therefore an integration sphere is used to concentrate the light. The integration sphere is a hollow sphere with a diffuse white coating on the inside. The incident light beam is shone through a hole in the sphere, after interacting with the sample the reflected light is bounces around the sphere until it collides with the detector. This allows the detector to function by exposing it to all available light.

2.3.3 The Photodesorption Effect

Materials that are adsorbed on the surface of a material can undergo photodesorption when exposed to photons of sufficient energy. There are two main models that describe this phenomenon.

The first is the Menzel, Gomer[138] and Redhead[139] model (also reported separately by Adams and Donaldson[140]). Photons absorbed by the adsorbate cause a Franck-Condon transition;[141,142] where the adsorbed substrate is electronically excited, whilst the nuclei have not moved due to their considerably slower speed.[143] The excited electrons result in an anti-bonding state between the surface and the adsorbent, causing movement of the nuclei away from the surface and subsequent desorption of the substrate.[144] There are several options for the desorption of the excited molecule, it can desorb in its excited state and radiatively relax to the ground state when away from the surface; or it can relax non-radiatively in proximity to the surface and desorb in its ground state; alternatively it can desorb as an ion and become neutralised at a later stage.[145]

An alternative model for the photo-induced desorption of adsorbed species has been put forward more recently by Antoniewicz.[146] In this model the adsorbed neutral species is excited to a cationic state. Due to the increased effective nuclear charge experienced by the valence electrons,

the new cationic radius is smaller than the previous molecular radius. The new, reduced radius of the adsorbed species shifts the surface-adsorbent distance equilibrium position towards the surface, causing the adsorbed species to accelerate towards the surface. Ionic neutralisation then takes place, either from an Auger electron or through electron tunnelling from the surface. This is demonstrated visually in figure 2.6. The kinetic energy of the adsorbed (now neutral) species is maintained, resulting in the total energy of the adsorbed species being the potential energy of the neutral species at the (now shorter) surface-adsorbent distance, plus the kinetic energy at neutralisation. Desorption will then take place if this total energy is larger than the binding energy.

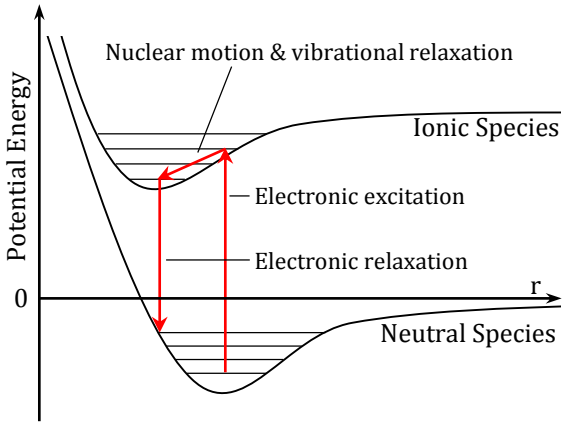

Figure 2.6. Approximate potential energy curves showing the principle behind Antoniewicz's model for photodesorption.[146] Electrons are photoexcited to a higher energy level of the ionic species, as the nuclei move to the new local minimum the electrons relax to a higher energy level of the neutral species, providing the molecule with increased potential energy (compared to the starting energy of the neutral species) and residual kinetic energy. The total energy may be sufficient to actuate desorption.

2.4 Synthesis of Titania Nanofibres

The technique used in this work for the formation of nanofibres is the electrospinning of a solution containing a metal oxide precursor,[147–149] typically a volatile liquid containing the metallic element required in the final nanofibre, and an organic polymer in an organic solvent. For the synthesis of TiO_2 nanofibres, the standard precursor is titanium tetraisopropoxide (TTiP) (titanium *n*-butoxide is also well documented[150]), whilst poly(methyl methacrylate) (PMMA) is a typical organic polymer.[151,152] In this work the organic solvent used is dimethylformamide (DMF). The polymer is required to both increase the viscosity of the solution and provide the nanofibre framework for the precursor. The nanofibres are formed using the apparatus shown in figure 2.7. The use of a syringe pump allows the controlled injection of the solution over extended time periods, with

a typical elution rate of 1 ml h^{-1}. A high positive voltage is applied to the solution by electrifying the needle tip. The collecting drum is grounded, and rotates to give the collected fibres a chance to dry before more fibres are layered on top.

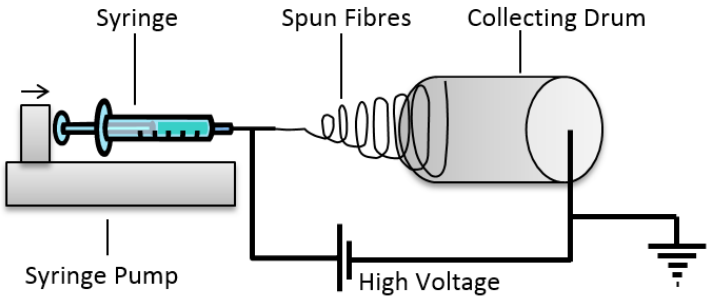

Figure 2.7. A typical electrospinning set-up.

As the spinning-solution reaches the end of the needle tip, it is held in place by its own surface tension. The high voltage applied to the solution builds up until, reaching a critical point, the electrostatic repulsive forces overcome the surface tension forces and a charged stream of spinning-solution is emitted towards the collecting drum. As the stream leaves the needle tip, it contains a high electronic voltage, approximately 20 kV. This causes the solution to 'whip' in flight, forming a Taylor cone and evaporation of the solvent.[153] Due to this whipping, the polymer left behind is extremely stretched out, forming nanofibres which are collected on the rotating earthed drum.[154]

The as-synthesised nanofibres contain PMMA and the TiO_2 precursor, TTiP. The TTiP is hydrolysed to $Ti(OH)_4$ by treatment with a steam bath. This involves placing the nanofibres above a heated (80 °C) bath of water, sealed loosely, for two hours. Calcination at 500 °C for 16 hours then removes all of the PMMA by oxidising it fully to CO_2 and H_2O, whilst simultaneously oxidising the titanium hydroxide to titanium dioxide. It is possible to forgo the hydrolysis step, however the volatile nature of TTiP causes the loss of precursor during the early stages of calcination, resulting in a significant yield drop.

2.4.1 Characterisation of Synthesised Nanofibres

2.4.1.1 Powder X-ray Diffraction

The pXRD pattern recorded for the calcined TiO_2 nanofibres is shown in figure 2.8. Generally, broadening of pXRD peaks is attested to a reduction in particle size, as quantified with the Scherrer equation.[155] However, the peaks in figure 2.8 are too broad to be solely due to this. The other main factor which will affect peak broadness is microstrain in the lattice. These can be irregular lattice

deformations, faults, grain surface relaxation or dislocations.[156] In this sample there is only the anatase phase present, referenced to the Inorganic Crystal Structure Database (ICSD) collection code 009853.[13] Anatase has a tetragonal crystal symmetry and a band gap of 3.26 eV for bulk samples.[157]

The sample was compared to known diffraction patterns in the ICSD. The XRD pattern of TiO_2 nanofibres shows peaks at 25.35°, 37.93°, 48.11°, 54.10°, 55.08°, 62.73°, 68.89°, 70.14°, 75.22° and 82.86°. These correspond to the (101), (004), (200), (105), (211), (204), (220), (107), (215) and (224) crystal planes, respectively.

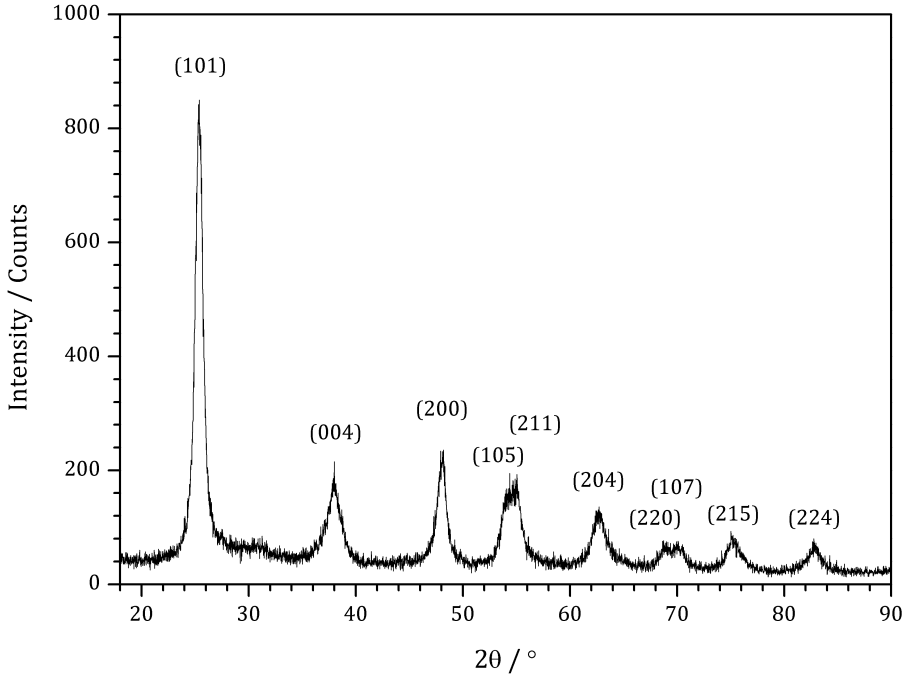

Figure 2.8. Powder X-ray diffraction pattern of calcined TiO_2 nanofibres. Only the anatase phase is visible. The miller indices are shown above the respective peaks.

2.4.1.2 Scanning Electron Microscopy and EDX

Scanning electron microscopy (SEM) work was conducted at a working distance of 25 mm, using an accelerating voltage of 30 kV. SEM images of the calcined nanofibres are show in figure 2.9. The nanofibres have an average thickness of approximately 300 nm, and are of no set length. Whilst the length is longer than measurable using this technique, nanofibres at least 85 µm in length have been imaged — see figure 2.9(A). It can be seen in the images that the nanofibres are homogenous, bead-free and uniformly distributed.

Slight crinkling can be seen in figure 2.9(B) & (C), which is characteristic of titania nanofibres. This is caused during the electrospinning process. As the nanofibres are extruded from the needle

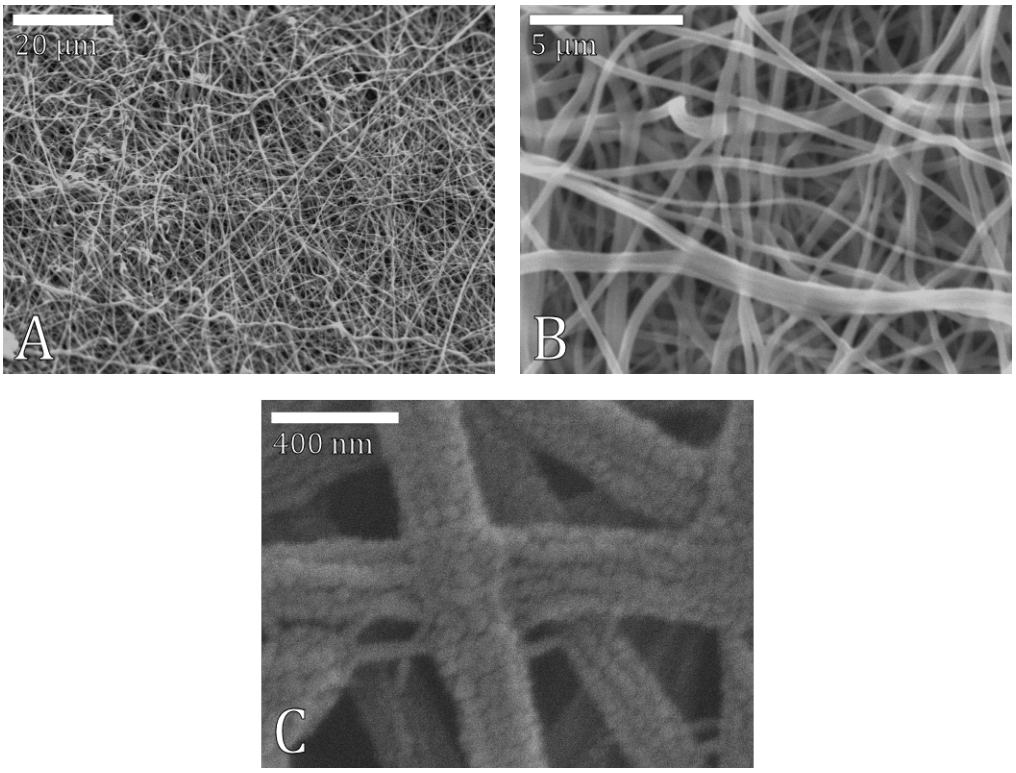

Figure 2.9. SEM images of calcined TiO_2 nanofibres, at three different magnifications. The scale bar is 20 µm, 5 µm and 0.4 µm in (A), (B) and (C), respectively.

tip at an immense velocity,[158] evaporation of the solvent occurs very quickly. This causes spinodal phase separation within the spinning solution, due to the fast onset of vitrification.[159] It is this separation that causes the nanostructured crinkling.[160] On calcination of the nanofibres, the smooth polymer is removed, exposing the surface features.

From the EDX spectrum shown in figure 2.10, it can be seen that there is only titanium present in the nanofibres. The emission at 4.51 keV is caused by K_α transition in titanium, whilst the emission at 4.93 keV is caused by the K_β transition.[161,162] Unfortunately the lower limit of the instrument prevents detection below atomic number 10 (neon).

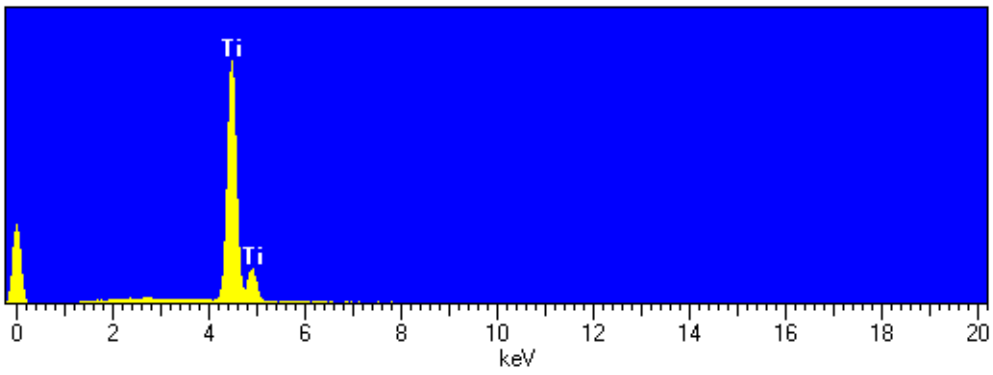

Figure 2.10. Energy-dispersive X-ray spectrum of TiO_2 nanofibres.

2.4.1.3 Band Gap Measurements

Diffuse reflectance UV-Vis spectroscopy was conducted on the synthesised nanofibres, in order to ascertain the band gap. From the resulting Tauc plot, shown in figure 2.11, the band gap was calculated to be 3.06 eV. This compares to 3.08 eV recorded for commercial P25. The two samples are similar, both in composition and dimensions, as such the similarity in the two band gaps is not surprising.

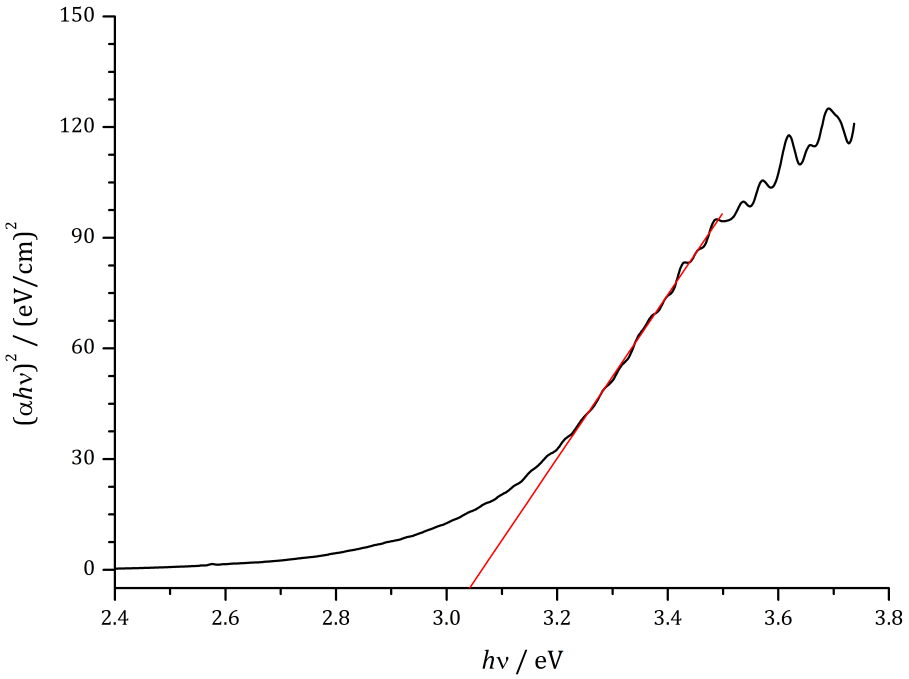

Figure 2.11. A Tauc plot of the synthesised TiO_2 nanofibres. The x-axis intercept gives a band gap of 3.06 eV.

2.5 The Use of Nanofibres to Degrade Siloxanes

2.5.1 Experimental Considerations

In order to ascertain the effectiveness of using TiO_2 nanofibres to degrade siloxanes in biogas, a model system was developed. A non-flow photoreactor system was created, using hexamethyldisiloxane (L2) as a model for siloxanes. L2 was chosen as a model because it has inherently useful properties. It is known to be present in biogas, it is easy to handle, and it is volatile enough to be used in the experiments. It's volatility can be demonstrated using the Antoine equation, shown in equation (2.3) where P is the vapour pressure of the compound in kPa; T is the absolute temperature in Kelvin; and A, B and C are compound specific constants, measured experimentally.

$$\log(P) = A - \frac{B}{T + C} \tag{2.3}$$

By taking Antoine constants for L2, D4 and D5 from the published literature,[163,164] vapour pressure data was plotted, shown in figure 2.12. From this the greater volatility of L2, compared to D4 and D5, can clearly be seen.

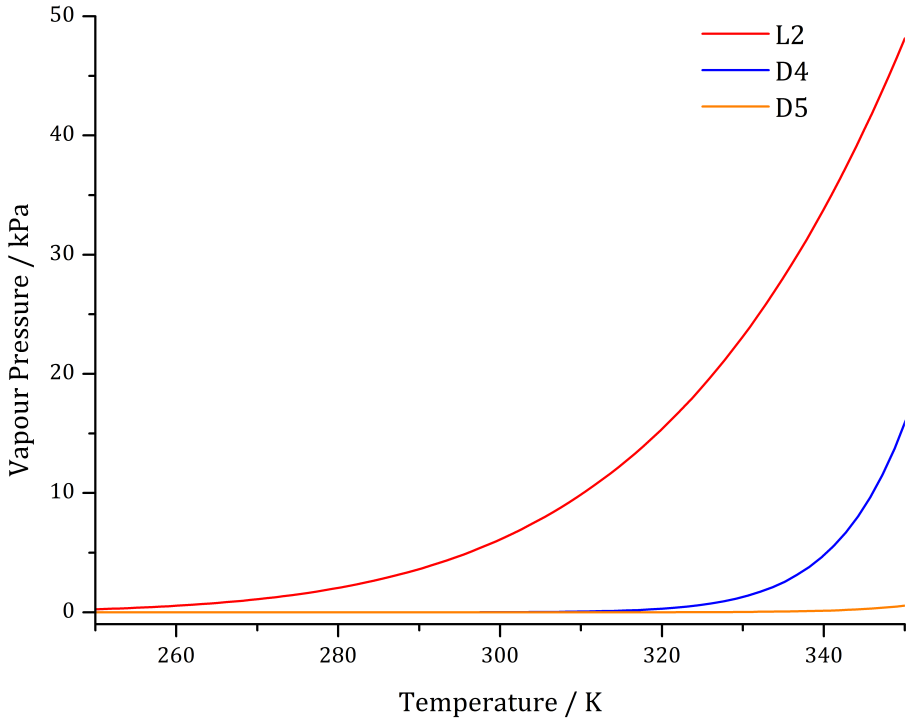

Figure 2.12. Variation of vapour pressure with temperature for L2 (red), D4 (blue) and D5 (orange). Functions are plotted using the Antoine equation, with constants taken from literature.[163,164]

The prepared titania nanofibres were used in a static photoreactor in order to ascertain their effectiveness in photodegrading siloxanes. The nanofibres were placed in a sealed vessel, and a known amount of gaseous siloxane was injected into the vessel using a Teflon-sealed gas-tight syringe. Throughout all these reactions, the mass of nanofibres used was maintained at 50 mg. The reaction vessel was exposed to UV_A light, concentrated around 365 nm (the spectrum is shown in figure 2.13), using a modified Spectrolinker XL-1500 UV Cross-Linker. Samples were regularly taken from the chamber, allowing for the concentration of the siloxane vapour to be monitored using gas chromatography-flame ionised detection (GC-FID). A schematic of this experimental setup is shown in figure 2.14.

L2 was used as a standard test siloxane due to its comparatively high volatility. The reaction chamber was prepared with 50 mg of TiO_2 nanofibres, before being sealed with an unpierced septum. Separately, 0.2 mL of L2 was added to a sealed round bottom flask, and heated to 130 °C

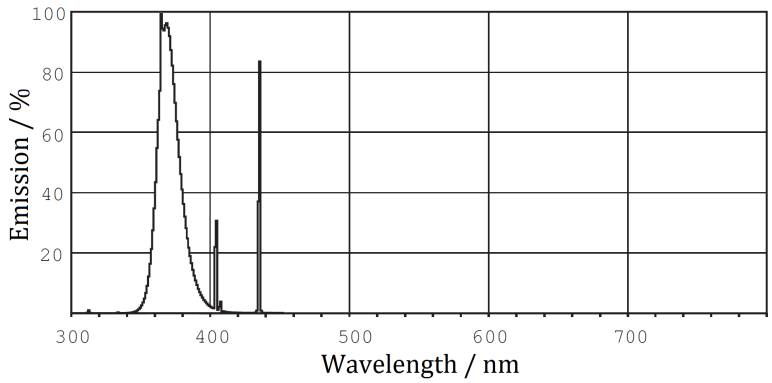

Figure 2.13. The emission spectrum of the UV_A fluorescent tubes. Spectrum is adapted from the data sheet of the product.[165]

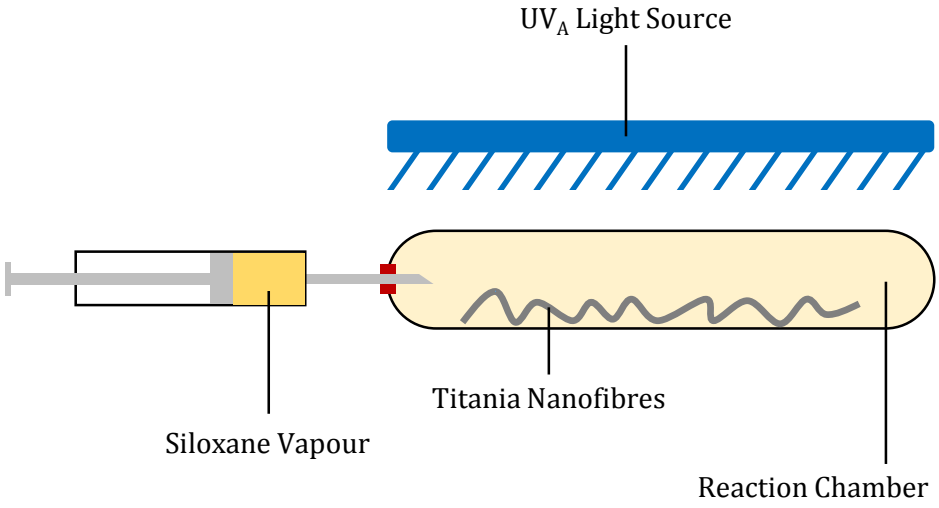

Figure 2.14. Schematic showing the experimental set-up for testing the photodegradative abilities of TiO_2 nanofibres.

in order to fully evaporated the L2 (*cf.* boiling point of 101 °C).[166] From this round bottom flask, 10 mL of L2 vapour was taken by air-tight syringe and added to the reaction chamber containing the TiO_2 nanofibres. Several data points were collected initially in order to confirm the stability of the system. This initial delay is to allow for the adsorption and desorption of L2 on the TiO_2 nanofibres to reach a steady state. After 1 hour, the UV_A lights were activated. As can be seen in the graph shown in figure 2.15, there is a small peak in siloxane levels, followed by an exponential decay.

The concentration of L2 first reaches a steady state in the reaction chamber. This is an equilibrium, and occurs when the flux of L2 both desorbing from and adsorbing to the nanofibre surface are equal. This results in a constant surface concentration of the adsorbate, L2. The initial rise in siloxane concentration is a phenomenon caused by two effects. The first is thermal desorption.

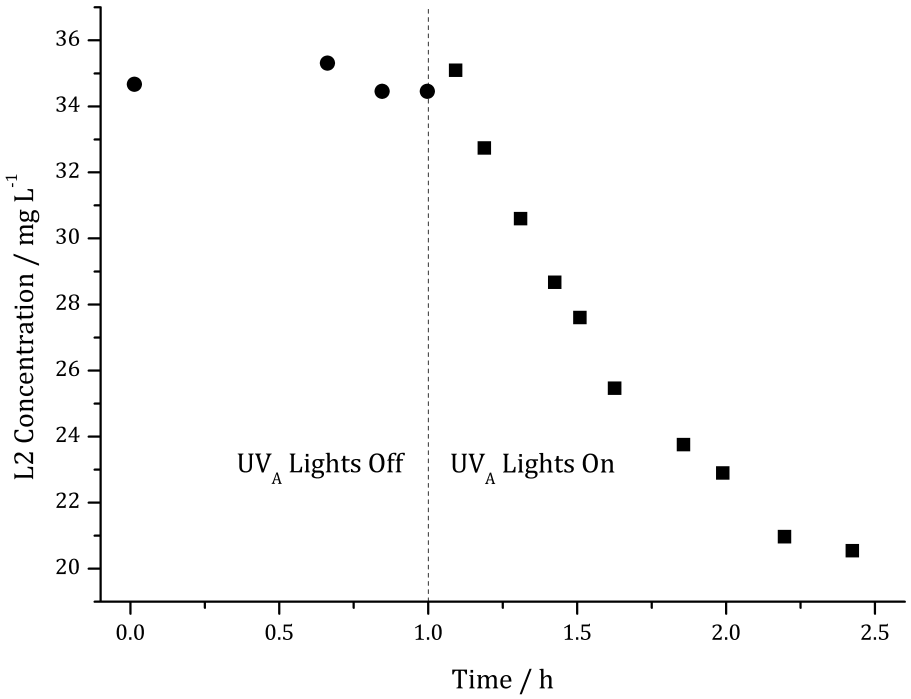

Figure 2.15. A plot of L2 concentration against time, showing the photodegradation of siloxane vapour once the lights were switched on, using 50 mg of TiO_2 nanofibres. The UV_A lamps were switched on at 1 h, shown by the dotted line. Circles indicate before illumination, squares indicate after illumination.

The formation of an adsorbate-adsorbent complex between L2 and TiO_2 is an enthalpically favourable reaction as it minimises surface energies, it is however, also entropically disfavoured. When at a steady state, these are balanced, resulting in no net change. However, when the UV_A lights turn on the system begins to raise in temperature — the fluorescent tubes used as the UV_A light source are not perfect systems, and therefore emit heat as unwanted waste energy. This additional thermal energy causes a shift in the equilibrium, making it energetically favourable for L2 to desorb. The second cause is the photo-induced desorption of L2 from the surface of the TiO_2 nanofibres, described in section 2.3.3.

2.5.2 Kinetic Analysis

A possible kinetic scheme for the catalytic removal of L2 is

$$\mathrm{A} + \mathrm{L2} \underset{k_{-1}}{\overset{k_1}{\rightleftharpoons}} \mathrm{A \cdot L2} \xrightarrow{k_2} \mathrm{A} + \mathrm{D}$$

where A represents the catalytic surface area, $A \cdot L2$ physisorbed L2 and D the decomposition products. The differential equations for A and $A \cdot L2$ are then

$$\frac{dA}{dt} = k_{-1}[A \cdot L2\,] - k_1 A[L2\,] + k_2[A \cdot L2\,] \tag{2.4}$$

and

$$\frac{d[A \cdot L2\,]}{dt} = k_1 A[L2\,] - k_{-1}[A \cdot L2\,] - k_2[A \cdot L2\,]. \tag{2.5}$$

Assuming the steady state approximation (SSA) for the concentration of $A \cdot L2$, then

$$\frac{d[A \cdot L2\,]}{dt} = 0 = k_1 A[L2\,] - k_{-1}[A \cdot L2\,] - k_2[A \cdot L2\,] \tag{2.6}$$

and so

$$[A \cdot L2\,] = \frac{k_1 A[L2\,]}{\left(k_{-1} + k_2\right)}. \tag{2.7}$$

Using this expression for $[A \cdot L2\,]$ in equation 2.4 leads to

$$\frac{dA}{dt} = \frac{k_{-1}k_1 A[L2\,]}{\left(k_{-1} + k_2\right)} - k_1 A[L2\,] + \frac{k_2 k_1 A[L2\,]}{\left(k_{-1} + k_2\right)} \tag{2.8}$$

which then simplifies through to give

$$\frac{dA}{dt} = \left(\frac{k_{-1}k_1}{\left(k_{-1} + k_2\right)} - \frac{k_1\left(k_{-1} + k_2\right)}{\left(k_{-1} + k_2\right)} + \frac{k_2 k_1}{\left(k_{-1} + k_2\right)} \right) A[L2\,] \tag{2.9}$$

$$\frac{dA}{dt} = \left(\frac{k_{-1}k_1 - k_1(k_{-1} + k_2) + k_2 k_1}{k_{-1} + k_2} \right) A[L2\,] \tag{2.10}$$

$$\frac{dA}{dt} = \left(\frac{k_1(k_{-1} - k_{-1} + k_2 - k_2)}{k_{-1} + k_2} \right) A[L2\,] \tag{2.11}$$

The quotient of rate constants therefore equals zero, ensuring that $\frac{dA}{dt} = 0$; thus the reformation of A in the last step ensures that A is truly catalytic, and so does not appear in the rate equation.

The standard differential form of the first-order rate law is shown in equation (2.12).

$$\text{Rate} = -\frac{d[L2]}{dt} = k[L2] \tag{2.12}$$

In equation (2.12), the rate of reaction is shown as the loss of the reactant, [L2], over time. This change in concentration, shown by the derivative, is condensed to the rate constant, k. Rearranging

equation (2.12) and integrating gives equation (2.13).

$$\text{Rate} = \ln[\text{L2}] - \ln[\text{L2}]_0 = -kt \tag{2.13}$$

In equation (2.13), the initial starting concentration is shown by $[A]_0$. Equation (2.13) can be rearranged to equation (2.14), which is a common form of the rate law.

$$\ln[\text{L2}] = \ln[\text{L2}]_0 - kt \tag{2.14}$$

By rearranging the components of equation (2.14) to form the new layout in equation (2.15), the rate law can be made analogous to the standard straight line equation.

$$\ln[\text{L2}] = -kt + \ln[\text{L2}]_0 \tag{2.15}$$
$$y = mx + c$$

By taking the natural log of the degradation shown in figure 2.15, and plotting it against time, the graph shown in figure 2.16 is produced. For a purely pseudo-first order reaction, the rate constant, k, would be calculated by measuring the gradient of the linear line of best fit. Shown as a black line, the measured initial gradient is $-0.582\,\text{h}^{-1}$, which when used in equation (2.15) gives an initial rate constant of $0.582\,\text{h}^{-1}$. However, it is clear that the plot is not linear.

The deviation from linearity observed in figure 2.16 can be attributed to a poisoning of the catalyst, which inhibits the rate of catalytic decomposition. This poisoning is caused by the build up of the photodecomposition product, SiO_2, on the surface of the TiO_2 nanofibres. This build up blocks pores and forms mono- and multi-layers on the surface of the nanostructured catalyst, preventing unreacted L2 from reaching the reactive surface and becoming degraded.

The build up of SiO_2 on the catalyst surface is similar to a phenomenon observed in the petroleum industry, called coking. Coking is the the build up of carbonaceous residues on the surface of the catalyst, hindering catalytic performance by covering active sites and blocking pores. There have been many attempts at modelling the coking of catalysts in literature, with the main consensus being the complexity of the kinetic and mechanistic details.[167,168] As such, a standard model for describing the build up of coke on a surface has become widely accepted. The model in question was described by Voorhies[169] using equation (2.16), where C_c is the amount of coke on the catalyst, A is a constant dependent on reaction setup; t is the reaction time; and n is a

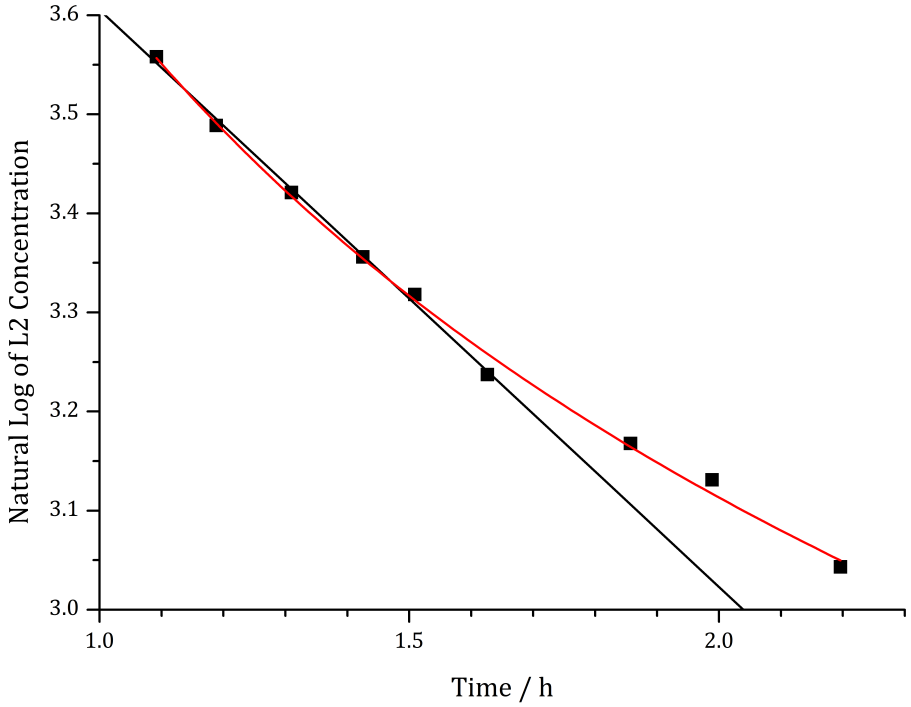

Figure 2.16. A first order kinetic plot, showing the variance in the natural log of L2 concentration with time, once the UV_A light source had been activated. The (black) linear line of best fit has an R^2 of 0.996; the gradient has a value of −0.582; and an intercept of 4.19. Data for the (red) power plot is shown in table 2.4.

deactivation-rate dependent exponent. An offset, y_0, can be added to this function.

$$C_c = At^n \tag{2.16}$$

It can be said that the deviation from linearity in figure 2.15 is caused by two effects: the decreasing concentration of L2, and the decreasing activity of the catalyst. By plotting the pseudo-first order function in figure 2.16, the effect of the decreasing L2 concentration has been nullified. This results in the non-linearity of the plot in figure 2.16 being solely dependent on the decreasing activity of the catalyst. The activity of the catalyst is directly related to the build-up of SiO_2, which is comparable to the coking problem observed by many petroleum catalysts.[170] Therefore, the equation proposed by Voorhies was used to fit the red curve shown in figure 2.16. The data was also fitted to a standard exponential function, traditionally used in chemical kinetics. However, by comparing the goodness-of-fit for the two plots, the R^2 and χ^2_{red} values, it is clear that the Voorhies plot better represents the data, the relevant details are tabulated in table 2.4. This is as expected, as the Voorhies function is the standard method for modelling catalyst deactivation.

It can be seen that the exponent n can be used as a measure of catalyst deactivation rate. As $n \rightarrow 1$, function $\rightarrow$ linear, and so the kinetic plot would have no input from the catalyst deactivation

Table 2.4. Constants, error and goodness-of-fit for the curved fit in figure 2.16.

Function	Parameters	Value	Standard Deviation	χ^2_{red}	R^2
$y = y_0 + Ax^n$	A	3.62625	0.00792	1.067×10^{-4}	0.9964
	n	-0.22007	0.0047		
	y_0	0	0		
$y = y_0 + Ae^{Rx}$	y_0	2.70497	0.10659	1.298×10^{-4}	0.9956
	A	2.06372	0.11294		
	R	-0.81108	0.15261		

function, equation (2.16). Therefore, the slower the deactivation of the catalyst, the closer n gets to unity. If the catalyst deactivation becomes inconsequential enough, then the loss of reactant in the reaction can be solely modelled using pseudo-first order kinetics.

2.6 Industrial Trials with Titania Nanofibres

In order to ascertain the effectiveness of the nanofibres with genuine, as oppose to simulated, biogas, a larger-scale photoreactor chamber was developed. This was conducted in collaboration with our industrial partners, PpTek Ltd. A photograph of the reactor is shown in figure 2.17. This photoreactor operated in a continuous-flow mode, as oppose to the static conditions used previously, for use at a commercial Wastewater Treatment Works.

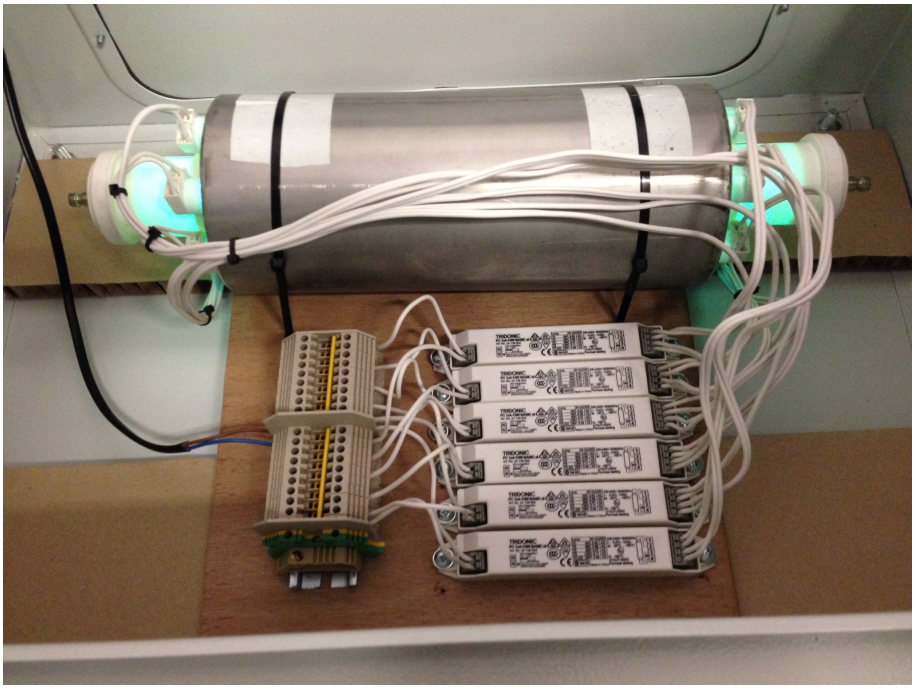

Figure 2.17. A photograph of the photoreactor designed. It was tested at a commercial Wastewater Treatment Works, in collaboration with PpTek Ltd.

The set up for this reactor was slightly different than the laboratory experiments. The nanofibres were coated onto glass beads using our new coating technique (patent pending[171]). Glass beads with an average diameter of 2.5 mm were refluxed in 6 mol dm^{-3} $NaOH_{(aq)}$ for two hours. After rinsing and drying, the beads were then placed in a rotating drum for 16 hours, with a sufficient quantity of nanofibres to achieve a loading of 4.5 mg_{TiO_2}/g_{beads}. These beads were then packed into the glass reaction tube, which was surrounded by six UV_A fluorescent lights. The biogas continuously flowed through the system for several days, with the concentration of D5 monitored by commercial GC-MS sampling every two days.

The siloxane loading of a biogas stream fluctuates substantially. In one example, on-site data showed that the concentration of D5 in the gas stream changed from 4.5 mg m^{-3} to 30.5 mg m^{-3} in a two day period. There is also a variation in the gas flow. Both of these phenomenon are caused by a combination of the type of waste that is being processed, and how active the microbes are on a given day. The microbial activity is highly sensitive, effected daily by the weather. For the reason of the chemical and physical variations, the experimental data shown in figure 2.18 is displayed in a different manner. For each data point, the concentration of D5 was measured at both the entrance to the catalyst ($D5_{in}$), and after the catalyst ($D5_{out}$). The y-axis shows $(D5_{in}-D5_{out})/D5_{in}$, which is the fraction of D5 which has been removed from the gas stream. This is akin to catalyst effectiveness.

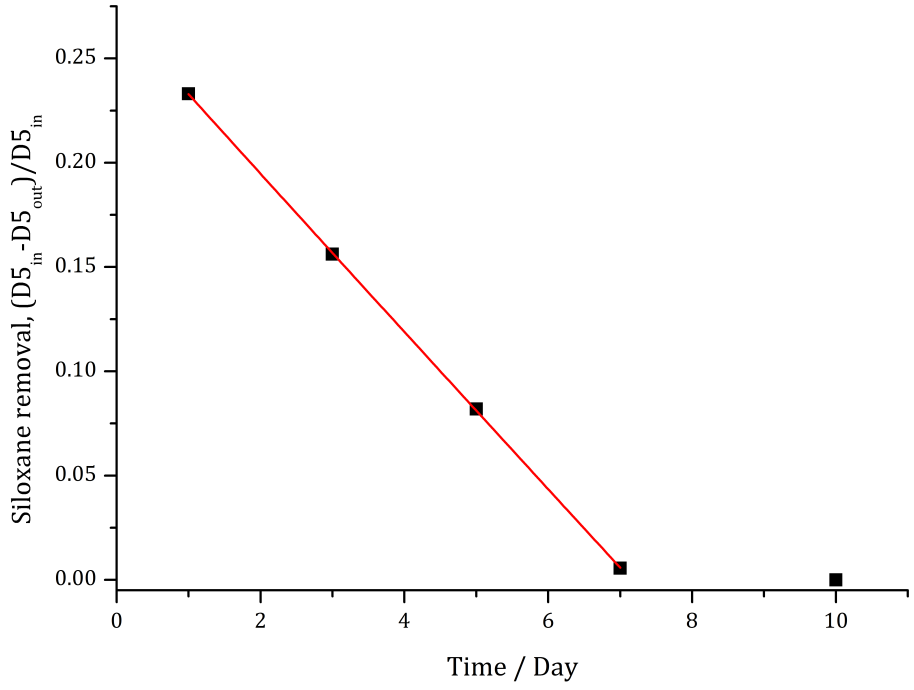

Figure 2.18. The variation of catalyst effectiveness with time, for the industrial photoreactor with real biogas. Photoreactor was run at a commercial Wastewater Treatment Works for 10 days. The y-axis indicates the fraction of removed D5. The (red) fitted line is a Voorhies plot, with $A = -0.039$, $y_0 = 0.272$ and $n = 0.99$; it has an R^2 of 0.999 and a χ^2_{red} of 9.49×10^{-7}.

In this system, the concentration of siloxane can be considered to be constant, as it is continuously being replaced by the nature of the gas-stream. Therefore, for an ideal catalyst one would expect a horizontal linear plot, demonstrating constant catalyst performance. Using Voorhies function, equation (2.16), this would be demonstrated by $n = 0$. As such, the data shown in figure 2.18 was fitted, from which $n = 0.991$. This large deviation from zero shows substantial catalyst deactivation.

The data was also fitted to an exponential function, to see if it could be modelled using more conventional kinetics. However, it was not possible to fit the data to an exponential function whilst maintaining a satisfactory goodness-of-fit.

The large rate of deactivation can be caused by many factors. Principally, as previously observed, this is likely to be due to a build up of SiO_2 on the TiO_2 surface. However, as demonstrated in table 2.3, there are many other containments in biogas. It is believed that due to the presence of these VOCs in the gas-stream, traditional coking of the catalyst took place.[168] Coking consists of the deposition of carbonaceous matter on the catalyst surface, which will deactivate the catalyst as effectively as SiO_2.

2.7 Doping Titania Nanofibres to Improve Photodegradation

Titanium dioxide is an *n*-type semiconductor. This means that in its undoped form, the main charge carriers in TiO_2 are electrons (as oppose to holes). When TiO_2 is exposed to photons of a sufficient energy they are absorbed, causing the excitation of an electron from the valence band to the conduction band. This charge carrier generation of an excited electron leaves behind a hole, creating an electron-hole pair. The electron and hole can become bound by the resulting electrostatic Coulombic force, creating a neutral quasiparticle known as an exciton.

The hole, once generated, reacts with water to generate reactive hydroxyl radicals, which in turn reacts with adsorbed siloxanes. The electron can react with adsorbed water, creating the superoxide radical $O_2^{\bullet -}$.[81] One of the limitations of using excitons to generate reactive radicals is that the electron and hole are charged opposites, and so regularly recombine too quickly to be useful. Doping is a method for increasing the number of excitons available to react, either by increasing the formation of electron-hole pairs by generating them quicker; or by reducing the recombination rate by increasing electron-hole mobility.

In an attempt to improve the catalytic performance, various doping agents were introduced to

the nanofibres. Several dopants were investigated, specifically silver, tungsten, cobalt and uranium. The level of doping was maintained at 1 % in order to analyse the effects between dopant identity.

2.7.1 Silver Doped Titania Nanofibres

2.7.1.1 Synthesis of Silver Doped Titania Nanofibres

Silver doped nanofibres were synthesised using a modified version of the standard TiO_2 nanofibre synthesis. To 10 g of dimethylformamide (DMF) was added 1.4 g of PMMA (with an average molecular weight of ~996 000 g mol^{-1}), by extended stirring. TTiP was added to this solution, followed by silver nitrate and acetylacetone with stirring. The solution was then made up to 18 g total with DMF. The resulting solution is referred to as the silver doped spinning solution.

The silver doped spinning solution was used to prepare nanofibres using the technique described in section 2.4. A positive potential of 20 kV was applied to the needle tip and the collecting drum was placed 20 cm from the needle tip. The silver doped spinning solution was eluted at a constant rate of 1 mL h^{-1}, controlled with a syringe pump.

After electrospinning, the silver doped nanofibres were steam treated for 2 hours before calcination. The nanofibres were heated to 500 °C for 16 hours, before being allowed to cool naturally to room temperature.

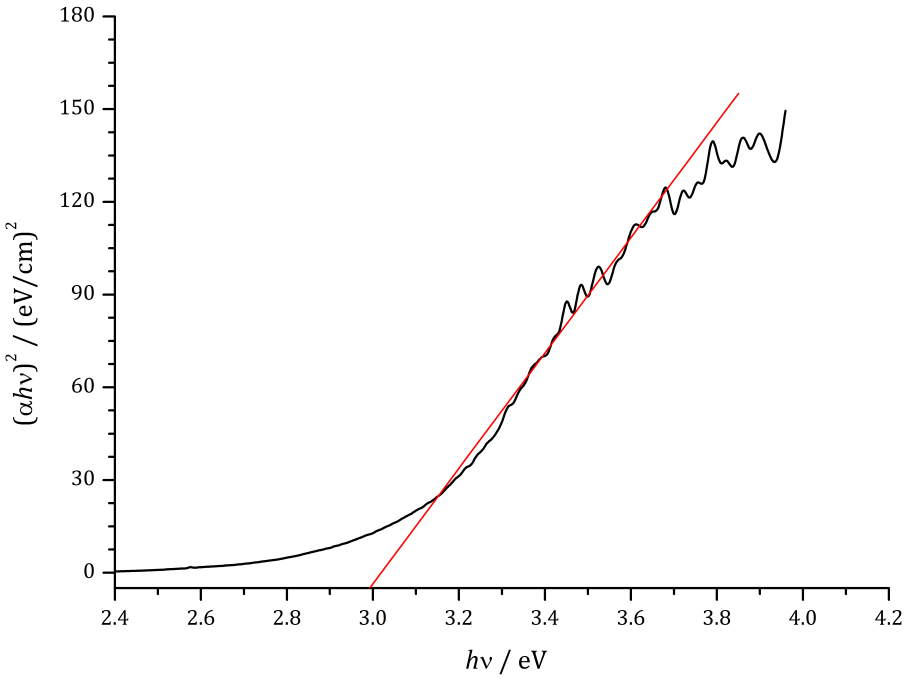

Figure 2.19. A Tauc plot of the synthesised TiO_2 nanofibres, using silver nitrate as a dopant. The x-axis intercept gives a band gap of 3.02 eV.

Diffuse reflectance UV-Vis spectroscopy was conducted in order to analyse the band gap of the newly synthesised doped nanofibres. From this data a Tauc plot was made, shown in figure 2.19. The Tauc plot indicates that doping with silver reduced the band gap of the nanofibres to 3.02 eV. This was expected, as the addition of dopants and crystal defects often creates interstitial energy levels.

Due to the low loading of silver in the nanofibres, the characterisation techniques, including EDX, SEM and pXRD, showed no discernible difference from the undoped TiO_2 nanofibres. Future analysis with X-ray photoelectron spectroscopy (XPS), transmission electron microscopy (TEM) and Brunauer-Emmett-Teller (BET) measurements would aid characterisation.

2.7.1.2 Photocatalytic Activity of Silver Doped Titania Nanofibres

The silver doped nanofibres were tested for photocatalytic activity using the experimental setup described in section 2.5. As before, the reaction vessel was charged with 50 mg of nanofibres, before being exposed to the L2 vapour in manner previously described. The resulting catalytic decomposition plot is shown in figure 2.20.

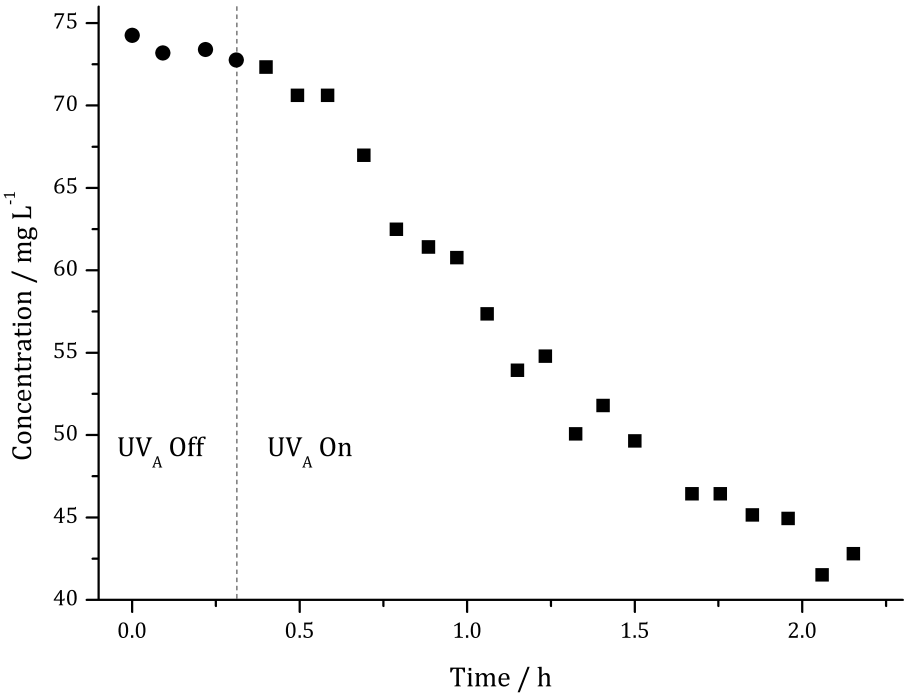

Figure 2.20. A plot of L2 concentration against time, showing the photodegradation of siloxane vapour once the lights were switched on, using 50 mg of silver doped TiO_2 nanofibres. The UV_A lamps were switched on at 18 min, shown by the dotted line. Circles indicate before illumination, squares indicate after illumination.

As can be seen in figure 2.20, the system reaches a steady state before the UV_A lights are

activated. Once switched on, the concentration of L2 drops in a predictable pseudo-first order manner. Kinetic analysis can be applied to this system, in order to obtain the rate constant for the loss of L2 vapour. The natural log of L2 concentration is plotted against time, as demonstrated in equation (2.15).

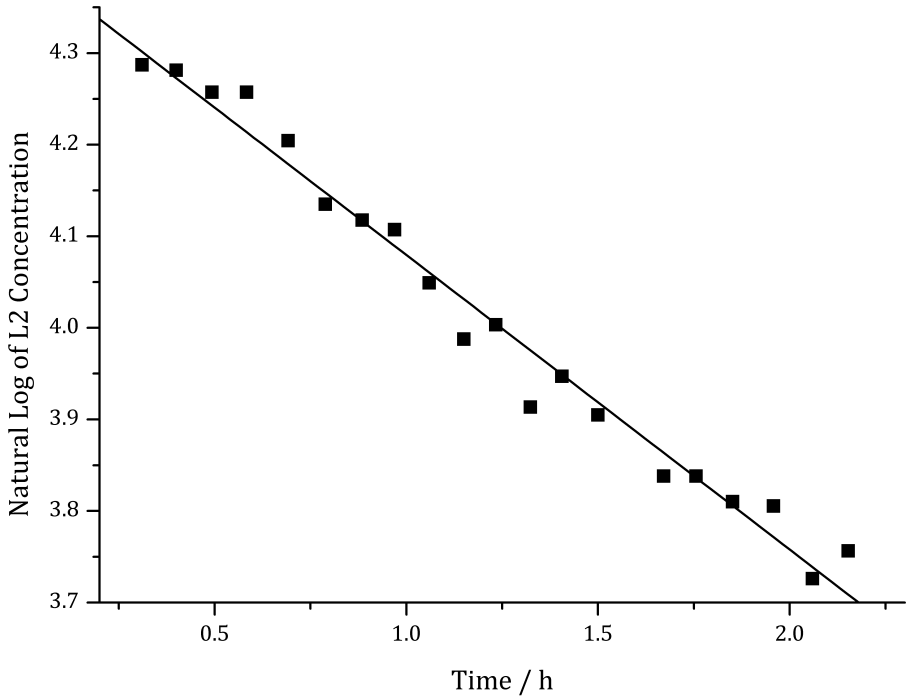

Figure 2.21. A first order kinetic plot, showing the variance in the natural log of L2 concentration with time, once the UV_A light source had been activated, using silver doped TiO_2 nanofibres. The linear line of best fit has an R^2 of 0.979; the gradient has a value of -0.322; and an intercept of 4.40.

Shown in figure 2.21 is the kinetic plot for the silver doped TiO_2 nanofibres. The rate constant, k, can be read as the negative gradient, as shown previously in equation (2.15). This gives a rate constant of $k = 0.322\,\mathrm{h}^{-1}$. It is noted that there is no deviation from linear in this kinetic plot, implying that the value for n from equation (2.16) is close to unity. It is suggested that this is due to the reduced activity of the silver-doped nanofibres. Lower activity results in less decomposition products on the surface of the catalyst, which in turn results in an extension of catalyst lifetime.

This drop in activity could be caused by a number of reasons. It is possible that the presence of silver is reducing L2's affinity for the nanofibre surface, which would in turn reduce L2's exposure to reactive radicals. Alternatively, the crystal structure of the nanofibres could be disrupted in an unfavourable manner, causing crystal defects. These can reduce the creation of excitons and also increase the rate of electron-hole recombination. In TiO_2, doped silver can form silver ion sites in the crystal lattice. These silver lattice sites can act as a draw for electrons, and cause an increase

in electron-hole recombination, reducing the rate of photodecomposition.[172,173]

Another possibility is that during the calcination process the silver nitrate oxidised to silver oxide, which then decomposed to silver(0). It is known that silver oxide decomposes above ~250 °C.[174] If this occurred then there is a possibility that the silver may have come out of the lattice, forming vacancies in the TiO_2 crystal lattice and nanoparticulate silver(0). As well as increasing electron-hole recombination this could have effected the morphology and surface area of the catalyst, both of which will have an effect on the catalytic rate constant.

It has been reported elsewhere[175,176] that the disadvantages of doping can outweigh the advantages. The desired decrease in band gap caused by the shift in flat band potential can often be outweighed by the resulting increase in electron-hole recombination caused by the presence of recombination centres (*i.e.* the doping ion). Leading to an overall loss in photoactivity.

2.7.2 Tungsten Doped Titania Nanofibres

Tungsten doped TiO_2 nanofibres were prepared using two different sources for the tungsten, tungsten(VI) hexachloride and tungsten(VI) trioxide. The two precursors were chosen because tungsten(VI) hexachloride is soluble in the electrospinning solvent (DMF), and tungsten(VI) trioxide is not. This difference will cause a substantial variance in the crystal lattice, the tungsten clusters and therefore, potentially the catalytic rate.

2.7.2.1 Synthesis of Tungsten Doped Titania Nanofibres using WCl_6

The tungsten doped nanofibres were synthesised in a similar manner as the previous nanofibres. PMMA (1.40 g) was dissolved in DMF (10 g) by extended stirring at room temperature. TTiP and acetylacetone were added, followed by tungsten(VI) hexachloride. The solution was then made up to 18 g total using DMF. This solution is referred to as the tungsten(VI) hexachloride doped spinning solution.

The tungsten(VI) hexachloride doped spinning solution was used to electrospray nanofibres using the following standards. The needle tip was subjected to a potential of 20 kV, and placed 20 cm from the collecting drum. The spinning solution was eluted at 1 mL h^{-1} using a syringe pump. The synthesised tungsten doped nanofibres were steam treated for 2 hours, followed by calcination at 500 °C for 16 hours.

Diffuse reflectance UV-Vis was conducted to ascertain the band gap of the tungsten doped nanofibres. The resulting Tauc plot is shown in figure 2.22, and gave a band gap of 3.03 eV. Once

again, due to the low loading of the dopant, other available characterisation techniques were unable to detect the presence of tungsten.

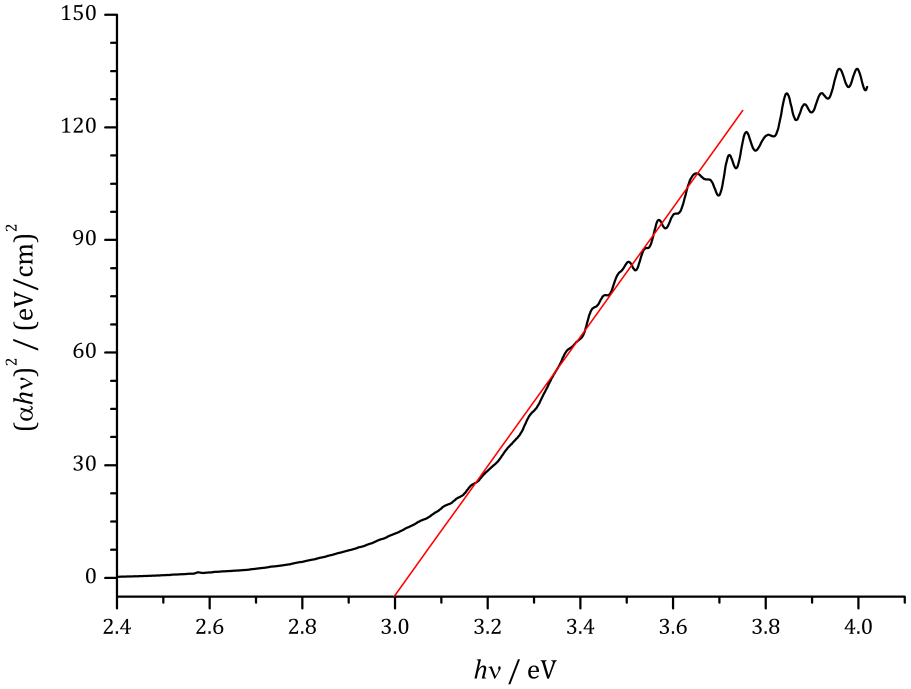

Figure 2.22. A Tauc plot of the synthesised TiO_2 nanofibres, with WCl_6 as a dopant. The x-axis intercept gives a band gap of 3.03 eV.

2.7.2.2 Photocatalytic Activity of WCl_6 Doped Titania Nanofibres

The synthesised tungsten doped nanofibres were tested to photocatalytic activity using the same experimental setup described in section 2.5. The nanofibres (50 mg) were placed in the photoreactor, which was then filled with L2 vapour. Once settled, the UV_A lights were activated and the development of the L2 concentration was monitored. The plot showing the change in L2 concentration with time can be seen in figure 2.23.

It can seen in figure 2.23 that the L2 concentration makes a steep decline after the lights have been activated at the 34 minute mark. However, there is the initial photo-induced desorption caused by the excitation of adsorbed L2, discussed previously in section 2.3.3. Once again the plot shows an exponential decline in the concentration of L2, as would be expected from a pseudo-first order reaction. The rate constant, k, is obtained by plotting the natural log of the concentration against time, using equation (2.15). This is shown in the kinetic plot in figure 2.24.

From figure 2.24 and equation (2.15) the rate constant can be inferred as $k = 0.344\,\mathrm{h}^{-1}$. This is larger than recorded for silver doping ($k = 0.322\,\mathrm{h}^{-1}$), but also smaller than that recorded for undoped TiO_2 nanofibres ($k = 0.582\,\mathrm{h}^{-1}$). This decrease in activity is again likely to be the reason

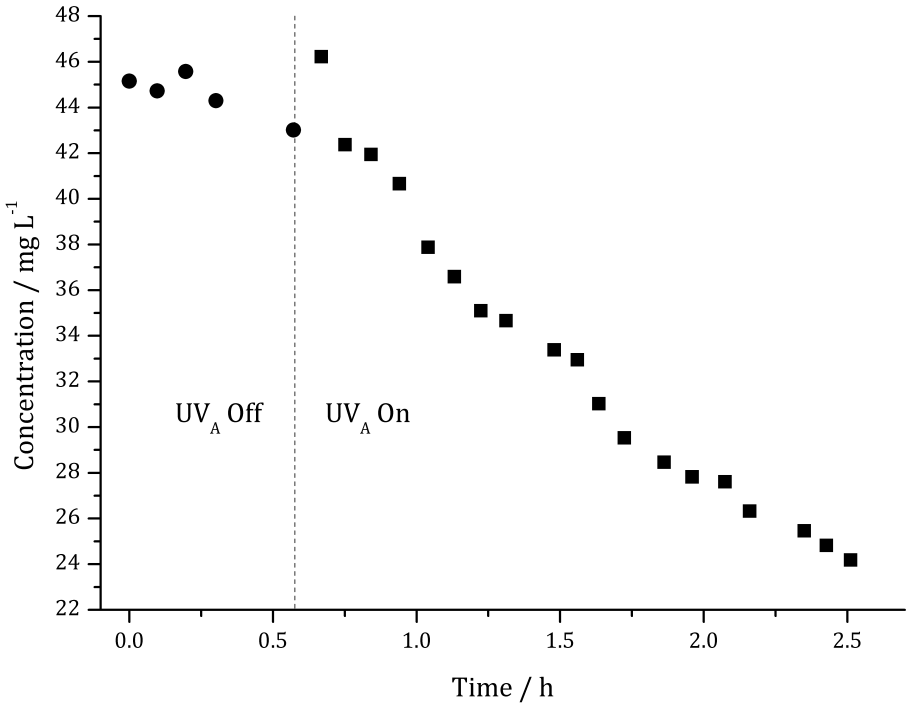

Figure 2.23. A plot of L2 concentration against time, showing the photodegradation of siloxane vapour once the lights were switched on, using 50 mg of WCl_6 doped TiO_2 nanofibres. The UV_A lamps were switched on at 34 min, shown by the dotted line. Circles indicate before illumination, squares indicate after illumination.

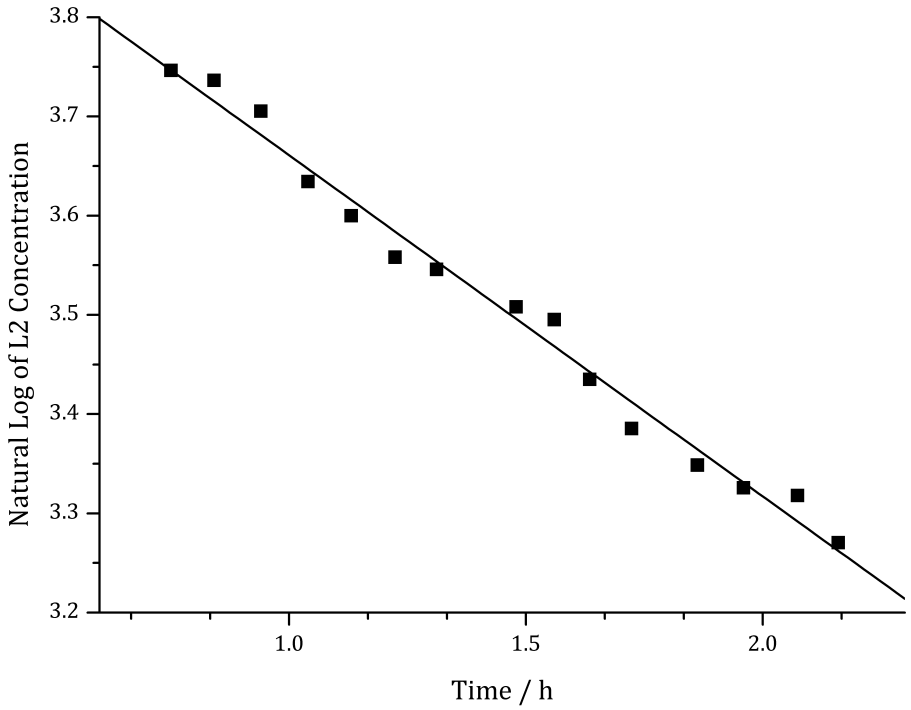

Figure 2.24. A first order kinetic plot, showing the variance in the natural log of L2 concentration with time, once the UV_A light source had been activated, using WCl_6 doped TiO_2 nanofibres. The linear line of best fit has an R^2 of 0.985; the gradient has a value of −0.344; and an intercept of 4.00.

that catalyst deactivation is not observed. The slight improvement over silver doping is ascribed to to interstitial energy levels allowing the absorption of higher wavelengths of light, as suggested by the reduced band gap of 3.03 eV. As discussed in section 2.7.1.2, it is suspected that the decrease in photocatalytic activity compared to undoped TiO_2 nanofibres is due to an increased electron-hole recombination rate, caused by the doping agent acting as recombination centres throughout the nanofibres. It is also possible that there remain some chlorine atoms on the surface of the catalyst, from the metal precursor. This would change the affinity of L2 for the catalyst surface, affecting the decomposition rate.

The absorption at longer wavelengths of light is a desirable quality as the majority of sunlight that reaches the planet's surface is of visible or longer wavelengths, whilst TiO_2 requires UV_A wavelengths to become excited. In this case however, the benefits provided by tungsten have been outweighed by the increased rate of electron-hole recombination, causing a drop in photoactivity compared to undoped TiO_2 nanofibres.

2.7.2.3 Synthesis of Tungsten Doped Titania Nanofibres using WO_3

Doping of titania nanofibres using tungsten(VI) trioxide was conducted in a similar manner as previous nanofibre syntheses. The PMMA (1.40 g) was dissolved in DMF (10 g) by extended stirring. TTiP, acetylacetone and tungsten(VI) trioxide were added. The solution was then made up to 18 g with DMF, followed by vigorous stirring to fully suspend the WO_3.

This solution was then used to electrospin nanofibres using the setup and conditions described in section 2.4. The nanofibres were then steam treated for 2 hours, before calcination at 500 °C for 16 hours.

To obtain the band gap of the synthesised nanofibres, diffuse reflectance UV-Vis spectroscopy was conducted. The resulting Tauc plot is shown in figure 2.25, and indicates a band gap of 2.93 eV. This is a considerably smaller band gap than for the previously recorded samples, and indicates that a greater amount of visible light is absorbed by the catalyst.

It was not possible to observe the dopant by pXRD. However, particulates of WO_3 were visible by SEM, shown in figure 2.26. The presence of particulate WO_3 was unsurprising, due to the insolubility of WO_3 in DMF. This results in the formation of a nanocomposite of WO_3/TiO_2.

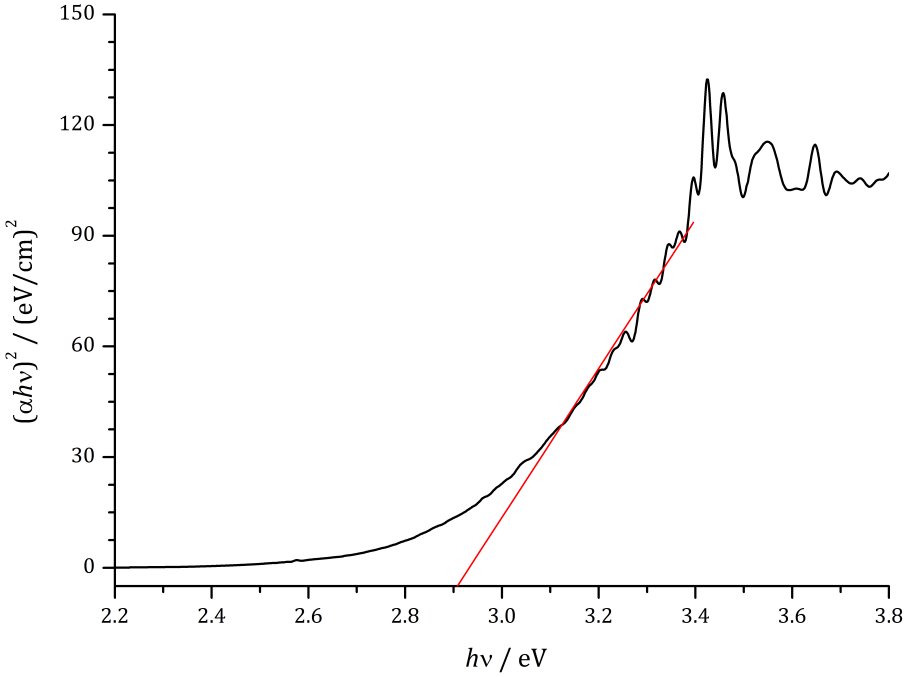

Figure 2.25. A Tauc plot of the synthesised TiO_2 nanofibres, with WO_3 as a dopant. The x-axis intercept gives a band gap of 2.93 eV.

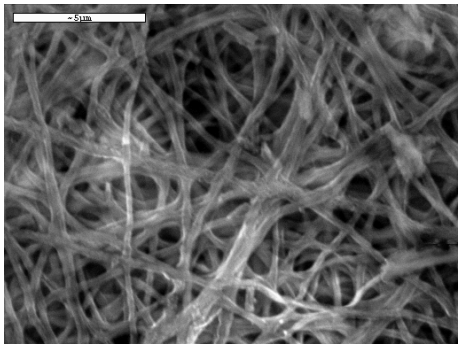

Figure 2.26. An SEM image of the WO_3 doped nanofibres. The WO_3 particulate is visible as the brighter dot. The scale bar is 5 µm.

2.7.2.4 Photocatalytic Activity of WO_3 Doped Titania Nanofibres

The photocatalytic activity of the synthesised WO_3 doped titania nanofibres was tested in the manner described in section 2.5. Fifty micrograms of the doped nanofibres were added to the reaction chamber, which was then filled with L2 vapour and, once equilibrated, exposed to UV_A radiation. The resulting change in L2 concentration was monitored by regular GC-FID injections, and the resulting plot is shown in figure 2.27.

In figure 2.27 the photocatalytic decomposition of L2 is clearly visible once the UV_A light source has been activated. There is also a small amount of photodesorption present, caused by the absorption of the photons by the substrate, as discussed previously in section 2.3.3. After the

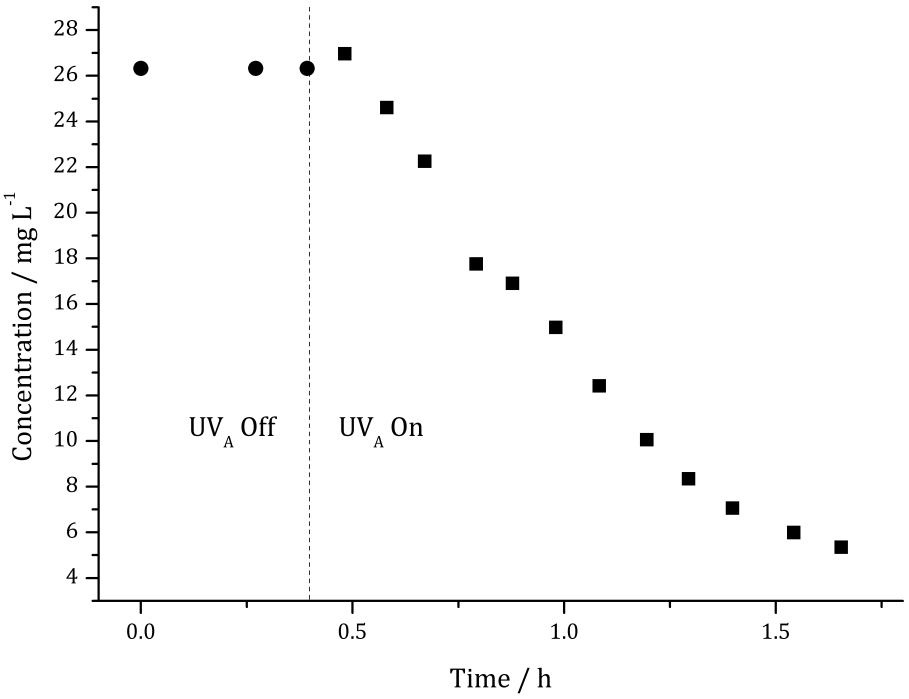

Figure 2.27. A plot of L2 concentration against time, showing the photodegradation of siloxane vapour once the lights were switched on, using 50 mg of WO_3 doped TiO_2 nanofibres. The UV_A lamps were switched on at 24 min, shown by the dotted line. Circles indicate before illumination, squares indicate after illumination.

photo desorption the L2 concentration decreases exponentially, as in previous examples, representing a pseudo-first order reaction. The rate constant, k, for this reaction can be calculated using equation (2.15) and plotting the resulting graph, shown in figure 2.28.

The rate constant, k, measured from the negative gradient of the linear line of best fit in figure 2.28, has a value of $1.46\,h^{-1}$. This is a marked improvement from the other doped samples, and also from the undoped TiO_2 nanofibres. Repeated testing with new samples confirmed the large increase in catalytic decomposition rate.

Previous reports of WO_3/TiO_2 composites in the literature suggest that the large increase in activity is not unusual.[177,178] In the work reported by Ismail *et al.*, a 3 % WO_3/TiO_2 nanocomposite achieved a 3.5-fold increase in photocatalytic efficiency,[179] which is comparable to the increase observed in this work. The possible reasons for this include WO_3 acting as a photocatalyst independently, or a symbiosis between the two semiconductors creating a reduction in recombination rate.

The difference in band gap levels in TiO_2 and WO_3 is a possible cause of the dramatic increase in catalytic rate. Tungsten(VI) trioxide is known to absorb light up to ~500 nm,[180] as well as being photoactive.[181] This increase in absorbed light generates more electrons and holes, consequently

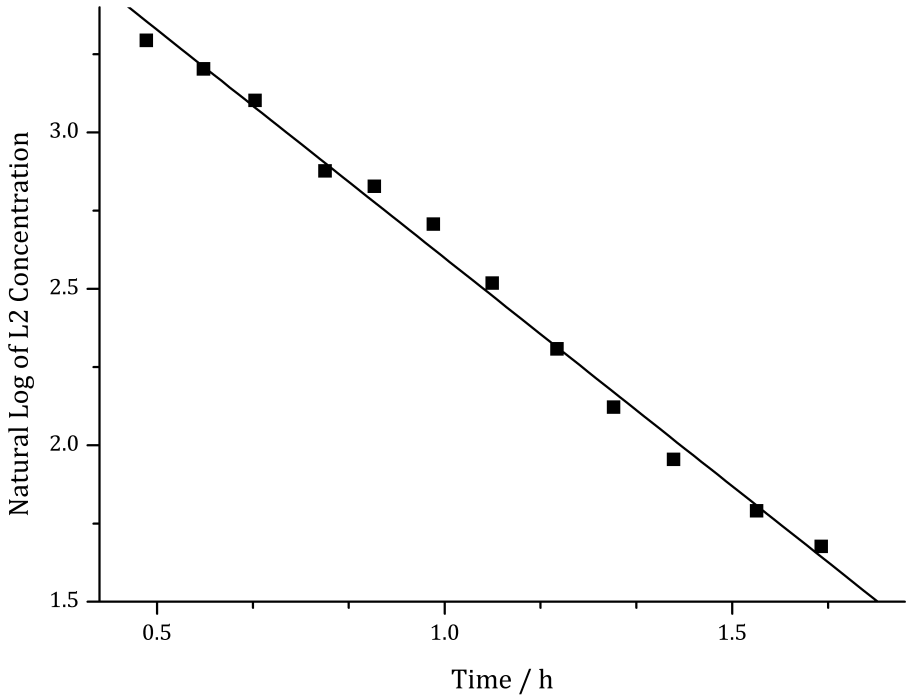

Figure 2.28. A first order kinetic plot, showing the variance in the natural log of L2 concentration with time, once the UV_A light source had been activated, using WO_3 doped TiO_2 nanofibres. The linear line of best fit has an R^2 of 0.993; the gradient has a value of -1.46; and an intercept of 4.06.

causing a greater rate of hydroxyl radical formation, and therefore an increase in the photodecomposition of L2. It should be noted that the reaction chamber was primarily irradiated with UV_A light (315 nm to 400 nm), however the light source was not completely UV_A, and some light towards the lower end of the spectrum was visible during experiments. Unfortunately, work within the group on the synthesis of pure WO_3 nanofibres was unsuccessful whilst this study was conducted.[182]

An alternative option is that the same number of excitons are being created by the TiO_2. The promoted electrons can then move down in energy by passing to the WO_3 particles, whilst the generated holes stayed in the valence band of the TiO_2 due to their slower speed. The relevant bands are shown in figure 2.29. This physical separation of the electron and the hole leads to a decrease in electron-hole recombination, which would in turn lead to an increase in the catalytic rate constant. This effect will be compounded with the extended exciton lifetimes observed in WO_3, as shown in table 2.5. Related work with WO_3 and TiO_2 has shown similar results, which are also explained by the movement of the TiO_2 promoted electrons relaxing into the WO_3 conduction band.[183]

Due to the insolubility of WO_3 in the spinning solution, it is likely that the tungsten is not distributed with the crystal lattice of the TiO_2. Instead there are particles of tungsten(VI) trioxide spread throughout the nanofibres. This physical separation is what allows for the effective physical

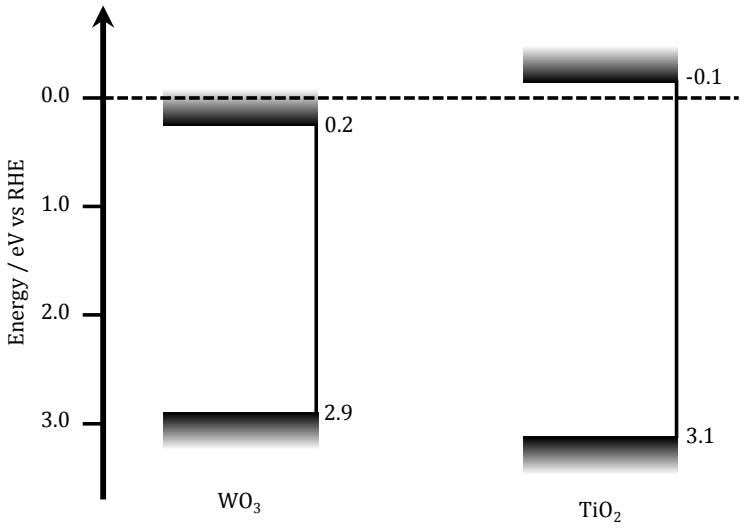

Figure 2.29. The band gap and flat-band potential of TiO_2 and WO_3 are shown, with reference to the reversible hydrogen electrode.[184–186] Electrons are excited from the TiO_2 valence band to the TiO_2 conduction band, before moving to the WO_3 conduction band; whilst, on the same time-frame, the holes stay in the TiO_2 valence band. This separation of the exciton reduces the rate of electron-hole recombination.

Table 2.5. Typical exciton lifetimes for tungsten trioxide and titania.[187,188]

Semiconductor	Exciton Lifetime / ns	Reference
WO_3	500	187
TiO_2	100	188

electron-hole separation. The hole remains in the TiO_2 valence band, allowing for the reduction of water to hydroxyl radicals.

It is probable that there is a combination of both these effects contributing to the increase in k. Electrons move from the TiO_2 valence band, via the TiO_2 conduction band, to the WO_3 conduction band. Due to the higher effective mass of holes, their mobility rate is lower than electrons. This allows the electrons to migrate away from the holes, shifting the electron-hole equilibrium.

There is no sign of catalyst deactivation in figure 2.28, *i.e.* $|n| \approx 1$. There are several possible reasons for this. One of which is that the degradation products are accumulating on the WO_3 sites, away from the hydroxyl generating sites on the TiO_2. Another possibility is that absolute number of active sites on the catalyst surface has increased, which would in turn delay the onset of catalyst deactivation. It is possible that the WO_3 has caused surface changes, such as an increase in surface area, a change in defect distribution, or an increase micropore size (which would consequently reduce pore blockage).

2.7.3 Cobalt Phosphate Doped Titania Nanofibres

2.7.3.1 Synthesis of Cobalt Phosphate Doped Titania Nanofibres

The cobalt phosphate doped titania nanofibres were prepared using the novel complex bis(dibutyl phosphate) cobalt, whose preparation is described in section 6.5.5. The PMMA (1.40 g) was dissolved in DMF 10 g with extended stirring at room temperature. TTiP was then added, followed by acetylacetone. The bis(dibutyl phosphate) cobalt was then added with stirring, creating a vibrant blue colour. This solution was diluted with DMF to a total of 18 g, and is referred to as the cobalt phosphate doped spinning solution.

The cobalt phosphate doped spinning solution was used to synthesise nanofibres using the electrospraying technique described previously in section 2.4. A potential of 20 kV was applied to the needle tip, which was positioned 20 cm from the collecting drum. The cobalt phosphate doped spinning solution was eluted from the needle tip at a steady rate of 1 mL h^{-1} using a syringe pump. The synthesised doped nanofibres with then steam treated for 2 hours, before being calcined at 500 °C for 16 hours.

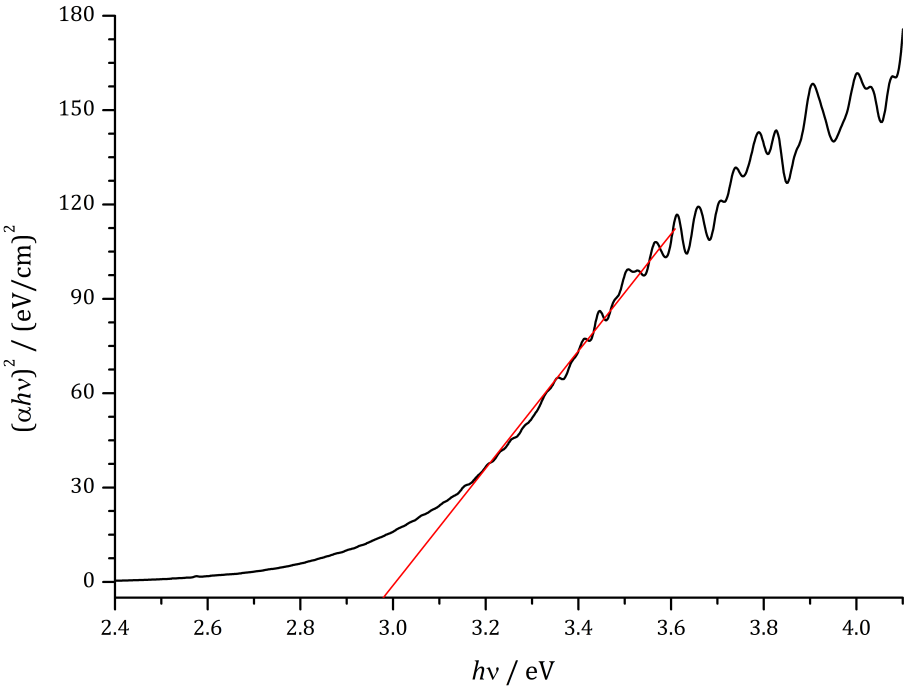

Figure 2.30. A Tauc plot of the synthesised TiO_2 nanofibres, with cobalt phosphate as a dopant. The x-axis intercept gives a band gap of 3.01 eV.

Diffuse reflectance UV-Vis spectroscopy was used to obtain the data for a Tauc plot. The resulting graph, shown in figure 2.30, indicates a band gap of 3.01 eV. This band gap is smaller than recorded for pure TiO_2 nanofibres, suggesting incorporation of the dopant into the nanofibres.

2.7.3.2 Photocatalytic Activity of Cobalt Phosphate Doped Titania Nanofibres

The photocatalytic decomposition ability of the prepared cobalt phosphate doped titania nanofibres was experimentally examined in the same manner as the other doped nanofibres, and as explain in section 2.5. The nanofibres (50 mg) were loaded into the reaction vessel, and L2 vapour vapour was added, before irradiation with UV_A light. The concentration of L2 in the reaction chamber atmosphere was monitored, and the resulting plot can be seen in figure 2.31.

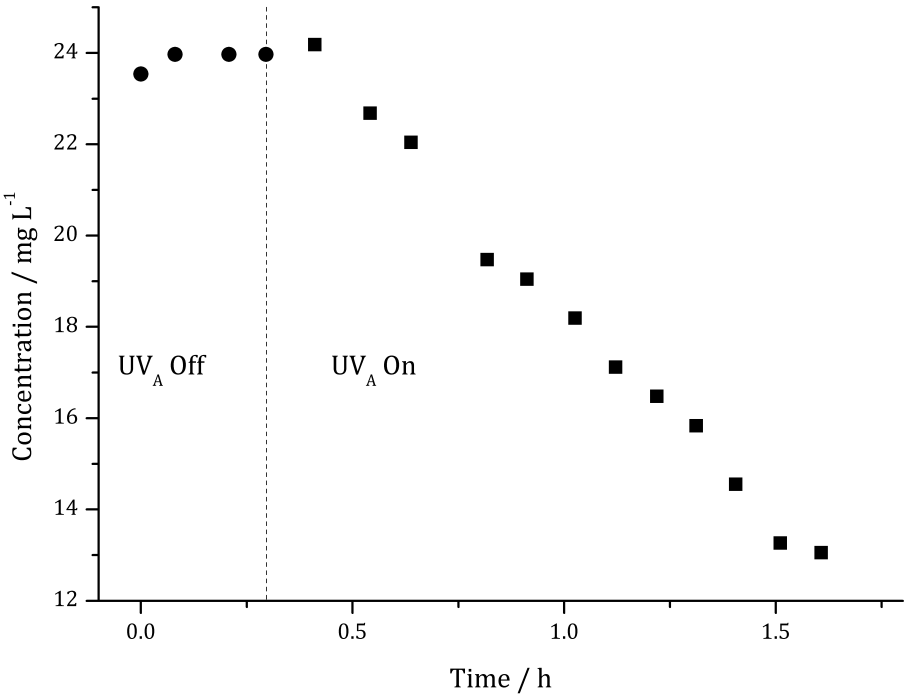

Figure 2.31. A plot of L2 concentration against time, showing the photodegradation of siloxane vapour once the lights were switched on, using 50 mg of cobalt phosphate doped TiO_2 nanofibres. The UV_A lamps were switched on at 18 min, shown by the dotted line. Circles indicate before illumination, squares indicate after illumination.

In figure 2.31 there is photoinduced desorption, visible as a slight increase in the L2 concentration immediately after the UV_A light source is activated, at the 18 minute mark. The mechanism behind the incipient photodesorption of the L2 from the nanofibre surface is discussed in section 2.3.3. After the photodesorption there is a sharp and marked decline in the concentration of L2. This decrease, caused by the catalytic decomposition of the L2, follows an exponential decay and can be monitored by pseudo-first order reaction kinetics. This is demonstrated in figure 2.32.

The catalytic decomposition using cobalt phosphate doped nanofibres follows psudeo-first order kinetics, shown by the linear line of best fit in figure 2.32 with an R^2 value of 0.988. The gradient of the linear plot is $-0.521\,h^{-1}$, which equates to a value for the rate constant of $k = 0.521\,h^{-1}$. This rate constant is slightly smaller than that recorded for undoped titania nanofibres

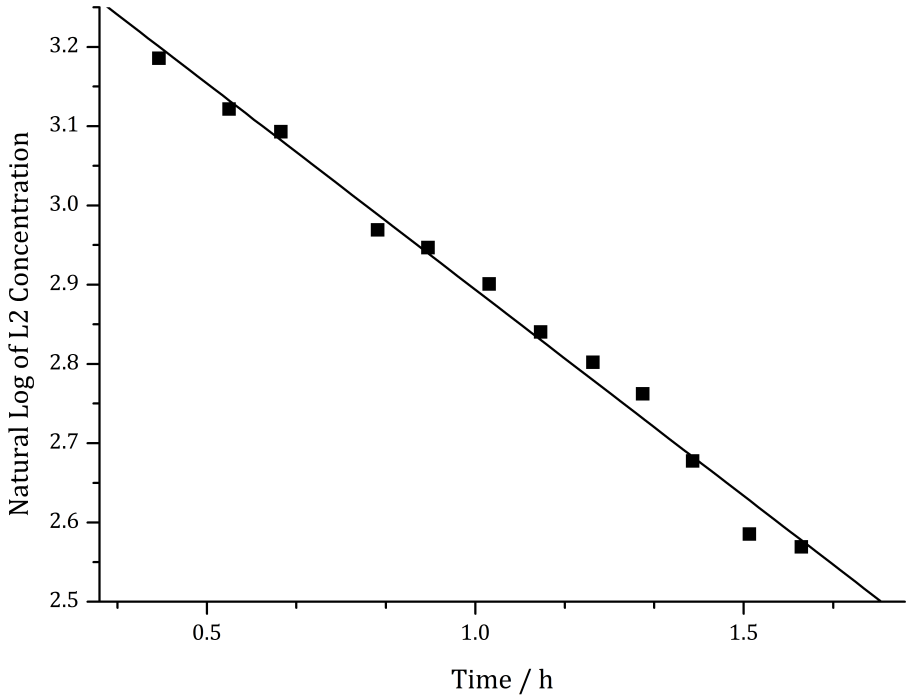

Figure 2.32. A first order kinetic plot, showing the variance in the natural log of L2 concentration with time, once the UV_A light source had been activated, using cobalt phosphate doped TiO_2 nanofibres. The linear line of best fit has an R^2 of 0.988; the gradient has a value of -0.521; and an intercept of 3.41.

(*cf.* $k = 0.582\,h^{-1}$). As before in section 2.7.1.2, an increase in electron-hole recombination is suggested as the likely cause for the drop in photoreactivity. Formation of ionic centres in the crystal lattice trap excitons, favouring recombination and a decrease in activity.

Once again, there is no sign of appreciable catalyst deactivation. Previously published work has suggested that the incorporation of Co^{2+} sites into the TiO_2 lattice leads to an increase in Ti^{3+} sites and oxygen vacancies.[189] This would result in an increase in active sites on the catalyst surface, and therefore an extension the catalyst lifetime.

The lack of a corresponding increase in activity is attributed the phosphate doping modifying the acidity of the nanofibre surface. Phosphates have been reported to have this effect on TiO_2.[190] This would change both L2 and waters affinity for adsorbing to the catalytic surface. Making the surface hydrophobic would make it less energetically desirable for L2 or water to be adsorbed to the catalyst surface and react. The hydrophilicity of L2 can been demonstrated through a calculation of its molecular electrostatic potential. Calculations were conducted using Gaussian 09 using the B3LYP functional and the standard 6-311G(d) basis set for all atoms.[191]

Shown in figure 2.33, the calculated electrostatic potential of L2 is visualised by mapping onto electron density. The Mulliken charges calculated for the silicon atoms are +1.101, and for the

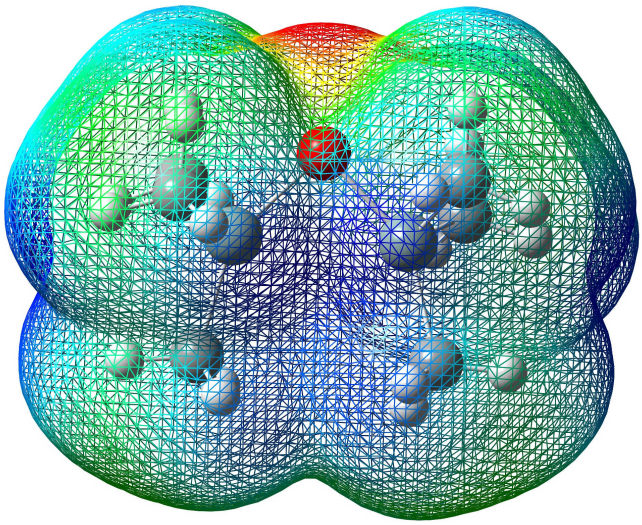

Figure 2.33. An image showing the calculated electrostatic potential mapped onto electron density. The red (oxygen atoms) indicates a build up of electronegative charge, whilst the blue (silicon atoms) shows a deficit of electronegative charge. The green (methyl groups) indicates a comparatively neutral charge.

oxygen atom is −0.445. These values indicate partial atomic charges, calculated from population analysis. This large difference indicates the polar nature of L2, making it and the whole siloxane family hydrophilic. If the nanofibre surface was made more hydrophobic by the doping, this would cause a decrease in affinity for L2, resulting in a decrease in catalytic activity.

2.7.4 Nanoparticulate Titania

In order to gain a better understanding of the advantages of using titania in nanofibre form, nanoparticulate TiO_2 was also tested for comparison. In these experiments, the TiO_2 was sourced from Sigma-Aldrich. Aeroxide P25 (product number: 718467) was used, with an average particle size of 21 nm as determined using transmission electron microscopy (TEM) by the manufacturer. The P25 was used as-provided, without further purification. The band gap for P25, as discussed in section 2.3.2.4 and shown in figure 2.5, is 3.08 eV.

The photocatalytic ability of P25 to decompose siloxanes was tested using the same experimental parameters as before, described in section 2.5. The nanoparticulate powder (50 mg) was loaded into the reaction vessel, which was then charged with L2 vapour and irradiated with UV_A radiation. The resulting change in the concentration of L2 was monitored by periodic GC-FID measurements. The resulting graph is presented in figure 2.34.

In figure 2.34 the photo-induced desorption is clearly visible as the increase in concentration at $t = 15$ min, after the UV_A lights have been activated. This phenomenon is discussed in detail in

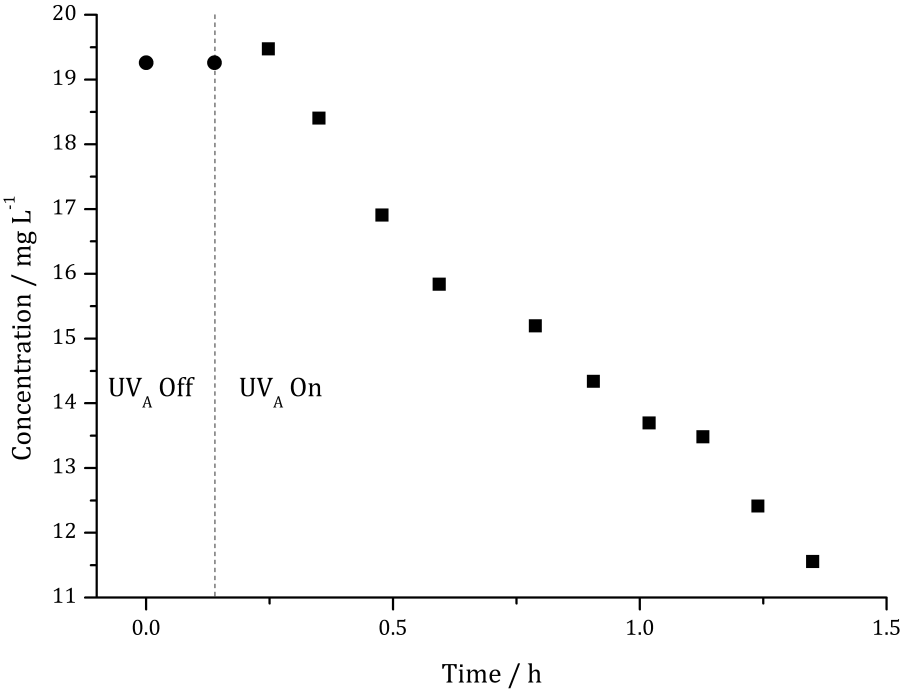

Figure 2.34. A plot of L2 concentration against time, showing the photodegradation of siloxane vapour once the lights were switched on, using 50 mg of P25. The UV_A lamps were switched on at 9 min, shown by the dotted line. Circles indicate before illumination, squares indicate after illumination.

section 2.3.3. After this initial rise in concentration, the concentration decreases in an exponential manner, as expected for a pseudo-first order reaction. In order to make comparisons the rate constant for the reaction needs to be calculated. This was achieved by plotting the natural log of the concentration against time, shown in figure 2.35.

Shown in figure 2.35, the kinetic plot follows a linear line of best fit with an R^2 value of 0.982, indicating very good correlation. Taking the negative of the gradient gives a kinetic rate constant of $k = 0.434\,h^{-1}$. As anticipated, this is lower than recorded for the TiO_2 nanofibres. The reason behind the drop in activity is the reduced surface area. The synthesised nanofibres have an elongated and rigged structure that prevents the aggregation that occurs in traditional nanoparticulate powder. This maintains the increased surface area of the nanostructure, allowing the higher activity levels to be maintained.

Also shown in figure 2.35 is the power function from equation (2.16), using $A = -0.434$, $y_0 = 3.056$ and $n = 0.992$. This fitting converged with an R^2 of 0.984 and a χ^2_{red} of 5.034×10^{-4}, which is slightly better than the linear fit. The slight curve exhibited by this plot, as evidenced by the value for n of 0.992 is due to the slight poisoning of the catalyst, as previously discussed. The deactivation is less pronounced than the undoped nanofibres because of the lower activity exhibited

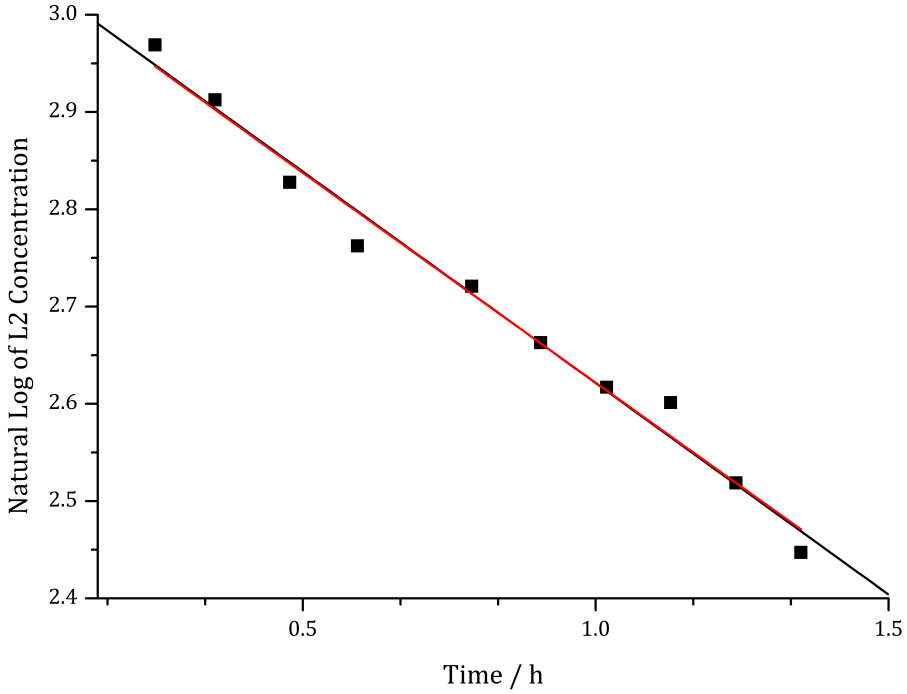

Figure 2.35. A kinetic plot, showing the variance in the natural log of L2 concentration with time, once the UV_A light source had been activated, using P25 as the catalyst. The (black) linear line of best fit has an R^2 of 0.982; the gradient has a value of −0.434; and an intercept of 3.06. The (red) power function uses equation (2.16) with $A = -0.434$, $y_0 = 3.056$ and $n = 0.992$; it has an R^2 of 0.984.

by P25. In addition, P25 is particulate, and so will have different surface morphology to the TiO_2 nanofibres.

2.8 Conclusions and Future Work

This chapter has investigated the catalytic photodecomposition of L2, as a model for the removal of siloxanes from waste biogas streams. The catalysts were all tested under the same conditions using UV_A irradiation to cause the photodecomposition of L2. The resulting decrease in L2 concentration was recorded and analysed using pseudo-first order reaction kinetics and the Voorhies model. The collated rate constants for this photocatalytic reaction are shown in figure 2.36.

It has been shown that the undoped titania nanofibres display improvement over commercially available P25. This anticipated increase is due to the maintenance of the high surface area, caused by the nano-architecture. Nanoparticulates have a tendency to aggregate and clump together, reducing the effective surface area available for photocatalysis. The branch-like structure of the nanofibres do not experience this phenomenon, providing them with an advantage.

Titania nanofibres were tested at a commercial waste water treatment facility, in order to ob-

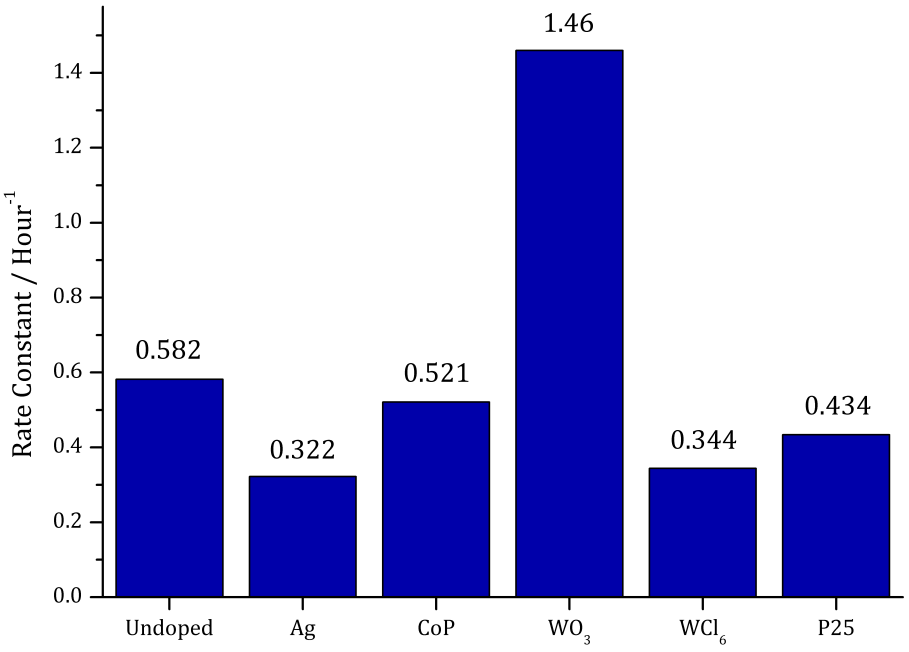

Figure 2.36. A bar chart showing the comparative rate constants, *k*, for the catalytic photodecomposition of L2 using either undoped or 1 % doped titania nanofibres, or commercial P25.

serve their effectiveness with genuine biogas. Using a new, patent-pending[171] coating procedure, nanofibres were loaded onto glass beads and packed into a glass cylinder. The beads were illuminated with UV_A, and the effectiveness of the catalyst monitored over 10 days. The nanofibre catalyst was shown to decompose the siloxanes initially, with the catalyst efficiency dropping to zero over a period of seven days. The deactivation is attributed to the build of of the degradation production, SiO_2, on the catalyst surface, which is supported by kinetic modelling of data from the model-systems used in the laboratory.

The silver- and tungsten-doped titania nanofibres both showed a substantial drop in photoactivity. This is due to a number of reasons, primarily the increase in recombination rate of electron-hole pairs. The recombination rate is increased due to the presence of new donor centres in the crystal lattice. These donor centres trap photo-holes, which then become positively charged, attracting photo-electrons and causing recombination. An alternative cause is the potential modification of the surface of the nanofibres.

The cobalt phosphate doped titania nanofibres showed a slight drop in photoactivity. This is again because of the increase in electron-hole recombination, due to the increase in donor centres promoting the recombination rate. The decrease is, however, not at large as for the silver- and tungsten-doped titania nanofibres. This suggests that the cobalt phosphate is providing additional interstitial energy levels between the valence and conduction bands, allowing for the creation of

new excitons with less energetic (higher wavelength) irradiation of the photocatalyst. This conclusion was supported by Tauc plot measurements.

The tungsten trioxide doped titania nanofibres had approximately a three-fold improvement over the undoped titania nanofibres. This is primarily due to the large decrease in electron-hole recombination rate, caused by the physical separation of the electrons and the holes. The photoelectrons, promoted to the TiO_2 conduction band, are relaxing into the WO_3 conduction band. The WO_3 is physically separate from the TiO_2, causing a separation of the electron-hole pair, and as such a decrease in the electron-hole recombination rate.

The 1 % tungsten(VI) trioxide doped titania nanofibres showed the greatest affinity for the photocatalytic decomposition of L2. Whilst encouraging resulting have been made using L2 as a model, further experimentation should be conducted using some of the other common siloxanes, such as L4, D4 and D5. The process should also be optimised using non-synthetic biogas, as the presence of VOC impurities has detrimental effects on the catalyst.

Chapter 3

The Coupling of Methane

The heterogeneous catalytic properties of titanium dioxide, used in the previous chapter to oxidise siloxanes, are further exploited in this chapter to oxidise methane. A novel approach is taken by removing oxygen from the system. Instead hydroxyl radicals are used, with an aim to partially oxidise methane to useful feedstock chemicals.

3.1 A Background to Methane

Methane is a hugely abundant gas in the Earth's crust. Worldwide reserves are comparable to crude oil, with known reserves growing at a similar rate, as demonstrated in figure 3.1.[192] A large amount of methane is obtained from the head space of oil wells, which is the conventional source for the gas. The same process that forms crude oil also creates natural gas, which is largely methane. Whilst this process can be completed on a kilogram scale in a few hours in the laboratory,[193] it takes millions of years for the right conditions to be created in nature before the process begins. An unfortunate issue with conventional methane sources is that they are often poorly located. The cost of transporting gases is much higher than for liquids, and whilst the energy density of gases like propane can be increased for transportation by compressing them into liquids, the considerably lower boiling point of methane makes this option both expensive and impractical. Additionally, compression of wet methane can result in the formation of methane hydrate, a solid which is known to block gas pipelines.[194] As a result, much methane is burnt off with an on-site flare, as the economics of delivering the gas to the end-user are unfavourable.

Alternative sources for natural gas are labelled 'unconventional'. The most abundant form of unconventional methane reserves is methane hydrates, with an estimated 1.5×10^{15} m^3 accumulated under the sea floor.[194] Whilst it has been known to form terrestrially, greater than 97 % of world reserves are beneath the ocean, where both water and methane come together at the appropriate temperature and pressure. The conditions required vary with ocean depth and therefore

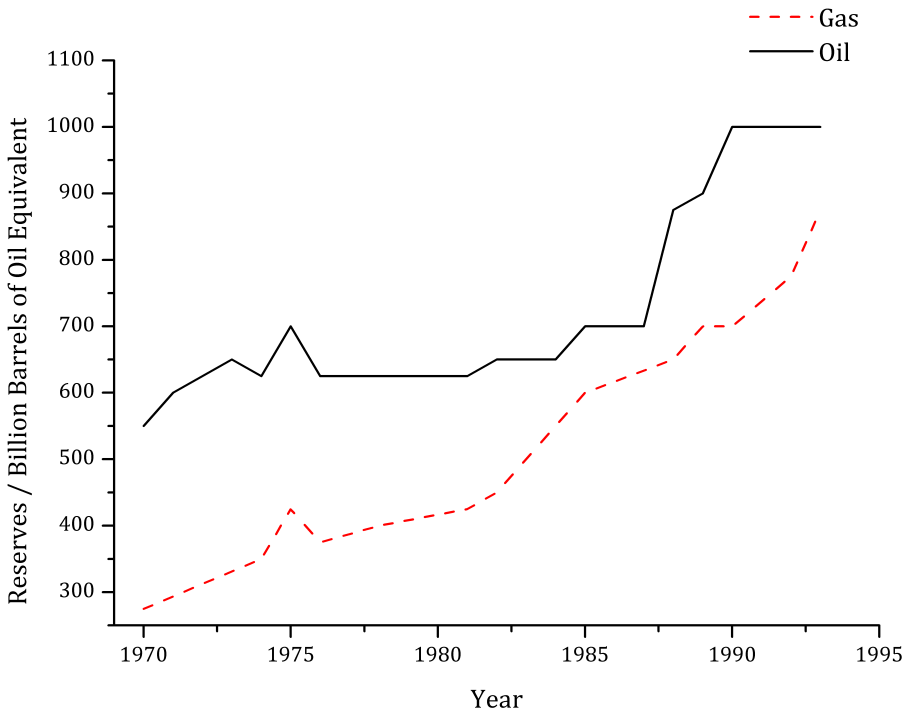

Figure 3.1. The proven oil and gas reserves worldwide, shown in billion barrels of oil equivalent. The black solid line indicates oil reserves, whilst the red dashed line indicates gas reserves.[192]

pressure, with a typical example being a seabed 500 m deep, under 51 bar of pressure from the water above it and at 5 °C.[195] Extracting and processing the methane hydrate however is extremely complicated, with current technology and economics making less than 1/1000 obtainable.

A comparatively new, and highly controversial, form of unconventional methane reserves is shale gas. In conventional gas reserves, the methane that is produced translates vertically through the ground in porous and permeable rock, such as sandstone. This continues until it reaches a non-permeable barrier called the cap-rock, for example limestone, creating an underground reservoir of gas and oil trapped in the porous and permeable rock. Shale is a type of rock that is porous (and so can contain trapped methane) but has low permeability, making extraction slow and difficult. Recent advances in this field has led to a rise in shale gas extraction. Miners drill down to the shale layer, then horizontally to create a hollow tube running through the shale layer. Hydraulic fluid (comprising of water with some additives) is then pumped into the newly formed tube at high pressure, creating cracks and fissures in the shale rock. These deformations greatly increase the permeability of the shale rock. The hydraulic fluid is then pumped out, leaving the tube hollow again for the natural gas that was trapped in the shale to flow out to the surface, where it is captured for transport and use.

Whilst the technique of hydraulically fracturing the shale rock is effective, controversies have

arisen. These are partly due to the location of the shale sites. In the UK, several of the most promising sites for extracting shale gas are in National Parks or Areas of Outstanding Natural Beauty. Another issue is raised by health and safety concerns. Early attempts at hydraulic fracturing of shale rock in the USA has caused several cases of contaminated drinking water supplies. This can be caused either by oil or gas diffusing into the drinking water, or by direct contamination of the drinking water with the hydraulic fluid. Despite these concerns, the use of shale gas has grown enormously in the USA, and licences for trial sites are being issued by the UK government. Conversely, some countries are taking a more cautious approach. France, for example, has banned all shale gas operations, citing environmental concerns.

The conventional issue of transporting the mined methane is also a problem for unconventional methane sources. Consequently, in the latter half of the 20$^{\text{th}}$ century there has been much research into the conversion of methane into more valuable and practically useful commodities. The ability to convert methane into propane would allow for easy liquidation, and therefore transport, of the resource. Alternatively, oxidatively coupling the methane to produce ethene is also highly desirable. Ethene is an enormously important chemical building block, with a worldwide production of 1.2×10^{11} kg in 2008.[196] It is used in the industrial-scale synthesis of many compounds such as polyethylene, ethylene oxide and vinyl chloride.

Maximising the potential use of methane as a non-renewable resource makes sense both economically and ethically. By converting methane into more valuable compounds, the 4 % that is flared can be eliminated.[197] Methane, and its combustion product carbon dioxide, are both greenhouse gases. Purposely releasing them into the atmosphere as waste is highly discouraged politically, economically and environmentally. Minimising this will help to maximise resource efficiency and minimise environmental contention.

3.2 Existing Light-Independent Activations of Methane

The uncontrolled, non-catalysed, partial oxidation of methane was known by 1903, when the formation of formaldehyde and formic acid by the heating of an oxygen/methane mixture was reported.[198] Since then, much work has been conducted in understanding the reactions of methane, and how to apply them economically on an industrial scale.

3.2.1 Syngas production

The most common activation of methane is in the production of synthesis gas. Synthesis gas (or syngas) is a highly useful gas mixture of carbon monoxide and hydrogen, with two parts hydrogen to one part carbon monoxide. Syngas is the primary source of hydrogen for the Haber-Bosch process, as well as being useful as a fuel in itself.[199,200] The three traditional processes used to produce syngas from methane are reforming with steam or carbon dioxide, and partial oxidation. Shown in scheme 3.1, both steam reforming and carbon dioxide reforming are endothermic reactions.[201]

$$CH_4 + H_2O \rightleftharpoons CO + 3\,H_2 \qquad \Delta H^{\ominus}_{298\,K} = 206\,kJ\,mol^{-1}$$
$$CH_4 + CO_2 \rightleftharpoons 2\,CO + 2\,H_2 \qquad \Delta H^{\ominus}_{298\,K} = 247\,kJ\,mol^{-1}$$

Scheme 3.1. Steam reforming and carbon dioxide reforming of methane. Note that both of these reactions are endothermic, and therefore require considerable energy input, normally through the combustion of a quantity of the starting methane.[201]

Modern facilities tend to favour the partial oxidation of methane for syngas synthesis, however. Shown in scheme 3.2, this involves the addition of half an equivalent of oxygen to the methane. The partial oxidation is an exothermic reaction, and so is more economical to run on a large scale. The reaction is conducted using a transition metal catalyst, such as Ru/TiO_2.[202]

$$CH_4 + {}^1/_2\,O_2 \rightleftharpoons CO + 2\,H_2 \qquad \Delta H^{\ominus}_{298\,K} = -35\,kJ\,mol^{-1}$$

Scheme 3.2. The partial oxidation of methane. This reaction is slightly exothermic, liberating heat in the forwards direction.[201]

To vary the final ratio of hydrogen to carbon monoxide, a combination of steam/carbon-dioxide reforming and partial oxidation can be used. This allows the control of the final H_2/CO ratio to be within 1 to 3, by controlling the $CO_2/H_2O/O_2$ feed ratio. The addition of oxygen whilst reforming can initiate some exothermic partial oxidation, reducing energy demands. Additionally, the presence of steam helps prevent the build up of carbon deposits, by the oxidation of $C_{(s)}$ to $CO_{(g)}$ and $H_{2(g)}$.[203]

The ultimate products of these processes are carbon dioxide, carbon monoxide and hydrogen gas. The presence of steam allows the water-gas shift reaction to take place. Shown in scheme 3.3, this reaction rapidly reaches equilibrium due to the high temperature in the reaction vessel.

$$H_2O + CO \rightleftharpoons H_2 + CO_2$$

Scheme 3.3. The water-gas shift reaction.

3.2.2 Direct Synthesis of Chemicals from Methane

3.2.2.1 Methanol & Methyl Bisulphate

Whilst the usefulness of syngas cannot be understated, it is also desirable to convert the methane directly to other products, without going via syngas. One of the ways this has been achieved in the laboratory (although not on an industrial scale) is the direct conversion from methane to methanol, using the Shilov system. Reported initially by Shilov[204] and worked on extensively by Labinger and Bercaw,[205–209] this catalytic cycle uses a chloro-aquo platinum(II) species as the active catalyst, under aqueous conditions. The exact identity of the active catalyst is unknown, although the homoleptic species, $[Pt(Cl_4)]^{2-}$ and $[Pt(H_2O)_4]^{2+}$, are believed to be unreactive. The catalytic cycle for this reaction is shown in scheme 3.4. The system starts with a $Pt(II)X_4$ complex, **8**, undertaking C-H activation of the methane. The accepted mechanism for this step is the coordination of CH_4 via associative-displacement oxidative-addition, yielding an alkyl-hydrido platinum complex, which then reductively eliminates HX, yielding compound **9**.[208,210] Using a stoichiometric amount of $[Pt(IV)Cl_6]^{2-}$, this species is oxidised to the Pt(IV) species, **10**.[206] The Pt(IV) complex undergoes dissociative nucleophilic attack by a solvent water molecule, followed by reductive elimination of methanol, reforming **8**.[205]

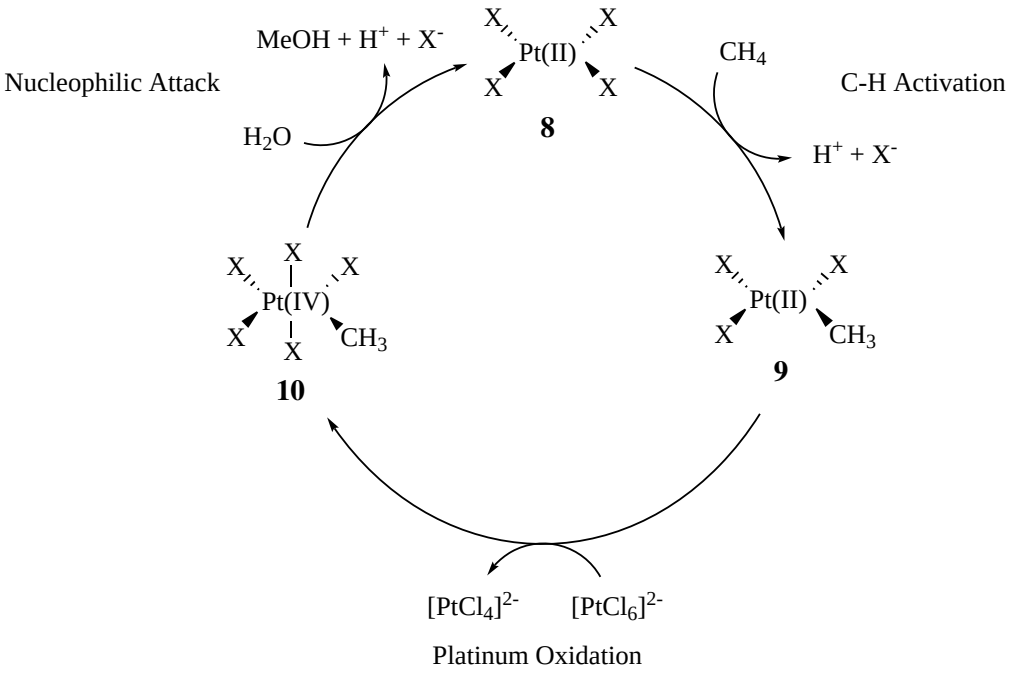

Scheme 3.4. The catalytic cycle of the Shilov system. Here, X equates to Cl^-, HO^- or H_2O.

In a typical experiment, *p*-toluenesulfonic acid is used to demonstrate the Shilov system, due to its water solubility. Using 10 mol% of the catalyst, Na_2PtCl_4, the system achieved a conversion of 31 % and selectivity to $ArCH_2OH$ of 80 %.[211] This catalytic system had promise, if the stoichiometric oxidant could be switched from the expensive Na_2PtCl_6 to a more financially viable alternative, such as oxygen. Using inspiration from the Wacker process,[212] Bercaw and Labinger attempted to couple the Pt(II)/Pt(IV) redox with an oxygen-driven Cu(I)/Cu(II) process. Whilst the reaction ran, the turnover number dropped drastically, due to the formation of a suspected copper-peroxide complex becoming a thermodynamic sink.[213]

Another homogeneous platinum catalyst has been developed for the direct conversion of methane to methyl bisulphate, as demonstrated by Periana *et al*. whilst working at Catalytica Inc.[214,215] They reported that the use of a chelating bipyrimidyl platinum(II) complex (shown in figure 3.2), in concentrated sulphuric acid, under 35 bar of methane, at 220 °C, for 2.5 h resulted in the catalytic formation of methyl bisulphate in 90 % conversion and 81 % selectivity. Turnover frequency (TOF) and turnover number (TON) was reported as 10^{-2} s^{-1} and 500, respectively.

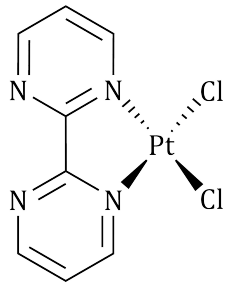

Figure 3.2. Periana's bipyrimidyl platinum(II) complex. Solvated in concentrated sulphuric acid, this catalyst has reported the formation of methyl bisulphate in 90 % conversion and 81 % selectivity.[214]

The formation of methyl bisulphate is useful as an intermediate in industrial synthesis of dimethyl sulphate, a useful methylating agent and solvent. It was speculated in the paper that this catalytic process could be coupled with an aqueous hydrolysis step to produce methanol and regenerate the sulphuric acid. Despite the large interest surrounding the conversion of methane to methanol, this combined process has not been demonstrated. However, Palkovits *et al*. have further developed this work, creating a triazine-based framework and reacting it with $PtCl_2$. This formed a solid analogue to Periana's bipyrimidyl platinum catalyst, which has been reported to achieve TONs above 250.

Previous to this, Periana *et al*. reported a mercury triflate catalyst.[216] Dissolved in 100 % sulphuric acid, the mercury(II) ions catalytically convert methane to methyl bisulphate, with conver-

sion at 50 % and selectivity at 85 %. The majority of the balance consists of CO_2. They progress to hydrolyse the methyl bisulphate to methanol, with another suggestion that this could be conducted catalytically, by coupling to an industrial reoxidation of sulphur dioxide to sulphuric acid with air, a process already performed on a large scale.

Nature has been a source of inspiration for many scientific endeavours, and this does not exclude the activation of methane. The enzyme methane monooxygenase (MMO) is found in methanotrophic bacteria, a commonly studied example being *Methylococcus capsulatus*, discovered in the hot water springs of Bath, UK.[217] This enzyme converts methane to methanol under ambient conditions. In an attempt to model the active site of MMO, Otsuka *et al*. synthesised a catalytic heterogeneous iron phosphate species as an analogue.[218] The iron phosphate converted methane to methanol and formaldehyde, in the presence of both hydrogen and oxygen, with moderate selectivity, though only at a conversion of 0.6 %. High temperatures (>350 °C) were also required, which creates a substantial safety risk when flammable gases and oxygen are involved.

3.2.2.2 Formaldehyde

Formaldehyde is also a target for the oxidation of methane. Used as precursor for chemicals such as melamine resin and 1,4-butanediol, it is also a disinfectant and embalming agent, with worldwide production at 1.5×10^7 t in 2005.[219] A vanadium(V) oxide catalyst on a silica support was employed by Herman *et al*., forming formaldehyde with a conversion and selectivity of 8.5 % and 16.6 %, respectively.[220] The majority of the balance is made up of unreacted methane, carbon monoxide, and completely oxidised carbon dioxide. This procedure requires temperatures exceeding 600 °C.

An iron-doped cerium-zirconium oxide catalyst was reported by Roger *et al*. for the conversion of methane to formaldehyde.[221] The catalyst has zero activity below 350 °C, reaching a maximum conversion of 6 % at 500 °C. Maximum selectivity for formaldehyde however, drops steadily from ~50 % at at 350 °C, to ~2 % at at 600 °C. Whilst the selectivity at 350 °C is impressive, at that temperature the conversion is only ~0.3 %. No methanol or carbon monoxide were formed during the experiment, with the carbon-containing balance comprising solely of CO_2.

Zeolites have been used as scaffolds for formaldehyde forming catalysts. A common hydrogen aluminosilicate zeolite, known as HZSM-5, was loaded with molydenum by Valverde *et al*. using an aqueous ammonium heptamolybdate solution, followed by calcination.[222] The catalytic run required temperatures of 600 °C, with a feed of methane and oxygen in a 5.3:1 ratio. This yielded

an optimal methane conversion rate of 6.5 %, with selectivity for formaldehyde at 10.6 %. The carbon balance is comprised solely of carbon monoxide and carbon dioxide in an approximate 2:1 molar ratio.

The use of a continuous flow recycling reactor has been demonstrated with a SiO_2 catalyst by Parmaliana *et al.*[223] Using commercial, pure SiO_2 with a surface area of 400 $m^2\,g^{-1}$, they reported the conversion and selectivity of methane to formaldehyde at 18 % and 64 %, respectively. The balance is comprised of CO and CO_2 in a 2:1 ratio. The optimised temperature for this reaction was reported as 650 °C. As previously, methane and oxygen gas are fed into the system in a 2:1 ratio, providing a significant safety risk at the high temperatures required.

Despite these encouraging experimental results, the industrial synthesis of formaldehyde is not currently using methane as a direct source.[224] Both methanol and formaldehyde are more prone to oxidation than methane. Consequently, the conversion and selectivity are not economically viable for industrial application.

3.2.3 Oxidative Coupling of Methane

The synthesis of ethene from methane is known as the Oxidative Coupling of Methane (OCM). Known since 1982,[225,226] OCM is of great interest to the industrial sector due to the huge demand for ethene (global ethene production in 2008 was 1.2×10^{11} kg,[196] and has grown largely since). Shown in scheme 3.5, the exothermic reaction is typically conducted at very high temperatures (500 °C to 1000 °C).

$$CH_4 + {}^1/_2\,O_2 \longrightarrow {}^1/_2\,C_2H_4 + H_2O \qquad \Delta H^{\circ}_{1073\,K} = -139\,kJ\,mol^{-1}$$

Scheme 3.5. The oxidative coupling of methane.[227]

The demand for ethene has driven a large amount of research into this field. A statistical review by Baerns *et al.* in 2011 found over 2,700 research articles, of which 421 unique reports of various catalysts, with 69 elements ranging from lithium to thorium.[228] Of this multitude of catalysts reported in scientific literature, only a select few will be mentioned here.

Traditional catalysts for OCM can be split into four distinct categories. Reducible metal oxides, non-reducible metal oxides, halogenated metal oxides and solid electrolytes. When a reducible metal oxide catalyst is in use, the gas feed is alternated between methane and an oxidising gas (generally oxygen). During the methane phase, oxygen ions from the catalyst oxidise the methane,

creating vacancies in the crystal lattice. These are replenished during the subsequent oxygen phase. A downside to this type of catalyst is the often low productivity; one example reports a two minute catalytic methane phase, followed by a 130 minute reoxygenation phase.[229]

On the other hand, non-reducible metal oxide catalysts are able to use a co-feed of methane and oxygen simultaneously. This has the advantage that there is no down time during catalyst regeneration. Generally, the gas feed is diluted ten-fold with helium, increasing selectivity for C_2 products over CO_x.

The addition of halogens to the metal oxide has been shown to increase catalyst effectiveness. Chlorinated catalysts liberate chlorine under the high temperatures required for the OCM reaction. It is believed that chlorine radicals are released from the crystal lattice, providing additional active sites on the catalyst, whilst also initiating free radical reactions in the gas-phase.[230]

Solid electrolyte catalysts are an interesting development. Working like a reducible metal oxide catalyst, they are characterised by their extremely high ion mobility. It is generally accepted that their ion mobility has to be at least twice their electron mobility.[231] In an OCM reactor, the methane is kept on one side of the catalyst, consuming the oxygen in the crystal lattice. The high ion mobility allows lattice oxygen to migrate to the impoverished side of the catalyst. At the same time the other side of the catalyst is exposed to oxygen, which replenishes the oxygen vacancies that were created by oxygen ions migrating to the methane side. This is demonstrated graphically in figure 3.3.

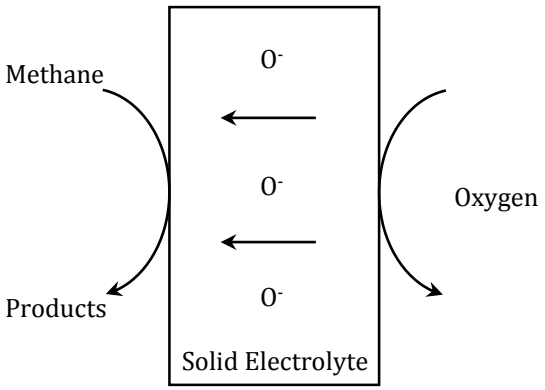

Figure 3.3. A diagram illustrating a typical solid electrolyte catalyst. The oxygen and methane are kept separate, whilst the oxygen ions migrate through the material to fill the vacancies created by the reacting methane.

Bostan *et al*. has reported impressive results with their reducible potassium-doped strontium manganese catalyst, $Sr_{0.75}K_{0.25}MnO_{3-x}$.[232] At a temperature of 1023 K and standard pressure, they report C_2 selectivity of 97.2 % with a methane conversion of 8.2 %. The selectivity for ethene

specifically was 40 %. As is typical with an OCM reductive catalyst, the gases are alternated across the catalyst. Methane and oxygen are alternatively pulsed for 1.5 min, with 5 min of helium in between each gas.

A co-fed OCM catalyst reported by Lin *et al*. comprised of a fluorite-structured yttrium and samarium doped bismuth oxide, $Bi_{1.5}Y_{0.3}Sm_{0.2}O_{3-x}$.[233] Using a high reactor temperature of 1223 K and a 2:1:3 methane to oxygen to helium ratio at 1 bar, a methane conversion of 44 % and C_2 selectivity of 62 % was achieved. This was conducted in a single pass with a modest flow rate of 150 mL min^{-1}. The C_2 products comprised of ethene and ethane, in approximately a 2.5:1 ratio.

A patent registered by the petrolchemical company HDR Corporation, has claimed the use of a barium-titanium-tin-chloro-oxide catalyst for OCM.[234] Running at atmospheric pressure and 800 °C, the reactor uses undiluted methane/oxygen in a 2:1 ratio at a respectable 100 mL min^{-1}. Achieving an ethene selectivity of 40 % and methane conversion of ~50 %, the reactor uses the liberated chlorine gas to initiate gas-phase reactions. Consequently, there is a noted drop in catalyst performance as the halogen is lost over time. This can be partially offset by the periodic injection of microlitres of carbon tetrachloride into the reactor.

A metal oxide solid-electrolyte catalyst was reported by Machida and Enyo.[235] A ytterbium-doped strontium cerium oxide, $SrCe_{0.9}Yb_{0.1}O_{1.95}$, showed ethene selectivity of 36 % with a methane conversion of 53 %. Requiring a reaction temperature of 1023 K, the catalyst is first preheated at 873 K under helium. The feed gas is a methane/oxygen/helium mix with a ratio of 2:1:12, with a flow rate of 50 mL min^{-1}. It is suggested by the authors that the selectivity could be related to conductivity, due to the observed correlation between ion conductance and selectivity.

Despite these developments, there has only been one example of an industrial-scale OCM reaction.[236] In 2015 Siluria Technologies opened and operated a demonstration plant for OCM. This took place after they successfully demonstrated three smaller pilot plants. After 16 successful runs of the new plant, Siluria Technologies is now planning on opening the first OCM commercial plant in 2018.[237] The technology behind the catalyst is unknown, though it has been stated by Siluria Technologies that their catalyst operates at 5 bar to 10 bar, ~350 °C and that they use heterogeneous nanowires as the catalyst — which could drastically increase the surface area available for catalysis.

3.2.4 Mechanistic Insights

The activation of methane over heterogeneous catalysts could follow a homolytic or heterolytic mechanism. The difference is where the electrons are located after the C−H bond is broken. In

homolytic fission, the two electrons are divided equally between each atom involved in the original bond — the surface oxygen and the carbon in this case. In heterolytic fission, the two bonding electrons both remain on one of the involved atoms. Whilst heterolytic fission was initially favoured for methane activation over metal oxides due to the often acidic surface, a homolytic mechanism is now more widely accepted.[238]

Initially postulated in 1986, the Lunsford mechanism is a general scheme centring around an oxygen radical on the metal oxide surface.[239–241] Shown in scheme 3.6, methane is first activated on the metal oxide surface, yielding gaseous $CH_3^{\bullet}$ and surface bound hydrogen.[242] The $CH_3^{\bullet}$ radicals either terminate by combining with another $CH_3^{\bullet}$, forming ethane, or follow traditional radical reaction pathways, discussed below. On the metal oxide surface water is liberated, leaving an oxygen vacancy, V_O. The oxygen vacancy, V_O, is then replenished by gaseous oxygen.

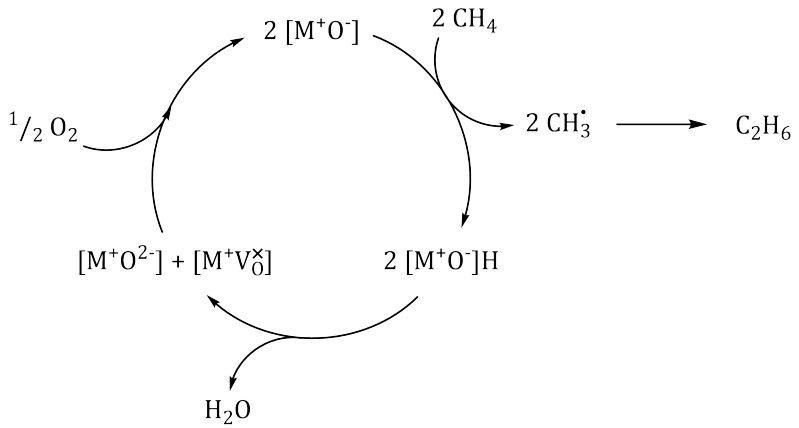

Scheme 3.6. A diagram illustrating the Lunsford mechanism for catalytic methane activation.[241] Gaseous methane reacts with the metal oxide surface, forming gaseous methyl radical and adsorbed hydrogen. Water is then released from the surface, with the oxygen vacancy replenished by gaseous oxygen. The methyl radicals either self terminate to form ethane, or follow standard radical reaction pathways.

The Lunsford mechanism closely follows the Mars-van Krevelen (MvK) mechanism for the reactions of gas molecules with solid surfaces.[243] In the MvK mechanism, a gaseous reactant forms a chemical bond with the reactive surface, becoming bound. The second gaseous reactant then reacts directly with the surface bound species, before the reaction product desorbs, leaving a vacancy which is filled by the bulk. In the Lunsford mechanism, this vacancy is filled by gaseous oxygen.

The hydrogen abstraction can occur via two different mechanisms, the direct 'harpoon' mechanism and an indirect, metal-mediated mechanism. Both mechanisms operate around an activated oxygen species, formed by ligand-metal charge-transfer (LMCT) from the oxygen to the metal.[244]

In the direct mechanism, methane approaches the surface oxygen radical and the proton is

directly transferred to the surface in a barrier-free reaction, demonstrated in scheme 3.7. This results in no long-lived complex between the methane and the surface. An extensively studied example of this mechanism is methane over V_4O_{10}.[245–247]

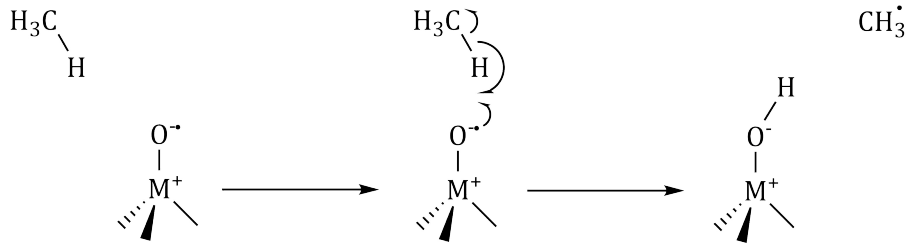

Scheme 3.7. A generalised scheme showing direct 'harpoon' proton abstraction, generating a methyl radical without forming a long-lived associated complex between the surface and the methane. Here, the metal oxide surface is shown as an ionic crystal.

The indirect, metal-mediated activation of methane involves the initial coordination of methane to the metal atom, shown in scheme 3.8. The coordinated methane translates and rotates, allowing the oxygen radical to abstract the proton, generating a coordinated methyl radical. This methyl radical rotates back to its initial position, before dissociating. A study on the activation of methane over magnesium oxide demonstrated that the the coordinated methane adduct was stabilised by 91.6 kJ mol^{-1} (21.9 kcal mol^{-1}), relative to non-associated methane and MgO.[248] Interestingly, once the coordinated methyl radical has been formed it can be thermodynamically more favourable for it to translate and rotate once more, this time inserting between the metal and oxygen, before dissociating as CH_3OH and MV_O; kinetically however, this is far less favourable.[248]

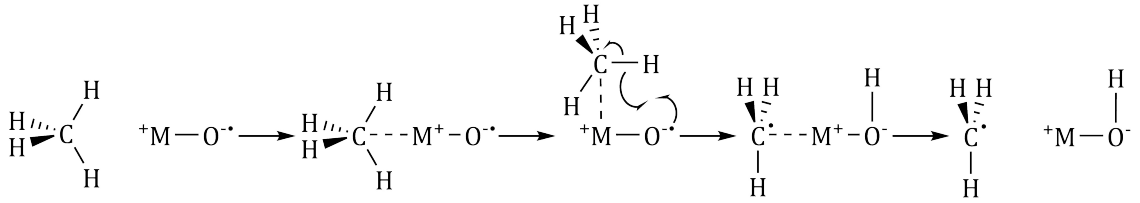

Scheme 3.8. A generalised scheme showing indirect proton abstraction. Methane first coordinates to the metal, forming a stable adduct. After rotation, the proton is abstracted by the oxygen radical generating a methyl radical. The methyl radical then rotates back to its initial position, before disassociating. Here, the metal oxide surface is shown as an ionic crystal.

Once the methyl radicals have formed, they can follow several reaction pathways. The simplest of these pathways is the homogeneous, self-terminating, homocoupling of two methyl radicals to form ethane, shown in scheme 3.9. This reaction is also catalysed by the presence of a surface, facilitating contact between radicals. The heterogeneous coupling is far more likely however, as gaseous radical collisions are unlikely due to concentration.

Once formed, the ethane is dehydrogenated to ethene, shown in scheme 3.10. Conveniently, most OCM catalysts are also apt at dehydrogenation under the reaction conditions, with ethane molecules undergoing the same mechanisms shown in scheme 3.7 and scheme 3.8. The $C_2H_5^{\bullet}$ radical intermediate can also take an alternative path however, reacting with oxygen to ultimately form carbon monoxide and hydrogen.

$$CH_3^{\bullet} + CH_3^{\bullet} \longrightarrow C_2H_6$$

Scheme 3.9. The homocoupling of methyl radicals.

$$C_2H_6 \overset{cat.}{\rightleftharpoons} C_2H_5^{\bullet} + H^{\bullet} \longrightarrow C_2H_4 + H_2$$
$$C_2H_5^{\bullet} + O_2 \overset{cat.}{\rightleftharpoons} C_2H_5O_2^{\bullet} \xrightarrow{multiple\ steps} 2\,CO + {}^5/_2\,H_2$$

Scheme 3.10. The radical pathway from ethane to ethene and carbon monoxide.

The methyl radicals also react with gaseous oxygen to form $CH_3O_2^{\bullet}$ or the metal oxide surface oxygen to form CH_3O^-. These species are considered to be precursors to the formation of CO_x.[249–251] The reactions are shown in scheme 3.11.

$$CH_3^{\bullet} + O_2 \rightleftharpoons CH_3O_2^{\bullet} \xrightarrow{multiple\ steps} CO + {}^3/_2\,H_2$$
$$CH_3^{\bullet} + O^{2-}_{surface} \rightleftharpoons CH_3O^- \xrightarrow{multiple\ steps} CO + {}^3/_2\,H_2$$

Scheme 3.11. The pathway from methyl radicals to $CH_3O_2^{\bullet}$, and on to carbon monoxide.

Unfortunately, carbon dioxide is the thermodynamic sink for all species in the OCM reaction. Shown in the simplified scheme 3.12, all species, including the desired product ethene, react under the reaction conditions to ultimately produce CO_2. In fact, due to the weaker C−H bond strength in ethane compared to methane, the ethane activates 5 to 20 times faster than methane.[252] Additionally, whilst the C−H bond strength in ethene is stronger than methane, ethene is the more reactive species due to the π-component of its C=C bond.[253] This problem, of the starting material being less reactive than the products under reaction conditions, is a major problem for OCM systems.

Another problem with OCM is the inherent limit to yield. It has been shown that there is a mechanistic limit on single-pass yield of approximately 30 % for reactions conducted at atmospheric pressure.[253] This limit can be raised by reducing the partial pressure of methane, though this is generally considered impractical for industry due to economics. The cause for this upper-limit

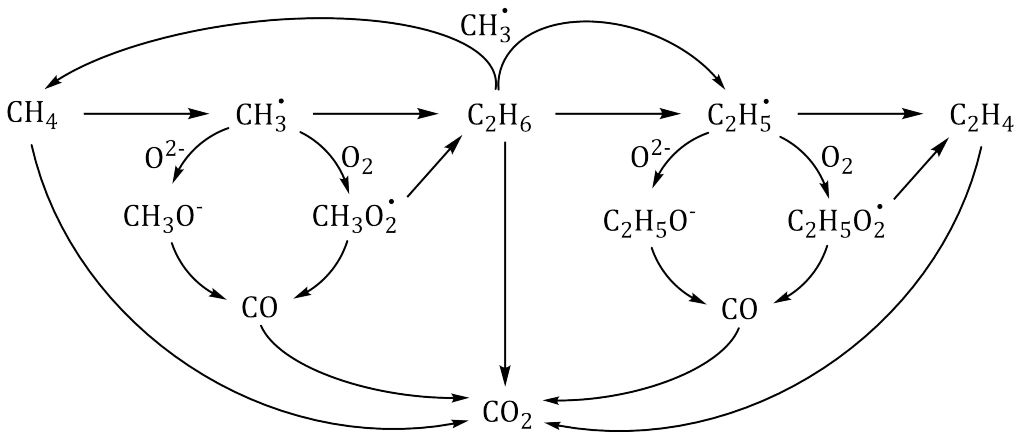

Scheme 3.12. A generalised and simplified overall total scheme showing some of the many possible pathways available during OCM.[240,249–251] Ionic species are coordinated to the catalyst surface. For clarity, by-products are not shown and molecular species are not balanced. All conversions to CO_2 take place on the catalyst surface using MvK or Lunsford-like mechanisms.

is the high reactivity of ethene. As conversion increases the primary precursor to CO_x becomes ethene, resulting in the product decomposing as fast as it is being produced.[253,254]

3.3 Existing Techniques for Photocatalytically Activating Methane

As the chemical drive to the thermodynamic sink of CO_2 is favoured by high reaction temperatures, there has been work to optimise the reaction at lower temperatures. By using photochemistry, the energy required for the reaction can be delivered directly to the system as photons, instead of heat. Methane is UV-Vis transparent down to ~140 nm,[255] giving an indication of the high photoenergy needed to excite it. In fact, having no functional group and a dielectric constant of 1.000 80,[256] the non-polar nature of methane results in a predictably high first ionisation potential of 12.6 eV (98.3 nm or 1.22×10^3 kJ mol^{-1}).[257]

The first reported investigation into the reactivity of methane with a photocatalyst was published in 1978. The authors were investigating the proposed formation of oxygen-holes when vanadium or TiO_2 were exposed to heat or UV illumination. Using a very low partial pressure of methane at 1.2×10^{-4} bar and a full spectrum UV lamp, they measured a small conversion to ethane with TiO_2, and a large conversion to CO_2 with vanadium as oxygen-hole sources.

The intentional photocatalytic oxidative coupling of methane was first reported in 1997 by Okabe *et al.*[258] They provided the energy required by the system both thermally, by operating at 200 °C, and photolytically, using a 100 W high-pressure mercury lamp emitting full spectrum UV and visible light. Under *recirculating* conditions for 20 hours, their use of a TiO_2 catalyst

resulted in a methane conversion of 13 % with selectivity for ethane at 3.9 %, an overall ethane yield of 0.51 %. The remainder of the converted methane yielded CO_x. The reaction was run with a methane/oxygen ratio of 4:1, with selectivity for non-CO_x products decreasing as the amount of oxygen was increased, and no reactivity without oxygen. The partial pressure of methane was 0.32 bar which, as previously noted, skews the results positively, at cost of industrial feasibility.

Vanadium supported on silica has become a widely studied photocatalyst for the partial oxidation of methane using oxygen as the oxidant.[259–261] Using V_2O_5/SiO_2, a high selectivity for formaldehyde of 78 % has been reported, with a corresponding yield of 0.48 %.[259] For the reaction to take place, temperatures in excess of 220 °C and illumination below 310 nm were both required. It was noted that the presence of water reduced methane's rate of reaction, but increased ethane's. It is likely that the water and methane are competing for the same active sites on the catalyst, whilst ethane is most likely activated at a different site. Subsequent optimisation of the system has shown that very low loadings of vanadium at 0.01 mol % show the highest selectivity for non-CO_x products.[262] It is suggested that this is due to the active site being unsaturated M=O species, which are less common in large crystallites of oxides.

The use of lanthanum doped tungsten oxide has shown some selectivity for the conversion of methane to methanol.[263] Under either visible or UV light, the powdered catalyst was suspended in water using mechanical stirring in the presence of the electron-transfer agent, 1,1′-dimethyl-4,4′-bipyridinium dichloride. At 70 °C a 1:3 methane/helium mix was bubbled through the water suspension in a flow system at 10 bar. The reaction achieved a conversion for methane of 4 %, with hydrogen, carbon monoxide and methanol as the main products, in an approximate ratio of 7:3:1. No reaction was observed below 70 °C, possibly due to the low solubility of methane in water. It is suspected that hydroxyl radicals are initially being formed, which then react with methane to create methyl radicals. The methyl radicals can then react with water, forming methanol and hydrogen.

The photocatalytic steam reforming of methane has also been reported.[264] Using a 0.1 % platinum doped TiO_2 microparticulate catalyst and a powerful 300 W full spectrum Xe light source, the reaction was optimised with a methane conversion of 0.02 % at 50 °C. The selectivity at this rate was 85 %. The reaction set up involved flowing a water-saturated methane/argon 1:1 mix over an illuminated catalytic bed, with the catalyst suspended with glass wool. During an induction period, a yellow-brown discolouration affects the catalyst, after which the reaction rate is increased. It is suggested that the discolouration is due to surface-bound $(CH_2O)_n$, an intermediate in the reaction.

In 2004, the photocatalytic synthesis of acetone from methane and CO_2 was reported.[265] A

high-pressure mercury lamp was used to provide full-spectrum UV illumination to the reaction. The photocatalyst employed was TiO_2 on a SiO_2 support, sensitised with copper nanoparticles and cadmium sulphide quantum dots, Cu/CdS - TiO_2/SiO_2. The recorded surface area of the catalyst was 264 $m^2\ g^{-1}$, by BET analysis. Operating at 120 °C and 1 bar, the selectivity of the reaction for acetone was 92 %. The conversion of methane and CO_2 was 1.5 % and 0.75 % respectively. The major downside to this set-up is the photocorrosion of CdS by TiO_2; causing conversion to drop to zero after approximately two hours.

3.4 Photoactivation of Methane using Titanium Dioxide

OCM is a radical-based process, as confirmed by the product ratios calculated by Labinger in 1988.[253] More recently in 2013, the presence of methyl radicals was experimentally observed by Huang *et al*. using synchrotron UV photoionisation mass spectroscopy.[242] Traditionally, OCM is conducted in the presence of O_2, which causes issues with combustion, ultimately forming CO_2. It is therefore suggested that a new approach to this problem would be to introduce the methyl radicals through a different mechanism. This work considers using ultraviolet light to generate the radicals. This has the joint advantage of removing the dioxygen, as well as removing the high temperatures that are currently always required in industry. This would dramatically reduce the cost of activating methane, making full use of the resource more feasible.

One of the possible ways to form methyl radicals is to excite the methane directly. The wavelength of light that is required to provide enough energy to directly activate methane is 98.3 nm. This first ionisation potential of methane is large, and the wavelength falls in the UV_C category of ultraviolet light — highly carcinogenic. This pathway was not investigated.

A second, safer pathway is to form the methyl radicals via the intermediate hydroxyl radical, $OH^{\bullet}$. By using UV_A light, with a wavelength of approximately 360 nm, it is possible to form hydroxyl radicals, $OH^{\bullet}$, from water with an appropriate catalyst.[266] Hydroxyl radicals have a remarkably high redox potential of 2.72 V (*cf.* ozone at 2.07 V and fluorine at 3.03 V).[267] This enables the hydroxyl radical to abstract a hydrogen atom from methane, forming water and a methyl radical, $CH_3^{\bullet}$. The methyl radicals can then react with water to form methanol or each other to form ethane, to name but a few possibilities. The reaction between methane and the hydroxyl radical has been shown to the facile, with a rate constant of $1.1 \times 10^8\ L\ mol^{-1}\ s^{-1}$, demonstrating that kinetically this pathway is sound.

3.4.1 Using a Static Reactor

3.4.1.1 Experimental Results

In order to investigate this, a static reaction system was established. The vessel consisted of a quartz glass cylinder with Suba-Seals at each end to ensure the system was gas tight. The catalyst, TiO_2 nanopowder (0.59 g), was made into a paste by mixing it with degassed and deionised water (0.32 g). This was then painted onto the bottom half of the reaction vessel. Accurate weighing at each point ensured that a known amount of photocatalyst was added to the vessel. The vessel was then sealed and purged with argon and methane, each at a flow rate of 10 L min^{-1}. The system was completely purged of ambient air because it was desired to remove any unessential components from the system, whilst leaving argon to slightly reduce the concentration of the methane. The experiment set-up is shown in figure 3.4.

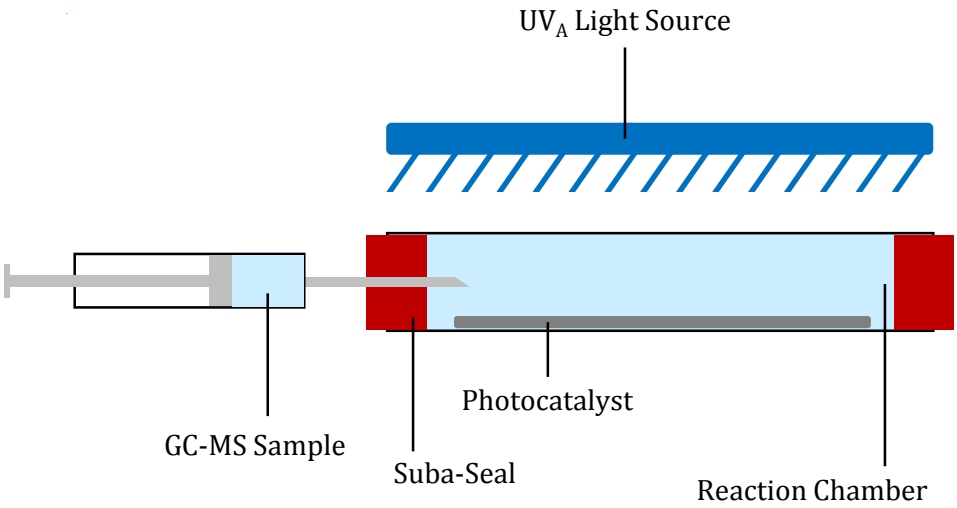

Figure 3.4. Schematic showing the static reactor used for conducting photocatalytic experiments with methane.

Once the experimental setup was complete, the partial pressures of the gases in the system could be analysed by periodic gas sampling and injections directly into a gas chromatography-mass spectrometer (GC-MS). From this, the water, argon and methane levels could be monitored.

An initial sample was taken at t=0, before the reaction mixture had been exposed to any illumination. The set-up was then illuminated with UV_A for extended periods of time, with periodic gas sampling. There was initially no sign of any reaction. After 16 hours however, there was both a noticeable change in the GC-MS data and the visible look of the system.

The GC-MS data showed a marked increase in the amount of water vapour in the system, as

well as a new signal at 44 m/z. The molecular ion mass, along with the fragmentation pattern, revealed the identity to be CO_2. The presence of this new carbon species can only be explained by the oxidation of the methane.

Visually it was observed that the catalyst had dried considerably throughout the duration of the experiment, and there was a small amount condensation on the side of the glass wall. This is attributed to the increase in temperature during the reaction causing the evaporation of an amount of water in the TiO_2 paste. The temperature change itself is a by-product of the UV_A illumination. The fluorescent tubes used as the UV_A light source are not perfect systems, and therefore emit heat as unwanted waste energy, heating the reaction chamber to approximately 50 °C.

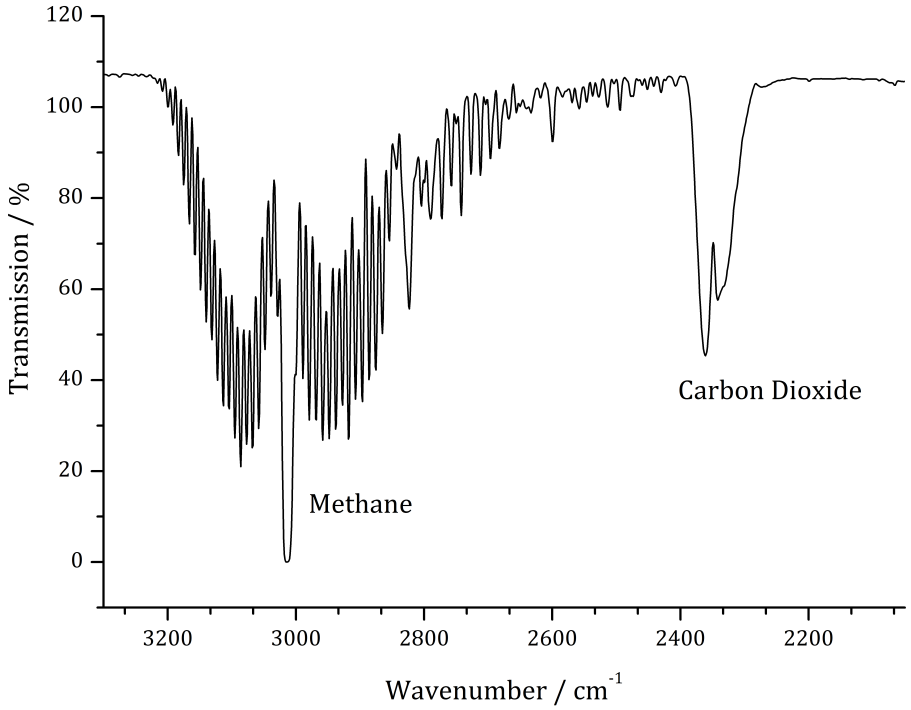

Figure 3.5. FTIR spectrum showing the fine structure of methane centred around 3013 cm^{-1}, and the absorbance of carbon dioxide at 2350 cm^{-1}.

Unfortunately, the available column in the GC-MS was unable to fully separate methane and CO_2. Therefore, in order to confirm the identity of the produced species, Fourier transform-infrared spectroscopy (FTIR) was conducted. A typical spectrum is shown in figure 3.5. From the spectrum it is possible to observe the CO_2 asymmetric stretch at 2350 cm^{-1}. The P and R bands are clearly visible, although the fine structure has not been resolved due to instrument limitations. There is no Q peak, because CO_2 has no transitions where the vibrational energy changes while the rotational energy does not. The high energy absorption of methane can also be seen at 3013 cm^{-1}. The fine structure of the methane PQR bands can be resolved, due to the larger spacing of the rotational

energy levels (for methane B = 5.178 cm^{-1}; for CO_2 B = 0.3915 cm^{-1}).[268,269]

By monitoring the reaction periodically by FTIR, it was possible to record the increase in CO_2 concentration with time. This plot is shown in figure 3.6, and clearly demonstrates an immediate increase in CO_2 concentration. The production rate slows as time progresses, which is due to consumption of available methane and the setting of a new rate limiting step of reactant diffusion. The methane absorbance, whilst unobstructed in figure 3.5, becomes overlapped with the wide ranged absorbance of water as the experiment progresses, due to the unintended side effect of evaporating water during UV_A illumination. This overlap prevented the simultaneous monitoring of CO_2 and methane concentrations.

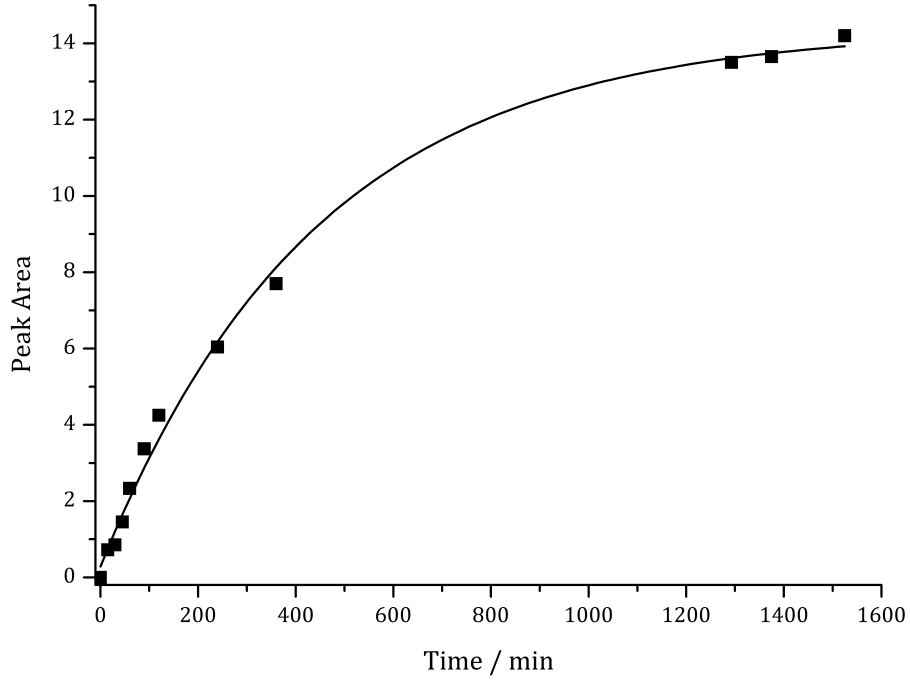

Figure 3.6. A plot showing the increasing concentration of carbon dioxide with time. The UV_A illumination was initiated at $t = 0$. The y-axis is raw peak integration data, in arbitrary units.

In order to confirm that atmospheric CO_2 had not simply diffused into the reaction vessel over-time a blank trial was run, this consisted of the water, methane and argon (but no TiO_2) in the reaction vessel, illuminated with UV_A light for 16 hours. Under these condition there was no evidence of CO_2. A blank trial was also run using argon, water, TiO_2, but no methane. After illumination there was no detectable CO_2 in the reaction vessel.

3.4.1.2 Electronic and Defect Considerations

A striking visual change was observed over the course of the reaction. The catalyst changed to a pale blue colour, in contrast to the initial bright white colour. This pale blue TiO_2 rapidly changed back

to white when exposed to air, over approximately ten minutes. Whilst powder X-ray diffraction (pXRD) analysis was attempted of the blue TiO_2, this time restraint made collection of a reliable pXRD pattern difficult. Indeed, all collection attempts yielded only patterns identical to the TiO_2 P25 starting catalyst. There are two major possibilities for this, either the cause of the blue colour was lost too quickly to detect, or pXRD was not capable of discerning the difference. One of the disadvantages of pXRD is that it is not sensitive to subtle changes, often requiring dopant concentrations of 10 % before they are detected. If, as is probable, the blue colour was only on the surface of the TiO_2, then the X-rays would be unaffected due to an insufficient number of unit cells.

A plausible explanation for the colour change of the catalyst is that the TiO_2 is being reduced through the formation of oxygen vacancies, V_O. There have been reports of blue TiO_2 occurring through reduction of the TiO_2, and the accompanying oxidation of another compound.[270] However, these previously reported results did not use methane as the reductant, and the newly found blue colour was long-lasting; in contrast to the short-lived blue TiO_2 reported herein. It is suggested that, as the blue colour is quickly lost on exposure to air, atmospheric oxygen is replacing the oxygen vacancies in the semiconductor through aerobic oxidation. This would effectively oxidise the TiO_2 to its original condition, and colour.

A possible type of ordered-disorder could have produced the blue colour. Magnéli phases of titanium oxide are a series of discrete compounds, with the general formula Ti_nO_{2n-1} where n is generally between three and ten. First reported in titanium oxide by Magnéli *et al*. in 1957,[271] these phases contain sheet defects caused by crystallographic shear. This involves the entire lattice sheets moving relative to each other. The result of this is the elimination of vacancies and creation of a cation-rich layer, containing interstitial titanium. The periodic modification of the structure, as oppose to random point defects, seems counter-intuitive entropically. However, theoretical calculations have shown that these sheet defects can be favoured when the materials dielectric constant, and thus its ability to polarise and relax, is large.[272] This is the case for titanium oxide. Magnéli phases of titanium oxide are characteristically blue in colour, however are generally stable to atmospheric oxygen.

A significant development from the formation of oxygen vacancies is the generation of defects. The formation of defects is known to add interstitial energy levels in the band gap, making it an indirect band gap. As implied by the name, this means that electrons do not need to be 'directly' excited to the conduction band, but can access intermediate energy levels, as demonstrated in figure 3.7. This lowers the energy and frequency of light needed to promote an electron.

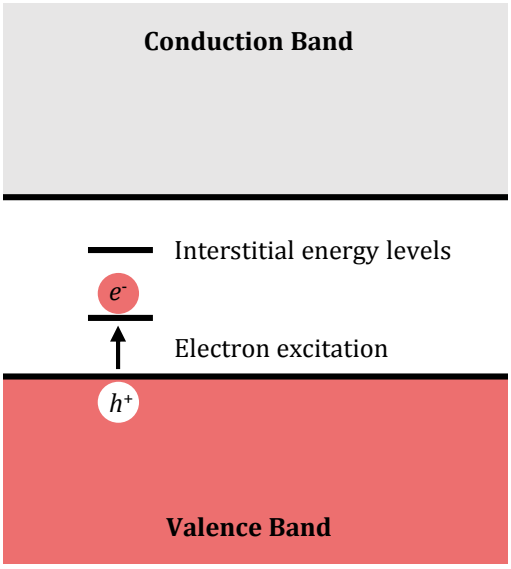

Figure 3.7. Diagram showing a band gap with additional interstitial energy levels. Electrons, e^-, can be promoted from the valence band to the conduction band (forming holes, h^+) via these interstitial levels. This results in red-shift of the semiconductors absorption range.

A further oxygen vacancy effect regards electron-hole recombination. Once an electron has been promoted, they tend to relax almost immediately, recombining with the generated hole — some compounds even fluoresce as this energy is emitted. When this recombination occurs, no chemical reaction can happen, and so it is necessary to find ways to spatially separate the electron and the hole, that is to minimise exciton collusion. An effective way of doing this is through the introduction of lattice defects.[273] The defects trap either the electron or the hole, whilst the continued mobility of the other causes electron-hole separation. This delay in recombination allows the electron to react (*i.e.* with water), increasing reactions rates and reactivity.

3.4.1.3 Mechanistic Insights

The presence of CO_2 confirms that the methane is being activated. The small amount of methane that has been converted, however, was not quantifiable using the GC-MS due to peak overlap. Whilst the blank trials confirm that it is the methane that has been oxidised, they unfortunately do not offer any insight towards the mechanism. This is either because of the very low gaseous concentration of intermediates, or because the reaction intermediates are all surface-bound. However, a plausible mechanism is shown in scheme 3.13.[81,274–276]

In these reactions the hydroxyl radical is formed through the photoexcitation of TiO_2. This then reacts with methane, forming the methyl radical and water. The methyl radical can then react with a hydroxyl radical, forming methanol. As the reactions are mostly confined to the surface of

$$H_2O \overset{cat.}{\rightleftharpoons} OH^{\bullet} + H^{\bullet}$$
$$OH^{\bullet} + CH_4 \longrightarrow CH_3^{\bullet} + H_2O$$
$$CH_3^{\bullet} + OH^{\bullet} \longrightarrow CH_3OH$$
$$CH_3OH + h^+_{surface} \xrightarrow{cat.} CH_3O^{\bullet} + H^+$$
$$CH_3O^{\bullet} \overset{cat.}{\rightleftharpoons} CH_2O + H^{\bullet}$$
$$CH_2O + OH^{\bullet} \rightleftharpoons CHO^{\bullet} + H_2O$$
$$CHO^{\bullet} \xrightarrow{cat.} CO + H^{\bullet}$$
$$CO + OH^{\bullet} \rightleftharpoons [HOCO] \longrightarrow CO_2 + H^{\bullet}$$

Scheme 3.13. Radical reactions that convert methane to carbon dioxide in the absence of dioxygen. Reactions labelled with *cat.* are either catalysed or surface mediated; h^+ is a lattice hole.[81,274–276]

the catalyst, the methanol will then quickly react with a hole, h^+, on the surface of TiO_2, forming $CH_3O^{\bullet}$. The $CH_3O^{\bullet}$ will then loose $H^{\bullet}$ whilst bound to the surface, forming the more stable formaldehyde. Formaldehyde is known to react with hydroxyl radicals, forming $CHO^{\bullet}$; and $CHO^{\bullet}$, mediated by a surface, is known to decompose to carbon monoxide and a hydrogen radical. The final step, oxidation of CO to CO_2, is well known to be facilitated by hydroxyl radicals; the consumption of hydroxyl radicals in this way is one of the major reactions in the atmospheric chemistry of the troposphere.

As this suggests, the reaction pathway from methane to carbon dioxide is complicated. The CO_2 generation data displayed in figure 3.6 does not follow zero, first or second order kinetics, further emphasising the complex nature of the reaction pathway. Some potential reaction intermediates are shown in table 3.1, along with their main IR absorbances. None of these species were observed in the gas phase. This suggests that once the methane has adsorbed to the surface of the catalyst, the compound is rapidly reacted along the oxidative pathway, not desorbing until it reaches CO_2. This could be either due to the speed of the reactions, or the involatile nature of some of the intermediates, or a combination of the two.

Table 3.1. Main IR absorbances for some possible intermediates in the photocatalytic conversion of methane to CO_2.

Potential Species	**IR absorbance / cm^{-1}**
CH_3OH	1031
CH_2O	1748
CO	2150
C_2H_6	1466
C_2H_5OH	1066

3.4.2 Using Flow Reactors

The activation of methane to CO_2 was encouraging, however the conversion of methane to carbon dioxide has been in practice for thousands of years.[277] In order to prevent the complete oxidation of methane to the thermodynamic sink of carbon dioxide (see section 3.2.4), it was decided to conduct the reaction under flow conditions, instead of the previous static conditions. By doing this, it was hoped that any formed intermediates would be carried away by the carrier gas, preventing any subsequent surface-mediated reactions, and thereby stopping the reaction before CO_2 was formed.

The first design for a flow reactor involved only minor changes to the experimental set-up. By slightly modifying the UV_A chamber, gas flow in and out of the reaction vessel was possible. The set-up is shown in figure 3.8.

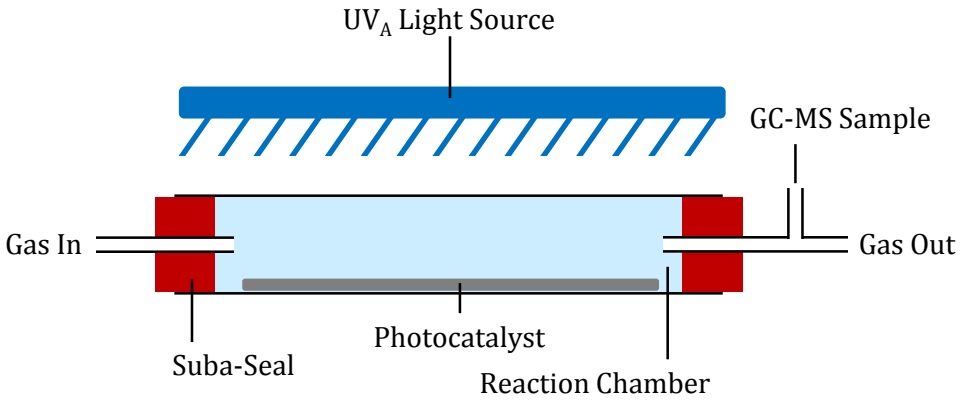

Figure 3.8. Schematic showing the first flow set-up for conducting photocatalytic experiments with methane.

The results from this experiment, however, showed no sign of carbon dioxide, but also no evidence for methane conversion. It was observed, however, that the TiO_2 paste quickly began to dry out, as evidenced by GC-MS, FTIR and visual observation; despite the use of water-saturated methane/argon as a carrier gas. This was caused by a combination of the increased temperature combined with the carrier gas flow. Attempts to simultaneously reduce the evaporation of water and increase the methane-TiO_2 contact time, by reducing the carrier gas flow, had no effect.

Consequently, a new flow set-up was devised, shown in figure 3.9. The new experimental set-up was designed to prevent the drying out of the catalyst, whilst increasing contact time between the gas and the catalyst. The TiO_2 was kept in suspension in deionised and degassed water, whilst water-saturated methane/argon was bubbled through the system.

The results of this experiment were difficult to observe by FTIR, due to the large amount of water vapour present in the gas stream. By GC-MS there was no sign of any reaction. It is possible

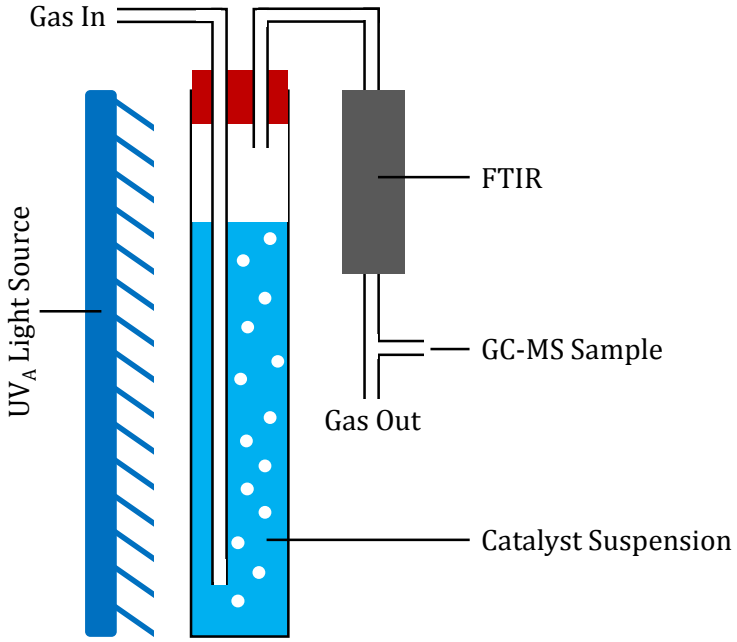

Figure 3.9. Schematic showing the second flow set-up for conducting photocatalytic experiments with methane.

that the level of reacted species were below detection limits. An alternative possibility is that the large bubbles created by the tube exit did not have a sufficient surface area to volume ratio to obtain meaningful contact with the catalyst.

Surface area is proportional to the volume of an idealised spherical bubble. As shown in equation (3.1), by minimising the radius, the surface area to volume ration can be maximised, thereby increasing contact between methane and the catalyst. Additionally, reduction in the size of the bubble radius leads to a reduced ascension velocity of the bubble, and therefore increase contact time with the catalyst. This is demonstrated in Stokes' equation shown in equation (3.2),[278] where u_∞ is the terminal velocity of the bubble; g is the acceleration due to gravity; r is the radius of the idealised spherical bubble; ρ_l is the density of the liquid; ρ_g is the density of the gas; and μ_l is the viscosity of the liquid. This reduced speed will also increase contact time.

$$\frac{\text{Surface Area}}{\text{Volume}} = \frac{4\pi r^2}{4/3\pi r^3} = \frac{3}{r} \propto r^{-1} \tag{3.1}$$

$$u_\infty = \frac{gr^2(\rho_l - \rho_g)}{72\mu_l} \propto r^2 \tag{3.2}$$

Therefore, in order to minimise the radius of the formed bubbles, the system was modified

to use a glass-fritted gas-dispersion tube, or sparger. These gas-dispersion frits are occasionally used for the thorough degassing of solvents by sparging, and have pore diameters of approximately 100 µm. The improved set-up is shown in figure 3.10, and the resulting gas bubbles were noticeably smaller than the previous set-up.

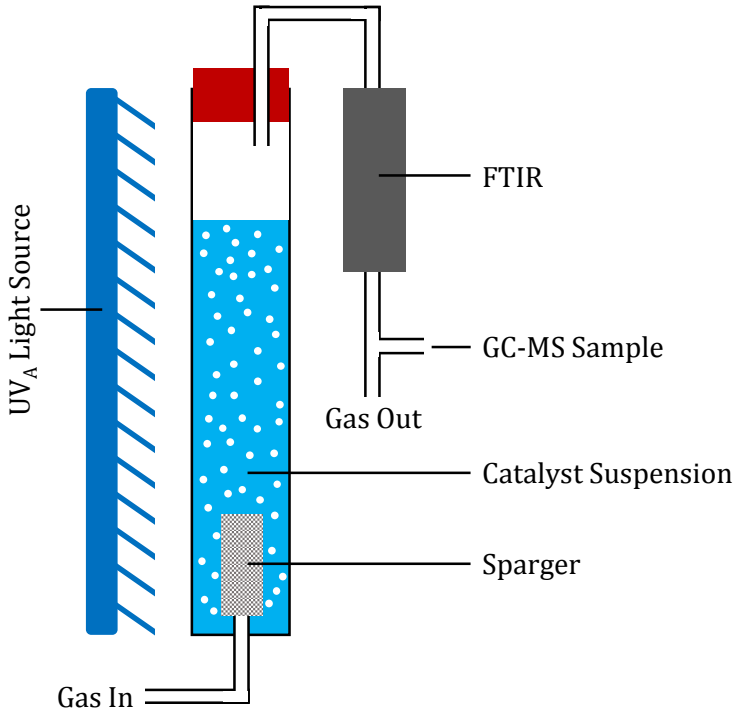

Figure 3.10. Schematic showing the third flow set-up for conducting photocatalytic experiments with methane. The use of a glass-fritted gas-dispersion tube, or sparger, results in the formation of smaller bubbles.

With this new set-up, a water-saturated methane/argon mixture was delivered through the system via the gas sparger. The resulting stream of bubbles agitated the liquid, keeping the TiO_2 in suspension. The gas outlet was observed via FTIR and GC-MS. Throughout this experiment only minimal levels of carbon dioxide were detected by FTIR and GC-MS. It appears that whilst the smaller bubbles did allow for the increase in contact between the reactants, CO_2 was still the only detectable product. It should be noted that the water was degassed prior to use, and that the gas flow-in contained no CO_2.

Modifications to the gas flow rate and amount of TiO_2 did not change the outcome of the experiment. It was concluded that the hydroxyl radical was too reactive and too non-selective for the system.

3.5 Photoactivation of Methane Using Other Metal Oxides

In order to supply less energy to the system, it was decided to replace TiO_2 with an alternative metal oxide semiconductor. The replacements tested have smaller band gaps than TiO_2, which results in less energetic reaction intermediates. The relevant band gaps are displayed in table 3.2.

Table 3.2. Band gaps of the relevant metal oxides.

Material	Band Gap / eV	Reference
TiO_2	3.0	3
WO_3	2.75	279
α-Fe_2O_3	2.2	280
UO_2	1.3	281

3.5.1 Tungsten trioxide

Tungsten(VI) oxide is a direct band gap semiconductor, investigated because it has a band gap slighter smaller than TiO_2. Whilst WO_3 is reasonably stable. it can be reduced to tungsten(V) under appropriate conditions. This oxidation state flexibility is as necessary for heterogeneous catalysts as it is for homogeneous catalysts. The smaller band gap of WO_3 does allow for the slight absorption of some visible light, however the band edges do not align fully for the complete splitting of water — the catalyst fails to produce hydrogen without a voltage bias. The band edges can be seen in figure 3.11. Accordingly, under the experimental conditions, water will not be fully split, leaving surface active species.

By switching to tungsten trioxide, the thermodynamics of the hydroxyl radical formation have not been altered, however the smaller band gap means that the kinetics of the system will change. The experiment was conducted under static conditions, as demonstrated previously in figure 3.4. The WO_3 was used as received. After 16 hours the amount of formed CO_2 was only slightly less than the amount witnessed with TiO_2. No other species were observed in the GC-MS. This suggests that the methane is being fully oxidised, and not being held at an intermediate.

3.5.2 Haematite

As the tungsten trioxide catalyst demonstrated the same features as TiO_2, another catalyst was tested. The use of haematite, α-Fe_2O_3, as a photocatalyst has become increasingly researched in the past five years.[283–285] This is primarily because it is non-toxic, cheap and abundant world-wide.[280] Haematite has a smaller band gap than WO_3, being only 2.2 eV,[280] however slow hydroxyl

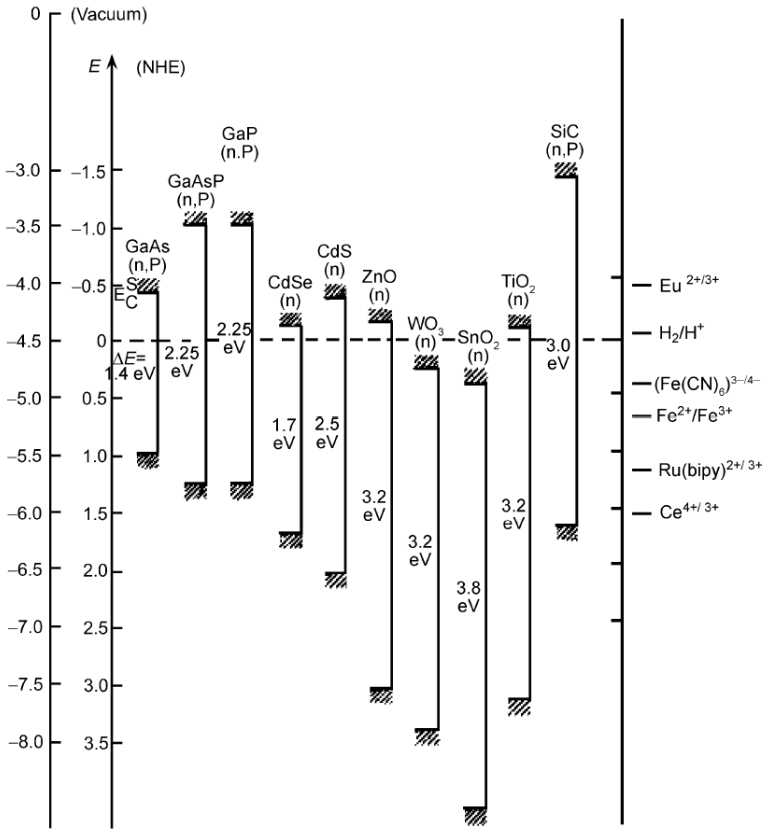

Figure 3.11. The band edge positions of several semiconductors in water at pH 1.[282] It can be seen that tungsten trioxide is below the H_2/H^+ level at 0 V.

formation has previously been reported.[286]

The experiment was once more conducted under the static conditions displayed in figure 3.4. The haematite was used as received. After 20 hours, only a tiny amount of CO_2 was detected by GC-MS. Unfortunately, there was no indication of any intermediates in the trace, or in careful analysis of the MS spectra. Haematite is known for ultrafast electron-hole recombination, which is on the order of 100 ps.[287] It is therefore suggested that the poor activity observed is due to the excited electrons recombining with holes before any chemistry can take place. This would result in a reduction of formed radicals and therefore a reduction in product produced. It is interesting to note that whilst only a small amount of CO_2 was detected, there were still no intermediates detected. It is possible that they were present in quantities below detection limits, or alternatively it is possible that all chemical pathways led to CO_2.

3.5.3 Urania

The final metal oxide tested was urania, UO_2. This was synthesised in two steps, first the complete oxidation of uranyl acetate to UO_3 was completed by heating to 400 °C for four hours in air. The

next step was to reduce UO_3 to UO_2; the classical method for this is to heat the UO_3 under hydrogen at 700 °C, which was not attempted due to safety concerns. Instead, the UO_3 was reduced by heating to 1100 °C for five hours under an active vacuum of approximately 0.1 mbar. This reduction technique had an unintended side effect of subliming uranium onto the crucible and quartz liner of the furnace. Subsequently, it was discovered that the UO_3 could be reduced by heating under a flow of argon, at 1100 °C for 30 hours, without any sublimation. These reactions are shown in scheme 3.14. The UO_3, UO_2 and the stable intermediate U_3O_8 were characterised using pXRD. The recorded pXRD pattern for UO_2 is shown in figure 3.12, and was referenced to ICSD collection code 061565.

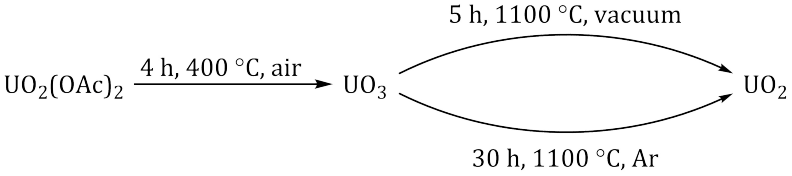

Scheme 3.14. Pathway for the synthesis of urania from uranyl acetate.

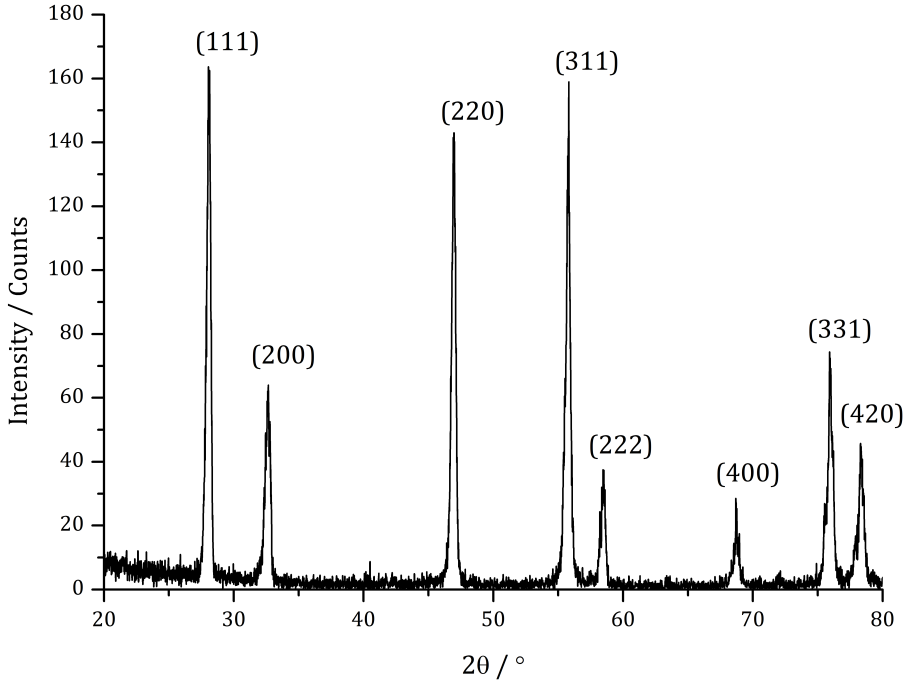

Figure 3.12. The pXRD pattern of UO_2, with miller indicies.

Urania has a small band gap of 1.3 eV,[281] and as such will not form large amounts of hydroxyl radicals. However, various uranium oxides have been investigated for their catalytic activity. These uses include the use of U_3O_8 and the uranyl ion, UO_2^{2+}, for the decomposition of VOCs.[288,289] Uranium dioxide has also been of interest to researchers for the reduction of nitrous oxides at high

temperatures.[290] This suggests that the surface of urania is active, and worthy of investigation.

The reaction was initially attempted using the flow set-up shown in figure 3.10, however, a good suspension could not be formed. This is a result of the high density of UO_2 compared to TiO_2 and water, being $10.96\,g\,cm^{-3}$, $3.84\,g\,cm^{-3}$ and $1.00\,g\,cm^{-3}$ respectively.[291,292] This resulted in minimal contact between gas and catalyst, and consequently no sign of reaction.

The static reactor shown in figure 3.4 was then tested with UO_2. It was noted to be difficult to form a paste with the oxide, despite the catalyst being finely ground with a pestle and mortar. The reaction used the same conditions as before, replacing the TiO_2 with UO_2. The results showed a marked increase in the formation of CO_2 compared to haematite, however there were no detectable signs of any intermediates.

It is suggested that the large amount of energy required to activate a Me−H bond, and the fact that every intermediate is more functionalised, results in any activated methane remaining adsorbed to the surface until it has completely oxidised.

3.6 Perfluorocarbons as a Medium

A possible cause for the slow reaction rates observed in the methane reactions could be the insolubility of methane in water, a mole fraction of only 2.86×10^{-5}.[293] A solvent class known for high gas-solubility is the perfluorocarbons, where the hydrogen atoms on the solvent molecule have been replaced with fluorine atoms. A good example to demonstrate this property is nitrogen, which has a solubility mole fraction of 1.83×10^{-5} in water, and 3.31×10^{-3} in perfluoromethylcyclohexane (pFMeCy), both at 298.15 K and 1 bar.[294] It is the weak intermolecular bonds in pFMeCy that causes this increase in solubility by two orders of magnitude.

In order to increase the ease of oxidation of the substrate, allowing simplification of testing the new pFMeCy solvent, a different starting material was used. Ethanol has a hydroxy functional group, making it far more active than methane. By mixing the ethanol with water and pFMeCy, a new reaction set-up was devised. The TiO_2 was made into a paste using a 10:1:1 pFMeCy/H_2O/EtOH solution. This paste was then applied to the inside of the static photoreactor, as shown in figure 3.4. The reaction vessel was then purged with water-saturated argon for 30 minutes at a flow rate of $20\,L\,min^{-1}$. Once purged, the vessel was placed in the photoreactor and illuminated for 45 minutes, after which a GC-MS sample was run, shown in figure 3.13.

As visible in the trace shown in figure 3.13, a portion of the ethanol has been oxidised to ac-

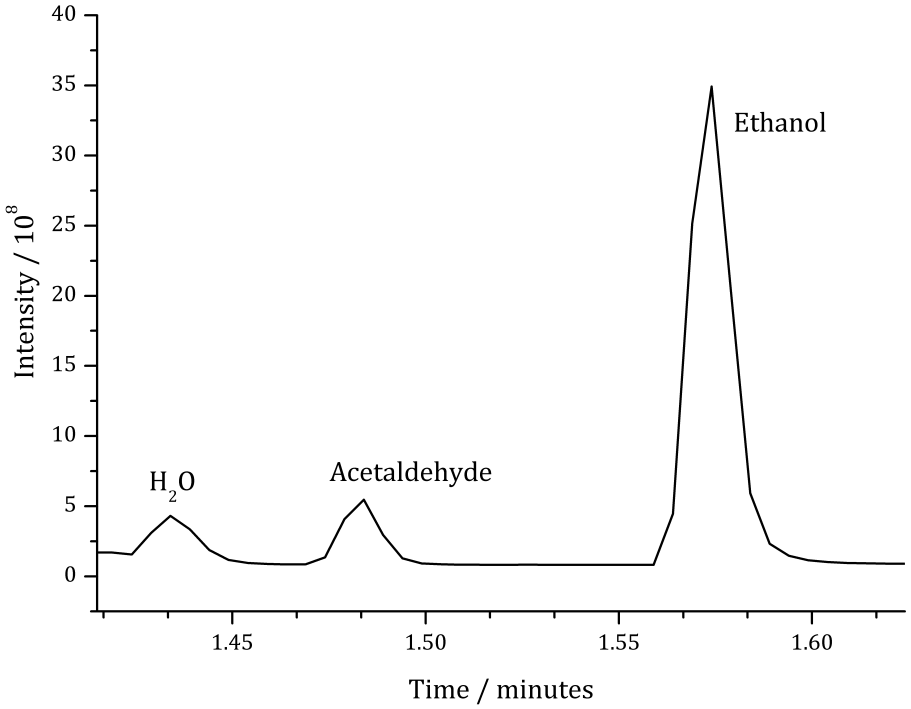

Figure 3.13. GC-MS trace of the vapour from the photocatalytic oxidation of ethanol, showing the formation of acetaldehyde.

etaldehyde. What is particularly encouraging is that there was no indication of CO_2 in the reaction vessel. A proposed mechanism for the oxidation is shown in scheme 3.15.

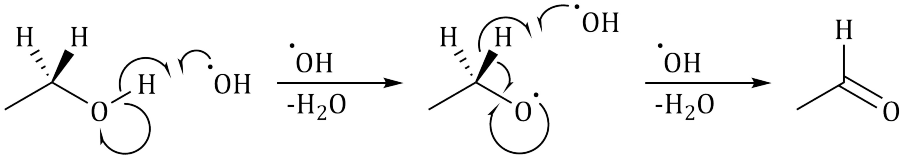

Scheme 3.15. Proposed mechanism for the photocatalytic oxidation of ethanol.

In the mechanism, the ethanol is first reacted with an hydroxyl radical, forming water and an $EtO^{\bullet}$ radical. In the next step a second hydroxyl radical removes a hydrogen from the α-carbon, allowing for the carbonyl to form and create acetaldehyde.

The reaction was also conducted in the presence of methane, from which there also no CO_2 formed. The success of the partial oxidation of ethanol under these conditions is very promising for the future partial oxidation of methane. The lack of any formed CO_2 suggests that TiO_2 does not oxidise all hydrocarbons completely to carbon dioxide, and that tailored activity is possible. As shown in table 3.3, the hydroxyl radical reacts more than ten times faster with ethanol than methane.[295] Therefore, ethanol is much more competitive then methane. Unfortunately, time restraints prevented the further probing of this reaction.

Table 3.3. Rate constants for the hydroxyl radical reacting with ethanol and methane.[295]

Reaction	Rate Constant / L mol^{-1} s^{-1}
$EtOH + OH^{\bullet} \longrightarrow EtO^{\bullet} + H_2O$	1.9×10^9
$CH_4 + OH^{\bullet} \longrightarrow CH_3^{\bullet} + H_2O$	1.1×10^8

3.7 Conclusions and Future Work

In this chapter, the existing techniques for the activation of methane have been reviewed. These vary in design, but tend to require high temperatures and very low partial pressures. There is a small amount of literature precedence on photocatalytic methane coupling, however they tend to require full spectrum UV light, and minimal progress has been published.

The activation of methane over TiO_2 using photocatalytically produced hydroxyl radicals with safe, low-powered UV_A illumination was reported. A variety of photoreactors were designed and tested, however the only product that was detected after or during the reaction was carbon dioxide.

In an attempt to change the kinetics of the system, a number of other photocatalysts were tested. These were WO_3, α-Fe_2O_3 and UO_2, in addition to the original TiO_2. Haematite showed the least activity, however all tested semiconductors only managed to produce carbon dioxide — no partially oxidised species were identified.

The rate of reaction was very slow, taking upwards of 16 hours to produce measurable levels of product. In attempts to circumvent this issue, a cophase was introduced which was inert to hydroxyl radicals and would maintain methane availability at the catalytic surface — pFMeCy. In order to make for simpler testing, ethanol was substituted for methane in the pFMeCy experiments. These experiments demonstrated the facile and fast partial oxidation of ethanol to acetaldehyde. Notably, no CO_2 was detected in the presence of methane, indicating some degree of selectivity.

Future work in this field should immediately continue with the investigation of perfluorocarbons, for solubility reasons. Additionally, experiments with unsaturated perfluorocarbons may also be prudent, as they have different solubility properties.

The use of a different column in the GC-MS would allow for the complete separation of methane and carbon dioxide. This would allow for investigation of each species, giving quantitative concentrations and enabling kinetic investigations to be conducted.

The testing of different semiconductors can be expanded. One promising candidate is zinc oxide, which is currently the topic of much research and discussion. Examples of the recent use of ZnO as a semiconductor include gas sensors,[296] water oxidation,[297] and UV sensors.[298]

Finally, by replacing powdered photocatalysts with nanostructured photocatalysts, the available surface area can be greatly increased. The use of nanowires,[299] nanofibres[300] or nanotubes[301] can massively increase the catalyst-substrate interaction, which would increase reaction activity. There should also be a separate investigation into the mechanics behind gas-solid substrate-catalyst interaction, as the optimisation of catalyst contact is also partly an engineering challenge.

Chapter 4

Synthesis and Reactivity of Triptycene Complexes

The use of homogeneous catalysts is also an important part of small molecule activation, allowing the easy control of electronic and catalytic properties. In this chapter, the design of new potential catalysts is investigated. A new bulky ligand precursor is discussed, with the first ever examples of a σ-bound triptycene ligand to a transition metal.

4.1 Triptycene as a Ligand

As previously discussed in section 1.4, the homogeneous activation of small molecules often requires the use of large and bulky ligands. This work focuses on triptycene to fulfil this role. Triptycene was first synthesised in 1942 by Bartlett *et al.*, via a Diels-Alder reaction.[302] It was initially only a molecule of intellectual curiosity, before being employed as a monomer in polymers by Klanderman and Faber.[303] It was not until 1970 that triptycene was used as a ligand, when it was reported as a side-bound π-complex by Pohl and Willeford.[304] The first example of triptycene σ-bonded to a metal was reported in 1989 by Chance *et al.*, who synthesised a tris(9-triptycene)germanium chloride complex.[305] More recently, the stereochemistry of a number of triptycylstannane halides has been investigated by Yamamoto *et al.*[306] They reported that encorporating four substituents yields a tetrahedral geometry around the tin centre, which is unsurprising given the bulk of the triptycene ligand.

Triptycene is electron rich, meaning it can stabilise high oxidation states of metals. As a member of the iptycene family, triptycene has D_{3h} symmetry around its central axis. It also has a large internal free volume, because of its inability to adopt a co-planar orientation. The sp^3 carbons on the backbone of the molecule and the sp^2 carbons in the aromatic rings form a rigid ligand frame-

work, with a high energy barrier for any deviation from the ideal 120° inter-ring angle.[307] Some of these properties are demonstrated in figure 4.1.

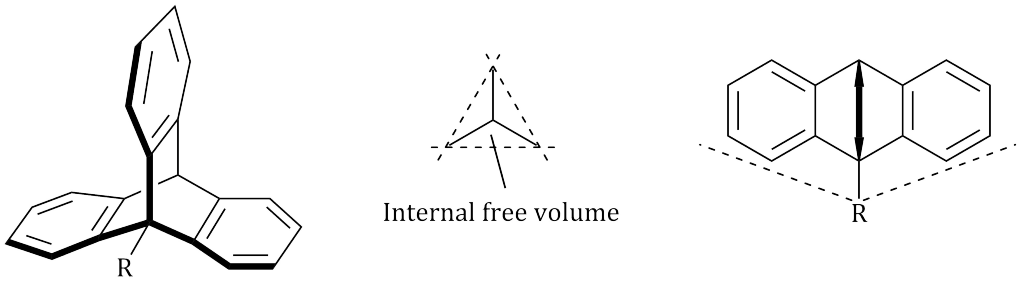

Figure 4.1. A diagram showing the 3D form of triptycene, a top view showing the internal free volume, and a side view showing the Tolman cone angle.

A systematic approach for quantifying the bulk of a ligand has been developed by Tolman.[308] The Tolman cone angle is defined as the apex angle of a cylindrical cone centred along the metal ligand bond, while touching the outermost atoms of the ligand. A schematic detailing the Tolman angle for triptycene is given in figure 4.1. From this work, the cone angle of triptycene has been measured as 129.9°. For comparison, trimethoxyphosphine has a cone angle of 107°, tripropylphosphine has a cone angle of 132°, and tri-*tert*-butylphosphine a value of 182°.[309] This means that whilst triptycene is a bulky ligand, it is not amongst the largest. Therefore, it is proposed that it should not be too large to hinder access of small molecules to the metal centre.

4.2 Synthesis and Characterisation of Lithium Triptycene

These reasons formed the foundation for triptycene, with its large steric bulk, to be an ideal candidate for synthesising coordinately unsaturated organometallic complexes. A triptycene salt, such as lithium triptycene, and a metal halide, were used in an ion-exchange reaction to synthesise the desired complexes. Instead of generating the lithium triptycene *in situ* it was decided to isolate the novel precursor, lithium triptycene, for future synthetic convenience.

Lithium triptycene was synthesised via 9-bromotriptycene, **11**, which itself was synthesised from 9-bromoanthracene, **12**, using a modified literature preparation.[310] The 9-bromoanthracene was reacted with anthranilic acid, **13**, in dichloroethane (DCE) under reflux. After distillation and recrystallisation from methanol, **11** was isolated as a pale yellow solid with 26 % yield. The full preparation can be seen in section 6.4.1, and the reaction scheme is shown in scheme 4.1.

Once bromotriptycene was synthesised, the synthesis of lithium triptycene was attempted. It was discovered that this preparation is highly solvent and condition sensitive. The starting material,

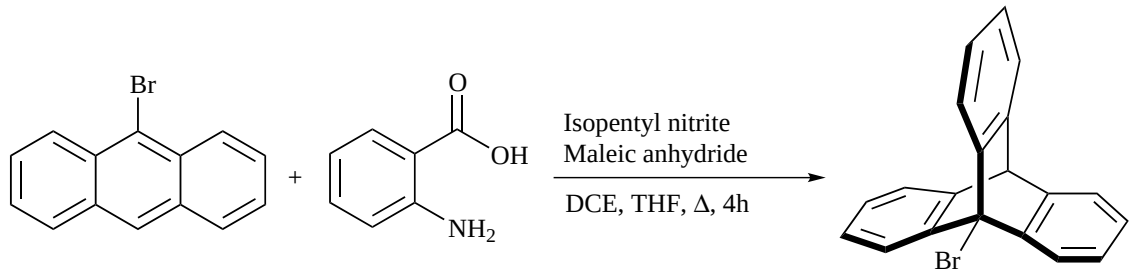

12 **13** **11**

Scheme 4.1. Synthesis of 9-bromotriptycene.

bromotriptycene, is not soluble in non-polar solvents, so a mixture of THF and a non-polar solvent was used for the reaction. Toluene was the preferred choice due to its low melting point and π-stacking abilities; though other solvents were also tested, including diethyl ether, benzene and hexane.

A variety of lithiating agents were tested during the reaction optimisation process. These included lithium metal, ^{n}BuLi, ^{t}BuLi and MeLi. Lithiating directly with the metal was found to be ineffective, and so alkyl lithium reagents were employed at −78 °C, −40 °C and room temperature. After optimisation, it was determined that the optimal preparation was to dissolve bromotriptycene in a 1:1 THF/toluene mixture, before cooling the solution to −40 °C. Prechilled ^{n}BuLi (−40 °C) was then added dropwise. After maintaining the reaction at −40 °C for an hour, the reaction mixture was filtered using a cold frit and washed with toluene (−40 °C), before drying *in vacuo* to yield an off-white powder in excellent yield of 89 %. The full preparation can be seen in section 6.4.2, and is shown in scheme 4.2.

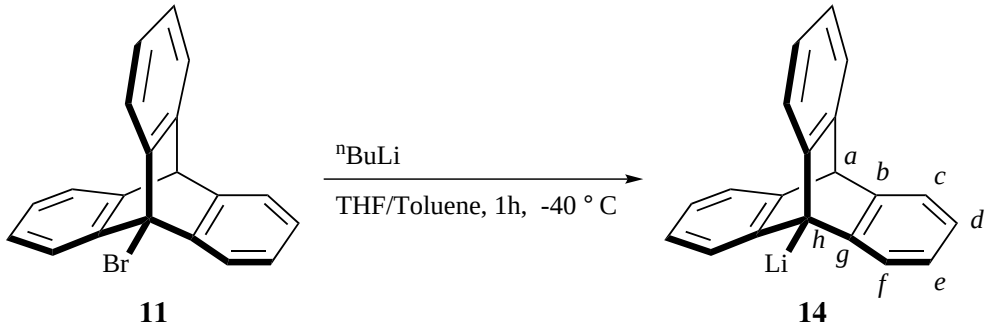

11 **14**

Scheme 4.2. The synthesis of 9-lithiotriptycene. The position labelling on **14** is used for NMR assignments below.

It was noted that the freshly prepared lithium triptycene, **14**, was very reactive towards some solvents. Unsurprisingly, the product was unstable in THF. However, **14** was also noted to decompose in toluene, rapidly at room temperature and over several hours at −40 °C. The compound was found to be indefinitely stable when solvated in benzene at room temperature. Whilst the electrons

in benzene are fully delocalised across the entire molecule; in toluene they are only delocalised across the ring. Those electrons in the methyl group remain localised in the methyl group. This results in a higher pK_a for benzene, compared to toluene — 43.0 and 40.9 respectively.[311] The lower pK_a of toluene is attributed as the cause of the instability exhibited by compound **14**.

The lithium triptycene was characterised using ^{1}H, ^{7}Li and ^{13}C NMR spectroscopy; these results are tabulated in table 4.1. The atom positions relate to the labelling scheme introduced in scheme 4.2. The ^{1}H signal at 5.49 ppm is a singlet, and is assigned to position *a*. The ^{1}H signals at 7.02 ppm, 7.48 ppm and 7.94 ppm are all multiplets with integrals of 6, 3 and 3, respectively. These are assigned to positions *d* & *e*, *c* and *f*, respectively. Positions *d* and *e* are chemically inequivalent, however they are sufficiently similar magnetically to be indistinguishable in the spectrum due to signal overlap. The two-dimensional NMR studies Heteronuclear Single Quantum Coherence (HSQC) spectroscopy and Heteronuclear Multiple-Bond Correlation (HMBC) spectroscopy were undertaken in an attempt to clarify the assignments. However, the HSQC and HMBC studies only showed that both positions resonate at 7.02 ppm.

There are also coordinated THF solvent molecules present in the spectrum. Despite repeated washings, these coordinated molecules were unable to be removed. They originate from the original synthesis, which is conducted in a THF/toluene mixture.

Table 4.1. NMR shifts, integrals and assignments for compound **14**.

Isotope	Assignment	Shift / δ	Integral
^{1}H	THF[a]	1.26	16
	THF[a]	3.32	16
	a	5.49	1
	d & *e*	7.02	6
	c	7.48	3
	f	7.94	3
^{7}Li	*h*	4.03	-
^{13}C	*a*	54.18	-
	c	123.15	-
	f	124.19	-
	d	126.11	-
	e	126.74	-
	h	127.21	-
	g	144.84	-
	b	144.98	-

[a] *The THF molecules are coordinated to the lithium metal, which is also the reason for their signal shift downfield.*

Mass spectrometry of **14** was conducted using electron ionisation (EI-MS). Only one strong signal was measured, with a value of 253 m/z. This is assigned to the triptycene fragment, with the lithium atom dissociated. EI-MS imparts a large amount of energy to the system, and it is common to only see fragments of samples. Unfortunately, the lithium atom that remains has a mass below that of the machines detection limit.

After repeated attempts it was possible to recrystallise the lithium triptycene, from a concentrated, chilled, THF solution over several months. The crystals formed were clear, needle-like, and suitable for analysis by single crystal X-ray diffraction. Diffraction was conducted using a molybdenum source (Mo K_{α} with a wavelength of 0.710 73 Å) and the structure was solved with an R-factor of 8.99 %. The crystal formed with the rhombohedral space group $R\bar{3}c$.

Shown in figure 4.2 is the molecular structure derived from the single crystal X-ray data. It can be seen that three THF molecules have coordinated to the lithium atom. This coordination of the solvent to the lithium stabilises the species, allowing it to crystallise. The coordination is also visible in solution by NMR spectroscopy, as discussed previously.

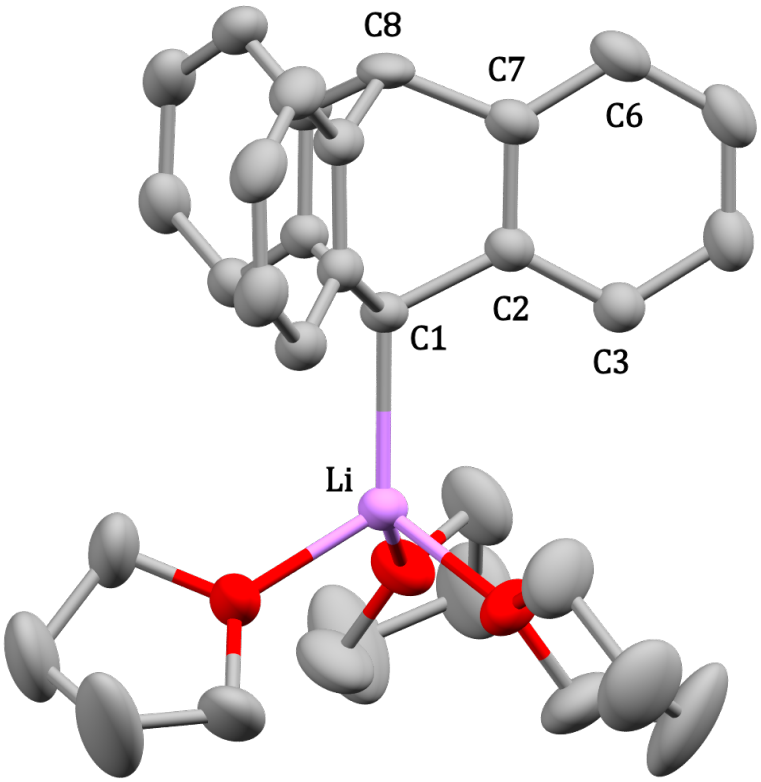

Figure 4.2. Molecular structure of lithium triptycene, derived from the single crystal X-ray structure. Ellipsoids are set to 40 % probability and hydrogen atoms are omitted for clarity. Crystal was solved with an R-factor of 8.99 %. Pink represents lithium; red represents oxygen; and grey represents carbon.

The Li−C bond length was measured as 2.162 Å. Comparing this to the crystallised Li−C bond

length of ^{t}BuLi and ^{n}BuLi, summarised in table 4.2, revealed that the lithium triptycene bond is shorter. The shorter bond suggests that the bond has more covalent, and less ionic, character to it compared to ^{t}BuLi and ^{n}BuLi. This in turn implies that the lithium triptycene is less acidic than both ^{t}BuLi and ^{n}BuLi. Though it should be noted that the ^{t}BuLi and ^{n}BuLi species are clusters.

Table 4.2. The bond lengths of some crystallised alkyl lithium species.[312,313]

Compound	Li−C Bond Length / Å
MeLi[312]	2.31
^{t}BuLi[313]	2.249
^{n}BuLi[313]	2.193
Lithium triptycene	2.162

Using Gaussian 09W, calculations were conducted on lithium triptycene to further investigate the bonding characteristics.[191] Optimisation was completed at the B3LYP level of theory using the 6-31+G(d) basis set (with five polarisation functions) for hydrogen and carbon, and the 6-311+G(d) basis set (with five polarisation functions) for lithium.[314,315] Vibrational frequencies were computed at the same level of theory, and used to check the nature of the stationary point; *i.e.* saddle point or energy minima. The highest occupied molecular orbital (HOMO) and the lowest unoccupied molecular orbital (LUMO) were then mapped onto the molecule, which is shown in figure 4.3.

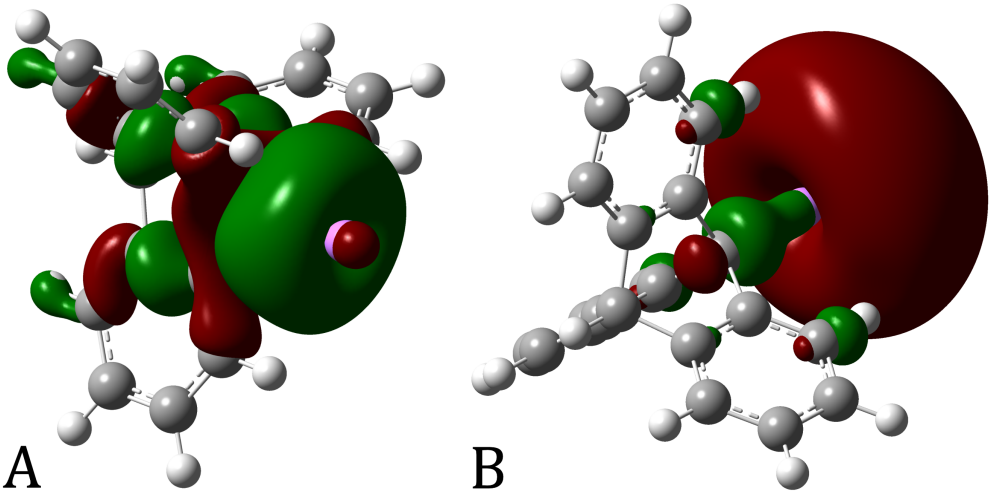

Figure 4.3. The (A) HOMO and (B) LUMO of lithium triptycene. For clarity, in (A) the molecule is orientated with the lithium atom pointing to the front, right; whilst in (B) the molecule is orientated with the lithium molecule pointing to the back, right.

These calculations support our theory that the C−Li bond has a large amount of covalent character, as is visible in the HOMO displayed in figure 4.3(B). This is evidenced by the high electron

density located between the lithium and carbon atoms, characteristic of covalent bonding character. In figure 4.3(B), the LUMO can be seen to be primarily located around the lithium atom. This emphasises the electrophilic nature of lithium in alkyl lithium species.

From the HOMO it can be seen that there is a reasonable amount of electron density distributed across the aromatic ring. From this, one would expect a change in these bond lengths as the substituent is changed from lithium. Comparing the bond lengths with bromotriptycene, as tabulated in table 4.3, shows that this is is observed experimentally. The C7-C8 bond has no electron density from the HOMO, and it can be seen that this bond does not change in length. Comparatively, when the substituent is replaced with hydrogen (*i.e.* in triptycene), the HOMO becomes redistributed and all of the bond lengths change.

Table 4.3. Selective bond lengths for lithium triptycene, and comparisons.[316,317]

Compound	Bond Length / Å				
	C1-C2	**C2-C3**	**C2-C7**	**C7-C6**	**C7-C8**
Lithium Triptycene	1.531	1.388	1.406	1.383	1.508
Bromotriptycene[316]	1.526	1.370	1.392	1.372	1.508
Triptycene[317]	1.532	1.390	1.409	1.392	1.529

4.3 The Reactivity of Lithium Triptycene

The reliable, reproducible and isolated synthesis of lithium triptycene marked the first successful formation of a difficult precursor. Previous attempts in literature have been made to isolate lithium triptycene, without realisation.[310] Using lithium triptycne as a ligand, the synthesis of metal complexes was conducted. Metal halides were used as standard precursors, reacting with lithium triptycene to yield the alkyl metal product and lithium halide as the by-product. The general reaction scheme for these reactions is shown in scheme 4.3.

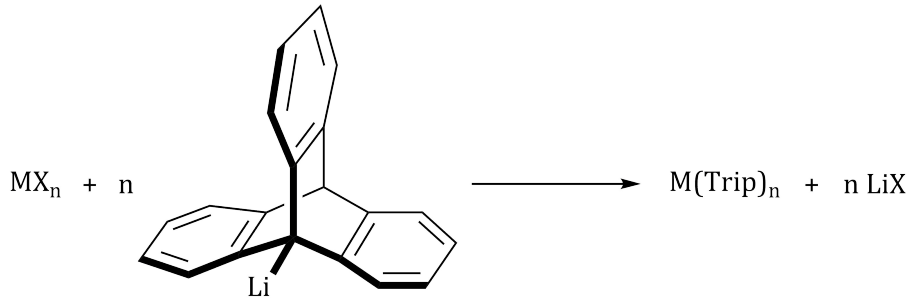

Scheme 4.3. General synthesis for metal triptycene complexes. M is any transition metal, Trip is triptycene and X is any halide.

4.3.1 Synthesis of Lithium Tritriptycene Tetrahydrofuran Cobaltate

Cobalt was chosen as the initial candidate for the metal centre. By using cobalt(II) chloride as the precursor, advantage could be taken of cobalt's small ionic radius and low initial oxidation state. By combining this with a large bulky ligand, such as triptycene, it was anticipated that a low-coordinate metal centre could by synthesised. Large ligands have been previously used with cobalt in order to gain access to unusual oxidation states, and so there is precedence for interesting electronic transfer properties in these species.[61]

Shown in scheme 4.4, the synthesis was conducted by solvating anhydrous cobalt(II) chloride in benzene by fast stirring, creating a royal blue solution. Once fully dissolved, three equivalents of lithium triptycene were added to the reaction vessel as a solid. The reaction was stirred for 2 hours, during which the lithium triptycene fully dissolved and reacted, causing a colour change to a deeper royal blue, suggesting no change in oxidation state. The reaction mixture was then filtered to collect the white by-product, assumed to be lithium chloride. The resulting blue solution was reduced *in vacuo* to yield a dark powder. This was resolvated in THF and again reduced *in vacuo* to yield the product, **15**, as a bright royal blue powder. Full preparatory details can be seen in section 6.5.1.

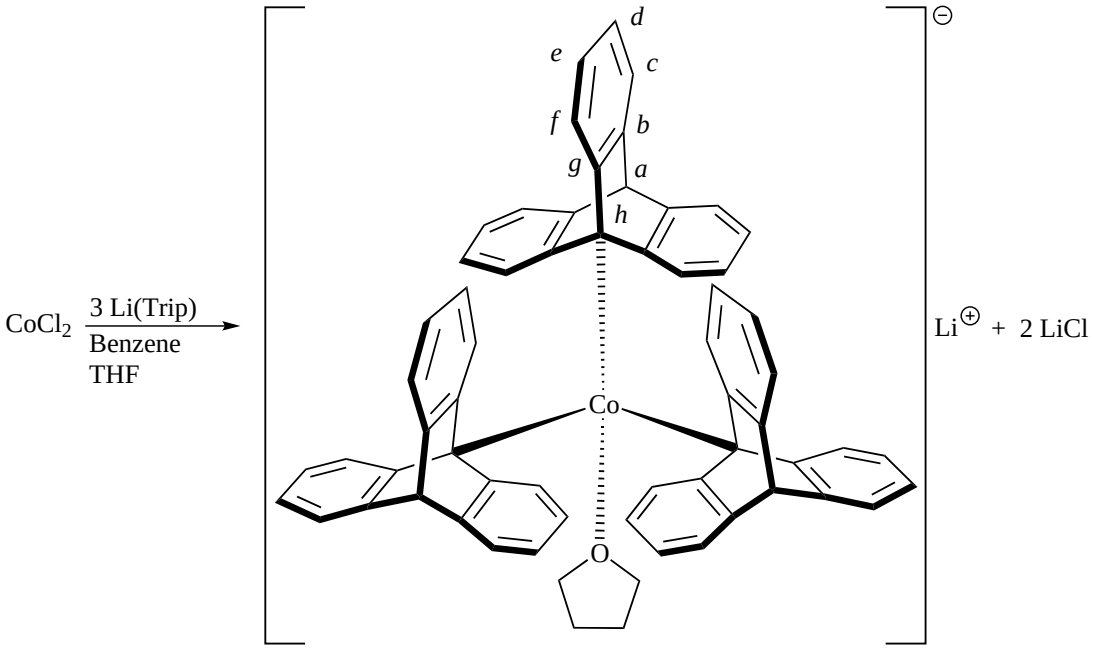

15

Scheme 4.4. Synthesis of lithium tritriptycene tetrahydrofuran cobaltate, **15**.

Initial attempts at the synthesis of a cobalt triptycene complex were conducted using THF as the solvent. These were unsuccessful because of the reactivity between lithium triptycene and

THF. Benzene was found to be a suitable alternative, despite lithium triptycene being only very sparingly soluble. However, as the small amount of dissolved lithium triptycene reacts, more is able to dissolve. This provides a driving force to draw the reagent into solution, allowing the reaction to proceed.

Multinuclear NMR spectroscopy was used for characterisation, and is summarised in table 4.4. The sample was run in deuterated THF for solubility reasons. Unfortunately this prevents the integration of coordinated THF molecules, due to overlap with residual protonated solvent THF. The coordination to the cobalt metal centre causes a paramagnetic broadening of all the signals.

Table 4.4. NMR shifts, integrals and assignments for **15**.

Isotope	Assignment	Shift / δ	Integral
^{1}H	THF[a]	1.72	-
	THF[a]	3.58	-
	a	5.49	1
	c, *d* & *e*	7.02	9
	f	7.94	3
^{7}Li	-	34.86	-
^{13}C	*a*	87.38	-
	b	124.25	-
	c	125.69	-

[a] *THF, used as the solvent, is coordinated to the cobalt metal. It is also used as the reference shift.*

Another consequence of the paramagnetic nature of the complex is signal shifting. This can be clearly observed in the ^{7}Li NMR spectrum. The signal range for ^{7}Li is normally constrained to approximately -15 ppm to 10 ppm, however in **15** the signal is shifted downfield to 34.86 ppm. This is commonplace in paramagnetic compounds, and is caused by the spin of the unpaired electron causing a change in the observed magnetic field at the nucleus.

Mass spectrometry was conducted on **15** using electrospray ionisation (ESI-MS), observing the negative ions. One large anion signal was recorded at 818.2200 m/z, which corresponds to $[Co(Trip)_3]^-$. It is uncommon to observe coordinated solvent molecules in ESI-MS, which explains the missing THF ligand.

Cobalt, a group 9 metal, is in the +2 oxidation state in complex **15**, and is therefore a d^7 metal centre. The Russell-Saunders ground state free-ion term symbol for Co(II) is ^{4}F. The ligand field splitting diagram for this compound is shown in figure 4.4. As the complex is tetrahedron in geometry, the metal has three unpaired electrons. It is these unpaired electrons that cause the

paramagnetic properties. Once the tetrahedral ligand field has been applied to the Co(II) metal centre, the ground state becomes $^4A_2$.

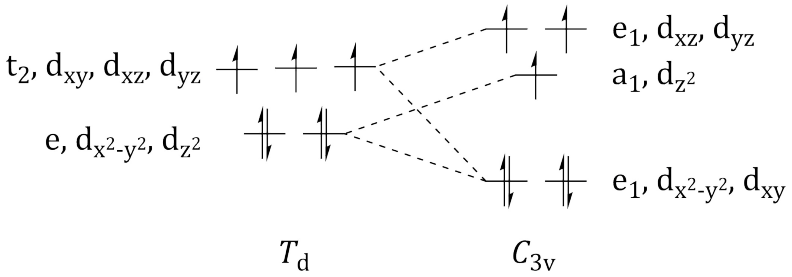

Figure 4.4. Ligand field splitting diagram for a d^7 metal centre with tetrahedral or C_{3v} geometry.

It should be noted however, that the true geometry of the complex is more likely to be C_{3v}, due to the large steric bulk of the three triptycene ligands compared to the THF molecule. The orbital splitting for a C_{3v} d^7 complex is also shown in figure 4.4. In complex **15**, the energy difference between the d_{xz} & d_{yz} orbitals, and the d_{z^2} orbital must be small because the complex is known to have three unpaired electrons, discussed below.

The UV-visible spectrum of complex **15** was recorded, and is displayed in figure 4.5. UV-visible spectra show absorbances at energy levels typical of d-d transitions, and as such they show electronic transitions that can be assigned using Tanabe-Sugano diagrams, assuming tetrahedral geometry.[318–320] These diagrams show electronic transitions and their corresponding energy relative to the ground state. Assignments can be made by comparing the ratio of the experimentally observed transitions with the ratios of those transitions published in literature. Shown in figure 4.5 are the transitions $^4A_2(F) \rightarrow {}^4A_2(F)$ at 14 005 cm^{-1}, and $^4A_2(F) \rightarrow {}^4T_1(P)$ at 32 572 cm^{-1}. The letters following the electronic states are the corresponding parental ground states. Unfortunately, as the ground state for the observed transitions changes, the measured absorptions cannot be used to calculate the ligand field splitting parameter. The absorption at 14 005 cm^{-1} is the excitation to the second excited state. Using the Tanabe-Sugano diagrams, a prediction can be made that the first excited state ($^4A_2(F) \rightarrow {}^4T_2(F)$) would occur in the near infrared region, at approximately 11 000 cm^{-1}.

The magnetic moment of paramagnetic solutes in diamagnetic solvents can be measured via NMR using the Evans method, first reported in 1959.[321] The measured magnetic susceptibility is the sum of the paramagnetic and diamagnetic contributions, shown in equation (4.1).

$$\chi^{meas} = \chi^{dia} + \chi^{p} \tag{4.1}$$

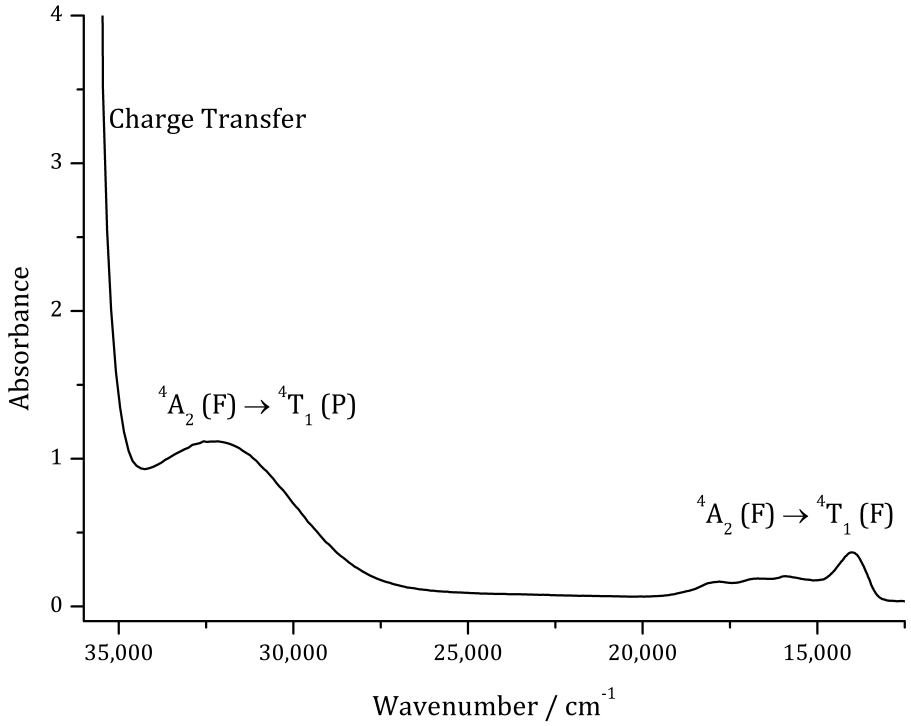

Figure 4.5. Recorded UV-Vis spectrum for complex **15**. Two electronic transitions and the charge transfer band are labelled.

Rearrangement of equation (4.1) allows calculation of the paramagnetic component. The original equation published by Evans contained a solvent correction term, which involved an estimated denominator and numerator, both of which tended to zero at low concentrations. It was determined by Grant in 1995 that removal of this component, and another separate component which generally cancelled it out, introduces less error on balance.[322,323]

$$\chi_{\mathrm{M}}^{\mathrm{p}} = \frac{\delta\nu^{\mathrm{p}} M^{\mathrm{p}}}{\nu_0 S_f m^{\mathrm{p}}} - \chi_{\mathrm{M}}^{\mathrm{dia}} \tag{4.2}$$

The resulting equation is shown in equation (4.2), where $\chi_{\mathrm{M}}^{\mathrm{p}}$ is the paramagnetic component of the molar magnetic susceptibility in emu mol^{-1}; $\delta\nu^{\mathrm{p}}$ is the shift in observed frequency in Hz; M^{p} is the molar mass of the paramagnetic compound in g mol^{-1}; ν_0 is the frequency of the NMR spectrometer in Hz; S_f is the shape factor of the magnetic field (taken as $4\pi/3$ for a cylindrical sample, parallel to the magnetic field, in a superconducting magnet); m^{p} is the concentration of the paramagnetic solute in g cm^{-3}; and $\chi_{\mathrm{M}}^{\mathrm{dia}}$ is the diamagnetic component of the molar magnetic susceptibility in emu mol^{-1}. It should be noted that whilst emu (electromagnetic unit) is not an SI unit, it is the most commonly used unit for magnetic susceptibility (1 emu = 1 cm^3).

The diamagnetic component, $\chi_{\mathrm{M}}^{\mathrm{dia}}$, is important because every molecule, even if paramagnetic,

has some diamagnetic character to it. It has been calculated for each compound individually in this work, by the summation of the diamagnetic susceptibility of each atom and bond in the compound of interest, shown in equation (4.3). The values for $\chi^{\text{dia}}_{\text{atom}}$ and $\chi^{\text{dia}}_{\text{bond}}$ are taken from the literature, first recorded by Pascal in 1910.[324–327] This led to them being known as Pascal's Constants.

$$\chi^{\text{dia}}_{\text{M}} = \sum_i \chi^{\text{dia}}_{\text{atom}_i} + \sum_i \chi^{\text{dia}}_{\text{bond}_i} \tag{4.3}$$

Once the paramagnetic component of the molar magnetic susceptibility has been calculated, the magnetic moment can be calculated using equation (4.4),[328] where μ_{eff} is the effective magnetic moment in μ_{B} (Bohr magnetons); k_{B} is the Boltzmann constant; T is the absolute temperature in Kelvin; N_{A} is Avogadro's number; and β is the Bohr magneton.

$$\mu_{\text{eff}} = \sqrt{\frac{3k_{\text{B}}T}{N_{\text{A}}\beta^2}\chi^{p}_{M}} \tag{4.4}$$

Using the Evans method with equations (4.2) and (4.3), the paramagnetic component of the molar magnetic susceptibility of **15** was calculated to be 9.063×10^{-3} emu mol^{-1}. When used in conjunction with equation (4.4), this gives an effective magnetic moment of 4.688 μ_{B}.

The effective magnetic moment can be used to determine the number of unpaired electrons in a compound. Using this, the spin-only magnetic moment can be calculated using the spin-only magnetic moment formula, shown as equation (4.5) where μ_{so} is the calculated spin-only magnetic moment with units of Bohr magnetons, μ_{B}; g is the gyromagnetic ratio for a free electron (generally taken as $g = 2.000$); and S is the total spin angular momentum quantum number (sum of unpaired spins in the compound). Tetrahedral d^7 metal complexes have three unpaired electrons, as demonstrated in figure 4.4. Using equation (4.5) with three unpaired electrons gives a spin-only magnetic moment of 3.873 μ_{B}.

$$\mu_{\text{so}} = g\sqrt{S(S+1)}\ \ \mu_{\text{B}} \tag{4.5}$$

The calculated spin-only magnetic moment value is slightly lower than the experimentally measured magnetic moment. This is due to a combination of different effects, one of which is that the first and second excited states of complex **15** have $^4T_2$ and $^4T_1$ symbols, respectively. These excited states, of the same multiplicity as the ground state, have a slight effect on the the effective magnetic moment. This effect can be accounted for by equation (4.6), where μ_{calc} is the calculated magnetic moment in μ_{B}; λ is the term spin-orbit coupling constant; and Δ is the crystal field

splitting, approximately 10 000 cm^{-1} for a strong-field, tetrahedral Co(II) complex, such as **15**.[320]

$$\mu_{calc} = \left(1 - \frac{4\lambda}{\Delta}\right)\mu_{so} \tag{4.6}$$

The term spin-orbit coupling constant, λ is defined in equation (4.7), where ζ is the electron spin-orbit coupling constant, equal to 515 cm^{-1} for a Co(II) ion;[329] and S is the total spin angular momentum quantum number, equal to 3/2 for a d^7 tetrahedral complex in a $^4A_2$ ground state. The nature of the sign of λ depends on the fill state of the orbitals. For d^n electrons, when $n < 5$, λ is positive; when $n > 5$, λ is negative; and when $n = 5$, $\lambda = 0$. Using this information with equation (4.7), gives equation (4.8).

$$\lambda = \frac{\pm\zeta}{2S} \tag{4.7}$$

$$\lambda = \frac{-\zeta}{3} = \frac{-515}{3}\ cm^{-1} \tag{4.8}$$

Use of equation (4.6) for complex **15** gives a calculated magnetic moment of 4.14 μ_B. This value is closer to the measured effective magnetic moment. There are however more effects to consider. When the term spin-orbit coupling constant, λ, is on a similar order of magnitude as k_BT, then first and second order Zeeman effects emerge. For complex **15**,

$$\lambda = \frac{-\zeta_{Co(II)}}{3} = \frac{-515}{3} = -171.7\ cm^{-1}. \tag{4.9}$$

When this is compared to the value for k_BT at 20 °C of 203.8 cm^{-1}, it is clearly seen that the values are similar within an order of magnitude. Since the value for λ is slightly less than k_BT, this would result in room temperature occupation of excited T states, where orbital angular moment is not fully quenched, further increasing the measured value of μ_{eff}. If this is the case, then one expects to see the effective magnetic moment vary as a function of absolute temperature. In figure 4.6, it can be seen that this is indeed observed experimentally.

The magnetic susceptibility exhibited by paramagnetic compounds is inversely proportional to temperature, as described by the Curie-Weiss law.[330,331] This is shown in equation (4.10), where χ_M is the molar magnetic susceptibility in emu mol^{-1}; C is the compound-specific Curie constant in emu K mol^{-1}; T is the absolute temperature in Kelvin; and T_C is the Curie point (or Weiss constant) in Kelvin.

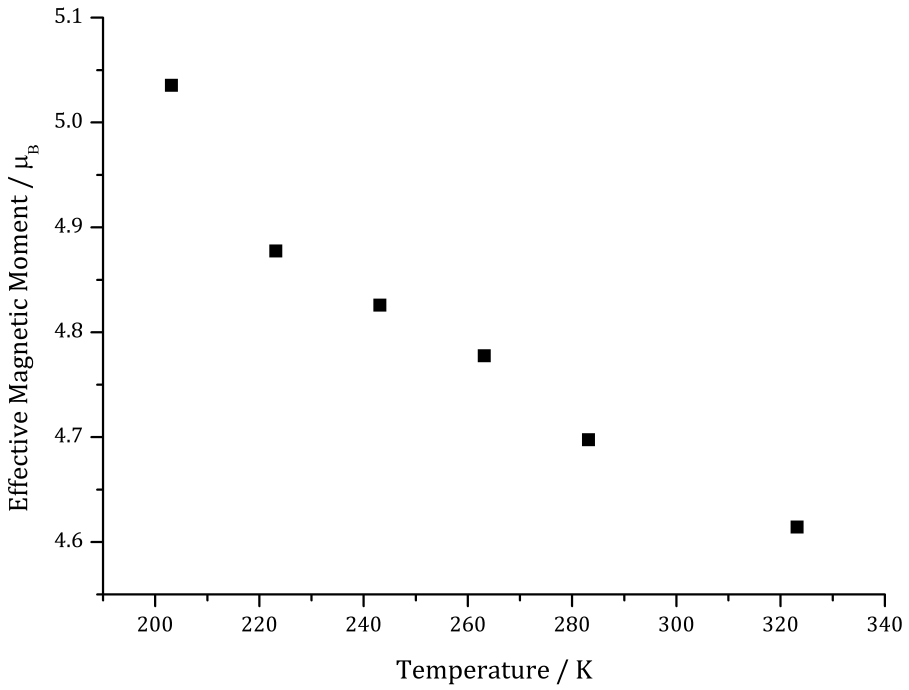

Figure 4.6. Plot of the effective magnetic moment of complex **15** varying as a function of absolute temperature.

$$\chi_M = \frac{C}{T - T_C} \tag{4.10}$$

This can be rearranged to the form of a linear equation, as shown in equation (4.11). The *y*-axis is the inverse molar magnetic susceptibility; the *x*-axis is the absolute temperature; the gradient is the inverse Curie constant; and the *y*-intercept is equal to $^{-T_C}/_C$.

$$\frac{1}{\chi_M} = \frac{1}{C}T - \frac{T_C}{C} \tag{4.11}$$
$$y = mx + c$$

Therefore, by measuring the magnetic susceptibility of a compound over a range of temperatures, and plotting against temperature, a Curie-Weiss plot is produced, as shown for complex **15** in figure 4.7. The linearity of the data indicates that the compound exhibits Curie behaviour. From this plot the Curie constant and Curie point for complex **15** are found to be 1.90 emu K mol^{-1} and 76.3 K respectively.

The anomalous result at 303.15 K was measured using a separate, more concentrated sample than the other data points. Whilst the concentration of the sample is taken into consideration in the

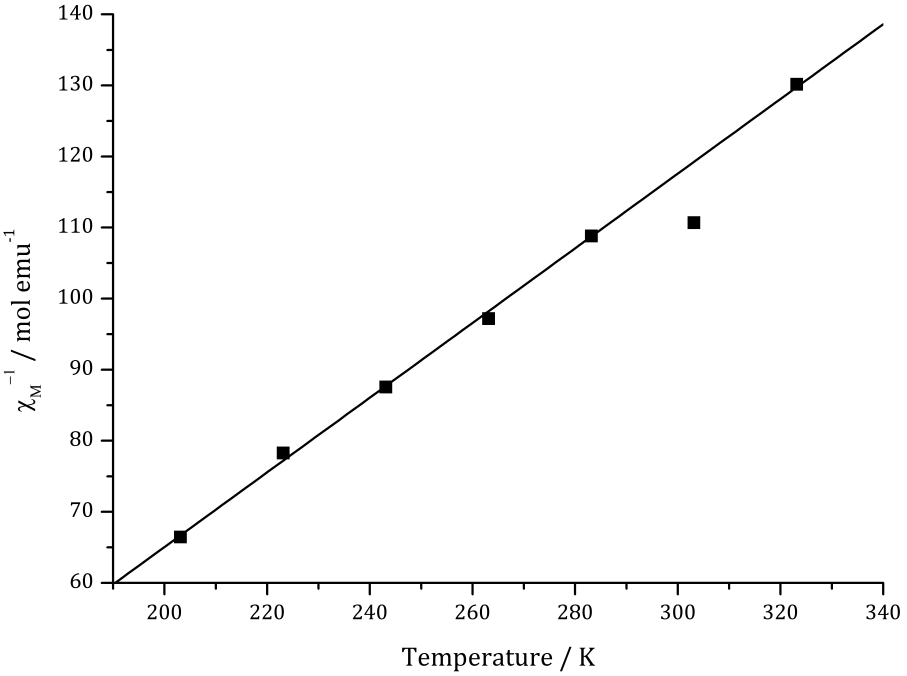

Figure 4.7. Curie-Weiss plot of complex **15**. The anomalous result at 303.15 K was not included in the line of best fit, which has a gradient of 0.5256, an intercept of −40.09 and a R^2 value of 0.9988.

calculation with the m^p component of equation (4.2), there are negative ramifications in making a sample too concentrated. When the concentration of the sample is increased, the likelihood of a paramagnetic compound interacting with another paramagnetic compound, instead of the diamagnetic solvent, is increased. These interactions are not accounted for in equation (4.2), and as such cause a slight deviation from the line of best fit.

4.3.2 Synthesis of Ditriptycene Tetrahydrofuran Iron

There is recent literature precedence for the synthesis of a low-coordinate iron complex. Reported by Long *et al*. in 2013, a divalent iron(I) trimethylsilane complex was synthesised, with potential use as a single molecule magnet due to its high barrier for magnetic relaxation.[332] Therefore, we attempted the synthesis of an iron triptycene complex. Two equivalents of lithium triptycene were reacted with iron dichloride using THF/toluene as a solvent, as shown in scheme 4.5. Ditriptycene tetrahydrofuran iron, **16**, is poorly soluble in THF, allowing easy isolation by vacuum filtration. The product was then washed with pentane and dried *in vacuo*.

Complex **16** is poorly soluble in most solvents, however a sample in deuterated benzene was made concentrated enough to get a ^{1}H NMR spectrum. The spectrum, tabulated in table 4.5, shows line broadening typical of paramagnetic compounds. The residual THF solvent was found to be

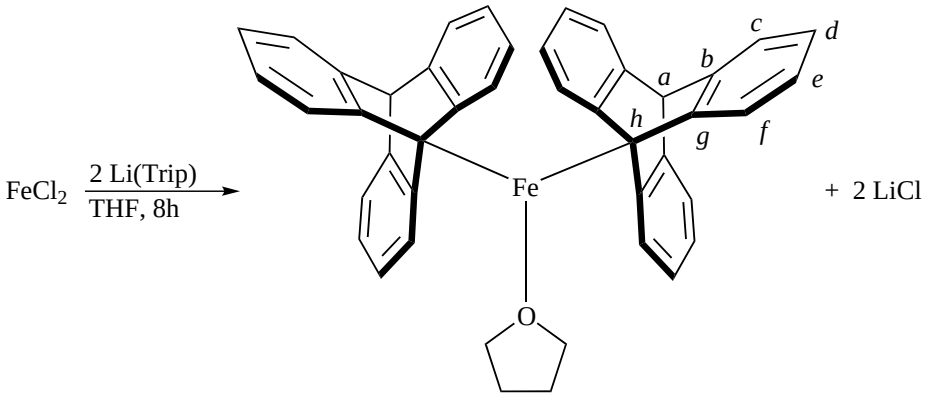

16

Scheme 4.5. Synthesis of ditriptycene tetrahydrofuran iron, **16**. The geometry shown is distorted-trigonal planar.

difficult to remove, even after several excessive washings with a variety of solvents. Consequently, this removed the possibility of integrating the THF peaks to discover the number of coordinated ligands.

Table 4.5. NMR shifts, integrals and assignments for **16**.

Isotope	Assignment	Shift / δ	Integral
^{1}H	THF[a]	1.42	-
	THF[a]	3.59	-
	a	5.20	1
	c, *d* & *e*	6.85	9
	f	7.29	3

[a] *THF, used during synthesis, was not removable even after excessive washings.*

EI-MS analysis of **16** was conducted, showing an M^+ peak at 562 m/z. This corresponds to complex **16** with dissociated THF. Also visible in the spectrum was a large signal at 253 m/z; which corresponds to a triptycene fragment lost during ionisation.

It was possible to grow X-ray suitable crystals of complex **16** from the slow evaporation of benzene. Shown in figure 4.8, the complex crystallised with pseudo-trigonal planar geometry. The pseudo aspect comes from two sources. Firstly, there is a deviation from flat geometry of 3.75°; this is due to the large steric effects of the triptycene ligands. Secondly, the bond angle C1-Fe1-C2 is strained at 140.0° (compared to the ideal 120°); this is also attributed to the large steric bulk of the two triptycene ligands.

Using the XRD data, the cone angle of triptycene bound to iron was measured as 129.9°. For comparison, trimethoxyphosphine has a cone angle of 107°, tripropylphosphine has a cone angle of 132°, and tri-*tert*-butylphosphine a value of 182°.[309] The average organoiron bond length in

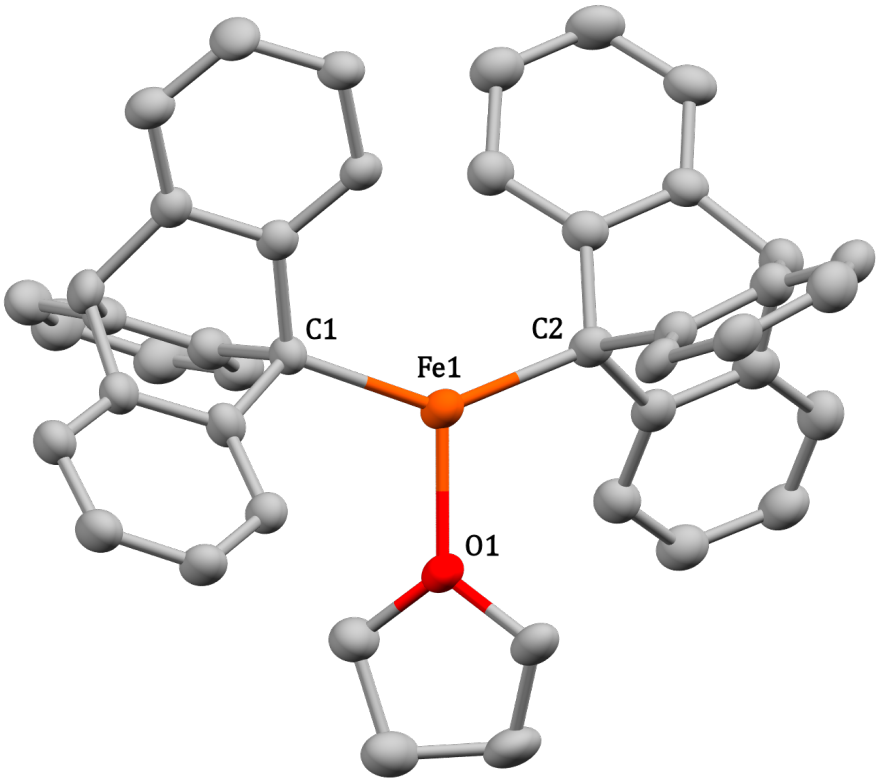

Figure 4.8. Molecular structure of ditriptycene tetrahydrofuran iron, **16**, derived from the single crystal X-ray structure. Ellipsoids are set to 40 % probability; hydrogen atoms and co-crystallised benzene solvent molecules have been omitted for clarity. Crystal was solved with an R-factor of 6.61 %. Orange represents iron; red represents oxygen; and grey represents carbon.

complex **16** is 2.089 Å. This is comparable to the average organoiron sp^3 bond lengths mentioned in textbooks (2.11 Å),[333] as well as the average organoiron sp^3 bond length of crystal structures deposited in the Cambridge Structural Database (2.098 Å).

Table 4.6. Selected bond lengths for complex **16**.

Parameter	Bond Length / Å
Fe1-C1	2.092(9)
Fe1-C2	2.086(8)
Fe1-O1	2.015(5)

The large angle at C1-Fe1-C2 distorts the geometry away from perfect trigonal planar, altering the symmetry at the metal centre. A perfect trigonal planar compound has the point group D_{3h}, however when the triptycene ligands force this angle to increase to 140.0° (away from the ideal 120°) the resulting symmetry becomes C_{2v}, effectively removing degeneracy from all orbitals. If the 3.75° deviation from flat geometry is also taken into account the symmetry becomes C_s around the metal centre, with just a single mirror plane. This, incidentally, returns some orbital degeneracy.

Table 4.7. Selected bond angles for complex **16**.

Parameter	Bond Angle / Å
C1-Fe1-C2	140.0(3)
C2-Fe1-O1	110.6(3)
O1-Fe1-C1	109.1(3)

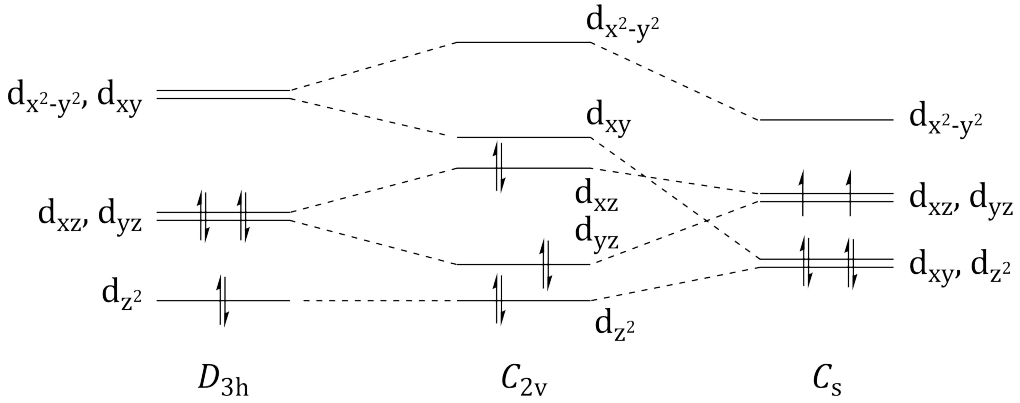

Figure 4.9. Ligand field splitting diagram for D_{3h} trigonal planar, and the changes in relative orbital energy and degeneracy when changed to C_{2v} and C_s. The electrons are filled according to a low-spin Fe(II) d^6 centre.

When changing from D_{3h} to C_{2v}, as shown in figure 4.9, the d-orbitals change in energy due to the relocation of the ligands. The $d_{x^2-y^2}$ raises slightly in energy as the ligands move toward Cartesian corners; for the same reason d_{xy} drops in energy as the ligands move away. Initially d_{xz} and d_{yz} are degenerate, but as the ligands move away from one set of orbitals and towards the other, they split in energy. The d_{z^2} orbital has no change in energy, as it has horizontal (specifically $D_{\infty h}$) symmetry.

When changing from C_{2v} to C_s, the $d_{x^2-y^2}$ orbital drops in energy as the ligands move out of the xy plane. For the same reason the d_{xy} orbital also drops in energy. The d_{z^2} orbital rises in energy as the ligands move towards its larger lobes, becoming degenerate with the falling d_{xy} orbital. The d_{xz} and d_{yz} orbitals also become degenerate again, as the ligands move along the z-axis.

This change in symmetry is important because it is responsible for the paramagnetism of the compound. Iron in the +2 oxidation state has six d-electrons, making it diamagnetic when trigonal planar, with both D_{3h} and C_{2v} symmetry, when low-spin. The new degeneracy formed in the C_s point group causes a low-spin d^6 configuration to have two unpaired electrons, which is the source of the sample's paramagnetism. This is supported by the ^{1}H NMR data reported above.

Iron is a group 8 metal, and in its +2 oxidation state (complex **16**) has a d^6 electron arrangement. Its free ion term symbol is $^5D_4$.

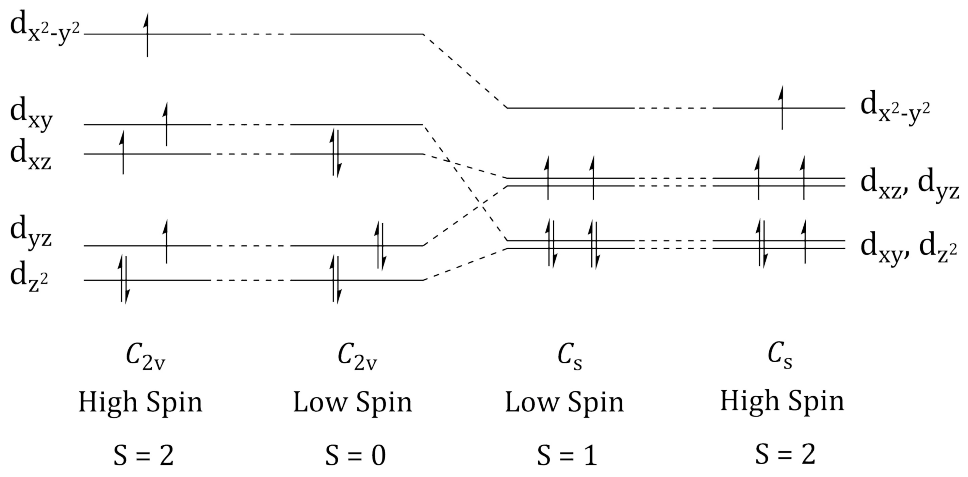

Figure 4.10. Ligand field splitting diagram for C_{2v} and C_s symmetry. High and low spin configurations are shown.

Likely electron configurations of a distorted trigonal planar complex are shown in figure 4.10. These include high and low spin occupations, in both C_{2v} and C_s symmetry. The number of unpaired electrons, and the resulting value of the total spin angular momentum quantum number, S, is tabulated in table 4.8.

Table 4.8. The resulting spin-only magnetic moment for different symmetries and spin states for distorted trigonal planar d^6 complexes.

Symmetry	Spin State	Unpaired Electrons	S	Spin-only Magnetic Moment / μ_B
C_{2v}	High Spin	4	2	4.90
C_{2v}	Low Spin	0	0	0.00
C_s	Low Spin	2	1	2.83
C_s	High Spin	4	2	4.90

Magnetic studies on complex **16** were conducted using the Evans method. Using equation (4.2), the paramagnetic component of compound **16** was determined to be 4.4439×10^{-3} emu mol^{-1}. This was then used with equation (4.4) to yield an effective magnetic moment of 3.28 μ_B. As demonstrated in table 4.8, when populated with 6 d electrons, the low-spin C_s ligand field gives 2 unpaired electrons. Using the spin-only formula, equation (4.5), this gives a magnetic moment of 2.83 μ_B, in good agreement with the experimental value.

It is the large steric bulk of the triptycene ligands that causes the paramagnetic nature of complex **16**. The deviation of only 3.75° from the perfect trigonal planar, and the resulting C_s symmetry instead of C_{2v}, provides the ligand-orbital realignment, resulting in two unpaired electrons that cause the complex to be paramagnetic. Being subject to the pseudo-trigonal planar C_s ligand field, the iron(II) metal centre has a ground state ^{5}A, with no degeneracy.

4.3.3 Synthesis of Tritriptycene Tetrahydrofuran Chromium

The synthesis of a chromium triptycene complex was achieved, using anhydrous chromium trichloride tris(tetrahydrofuran) adduct as the precursor. The reaction was conducted in benzene with stirring for eight hours at room temperature, as shown in scheme 4.6. During the reaction a solid was seen to precipitate from solution. This was collected by vacuum filtration and washed with THF before drying *in vacuo*, yielding a bright green powder, complex **17**.

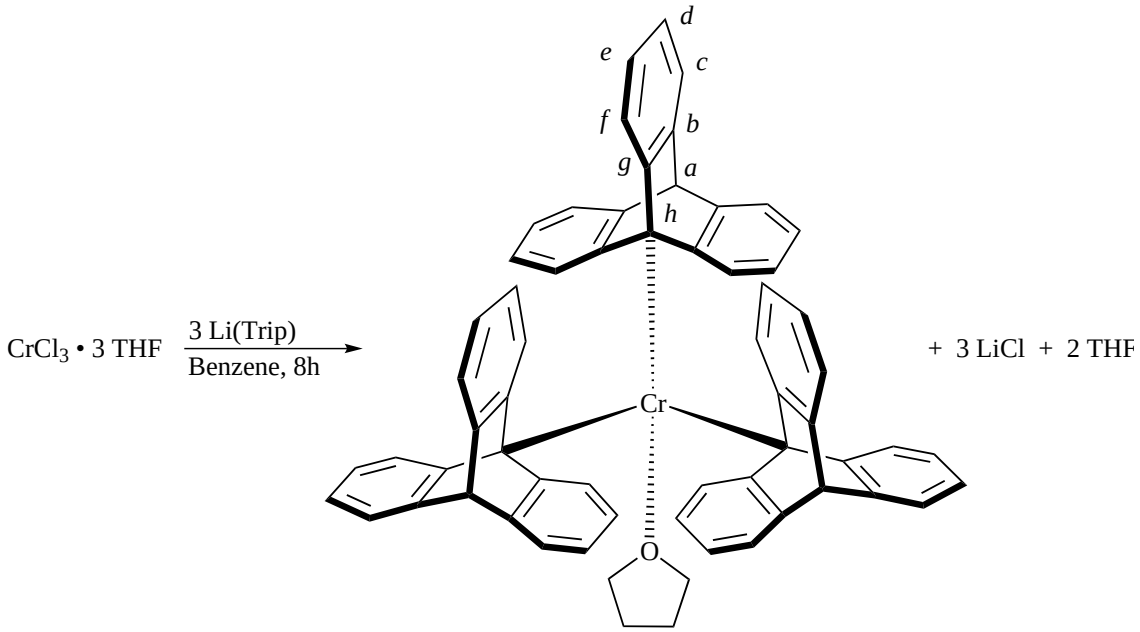

17

Scheme 4.6. Synthesis of tritriptycene tetrahydrofuran chromium, **17**.

Complex **17** was poorly soluble in most solvents, however a sufficiently concentrated sample was made in benzene-d_6, such that collection of a ^{1}H NMR spectrum was possible. The resulting signals are tabulated in table 4.9. No signals were detected in the ^{13}C NMR spectrum, despite increased scan numbers. This is a common phenomenon in paramagnetic compounds.

Table 4.9. NMR shifts, integrals and assignments for **17**.

Isotope	Assignment	Shift / δ	Integral
^{1}H	THF	1.40	4
	THF	3.55	4
	a	5.18	3
	c	6.82	9
	d, *e* & *f*	7.14	27

From the ^{1}H NMR spectrum it can be seen that there is one THF molecule present for every three triptycene molecules. This ratio is consistent, even without the THF washing; it is thought

that the source of the THF is the chromium precursor. Based this information, a pseudo-tetrahedral structure is proposed, as shown in scheme 4.6. Square planar geometry is unlikely due to the steric bulk of the triptycene ligands and the d^3 electron count, which is discussed shortly.

EI-MS of complex **17** was conducted. This showed a peak at 811 m/z, corresponding to chromium tetrahydrofuran tritriptycene with the THF molecule dissociated. Also visible were peaks at 253 m/z and 506 m/z, corresponding to non-coordinated triptycene fragment and ditriptycene respectively. It is simple to attribute these species to the ionisation process of the MS, as no diamagnetic signals were observed in the ^{1}H NMR spectrum.

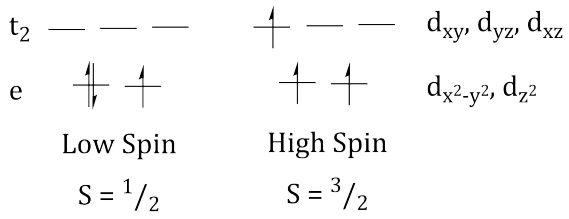

Figure 4.11. High- and low-spin ligand field splitting diagrams for d^3 metal centres with tetrahedron geometry.

Chromium in the +3 oxidation state is d^3, giving it the free-ion term symbol $^4F_{3/2}$. Tetrahedral d^3 complexes can be either high spin or low spin, as shown in figure 4.11. For complex **17** this means there are either three or one unpaired electron(s). The possible spin-only magnetic moments associated with these two states can be calculated using equation (4.5), and are shown in table 4.10.

Table 4.10. The resulting magnetic moments from low and high spin states for tetrahedral d^3 complexes.

Spin State	Unpaired Electrons	S	Calculated Magnetic Moment / μ_B
Low Spin	1	½	1.73
High Spin	3	3/2	3.87

Measurement of the effective magnetic moment of complex **17** was conducted using the Evans method. Using equations (4.2) and (4.3), this gave a paramagnetic molar magnetic susceptibility of 1.428×10^{-3} emu mol^{-1}. When this is used in conjunction with equation (4.4), it gives an effective magnetic moment of 1.86 μ_B. This is in good agreement with the low-spin electronic distribution noted in table 4.10, with a single unpaired electron. Due to this, complex **17** is assigned the tetrahedral ligand field ground state term ^{2}E, with the electron arrangement shown as S = ½ in figure 4.11.

Low-spin tetrahedral complexes are uncommon, due to the lower splitting energy of tetrahedral ligand fields compared to octahedral ligand fields ($\Delta_{Tet} \approx 4/9\Delta_{Oct}$). However, as a tertiary carban-

ion, triptycene is a high-field ligand that forms strong σ-bond interactions.[62] Metal centres can also be ranked loosely by their ligand field splitting ability; chromium(III) is at the upper end of this series, being known to have a larger ligand field splitting compared to analogous complexes.[320] Therefore, it is not entirely surprising that complex **17** is low spin. Indeed, a low-spin, first-row tetrahedral complex was first reported by Theopold *et al*. in 1986 with a cobalt(IV) species, **18**;[63] while a low-spin, tetrahedral cobalt(II) complex, **19**, was isolated by Peters *et al*. in 2002.[334]

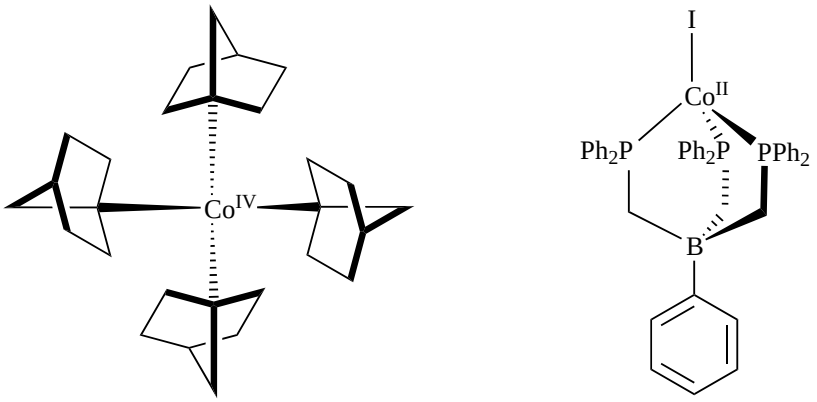

18 **19**

Figure 4.12. Examples of previously published low-spin tetrahedral metal complexes. Complex **18** was reported by Theopold *et al*. in 1986[63] and complex **19** was reported by Peters *et al*. in 2002.[334]

4.3.4 Synthesis of Dichloro,ditriptycene Zirconium

A zirconium triptycene complex was formed by the reaction of zirconium tetrachloride with two equivalents of lithium triptycene, as shown in scheme 4.7. The reaction was conducted in THF for eight hours, before filtering to remove the precipitated lithium chloride. The filtrate was then reduced *in vacuo*, before being washed with hexane. Complex **20** was isolated as a yellow powder.

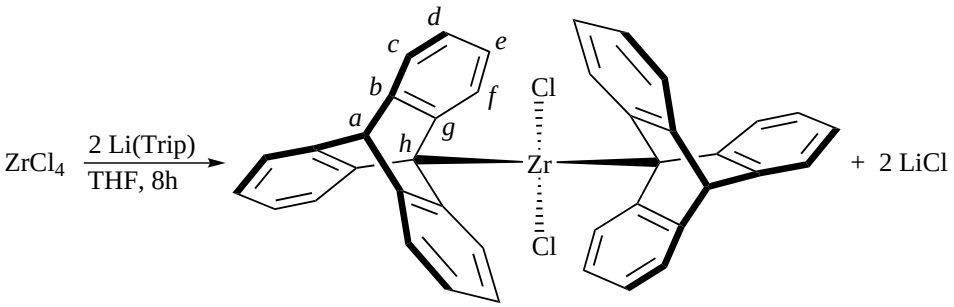

20

Scheme 4.7. Synthesis of dichloro,ditriptycene zirconium, **20**.

Complex **20** was dissolved in benzene-d_6 for ^{1}H and ^{13}C NMR analysis. Signals and integra-

tions are shown in table 4.11. Only four signals were observed in the ^{13}C NMR spectrum. It was not possible to remove the residual THF from the complex by either washing or extended time under reduced pressure.

Table 4.11. NMR shifts, integrals and assignments for **20**.

Isotope	Assignment	Shift	Integral
^{1}H	THF	1.40	-
	THF	3.59	-
	a	5.21	1
	c	6.84	3
	d, e & f	7.19	9
^{13}C	*a*	67.32	-
	b	123.90	-
	c	125.41	-
	d	145.88	-

Zirconium is a group 4 metal, and as such has no d electrons in its +4 oxidation state. The d^0 electron count means it cannot have unpaired electrons, and therefore complex **20** is diamagnetic. This is demonstrated in the ^{1}H NMR spectrum, which yields sharp and unshifted signals, unlike the previously reported complexes, **15**, **16** and **17**. A pseudo-tetrahedral geometry is assigned to complex **20**, though a likely symmetry is C_{2v} due to the large bulk of the triptycene ligands compared to the chlorine atoms. The ligand field splitting diagram for tetrahedral and C_{2v} complexes is shown in figure 4.13.

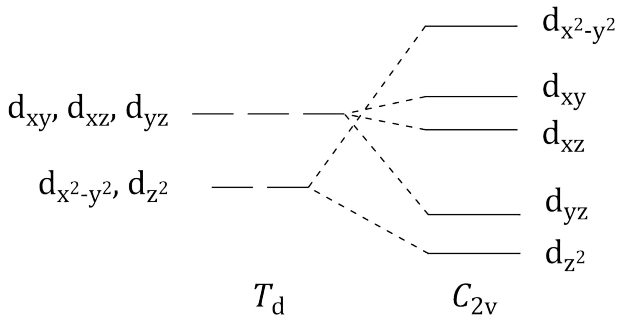

Figure 4.13. Ligand field splitting diagram for tetrahedral and C_{2v} complexes.

It should be noted that zirconium has four ligands bound in complex **20**, despite the large steric bulk of two triptycene ligands. This is in contrast to the three bound ligands in complex **16**. The cause of this is the increased atomic radius of zirconium as a second row d-block element, examples of which are shown in table 4.12. In zirconium, the 4d electrons are the outer shell, compared to the 3d electrons in chromium, iron and cobalt. This additional layer of electron density increases

the size of the atom, giving it a larger radius and therefore more space for large and bulky species. Interestingly, this trend does not continue for 5d elements, as the presence of the complete 4f electron shell causes a large increase in effective nuclear charge. This pulls the outer 5d electrons in to approximately the same radius as the corresponding 4d elements, known as the lanthanide contraction.

Table 4.12. Atomic radii of relevant elements.[335]

Element	Position in d-Block	Van der Waals Radius / Å	Covalent Radius / Å
Co	1st row	2.00	1.18
Fe	1st row	2.04	1.24
Cr	1st row	2.06	1.30
Zr	2nd row	2.23	1.64

EI-MS was also conducted on complex **20**. Zirconium is an unusual d-block metal, in that it has many naturally abundant isotopes. In order of abundance these are ^{90}Zr, ^{94}Zr, ^{92}Zr, ^{91}Zr and ^{96}Zr. The natural abundance and half-life of these isotopes are shown in table 4.13. Coupled with the presence of bi-isotopic chlorine (^{35}Cl and ^{37}Cl), this large range of isotopic combinations makes the MS spectra very broad, as each isotope generates a different peak.

Table 4.13. Natural isotopes of zirconium.[336]

Isotope	Natural Abundance / %	Half-life
^{90}Zr	51.45	Stable
^{94}Zr	17.38	Stable
^{92}Zr	17.15	Stable
^{91}Zr	11.22	$>1.1 \times 10^{17}$ years
^{96}Zr	2.80	$>2 \times 10^{19}$ years

Assignments can still be made however, and a selection of MS peaks are shown in table 4.14. The MS peaks agree with the structure shown for complex **20** in scheme 4.7. The table also hints at the large combination of isotopes that can each add up to the same mass ion.

Table 4.14. A selection of MS peaks recorded for complex **20**, and their assignments.

Mass / m/z	Assignments		
614	$C_{36}H_{22}{}^{35}Cl_2{}^{90}Zr$		
616	$C_{36}H_{22}{}^{35}Cl_2{}^{90}Zr$	$C_{36}H_{22}{}^{35}Cl^{37}Cl^{90}Zr$	
666	$C_{40}H_{26}{}^{35}Cl_2{}^{90}Zr$		
670	$C_{40}H_{26}{}^{37}Cl_2{}^{90}Zr$	$C_{40}H_{26}{}^{35}Cl_2{}^{94}Zr$	$C_{40}H_{26}{}^{35}Cl^{37}Cl^{92}Zr$

4.4 Reactivity of Metal Triptycene Complexes

In an order to probe the reactivity of the synthesised metal complexes **15**, **16**, **17** and **20**, studies were undertaken on the metal triptycene complexes with the small molecules oxygen, nitrogen, carbon monoxide and carbon dioxide, as demonstrated in scheme 4.8.

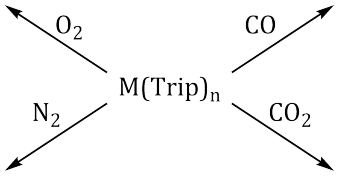

Scheme 4.8. Potential reactivity of metal triptycene complexes. Here, $M(Trip)_n$ refers to complexes **15**, **16**, **17** and **20**.

4.4.1 Reaction of Lithium Tritriptycene Tetrahydrofuran Cobaltate with Oxygen

Complex **15** was reacted with an equimolar amount of oxygen, as shown in scheme 4.9. This experiment was conducted by the addition of 1 molar equivalent of oxygen to a glass ampoule of known volume. In a separate Young's NMR tube, complex **15** was dissolved in THF with agitation. The solution was degassed thrice using the freeze-vac-thaw technique, after which the oxygen in the first ampoule was vac-transferred to the solution containing NMR tube, allowing the THF to freeze. Once the transfer was complete the reaction vessel was allowed to warm to room temperature. Over 16 hours, the colour of the solution changed from a rich royal blue to an emerald green, with no indication of precipitation.

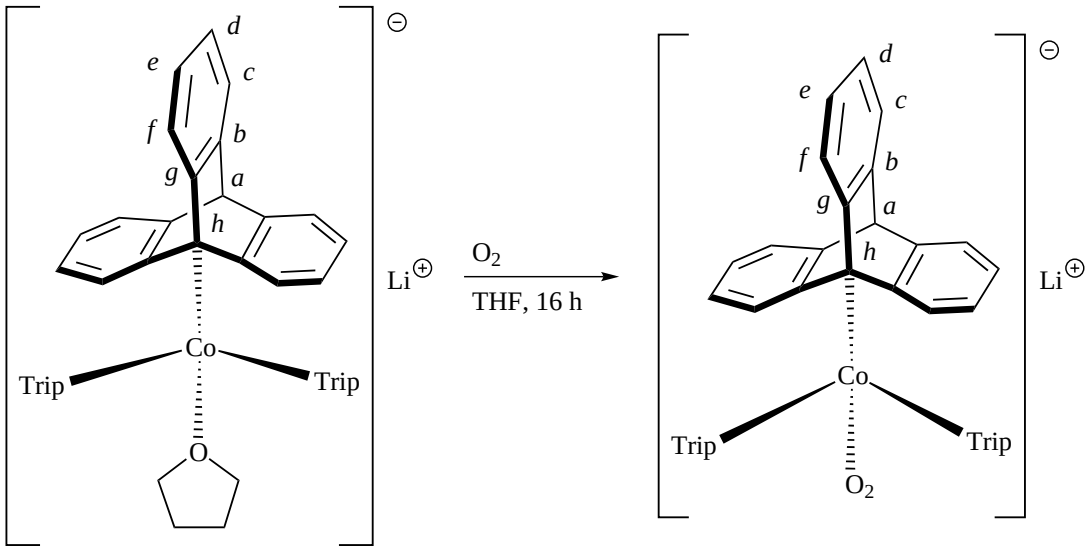

15 **21**

Scheme 4.9. Reaction of lithium tritriptycene tetrahydrofuran cobaltate with oxygen.

The colour change is a clear indication that a reaction has proceeded. Work published by Theopold *et al*. on a similar species suggests that the emerald green colour is indicative of a Co(III) species.[63]

Multinuclear NMR spectroscopy was conducted on complex **21**. Showing signs of paramagnetic line broadening, the spectra are tabulated in table 4.15. It can be seen that compared to the non-oxygenated complex **15**, the signal for proton *a* has been shifted slightly upfield. The same is true for the other signals. Interestingly, the ^{7}Li signal has shifted upfield by 21.43 ppm, suggesting that the lithium atom is in a more shielded environment. It should be noted that the lithium signal is very broad, having a full-width at eighth-maximum of 2.62 ppm (407.5 Hz), indicating its continued association with the complex.

Table 4.15. NMR shifts, integrals and assignments for **21**.

Isotope	Assignment	Shift / δ	Integral
^{1}H	*a*	5.20	1
	c, *d*	6.93–7.25	6
	e	7.44	3
	f	7.55–7.80	3
^{7}Li	-	13.41	-
^{13}C	*a*	55.19	-
	b	124.37	-
	c	125.80	-
	d	146.74	-

Oxygen can bind to metal centres in either a one-electron or two-electron process, forming either a superoxide or peroxide species, respectively. These binding modes, and corresponding data, can be seen in table 4.16. When the oxygen binds to the metal centre, it is oxidised by +1 for the superoxide, and +2 when the peroxide is formed. It is typical for a first-row transition metal to bind oxygen in a one-electron oxidative addition process to form the superoxide, though there are exceptions. Oxygen can also bind in different ways, as shown in figure 4.14. It can bind end on, η^1, or side on, η^2; it can also bridge between two metals, in which case μ is added as a prefix.

Table 4.16. Typical binding modes of molecular oxygen.[337]

Species	Chemical Formula	Bond Order	Stretching Frequency / cm^{-1}
Molecular Oxygen	O_2	2	1555
Superoxide	O_2^-	1.5	1200–1070
Peroxide	O_2^{2-}	1	930–750

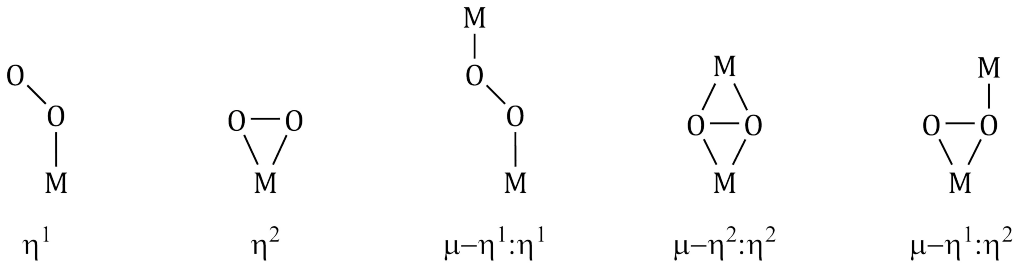

Figure 4.14. Typical binding modes of molecular oxygen.

As suggested in table 4.16, the binding mode of coordinated dioxygen can be determined through Fourier transform-infrared spectroscopy (FTIR) analysis. The FTIR spectrum for the un-oxygenated complex **15** is shown in figure 4.15. The sample was prepared in a glovebox, by preparing a THF solution of complex **15** and pipetting a single drop of the solution onto a salt window. This was allowed to dry before the next drop was added, with the process repeated several times. The dried sample was then placed between a second salt window, and held in place with a vice. The sample was then taken out of the glovebox and immediately run on the FTIR instrument in order to minimise any possibility of atmospheric reactions. The spectral background applied was atmospheric air. Some easily distinguishable features include C−H stretches around 3000 cm^{-1}, aromatic C=C stretches & alkane C−H bending at 1450 cm^{-1}, and THF's strong absorbance at 914 cm^{-1} caused by the C−O stretch.

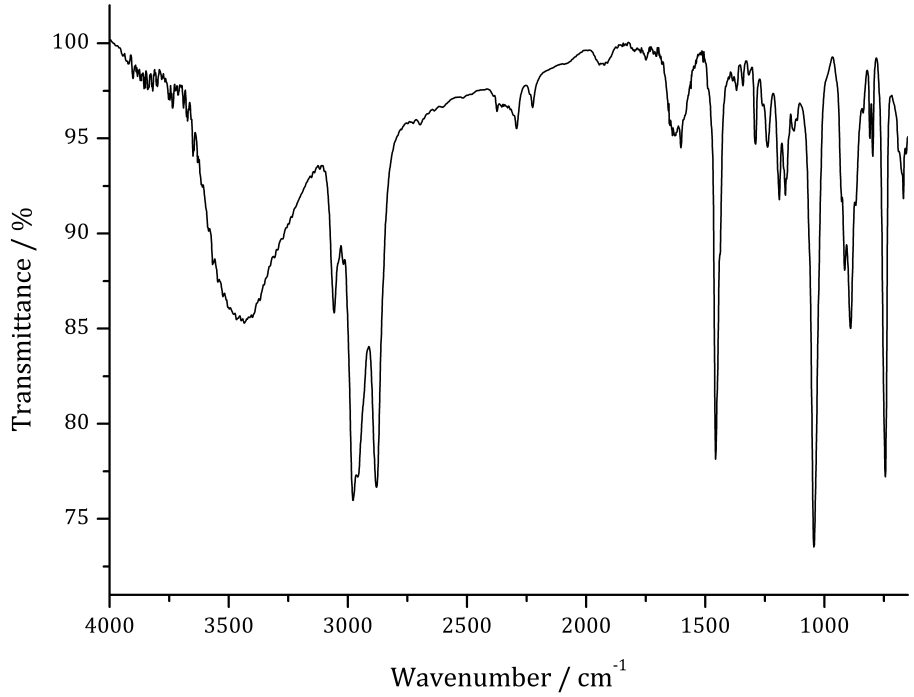

Figure 4.15. The FTIR spectrum of complex **15**. The absorbances at 1640 cm^{-1} and 3400 cm^{-1} are caused by moisture degrading the salt windows.

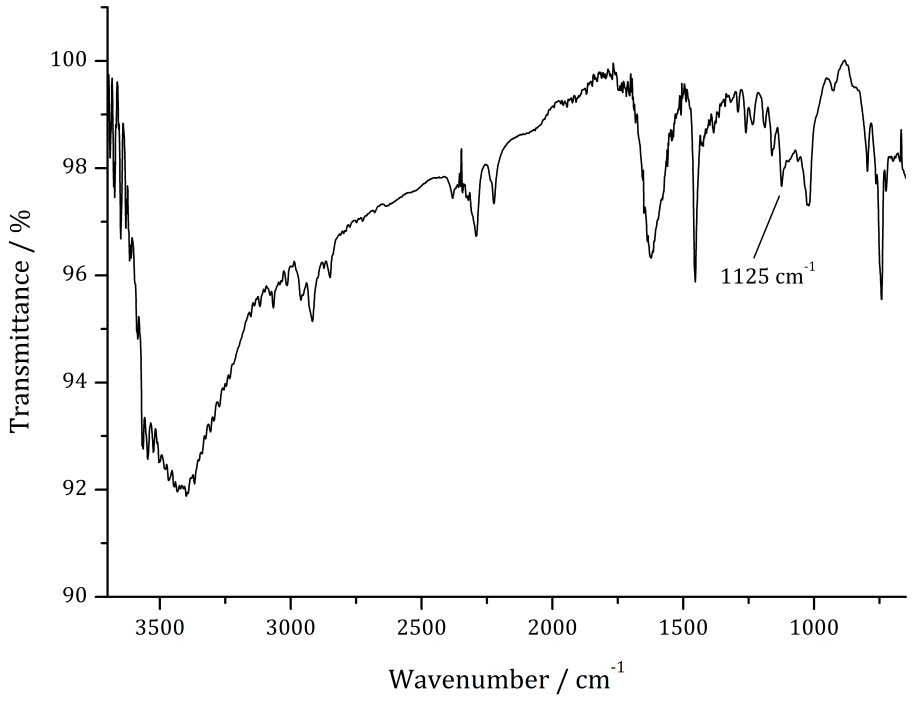

Figure 4.16. The FTIR spectrum of complex **21**. The absorbances at 1640 cm^{-1} and 3400 cm^{-1} are caused by moisture degrading the salt windows.

The FTIR spectrum for the oxygenated complex **21** can be seen in figure 4.16. Some of the same features can be seen, such as the C−H stretches around 3000 cm^{-1} and the aromatic C=C stretches & alkane C−H bending at 1450 cm^{-1}, however there are some important differences. One of these is the loss of the 914 cm^{-1} absorbance, which confirms the loss of coordinated THF. The other important difference is the new peak at 1125 cm^{-1}. Comparing this value to the possible binding modes of dioxygen displayed in table 4.16, this means that the dioxygen has bound η^1 as a superoxide. This binding type for dioxygen is typical for Co(II)/Co(III) species, with several examples previously published in literature.[67,338,339]

Evidence for the tetrahedral nature of complex **21** can be gathered from the UV-visible spectrum, which is shown in figure 4.17. From this spectrum, one can clearly see the leading edge of the charge transfer band at approximately 35 000 cm^{-1}. Also visible are a number of d-d transitions at 14 246 cm^{-1}, 15 059 cm^{-1} and 16 948 cm^{-1}. These are are assigned to the electronic transitions $^3T_1(H) \rightarrow {}^5E(D)$, $^3T_1(H) \rightarrow {}^1T_2(I)$ and $^3T_1(H) \rightarrow {}^1E(I)$ respectively. As the ground state changes this information cannot be used to calculate the ligand field splitting.

Magnetic considerations are important for complex **21**. Cobalt(III) has six d-electrons, which in a tetrahedral ligand field can be situated in either a high-spin or low-spin arrangement. The free-ion ground state term symbol for cobalt(III) is $^5D_4$, which is transformed into ^5E for the high-spin case, and $^3T_1$ for the low-spin case. This is demonstrated in figure 4.18.

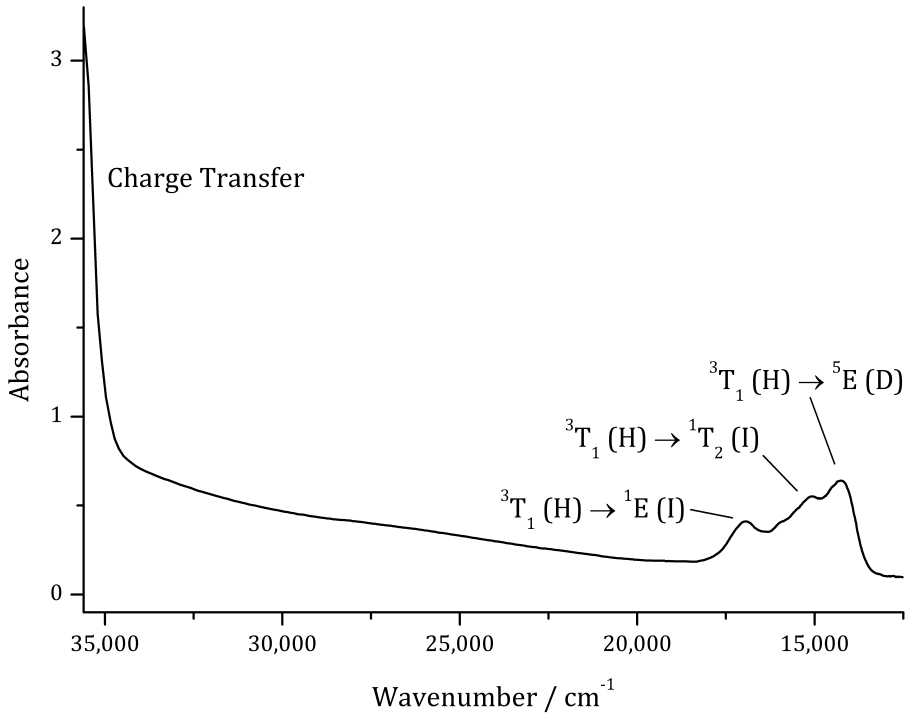

Figure 4.17. Recorded UV-Vis spectrum for complex **21**. Three electronic transitions and the charge transfer band are labelled.

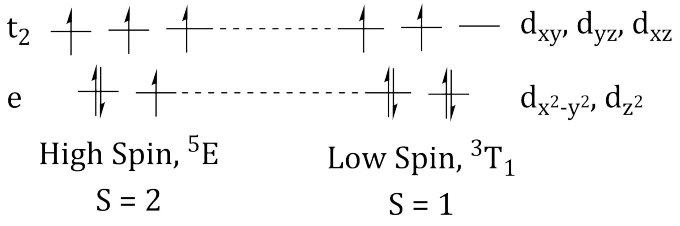

Figure 4.18. High- and low-spin arrangements for d^6 tetrahedral complexes.

Measurement of the magnetic moment of **21** was conducted using the Evans method and equations (4.2) to (4.4). This yielded an effective magnetic moment of 3.77 μ_B, which is higher than the spin-only calculated value for two unpaired electrons (2.83 μ_B), and considerably lower than the spin-only calculated value for four unpaired electrons (4.90 μ_B).

As the low spin arrangement of electrons yields a T state, there will be a considerable contribution to the effective magnetic moment from the unquenched orbital angular momentum. This can be accounted for using equation (4.12), where μ_{s+l} is the spin and orbital magnetic moment with units of Bohr magnetons, μ_B; and L is the total orbital angular momentum quantum number.

$$\mu_{s+l} = \sqrt{4S(S+1) + L(L+1)}\ \mu_B \tag{4.12}$$

For complex **21** in the $^3T_1$ state, the value for S is 1 and the value for L is 2. Using equa-

tion (4.12), this gives a value for μ_{s+l} of 3.74 μ_B, in much better agreement with the experimentally derived effective magnetic moment. This supports the assignment of the low-spin $^3T_1$ state as the ground state, which is consistent with the high-field nature of the triptycene ligands both anticipated, and previously observed experimentally in complexes **15**, **16** and **17**.

Generally, equation (4.12) gives a maximum value for the effective magnetic moment. This is because it assumes that there is no quenching of the orbital angular momentum contribution, which is often untrue. In this case μ_{s+l} matches well with μ_{eff}, which may indicate that there is minimal quenching of the orbital angular momentum, or that there is some quenching in addition to a further contribution towards μ_{eff} from another source, such as ferromagnetism.

In order to determine if complex **21** had some ferromagnetic character, and in order to see if it obeyed Curie behaviour, Curie-Weiss measurements were conducted. This was performed using the Evans method of measuring magnetic susceptibility and Variable Temperature NMR (VT-NMR). Using equation (4.11), the plot shown in figure 4.19 was produced. From this plot the Curie constant and Curie point was determined to be 1.29 emu K mol^{-1} and 70.3 K, respectively.

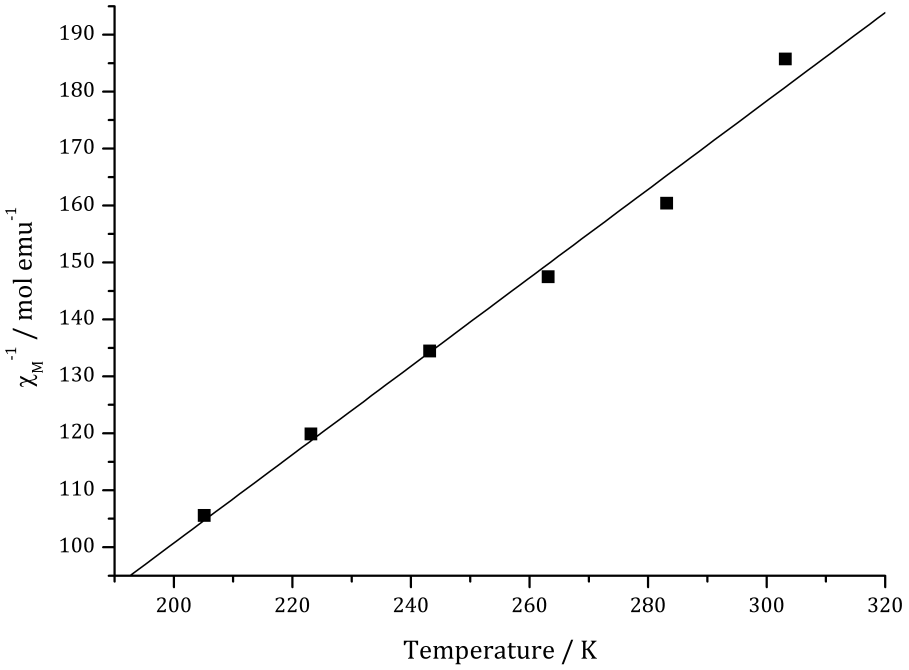

Figure 4.19. Curie-Weiss plot of complex **21**. The line of best fit has a gradient of 0.7762, an intercept of −54.49 and an R^2 value of 0.9834.

A large positive value for the Curie point indicates that complex **21** does exhibit some ferromagnetic behaviour, which will slightly enhance the effective magnetic moment. This was also observed for the cobalt precursor complex **15**. The plot in figure 4.19 exhibits a strong linear relationship, with an R^2 value of 0.9834. This confirms that the complex exhibits Curie behaviour, as

anticipated for paramagnetic complexes.

Complex **15** was also exposed to an excess of oxygen. This yielded the same product, complex **21**, as produced during the equimolar reactions. From this it can be implied that complex **21** is stable to oxygen. Using this information and the known standard redox potentials of dioxygen, superoxide and peroxide (shown in figure 4.20),[340] some details can be obtained about the complexes. For complex **15** to be oxidised by a molar equivalant of oxygen, it must have a redox potential of $\leqslant -0.16$ V; and for complex **21** to be stable in an excess of oxygen, it must have a redox potential of $\geqslant 0.89$ V.

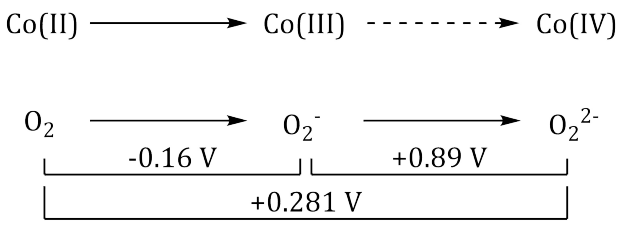

Figure 4.20. A potential diagram for oxygen, and the corresponding cobalt oxidation states. Values taken from Wood.[340]

4.4.2 Lithium Cobalt Tritriptycene Tetrahydrofuran Complex with Other Gases

Attempts were also made to react complex **15** with carbon monoxide, carbon dioxide and nitrogen. Unfortunately, none of these gases reacted with the cobalt complex. A variety of conditions were attempted, including an excess of the gas and overnight heating, though no change in colour or NMR spectra was detected.

The case for nitrogen is not surprising, nitrogen is very well known to be a particularly inert gas. It is so unreactive that nitrogen is often used as the inert gas in Schlenk lines and glove-boxes. However, there is some literature precedence for cobalt to bind atmospheric nitrogen, as first demonstrated by Ikeda *et al*. in 1967 with their tris(triphenyl) cobalt complex.[341] More recently a tris(trimethylsilyl)bipyridine cobalt complex has been shown by Nishibayashi *et al*. to be an effective catalyst for the formation of tris(trimethylsilyl)amine from nitrogen gas.[342]

Cobalt is also well known for binding carbon monoxide. The classic and toxic octacarbonyldicobalt is popular both as a catalyst for carbonylation and also as a precursor for other organocobalt complexes.[343] There are also literature examples of cobalt complexes binding carbon monoxide at atmospheric pressure. An example of this is the trichelating (2-naphthalene-1-ylvinyl)pyridine tetrakis(trimethylphosphine) cobalt complex reported by Beck *et al*., which binds carbon monoxide

at one atmosphere by dissociating the pyridine to become bichelating.[344]

The binding of carbon dioxide to cobalt metal centres is also reported in literature, though it is unusual. An example is potassium ^{n}propyl-salen cobaltate, reported by Floriani *et al*., which coordinates dissolved carbon dioxide in a THF solution at room temperature.[345] Reported by Darensbourg *et al*., a variation on this complex, incorporating 2,4-dinitrophenoxide as a ligand, has also been used in the catalytic synthesis of poly(indene carbonate) using carbon dioxide as a precursor.[346]

A possible reason for complex **15** not reacting with nitrogen, carbon monoxide or carbon dioxide is that the cobalt centre may not be nucleophilic enough. Binding to all of these gases requires a degree of back-bonding to the small molecule's π^* orbitals. If there is insufficient electron density on the metal centre then this will not take place. This is not likely however, as the cobalt is negatively charged and the triptycene ligands will donate electron density to the metal centre.

A more plausible explanation is steric effects. The large bulk of the three triptycene ligands would have made coordination of additional ligands difficult. The orbitals of participating parties need to be able to align correctly for bonding to occur, if steric bulk is preventing this then no reaction can take place.

4.4.3 Other Triptycene Complexes with Small Molecules

Complexes **16**, **17** and **20** were also tested for reactivity with oxygen, nitrogen, carbon monoxide and carbon dioxide. No reactions were observed, despite extended heating. This is likely to be due to a combination of the steric bulk of the triptycene ligands and an insufficient amount of nucleophilicity on the metal centre. This suggests that the anionic nature of complex **15** is the reason it binds molecular oxygen, due to the increased nucleophilicity provided. This property is lacking in the other complexes.

4.5 Conclusions and Future Work

In this chapter, the novel and useful precursor lithium triptycene, **14**, has been synthesised, isolated and fully characterised for the first time. The synthetic approach started with commercially available bromoanthracene, which was converted to bromotriptycene with a modified literature preparation, which was in turn converted to lithium triptycene, using ^{n}BuLi as the lithiating agent. This marks the first time lithium triptycene has been isolated. Characterisation techniques per-

formed on the isolated lithium triptycene involved ^{1}H, ^{7}Li and ^{13}C NMR, EI-MS and a refined crystal structure, solved with an R-factor of 8.99 %. Comparison of the Li−C bond in the crystal structure showed that the bond was slightly shorter than in those reported for crystalline ^{n}BuLi and ^{t}BuLi, implying more covalent bonding character. This was investigated with computational calculations, which showed that the HOMO of lithium triptycene is delocalised around the Li−C bond, whilst the LUMO is almost entirely localised to the lithium, reinforcing the idea of the polar nature of the covalent Li−C bond.

Lithium triptycene was then used as a sterically bulky ligand for the synthesis of sterically-hindered metal centres. The first example used cobalt dichloride as the metal precursor, reacting with three equivalents of lithium triptycene to yield the tetrahedral, anionic complex **15**. Complex **15** was fully characterised by ^{1}H, ^{7}Li and ^{13}C NMR, ESI-MS and UV-Visible spectroscopy. From the UV-Visible spectrum it was possible to assign the electronic transitions (d-d electron excitations). The effective magnetic moment of complex **15** was determined, with a Curie plot also conducted at varying temperatures. This revealed a moderately sized positive value for the Curie point. This contrasts with the only other published sterically hindered monomeric CoR_x system, where the Co^{II} species was never synthesised, only Co^{III}, Co^{IV} and Co^{V}.

Tetrahydrofuran ditriptycene iron, complex **16**, was synthesised from the reaction of two equivalents of lithium triptycene with anhydrous iron dichloride in THF. Multinuclear NMR analysis was conducted on the complex, as well as EI-MS, suggesting the trivalent form. It was possible to grow X-ray quality crystals of complex **16**, and a crystal structure was resolved with an R-factor of 6.61 %. From this, the structure was confirmed to be distorted trigonal planar, with symmetry group C_s. Magnetic studies showed the complex has two unpaired electrons, meaning the large ligand-field exhibited by the triptycene ligands result in a low-spin system. The crystal structure shows a deviation from the plane of 3.75°. It is this deviation which causes the change from C_{2v} to C_s, giving the two unpaired electrons.

The synthesis of tetrahydrofuran tritriptycene chromium, complex **17**, was conducted by reacting three equivalents of lithium triptycene with chromium trichloride tetrahydrofuran adduct, in benzene. NMR was used for characterisation, though there were no signals visible in the ^{13}C spectrum. ESI-MS was also conducted, confirming the tetrahedral nature of the complex. The effective magnetic moment of complex **17** was measured, revealing a single unpaired electron. This implies a low-spin tetrahedral complex, as observed in other triptycene complexes. Whilst these systems are unusual, this is explained by the large ligand-field of the tertiary carbanion.

Using tetrachlorozirconium as a precursor, the reaction with two equivalents of lithium triptycene in THF yielded tetravalent zirconium, complex **20**. ^{1}H and ^{13}C NMR was conducted on the compound, in addition to EI-MS, confirming its identity. Zirconium has five naturally occurring metastable isotopes, four of which are more than 10 % naturally abundant. Combined with the diisotopic nature of chlorine, this created a large number of m/z values for each fragment, which were visible in the mass spectrum. Complex **20** contains zirconium in its +4 oxidation state, giving the metal centre a d-electron count of zero.

The ionic cobalt triptycene complex, **15**, was reacted with an equimolar quantity of oxygen gas in order to investigate its reactivity with small molecules. On exposure, the solution of complex **15** changed from a royal blue to an emerald green, forming complex **21**. Full ^{1}H, ^{7}Li and ^{13}C NMR was conducted on the sample, which indicated a change in magnetic environment. In order to identify the binding mode of the dioxygen, an FTIR spectrum was taken of complex **21** and compared to that of complex **15**. This both confirmed the loss of coordinated THF, as well as the η^1 superoxide binding of the dioxygen. A UV-Visible spectrum was acquired, and the electronic transitions were determined and assigned. The effective magnetic moment of complex **21** was calculated using the Evans method. This showed, in combination with the Curie plot, that the compound is also an example of a low-spin tetrahedral complex. There is considerable contribution to the effective magnetic moment from the orbital angular momentum, resulting from the electronic ground state being $^{3}T_1$.

By comparing the redox potentials of oxygen, superoxide and peroxide, it was determined that complex **15** has a redox potential of $\leqslant -0.16$ V. It was equally determined that complex **21** has a redox potential of $\geqslant 0.89$ V. This gives a potential two electron Co(II)/Co(IV) redox couple of $\geqslant 1.05$ V, which is comparable, though slightly under, the required minimum redox couple of 1.23 V for splitting water. The previously mentioned cobalt phosphate complex reported by Nocera *et al.* used a multistep Co(II)/Co(IV) redox coupling of ~1.3 V.[53]

Other small molecules were also investigated with complex **15**. These attempts showed no sign of reaction, either in the NMR spectra or in colour. The complexes **16**, **17** and **20** were also surveyed for reactions with oxygen and other small molecules, but showed no reactivity.

With further work, it should be possible to obtain crystal structures of the other ligated metal complexes. This could be achieved by varying the crystallisation conditions, including solvent, temperature and diffusion mode. The formation of more reactive species should also be attempted using different metal precursors. By starting with a metal in a higher oxidation state, such as iron

trichloride, new species could be formed. Alternatively, it may be possible to reduce or oxidise the existing complexes to more extreme oxidation levels, using KC_8 or sodium amalgam to reduce, and ferrocenium hexafluorophosphate or a triarylaminium radical cation to oxidise.

Successful synthesis of a cobalt(II) and cobalt(III) complex with the high-field and sterically large triptycene ligand shows a marked difference to Theopold's work.[61,63] His norboryl ligand could only be used to access cobalt(III) and cobalt(IV). It appears that using triptycene, a cobalt(IV) complex is inaccessible. This leaves a molecular model of Nocera's cobalt(II/III/IV) catalyst[52] still out of reach.

Chapter 5

Synthesis and Reactivity of Phosphate Complexes

This chapter uses inspiration from an existing heterogeneous cobalt oxide catalyst to design a homogeneous molecular catalyst. The aim is to synthesis new model complexes of an existing water-splitting catalyst. This allows for the easy tuning and control of the electronic and catalytic properties. Additionally, a new and better understanding of the original system can be obtained by taking advantage of the increased number of *in situ* analysis techniques available in the solution phase.

5.1 Attempted Silylphosphate Ligand Synthesis

Leading on from the work of Nocera (see section 1.3.1),[52] it was postulated that the active catalytic site on the surface of the cobalt catalyst could be reproduced as a molecular species, and study of the resulting activity could direct future research directions. Silyl ligands have been previously used as surface mimics,[64] and so initial investigations began with them.

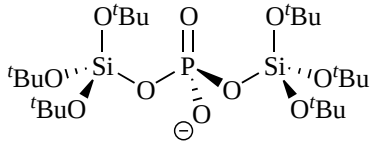

22

Figure 5.1. The designed silylphosphate ligand for a cobalt metal centre, **22**.

The designed surface mimic needed to be bulky, in order to simulate the surface bulk of a heterogeneous catalyst. As it would be likely to be bound to silica as a support, it should include silyl groups in order to mimic the electronic properties of the future surface-bound catalyst. The active species in the original work was cobalt phosphate, so cobalt was chosen as the metal centre. Compound **22**, shown in figure 5.1, is the designed ligand. It incorporates the silyl and phosphate

motifs, as well as including a large amount of steric bulk from the *tert*-butyl groups.

Synthesis of the ligand began from the commercially available silanol, tris(*tert*-butoxy)silanol, **23**. This was then reacted in equimolar quantities in a salt metathesis reaction with potassium hydride, to form potassium tris(*tert*-butoxy)silanolate, **24**. This was found to proceed with excellent yields.

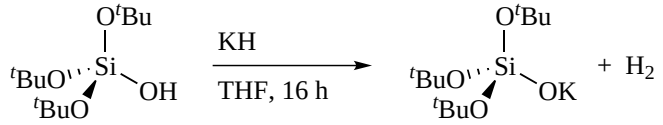

23 **24**

Scheme 5.1. Synthesis of potassium tris(*tert*-butoxy)silanolate, **24**.

Attempts were then made to attach compound **24** to a source of phosphorus. Initially, phosphorus trichloride was used, with an intent to then oxidise to the phosphorus(V) species with oxygen or potassium chlorate at a later stage. Unfortunately, using this approach proved infeasible due to the mix of species that was formed. Even a dropwise addition of a very dilute solution of compound **24** to phosphorus trichloride, at −78 °C, over six hours with rapid stirring produced a large mixture of the mono-, bis- and tris-substituted products, as demonstrated in scheme 5.2. Solvent buffers were also attempted, with no success. Once formed, it was not possible to separate the mixture of substituted products. An alternative synthetic approach using diethyl phosphite also proved unfruitful.

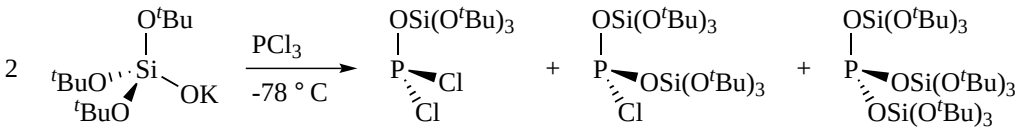

24

Scheme 5.2. Reaction of compound **24** with PCl_3, yielding a mix of inseparable, substituted products.

It is possible that the substituted species were inter-reacting, causing a distribution of coordination. Consequently a different approach was taken, using phosphorus oxybromide as the phosphorus source. This has two advantages over the use of phosphorus trichloride, firstly the phosphorus is already in the +5 oxidation state, removing the requirement for the subsequent oxidation; and secondly the loss of the lone pair would hinder the nucleophilic substitution (S_N2) reaction causing the mixture of products. Shown in scheme 5.3, the dropwise reaction proved successful, with the desired product, **25**, formed in excellent yield with no creation of undesired by-products. The formed potassium bromide was easily removed by filtration.

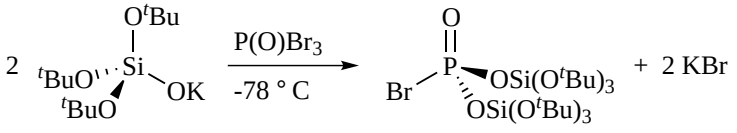

24 **25**

Scheme 5.3. Synthesis of the desired silyl phosphorobromidate species, with no undesired by-products.

With the successful synthesis of compound **25**, the next step was hydrolysis to the corresponding phosphate, **26**, which could then be converted to a potassium salt, **27**, allowing easy coordination to the cobalt metal centre. This is demonstrated in scheme 5.4.

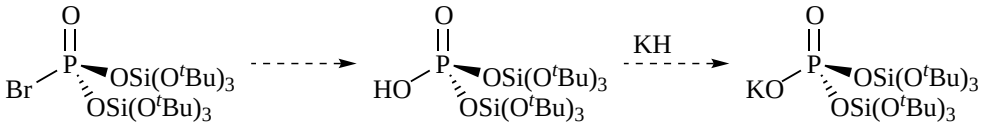

25 **26** **27**

Scheme 5.4. Proposed synthesis of the desired silylphosphate, **26**, and related potassium salt, **27**.

Unfortunately, the first step proved to be problematic. It was initially thought that hydrolysis to the silylphosphate could be achieved by reacting compound **25** with an equimolar amount of NaOH under anhydrous conditions, formed by reacting sodium metal with a precise amount of water. This unfortunately only produced an insoluble white precipitate, with no phosphorus species in the resulting supernatant (tested by ^{31}P NMR). Solvents tested for sample solubility include acetone, benzene, diethyl ether, hexane, isopropanol, methanol, pentane, pyridine, THF, toluene and water.

Pyridine hydroxide was tested as an alternative hydroxylating agent, this however, produced the same result. An equimolar amount of water was then tested, both with and without a catalytic amount of potassium iodide in order to help ion-exchange. This also produced the same insoluble white powder. Both an excess of water in pyridine and aqueous NaOH were also tested, both yielding the same result.

The insoluble white powder from each attempt was submitted for EI-MS analysis in order to identify them, however no signal was observed from the samples. The EI process heats the sample to several hundred degrees Celsius, so a complete lack of signal suggests a highly non-volatile species. Attenuated-total-reflectance-FTIR (ATR-FTIR) was also conducted on each of the samples, with each sample giving the same result. A typical collected spectrum is shown in figure 5.2.

The strong absorbances at 1002 cm^{-1}, 1068 cm^{-1} and 1156 cm^{-1} (visible as a shoulder) are characteristic of Si−O, P−O and P=O stretches, respectively. These stretches show that the white

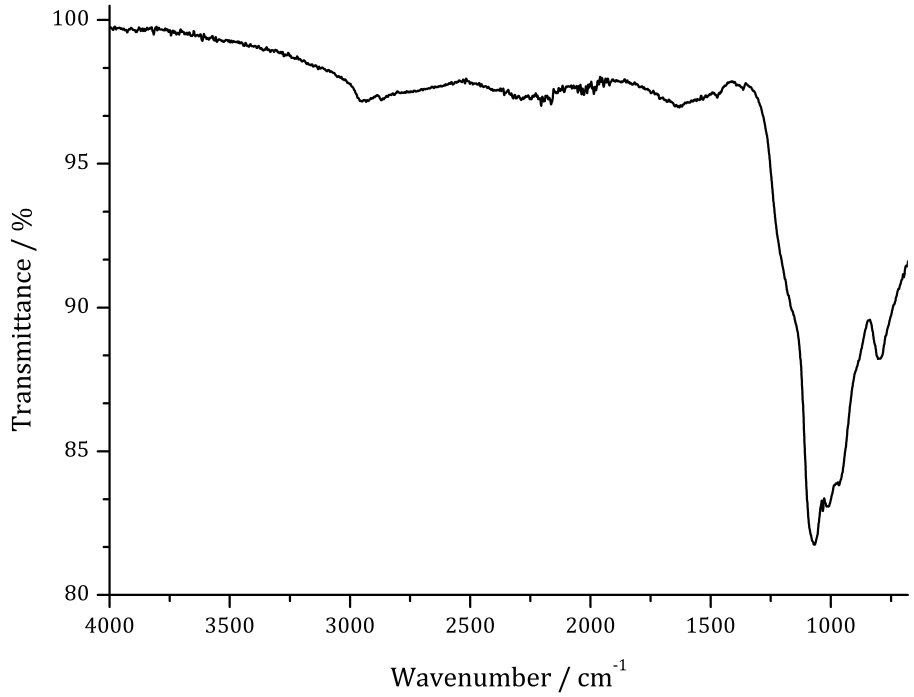

Figure 5.2. ATR-FTIR spectrum of the insoluble powder produced during the attempted synthesis of the silylphosphate ligand.

powder is a silicon phosphate species. The moderate absorbance at 796 cm^{-1} is typical of both C−H rocking and a C=C bend, though the expected accompanying C=C asymmetric stretch at ~2000 cm^{-1} is missing. The broad weak absorbance at ~2922 cm^{-1} is characteristic of a C−H stretch, and the lack of any defined absorbances greater than 3000 cm^{-1} suggests an absence of alkenes. The other conspicuously missing absorbance is the *tert*butyl CH_3 symmetric deformation at ~1364 cm^{-1}.[347] The P−Br stretch occurs at approximately 408 cm^{-1},[348] which is below the detection limit of the machine due to the ATR-crystal used.

Using a combination of the ATR-FTIR data and the extremely low volatility discovered from the EI-MS, it is believed that the insoluble white powder formed is inorganic phosphosilicate. This would explain the lack of C−H stretching in the infrared spectrum. There is some literature precedence for the deposition of phosphosilicate using the hydrolysis of phosphorus oxychloride and organosilicates.[349,350] Generally when synthesising inorganic phosphosilicates, the samples require annealing at several hundreds of degrees Celsius, however it has been shown that inorganic phosphosilicates can form from the room temperature reaction between phosphorus oxychloride, organosilicates and water. It is therefore suggested that the intra- and intermolecular reaction of compound **26** would be facile, leading to decomposition and subsequent precipitation of phosphosilicates. This marks a new, easy and highly adaptable pathway for the synthesis of phosphosilicate

glass ($SiO_2 \cdot P_2O_5$). By modifying the precursors, or by adding dopants, it could be possible to easily synthesis a range of phosphosilicate glasses with varying properties.

5.2 Phosphate Ligand Synthesis

Due to the complications that arose from the silylphosphate ligand, it was decided to pursue bulky phosphate ligands instead. By maintaining the necessary bulk, large phosphates would be a good surface mimic, and the essential phosphate element would still be present to provide catalytic activity.

5.2.1 Dibutyl Phosphate

Dibutyl phosphate (DBP), **28**, was chosen as a potential ligand due to its long alkyl chain and commercial availability. It was hoped that the alkyl chain would provide a convenient NMR handle to aid in characterisation and monitoring. The DBP was deprotonated using potassium hydride to give the potassium salt, **29**, shown in scheme 5.5. The reaction proceeds very quickly, liberating hydrogen gas at speed. Whilst the reaction rate drops substantially after a few hours, the reaction was left overnight to allow it to go to completion.

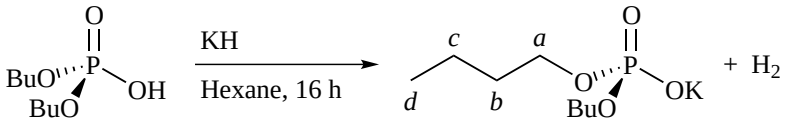

28 **29**

Scheme 5.5. Synthesis of potassium diphenyl phosphate, **29**.

Once the reaction was complete, the solution was reduced *in vacuo* and the white powder dried, before being characterised. The multinuclear NMR signals are tabulated in table 5.1. It can be seen that the individual CH_2 and CH_3 groups are easily discernible, moving downfield as the nuclei becomes more deshielded by the electronegative nature of the oxygen. This phenomenon can be observed in both the ^1H and ^{13}C NMR spectra. The phosphorus signal measured at 0.17 ppm is not unexpected, as compound **29** is similar to the phosphorus NMR reference compound phosphoric acid ($\delta = 0.00$ ppm).

Negative-ion ESI-MS was also performed on compound **29**. The main signal recorded equated to an M^- of 209.0935 m/z, corresponding to the negative ion of compound **29**, $C_8H_{18}O_4P^-$, formed by the loss of K^+. This is the expected ionisation pattern for the potassium salt.

Table 5.1. NMR shifts, integrals and assignments for **29**.

Isotope	Assignment	Shift / δ	Integral
^{1}H	*d*	1.09	3
	c	1.61	2
	b	1.85	2
	a	4.16	2
^{13}C	*d*	14.30	-
	c	19.73	-
	b	33.70	-
	a	163.48	-
^{31}P	-	0.17	-

5.2.2 Bis(2-ethylhexyl) Phosphate

Bis(2-ethylhexyl) phosphate (BEHP), **30**, was also investigated as a ligand, due to it being highly prolific. BEHP is synthesised on an industrial scale from 2-ethylhexanol, which is used on a yearly megaton scale for multiple purposes. BEHP itself is used in the mineral extraction of uranium and other rare earth metals, making it readily available and therefore cheap.

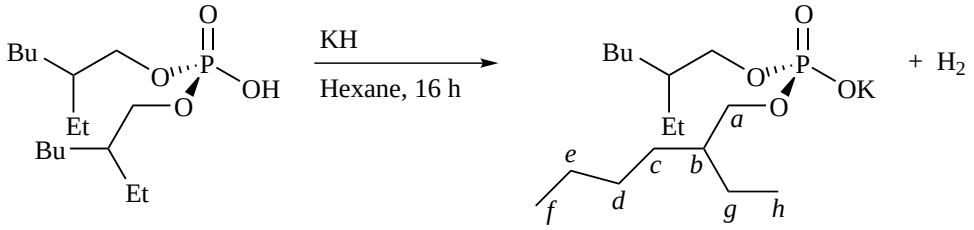

30 **31**

Scheme 5.6. Synthesis of potassium bis(2-ethylhexyl) phosphate, **31**.

The deprotonation of BEHP was achieved using potassium hydride in hexane, as shown in scheme 5.6. During the deprotonation the solution became extremely viscous due to the insolubility of compound **31** in hexane. Once complete, the reaction mixture was reduced *in vacuo* and the product taken up in THF, before being filtered and dried *in vacuo*. Despite extensive drying, this technique gave a sticky and gelatinous solid, which was difficult to work with. In an attempt to desolvate the product, the compound was frozen with liquid nitrogen, in a Schlenk tube, under a fast flowing stream of argon. Once at temperature, the solid was granulated using a spatula. The Schlenk tube was then sealed and placed under vacuum simultaneously, whilst allowing the vessel to warm to room temperature under active vacuum. This process was repeated three times, yielding a free-flowing white powder.

Compound **31** was dried, and analysed by multinuclear NMR. The resulting signals are shown in table 5.2. It can be seen that, due to the nature of the 2-ethylhexyl alkyl chain, there are many overlapping proton signals. In particular, the signals at 1.02 ppm and 1.45 ppm were composed of complex multiplets with extreme overlapping, making deconvolution of the individual signals difficult.

Table 5.2. NMR shifts, integrals and assignments for **31**.

Isotope	Assignment	Shift / δ	Integral
^{1}H	*f* & *h*	1.02	6
	c, *d*, *e* & *g*	1.45	8
	b	1.77	1
	a	4.10	2
^{13}C	*h*	11.10	-
	f	14.27	-
	e	23.36	-
	g	23.67	-
	d	29.27	-
	c	30.37	-
	b	40.49	-
	a	69.72	-
^{31}P	-	0.44	-

Negative-ion ESI-MS was also conducted on compound **31**. The acquired spectrum showed an M^- ion of 321.2176 m/z, which corresponds to $C_{16}H_{34}O_4P^-$. This is the phosphate anion formed by the loss of the potassium atom.

5.2.3 Diphenyl Phosphate

Diphenyl phosphate (DPP), **32**, was investigated as a potential ligand because the *para* proton was expected to provide a useful and convenient NMR handle. Equally, the *ortho* and *meta* protons were expected to provide a clear signal, each in a 2:1 ratio with the *para* proton. Compound **32**, was initially synthesised using a modified literature preparation;[351] reacting phosphorus oxychloride with phenol to produce diphenyl phosphorochloridate, which was then hydrolysed using water/acetone to yield DPP, as shown in scheme 5.7. The full synthetic procedure can be seen in section 6.4.12.

Using benzene as the solvent, DPP was then deprotonated with potassium hydride to yield potassium diphenyl phosphate, **33**, shown in scheme 5.8. It was discovered that compound **33** is very poorly soluble in most solvents, with the most solvating solvent being THF, which it was

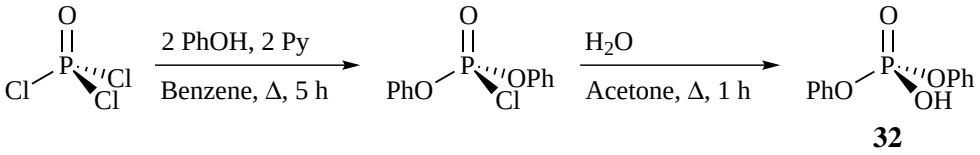

Scheme 5.7. Synthesis of diphenyl phosphate, **32**.

slightly soluble in. Conveniently, this allowed for the liberal washing of the product with multiple solvents.

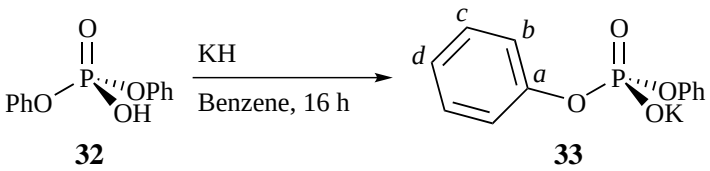

Scheme 5.8. Synthesis of potassium diphenyl phosphate, **33**.

By heating compound **33** in an NMR tube, it was possible to get a sample concentrated enough for NMR analysis. The tabulated signals are shown in table 5.3. From this it can be seen that the *para* proton, *d*, does indeed provide a clear and convenient NMR handle.

Table 5.3. NMR shifts, integrals and assignments for **33**.

Isotope	Assignment	Shift / δ	Integral
^{1}H	*d*	6.93	1
	c	7.15	2
	b	7.21	2
^{13}C	*b*	119.83	-
	d	124.30	-
	c	128.65	-
	a	152.53	-
^{31}P	-	−11.58	-

Negative-ion ESI-MS was conducted on compound **33** by heating the sample to aid solubility. A peak was observed at 249.0303 m/z corresponding to $[C_{12}H_{10}O_4P]^-$. This is the fragment formed from the loss of the potassium atom. In order to confirm the full deprotonation of compound **33**, FTIR analysis was performed. DPP, **32**, has a characteristic vibration at 2567 cm^{-1} caused by the P−O(H) group.[352] This was found to be completely absent from the collected FTIR spectrum of compound **33**, indicating complete conversion of compound **32** to **33**.

5.3 Cobalt Phosphate Complexes

The ligation of the cobalt metal centre was performed using a metathesis reaction between a potassium phosphate and a cobalt halide. Anhydrous cobalt chloride was used for the cobalt precursor due to its cost and ease of use. The phosphate would displace the halide, precipitating potassium chloride as a by-product, which drives the reaction to completion. A general scheme for this reaction is shown in scheme 5.9.

Scheme 5.9. General reaction scheme for the synthesis of cobalt phosphates. R = Bu, 2-ethylhexyl, Ph; X = Cl, I.

5.3.1 Bis(dibutyl Phosphate) Cobalt

Bis(dibutyl phosphate) cobalt, **34**, has been reported once in the literature previously. The slightly brutal technique employed by Kantacha and Wongnawa[353] in 1987 involved dissolving hydrated $CoCl_2$ into tributyl phosphate, using the tributyl phosphate both as the reactant and solvent. The solution was then refluxed at 289.6 °C for four hours, before removing the unreacted tributyl phosphate by vacuum distillation, at 180 °C for 16 hours. No NMR characterisation data was reported.

For this work, complex **34** was synthesised by reacting two equivalents of compound **29** with anhydrous cobalt chloride, by dropwise addition over several hours, with THF as the solvent. THF solvated cobalt chloride is light blue in colour, and throughout the duration of the reaction the colour was noted to change to a cloudy deep royal blue. The reaction mixture was then filtered to remove the precipitated KCl salt, before being reduced *in vacuo* to yield bis(dibutyl phosphate) cobalt, **34**, as a smooth, dry, royal blue paste. The reaction is shown in scheme 5.10.

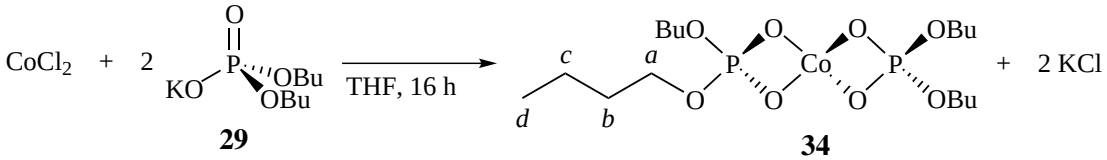

Scheme 5.10. Synthesis of bis(dibutyl phosphate) cobalt, **34**.

Multinuclear NMR spectroscopy was used for characterisation of complex **34**, which has been summarised in table 5.4. The complex has good solubility in aromatic solvents, and so deuterated benzene was chosen for the NMR solvent. The cobalt(II) metal centre is paramagnetic, causing line

broadening in the spectra. This phenomenon becomes more pronounced as the distance between the resonating protons and the cobalt centre is reduced. Consequently, the signal from proton environment *a* has substantial line broadening of 3.5 ppm (1396.9 Hz) for full-width at eighth-maximum. There are no signals observed for either ^{13}C or ^{31}P nuclei, which is not uncommon for paramagnetic complexes due to the line broadening becoming extreme enough to render signals indistinguishable from the background noise. Paramagnetic cobalt complexes regularly do not display large signal shifts, often resulting in the large signal broadening being the only observable paramagnetic effect.[354]

Table 5.4. NMR shifts, integrals and assignments for **34**.

Isotope	Assignment	Shift / δ	Integral
^{1}H	*d*	0.23	3
	c	0.69	2
	b	1.68	2
	a	5.62	2

Attempts were made to analyse complex **34** by both EI-MS and ESI-MS. Unfortunately, the complex was too thermally unstable to undergo EI without degrading. Without an easily ionisable ligand, or a halide to fragment, ESI-MS also proved inconclusive.

Complex **34** has cobalt in the +2 oxidation state, making it a d^7 metal centre. This gives cobalt a free-ion term symbol of $^{4}F_{9/2}$. In complex **34**, the cobalt is in a d^7 populated tetrahedral ligand field, the splitting diagram for which is shown in figure 4.4 in chapter 4, giving it a ground state of $^{4}A_2$.

Magnetic susceptibility measurements were taken using the Evans method, as described in chapter 4. Using the spin-only equation, equation (4.5), a spin-only magnetic moment of 3.87 μ_B is calculated for complex **34**. This is slightly below the observed effective magnetic moment of 4.26 μ_B.

Having a ground state of $^{4}A_2$, it is expected for the ligand to have minimal orbital-contribution to the magnetic moment. However, the spin-only value can be improved upon by taking into account the Zeeman effects, using equations (4.6) and (4.7). For an average field-splitting Co(II) complex, a value of 5000 cm^{-1} has been taken for the crystal field splitting, Δ.[320] As shown in equation (5.1), this gives a calculated effective magnetic moment of 4.40 μ_B, in good agreement with the experimental value. For ease of viewing, the observed and calculated magnetic moments are displayed in table 5.5.

$$\mu_{\text{calc}} = \left(1 - \frac{4\lambda}{\Delta}\right)\mu_{\text{so}} = \left(1 - \frac{4(-515/3)}{5000}\right)3.87 = 4.40\,\mu_{\text{B}} \tag{5.1}$$

Table 5.5. Observed and calculated effective magnetic moments for complex **34**.

Method	Equations Used	Effective Magnetic Moment / μ_{B}
Observed	(4.2) to (4.4)	4.26
Spin-only	(4.5)	3.87
Zeeman Effects	(4.6) to (4.8)	4.40

5.3.2 Bis(bis(2-ethylhexyl) Phosphate) Cobalt

Bis(bis(2-ethylhexyl) phosphate) cobalt, **35**, was synthesised in a similar manner as the previous cobalt phosphate. Shown in scheme 5.11, two equivalents of compound **31**, solvated in THF, were added dropwise to a stirring solution of $CoCl_2$ over a period of one hour, the reaction was then left to go to completion overnight. During this time a large amount of white precipitate formed, and the solution became a deep royal blue. The reaction mixture was then filtered to remove the KCl and reduced *in vacuo* to yield the product as a royal blue solid.

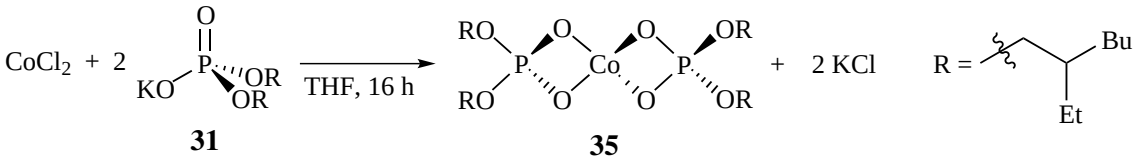

31 **35**

Scheme 5.11. Synthesis of bis(bis(2-ethylhexyl) phosphate) cobalt, **35**. R = 2-ethylhexyl.

The product was then analysed by NMR, and the ^{1}H NMR spectrum is shown in figure 5.3. The ^{13}C and ^{31}P NMR spectra showed no signals due to the paramagnetic nature of the complex. In figure 5.3, the single sharp signal at 7.16 ppm is C_6D_6, used as the reference. The large collection of signals that can be seen are extremely overlapping due to the paramagnetic broadening and highly similar proton magnetic environments. This paramagnetically-induced overlap makes deconvolution of the signals very difficult.

The synthesis of complex **35** was also attempted with CoI_2. Due to the different cobalt precursor, the reaction started a dark green colour, before turning the same royal blue as with the $CoCl_2$ precursor. This further suggests that no halides remain coordinated to the cobalt. After filtering the solution and reducing *in vacuo*, the reaction mixture produced the same ^{1}H NMR as the $CoCl_2$ reaction shown in scheme 5.11. Despite washings and recrystallisation attempts, the NMR spectrum could not be improved.

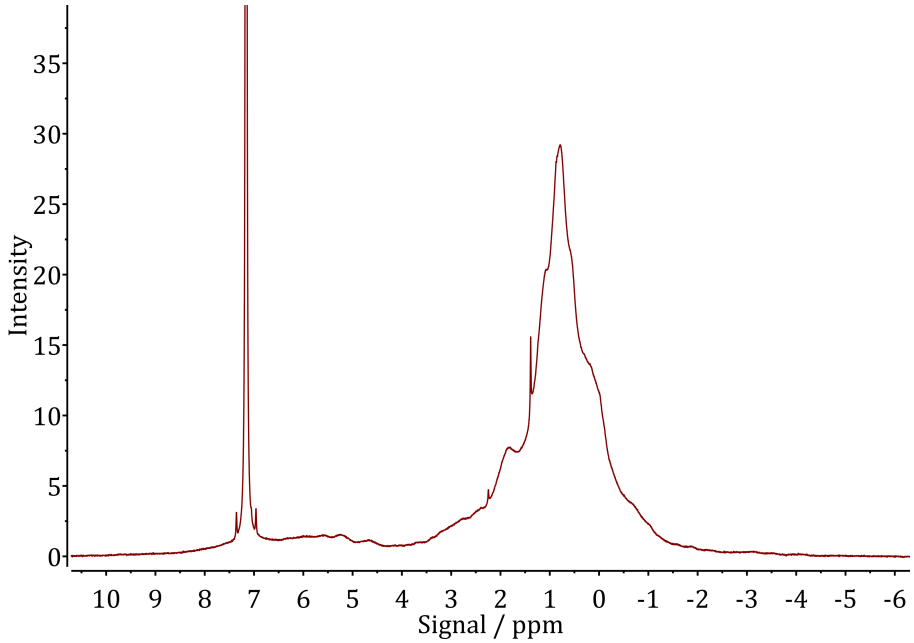

Figure 5.3. ^{1}H NMR spectrum of complex **35**. The sharp solvent signal at 7.16 ppm is C_6D_6, used as the reference. The large collection of overlapping signals is caused by the highly similar proton magnetic environments.

The lack of ^{13}C NMR signals, due to the paramagnetic nature of complex **35**, meant that using two-dimensional NMR techniques such as HSQC and HSBC to assign the ^{1}H NMR spectrum was not possible. As with complex **34**, both EI-MS and ESI-MSI proved inconclusive due to thermal decomposition and low ionisation potential, respectively.

Due to these difficulties, it was determined that the benefits of this compound were outweighed by the complications. Therefore, it was decided prudent to no longer proceed with this complex, and to focus efforts elsewhere.

5.3.3 Bis(diphenyl Phosphate) Cobalt

As with the previous cobalt phosphate complexes, bis(diphenyl phosphate) cobalt, **36**, was synthesised using a metathesis reaction between anhydrous cobalt chloride and the appropriate potassium salt, compound **33**. Cobalt chloride was first dissolved in THF with rapid stirring, before a suspension of compound **33** in THF was added. Compound **33** is only sparingly soluble in THF, however as the solvated compound is ligated more of the starting material is drawn into solution, allowing the reaction to proceed to completion. This effect has the additional feature of controlling the rate of reaction, as only a small amount of ligand is dissolved at any point in time.

Shown in scheme 5.12, the reaction produces potassium chloride as a by-product, which is removed by filtration before reducing *in vacuo* to yield a bright blue solid. The solid was washed

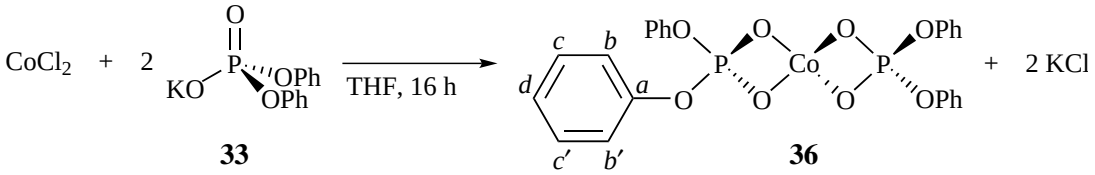

Scheme 5.12. Synthesis of bis(diphenyl phosphate) cobalt, **36**.

with a small amount of cold THF and pentane, before being dried *in vacuo*. The product was readily soluble in THF after extended stirring, unlike the two starting materials, and so multinuclear NMR analysis was conducted in THF-d_8. The collected ^{1}H NMR signals are shown in table 5.6; no signals were detected for either ^{13}C or ^{31}P nuclei, as anticipated for these paramagnetic complexes.

Table 5.6. NMR shifts, integrals and assignments for **36**.

Isotope	Assignment	Shift / δ	Integral
^{1}H	b, b' & d	7.32	3
	c	9.19	1
	c'	11.09	1

The ^{1}H NMR for complex **36** show two broad signals and one very broad signal, all overlapping. The very broad signal has a full-width at eighth-maximum of 4.53 ppm (1807.9 Hz). Despite the overlapping, due to the reduced number of signals and their comparatively increased spacing, deconvolution of the signals was possible by fitting three Lorentzian functions to the spectrum. Lorentzian functions provide an idealised line-shape of a processed spectrum, and so are often used to model NMR signals.[355] A Lorentzian function is shown in equation (5.2); where γ is the half-width at half-maximum, and x_0 is the peak of the distribution. By integrating under these functions, the integrals of the respective signals can be found.

$$f(x; x_0, \gamma) = \frac{1}{\pi\gamma}\left(\frac{\gamma^2}{(x - x_0)^2 + \gamma^2}\right) \tag{5.2}$$

The fitted spectrum can be seen in figure 5.4, where the maroon line is the observed signal, the blue line is the calculated fits, the purple line is the summation of the fits, and the red line is the residual. In the spectrum the three convoluted signals can be seen, as well as the THF solvent peaks.

The integrals, shown in table 5.6, have a signal integration ratio of 3:1:1. The signal with an integral of 3 at 7.32 ppm has been assigned to the *ortho* and *para* protons. The large broadness of the signal indicates that the responsible protons are in close proximity to the metal centre (*i.e.* the *ortho* position), and the delocalised nature of the phenyl ring means that the paramagnetic

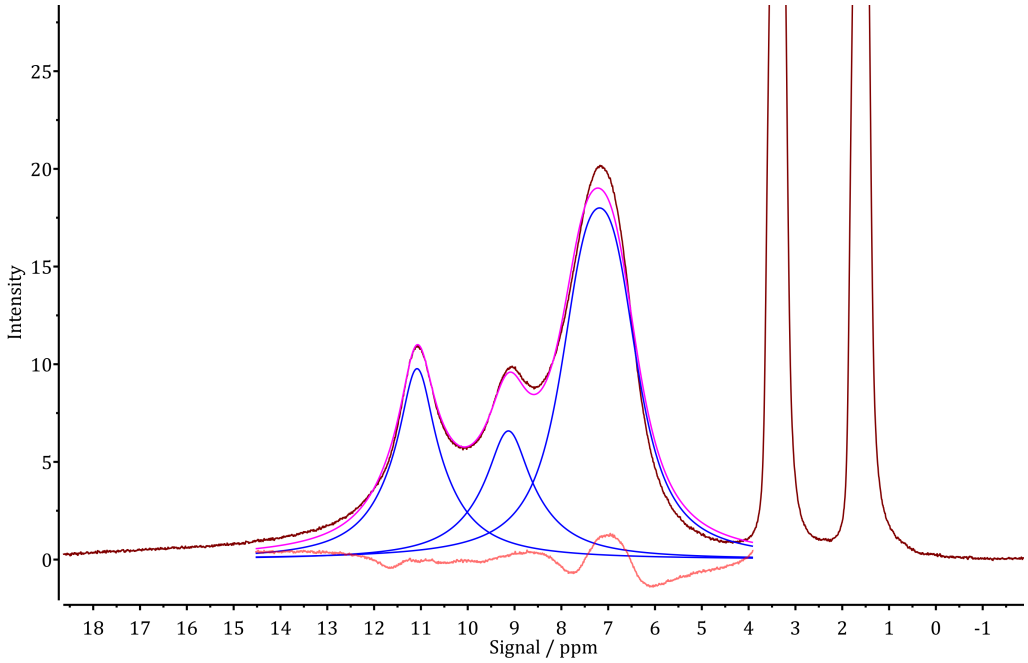

Figure 5.4. The fitted ^{1}H NMR spectrum for complex **36**. The maroon line is the observed signal, the blue line is the calculated fits, the purple line is the summation of the fits, and the red line is the residual.

effects are passed along to the *para* protons too. The combination of signals is then lost in one large Lorentzian shaped signal. The two signals at 9.19 ppm and 11.09 ppm are the *meta* protons, *c* and *c′*. The two signals implies that these protons, whilst chemically equivalent, are magnetically inequivalent. Taking position *c* as an example, this occurs because whilst *b* and *b′* are chemically equivalent, they are a different number of bonds away from position *c* and so will have different J-coupling constants. The larger range of shifts in paramagnetic complexes can therefore allow for chemically equivalent, magnetically inequivalent environments to be resolved, which is generally not possible with diamagnetic compounds.

Pleasingly, it was possible to analyse complex **36** by EI-MS, without any thermal degradation. Multiple peaks were detected and assigned, with an M^+ ion measured at 557 m/z corresponding to the molecular ion $[C_{24}H_{20}CoO_8P_2]^+$. The other major detected peaks and their assignments are shown in table 5.7, where it can be seen that the molecule fragments predictably. It is believed that the additional stability provided by the aromatic phenyl rings is responsible for the lack of visible thermal degradation, which conversely, was observed with the similar complexes **34** and **35** during the MS ionisation stage.

As with complexes **34** and **35**, complex **36** has a cobalt(II) metal centre, and so has a d-electron count of d^7. This gives it the free-ion term symbol $^4F_{9/2}$. In a tetrahedral ligand field, the splitting diagram for which is shown in figure 4.4 in chapter 4, the ground state becomes $^4A_2$.

Table 5.7. A selection of MS peaks recorded for complex **36**, and their assignments.

Mass / m/z	Assignment	Description
557	$C_{24}H_{20}CoO_8P_2$	Molecular ion
541	$C_{24}H_{20}CoO_7P_2$	Loss of oxygen atom
479	$C_{18}H_{15}CoO_8P_2$	Loss of phenyl group
324	$C_{12}H_{10}CoO_5P$	Loss of phosphate ligand

Displayed in figure 5.5 is the UV-vis spectrum measured for complex **36**, at a temperature of 295 K. There is one primary absorbance visible, centred around 16 978 cm^{-1}. The peak has three measurable features at 16 103 cm^{-1}, 17 271 cm^{-1} and 18 349 cm^{-1} caused by spin-orbit coupling. This coupling between the spin and the orbital angular momentum of electrons removes the degeneracy of energy levels. Generally, however, this is only observed at very low temperatures. The exception to this is the tetrahedral Co(II) ion, where the fine structure can often be deduced at room temperature, and to which this example compares with well.[320,353,356] The strong absorbance at 16 978 cm^{-1} can be assigned to the $^4A_2(F) \rightarrow {}^4T_1(P)$ transition. Of the three spin-allowed transitions available to tetrahedral d^7 compounds, it is typical for tetrahedral cobalt(II) phosphates to have a single absorbance, ν_3, in the visible region; with the other two transitions, ν_2 and ν_1, in the near- and mid-infrared region, respectively.[357,358] As only a single transition is within the detectable range of the spectrum, it is not possible to calculate the ν_2 and ν_1 absorption using Tanabe-Sugano diagrams. However with the Tanabe-Sugano diagram and literature precedence, the ν_2 and ν_1 absorptions can be estimated at 10 000 cm^{-1} and 5900 cm^{-1} for excitations from $^4A_2(F)$ to $^4T_1(F)$ and $^4T_2(F)$, respectively.[359]

The strong absorbance at 16 978 cm^{-1} equates to a wavelength of 589 nm. This wavelength is in the orange region of the visible spectrum. Using a traditional colour wheel, substances that absorbance in the orange region appear blue, which correlates exactly with the observed colour of complex **36**.

It was possible to grow X-ray suitable crystals of complex **36** through the slow evaporation of benzene and THF. The crystals grew in the triclinic space group $P\bar{1}$, and were solved with an R-factor of 7.71 %. The resulting crystal structure is shown in figure 5.6, where the phenyl rings have been truncated to methyl groups in order to aid in visual clarity. The atoms are labelled according to the solved crystal structure, where atom labels with a superscript are identical to their non-superscripted counterpart. The identical atoms have been included to enable clear viewing of the structure.

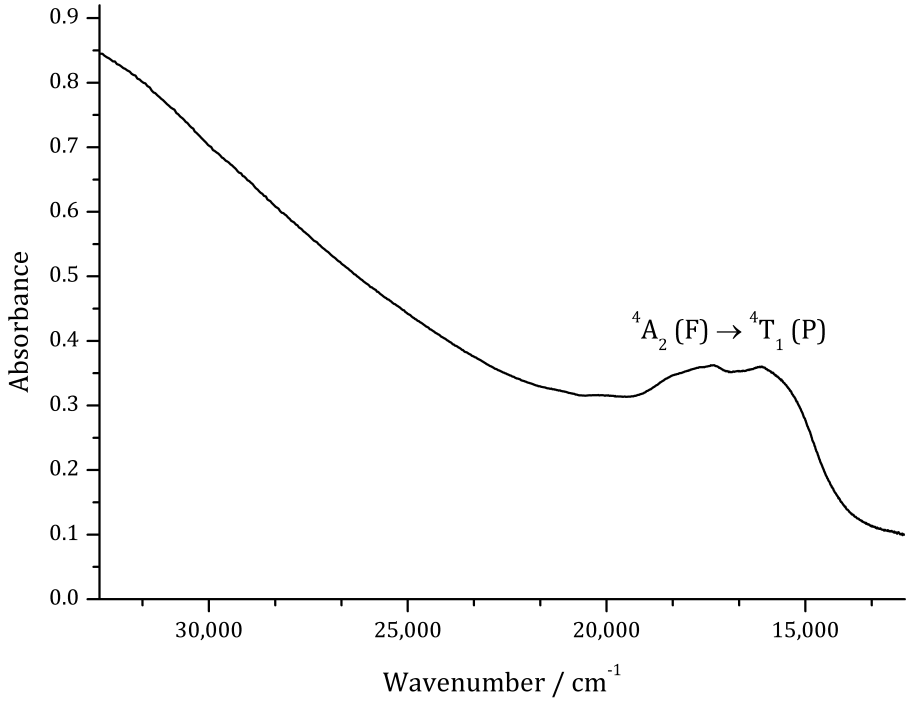

Figure 5.5. Recorded UV-Vis spectrum for complex **36**, at 295 K. The single electronic transition is labelled.

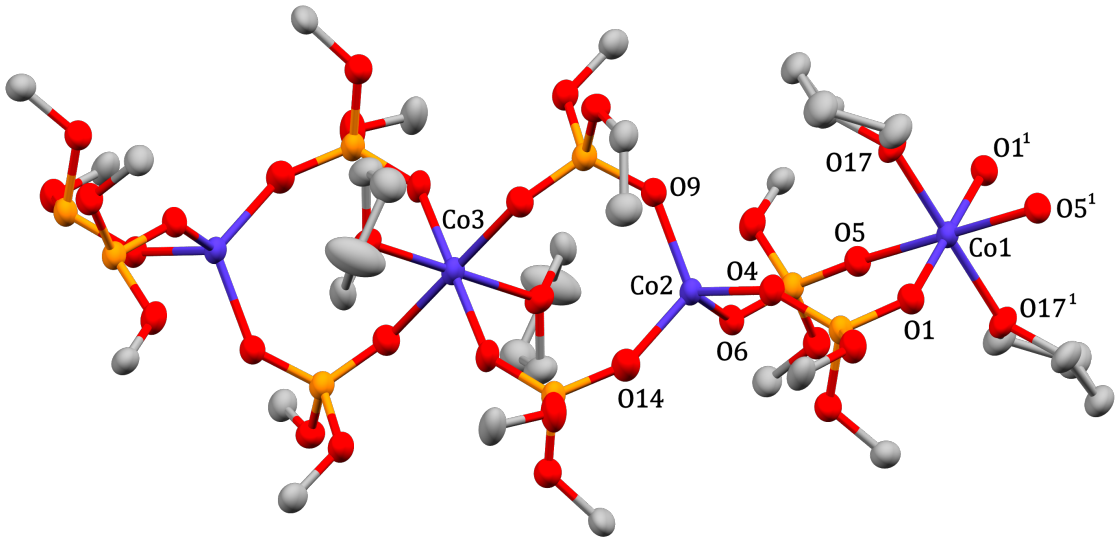

Figure 5.6. Single crystal X-ray structure of bis(diphenyl phosphate) cobalt, **36**, showing an extended unit cell. Ellipsoids are set to 40 % probability; hydrogen atoms and co-crystallised benzene solvent molecules have been omitted for clarity. Phenyl groups have been reduced to methyls, also for clarity. Crystal was solved with an R-factor of 7.71 %. Blue represents cobalt; light orange represents phosphorus; red represents oxygen; and grey represents carbon.

It is interesting to note that complex **36** does not crystallise as a single molecule, favouring instead an extended, polymeric and continuous sheet. As well as being visible in the crystal structure, this was recognised when manipulating the crystals, as the many sheets would break apart

and slide across one another with ease during handling.

A further point of interest is the coordination number of the cobalt metal centre. From left to right in figure 5.6, the coordination number of the (blue) cobalt atoms changes 4-6-4-6. When having a coordination number of four, the metal centre is tetrahedral and bound to four separate bridging phosphate ligands. When the coordination number is 6, the metal centre is octahedral and bound to four separate bridging phosphate ligands and two separate THF molecules. This is distinctly different to the structure in solution, which has two phosphate ligands bound to each cobalt. It is suspected that this change in coordination is the cause for the slow rate observed when dissolving complex **36** in THF. It also explains the slight darkening of colour observed when dissolving the complex. As a solid the complex has a mix of strongly coloured tetrahedral centres and weakly coloured octahedral centres, whilst in solution the attenuating effect of the octahedral sites is not present.

The distance between the cobalt atoms are 4.898 Å and 4.454 Å, as detailed in table 5.8, indicating that there is no direct bonding between the cobalt atoms. The difference in these two values demonstrates the flexibility of the diphenyl phosphate ligand, which is able to bridge across a wide range of distances. The bond lengths vary between the 4-coordinate and 6-coordinate cobalt sites; it can be seen that the metal-oxygen bonds at the 4-coordinate sites are approximately 0.15 Å shorter on average than at the 6-coordinate site. This is expected, as the steric effects of having additional ligands around a metal centre means that each ligand has to be located further away in space. Furthermore, the additional electron density provided by the two THF ligands will slightly increase the radii of the electron orbitals. This variation of bond length by coordination-number is consistent with a similar complex reported in the literature.[360]

Shown in table 5.9, the bond angles between the ligands distinctly demonstrate both the steric effects of the ligands and packing effects from crystallisation. The bond angles clearly indicate that the 4-coordinate metal centre is far from the ideal 109.5°, and is in fact pseudotetrahedral. The same is true at the 6-coordinate metal centre, where the angles around the equatorial plane vary from 86.85° to 93.15°, conferring upon it a pseudo-octahedral geometry.

Both in the bond lengths (table 5.8) and bond angles (table 5.9) there are values which are identical. Additionally, there are some bond angles which are *exactly* 180.00°. These phenomenon both come about because a small number of the atoms in the structure displayed in figure 5.6 are from the inversion centre of the structure. Consequently, for example, the bond angle across O1-Co1-O1[1] is *exactly* 180°, by definition. These atoms are included in the figure to improve viewing.

Table 5.8. Selected bond lengths for complex **36**.

Cobalt Geometry	Bond	Length / Å
	Co1-Co2	4.898(8)
	Co2-Co3	4.454(8)
Tetrahedral	Co2-O14	1.947(5)
	Co2-O4	1.958(5)
	Co2-O9	1.965(4)
	Co2-O6	1.934(5)
Octahedral	Co1-O5	2.148(4)
	Co1-O1	2.061(4)
	Co1-O17	2.098(4)
	Co1-O5^{1}	2.148(4)
	Co1-O1^{1}	2.061(4)
	Co1-O17^{1}	2.098(4)

Table 5.9. Selected bond angles for complex **36**.

Cobalt Geometry	Parameter	Bond Angle / °
Tetrahedral	O6-Co2-O4	105.79(18)
	O6-Co2-O14	112.21(19)
	O6-Co2-O9	109.69(18)
	O4-Co2-O9	106.88(17)
	O14-Co2-O4	104.31(19)
	O14-Co2-O9	117.07(19)
Octahedral	O17^{1}-Co1-O17	180.00(00)
	O17^{1}-Co1-O5^{1}	92.26(16)
	O17^{1}-Co1-O5	87.74(16)
	O17-Co1-O5	92.26(16)
	O17-Co1-O5^{1}	87.74(16)
	O1^{1}-Co1-O17	91.21(18)
	O1^{1}-Co1-O17^{1}	88.79(18)
	O1-Co1-O17^{1}	91.21(18)
	O1-Co1-O17	88.79(18)
	O1-Co1-O1^{1}	180.00(00)
	O1^{1}-Co1-O5	86.85(17)
	O1^{1}-Co1-O5^{1}	93.15(17)
	O1-Co1-O5^{1}	86.85(17)
	O1-Co1-O5	93.15(17)
	O5-Co1-O5^{1}	180.00(9)

The variable coordination number of the cobalt metal centre is likely a result of entropic forces. From work discussed later in section 5.4, it is known that the energy difference between the octahedral and tetrahedral geometries is approximately 50 cm^{-1}, meaning that both geometries can be accessed. Entropically, 1-2-1-2 is favoured over 1-1-1-1 or 2-2-2-2, and consequently resulted in the mixed valence crystal. A small contribution from crystal packing forces is likely to have also had an effect. This phenomenon is not unique, though it is unusual with only a handful of reported crystal structures reporting this feature. One of these is the impressionist inorganic pigment known as cobalt violet, or cobalt orthophosphate ($Co_3(PO_4)_2$), which forms purple crystals with the monoclinic space group $P2_1/c$.[361] This complex has an alternating coordination number of 5-6-5, with separate bridging oxygen atoms and phosphate groups. A dibenzyl phosphinate cobalt complex has also been recently reported, crystallising from DCM as blue crystals in the cubic space group $I23$.[360] The dinuclear cobalt metal centres are separated by bridging phosphinate ligands, and have tetrahedral and octahedral geometry.

The cobalt in complex **36** is in the +2 oxidation state, which means it also has a free-ion term symbol of $^4F_{9/2}$ due to its d^7 electron count. In solution the complex is tetrahedral, and the resulting ligand field gives the ground state term $^4A_2$, the splitting diagram for which is shown in figure 4.4 in chapter 4.

Using the NMR Evans method, the molar magnetic susceptibility of complex **36** was measured as 7.31×10^{-3} emu mol^{-1} at room temperature, which equates to a magnetic moment 4.30 μ_B. This is in good agreement with the calculated spin-only magnetic moment of 3.87 μ_B for three unpaired electrons. As with complex **34**, Zeeman effects can also be taken into consideration. These account for spin-orbit coupling using reference spin-orbit coupling parameters and field splitting energy (equations (4.6) to (4.8), in chapter 4). For a typical field-splitting value of 5000 cm^{-1},[320] this provides a calculated magnetic moment of 4.53 μ_B, which is in excellent agreement with the observed value.

Magnetic studies of complex **36** were also conducted using an Evans balance.[362] Whilst the NMR Evans method measures the magnetic susceptibility of a sample in a very dilute solution, the Evans balance can measure the sample in its solid state, although a comparatively large amount of sample is required for measurements (~3 mg for NMR Evans method, compared to ~300 mg for Evans balance).

The Evans balance is a modern modification of a Gouy balance. In a Gouy balance, a known amount of sample is accurately weighed both in the absence, and presence, of an externally ap-

plied magnetic field. The difference in the recorded weight is directly related to how much the sample interacts with the external magnetic field, and therefore by extension, the number of unpaired electrons in the compound. With an Evans balance, instead of measuring the difference in recorded weight, the force on the magnet exerted by the sample causes a slight movement of the magnet, which is monitored by an optical transducer. A magnetic field is then generated with an electromagnet to restore the optical beam to its original position. The current required to produce the necessary repelling magnetic force is then proportional to the magnetic susceptibility of the sample.

The equation used for calculating the magnetic susceptibility of a solid with an Evans balance is shown in equation (5.3); where χ_g is the mass magnetic susceptibility in emu g^{-1}; C_{Bal} is the calibration constant for the instrument, normally around unity; R is the reading of the sample in the tube; R_0 is the reading of the empty tube; l is the length of the sample in the tube in cm; and m is the mass of the sample in g.

$$\chi_g = \frac{C_{Bal}(R - R_0)l}{10^9 m} \tag{5.3}$$

A measurement for R_0 is required because the glass is diamagnetic. This counters the paramagnetism of the sample, creating an artificially depressed reading. It is important to ensure that the sample is homogeneous and densely packed in the sample tube; both to avoid mismeasurement of l and the consequent artificial elevation of the reading, as well to reduce air pockets to negligible volumes. This is achieved by pregrinding of the sample in order to obtain a regular and small grain size, and by adding the sample to the tube slowly, with regular tapping to ensure the powdered sample has completely settled before adding more.

Once the mass magnetic susceptibility has been calculated, the molar magnetic susceptibility can be calculated by multiplying by the molecular weight of the compound. This is shown in equation (5.4) where M^p is the molar mass of the paramagnetic compound in g mol^{-1}; and χ_M is the molar magnetic susceptibility in emu mol^{-1}.

$$\chi_M = \chi_g M^p \tag{5.4}$$

Using these equations, as well as the diamagnetic corrections discussed with equations (4.1) and (4.3), the solid state molar magnetic susceptibility was measured to be 8.29×10^{-3} emu mol^{-1}. This corresponds to an effective magnetic moment of 4.44 μ_B, which is in excellent agreement both

with the previously calculated magnetic moment, as well as the empirically derived value from the NMR Evans method.

The similarity between the observed effective magnetic moment in both the solid state and in solution, suggests that the tetrahedral and octahedral cobalt centres in the crystal structure have the same number of unpaired electrons. This in turn implies a weak-to-intermediate strength ligand field, which is in line with previous observations, forming a high-spin metal centre with the ground term $^4T_{1g}$ at the octahedral sites, and $^4A_2$ at the tetrahedral sites. These are shown in figure 5.7.

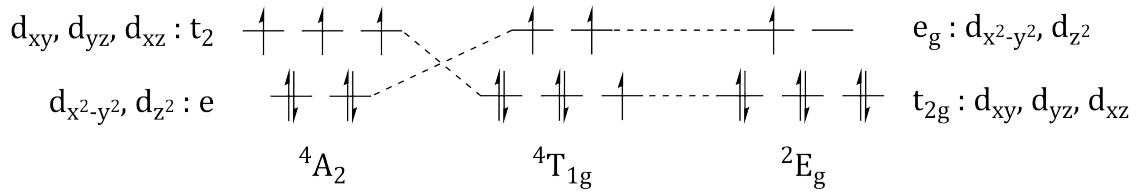

Figure 5.7. The d^7 electron arrangement for tetrahedral ($^4A_2$), high-spin octahedral ($^4T_{1g}$) and low-spin octahedral (^2E_g) complexes.

The similarity of the effective magnetic moment is actually unexpected, because of the change in the ground state term from $^4A_2$ to $^4T_{1g}$, and the ensuing contribution from orbital momentum. The parallel of the measurements suggests that there is minimal orbital contribution to the effective magnetic moment.

Orbital momentum arises from the movement of electrons from one orbital to another degenerate orbital. Rotation around the *x*-axis can be seen to translate d_{xy} to d_{xz}, and equally a rotation around the *y*-axis translates d_{yz} to d_{xy}. Conversely, there is no rotation which can translate $d_{x^2-y^2}$ onto d_{z^2}, partly because they are different shapes. From this, it can be said that cubic ligand fields quench all orbital momentum in the $e_{(g)}$ orbitals. For $t_{2(g)}$ orbitals, electron motion to an allowed orbital must observe the Pauli exclusion principle, *i.e.* two electrons cannot have the same quantum spin number ($\pm 1/2$) in the same orbital. Therefore, orbital momentum can only occur by an electron in a $t_{2(g)}$ orbital, and the electron can only move to a degenerate orbital which is not currently occupied by an electron with the same quantum spin number. This results in orbital momentum being quenched in all $A_{(g)}$ and $E_{(g)}$ terms, and partially conserved in $T_{(g)}$ terms.

A reason for the minimal orbital contribution observed in complex **36**, is that the octahedral geometry is actually pseudo-octahedral, as can be seen in the bond lengths and angles in tables 5.8 and 5.9. This distortion breaks the degeneracy of the octahedral system, increasing the barrier for orbital momentum.

5.4 Variable Temperature Studies of Co(II) Complexes

5.4.1 Variable Temperature Studies of Bis(diphenyl Phosphate) Cobalt

It was observed that complex **36** was thermochromic, undergoing a colour change when the dissolved complex was cooled to below ~−60 °C. The solution has an intense royal blue colour at 295 K, and a pale pink colour at 210 K. This colour change can be seen clearly in figure 5.8. There was no notable colour change on heating the solution.

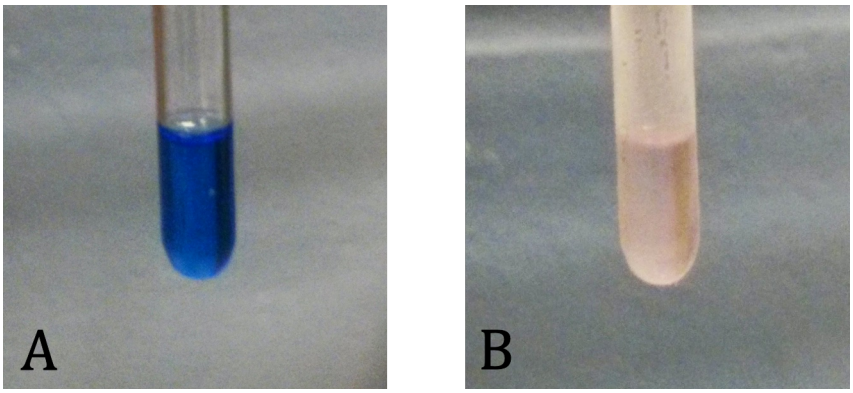

Figure 5.8. The observable colours of complex **36** dissolved in THF, at (a) 22 °C and (b) ~−60 °C.

The temperature-dependent colour change only occurred when the complex was dissolved in THF, there was no notable change when dissolved in any other solvent or in the solid state. This suggests that the colour change is due to the coordination of THF to the cobalt metal centre at lower temperatures, forming complex **37**, as demonstrated in scheme 5.13.

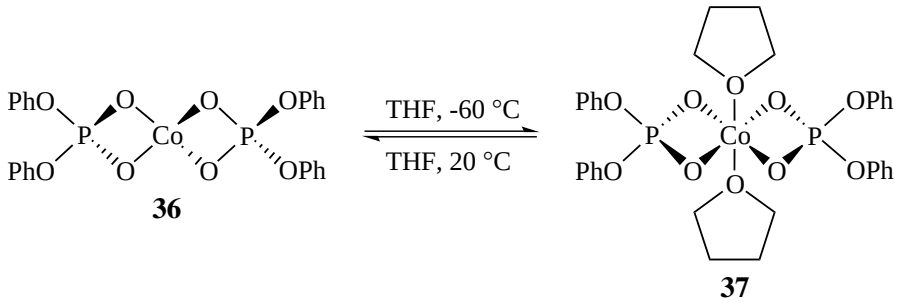

Scheme 5.13. Reversible coordination of THF to complex **36** at low temperatures, leading to formation of complex **37**; of which the *trans* isomer is shown.

While tetrahedral complexes have no restrictions on d-d electron excitation, octahedral complexes are restricted by the Laporte rule. This spectroscopic selection rule states that if a compound has symmetry or antisymmetry around an inversion centre (*g* or *u*, respectively), then any electron transition must not conserve parity, *i.e.* the symmetry must change $g \rightarrow u$, or $u \rightarrow g$. Tetrahedral complexes do not have an inversion centre due to partial d-p orbital mixing, and so are not affected

by this rule. Many complexes do not have perfect octahedral symmetry however, and for those that do, the symmetry is often disrupted by the Jahn-Teller effect and thermal vibrations. As such, while d-d electron transitions are theoretically forbidden in octahedral complexes, they are often weakly observed.

As d-d electron transitions regularly occur at energies within the visible spectrum, one of the consequences of the Laporte rule is that tetrahedral complexes generally have a strong colour, while octahedral complexes tend to be much paler. This is observed for complexes **36** and **37**, as demonstrated in figure 5.8. A summary of typical extinction coefficients depending of observed rules is shown in table 5.10.[320]

Table 5.10. Order of magnitude of the extinction coefficients typically observed for different electronic transitions in complexes.[320]

Electronic Transition	Spin?	Laporte?	Typical Extinction Coefficient
d-d	Forbidden	Forbidden	0.1
d-d	Forbidden	Allowed	1
d-d	Allowed	Forbidden	10
d-d	Allowed	Allowed	100
Charge transfer	Allowed	Allowed	1000

The change in geometry also causes a change in the electronic term symbol, resulting in a change in excited states. For tetrahedral complexes, it is usual for one or two transitions to be observed in the UV-Visible range,[359,363] while for octahedral complexes it is normal for two or three transitions to be observed.[364,365] For d^7 high-spin octahedral complexes, these transitions are from the ground state $^4T_{1g}(F)$ to $^4T_{2g}(F)$, $^4A_{2g}(F)$ and $^4T_{1g}(P)$, labelled as ν_1, ν_2 and ν_3 respectively. The transition ν_2 involves an intermediate step, shown in scheme 5.14, and so is expected to be weaker than the other two transitions.[366]

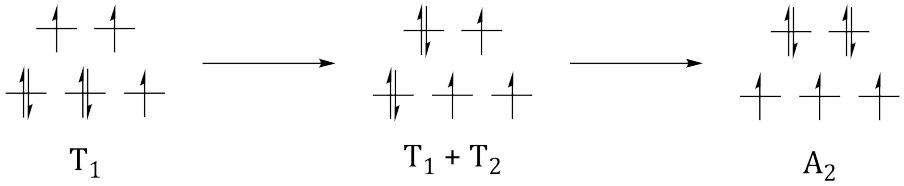

Scheme 5.14. The ν_2 transition for high-spin d^7 octahedral complexes, shown by labelled electron energy levels. The transition shown is $^4T_{1g}(F) \rightarrow {}^4A_{2g}(F)$.

All three of these transitions can be seen labelled in the UV-Vis spectrum of complex **37**, taken at approximately −60 °C and shown in figure 5.9. The shoulder at 26 037 cm^{-1} is the anticipated weaker transition ν_2, $^4T_{1g}(F) \rightarrow {}^4A_{2g}(F)$. The roughness of the spectrum is caused by condensation

and frosting occurring on the outside of the cuvette, due to the required low temperature of the sample.

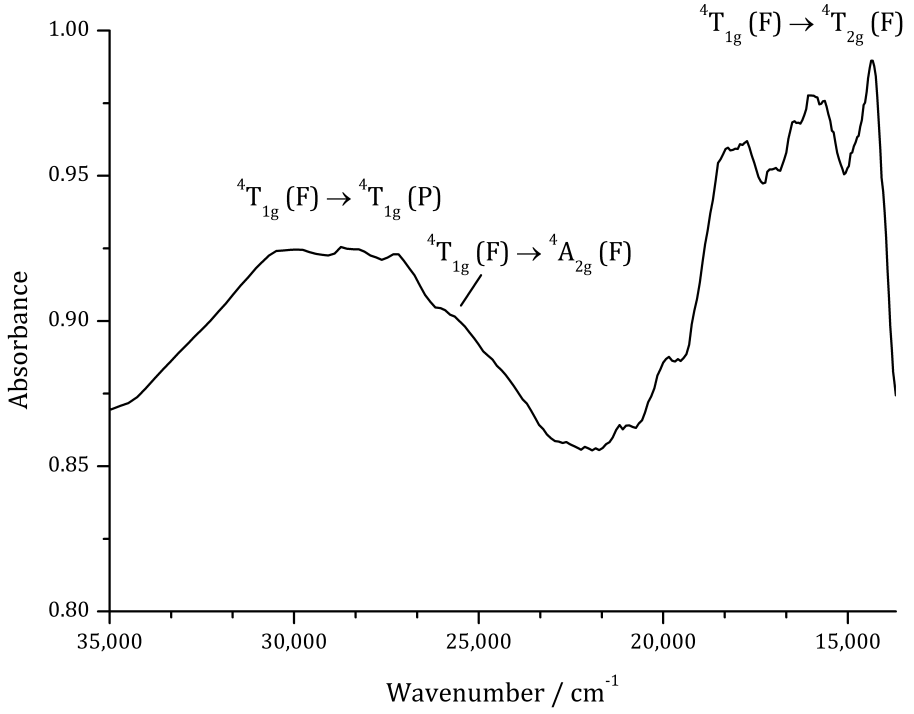

Figure 5.9. Recorded UV-Vis spectrum for complex **37**, at ~210 K. Three electronic transitions are labelled. The $^4T_{1g}(F) \rightarrow {}^4A_{2g}(F)$ transition can be seen as a shoulder.

The spectrum in figure 5.9 also shows the ν_1 transition at 16 020 cm^{-1} and the ν_3 transition at 28 900 cm^{-1}. The ν_1 transition is composed of three very distinctive features at 14 367 cm^{-1}, 15 873 cm^{-1} and 17 794 cm^{-1}. There are several effects in octahedral complexes that could be the cause of these features. The most likely is a combination of low-symmetry components combined with thermal vibration, exaggerating the pseudo-octahedral geometry of the complex. This will cause a change from perfect-cubic symmetry and generate additional, complex energy levels for electronic transitions. A possibility that can be ruled out, however, is spin-orbit coupling. This is because the perceived features are spaced much wider than the spin-orbit coupling for a Co(II) species (515 cm^{-1}).[329] It is possible that the frosting up of the cuvette, as previously mentioned, may have distorted the signal and consequently formed these features.

The total number of absorbances, and their respective intensity, in the UV-Vis spectra displayed in figures 5.5 and 5.9 correlate with tetrahedral and octahedral complex geometries, respectively. This is in agreement with the previously reported structures of complexes **36** and **37**.

5.4.2 Variable Temperature Magnetic Studies of Bis(diphenyl Phosphate) Cobalt

As previously mentioned, the temperature-dependent coordination of THF to complex **36**, forming complex **37**, results in a change in the geometry of the complex, and consequently also a change in the electronic term symbol. In the absence of coordinated THF, as complex **36**, the ground state is $^4A_2$. Once THF has coordinated, as complex **37**, the ground state changes to $^4T_{1g}$. This change is notable because, as discussed above, T terms conserve orbital momentum, and as such have a contribution to the effective magnetic moment from spin-orbit coupling — while A terms quench orbital momentum, and so have no spin-orbit contribution to the effective magnetic moment.

From this, it is reasonable to expect that the effective magnetic moment would increase with a decrease in temperature. As more THF is coordinated, a higher fraction of the compound has a ground T state, leading to a greater contribution of spin-orbit coupling to the magnetic moment. This change in magnetic moment was recorded using the variable-temperature Evans NMR method, and can be seen in the graph shown in figure 5.10.

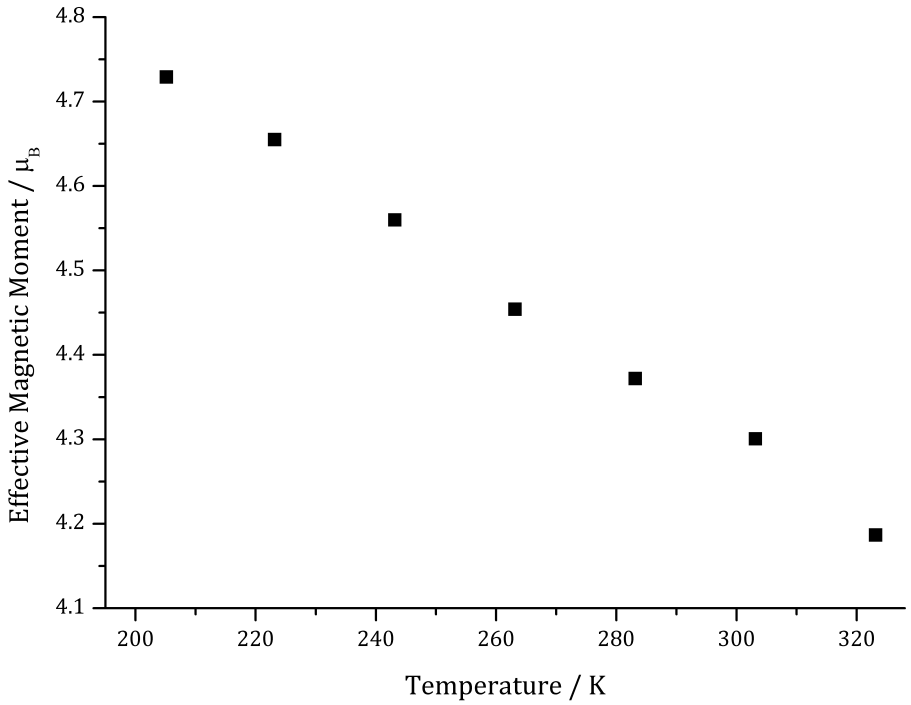

Figure 5.10. The variation in the effective magnetic moment as complex **36** coordinates THF at low temperatures, forming complex **37**.

A reasonably sharp cut-off point between the two geometries was anticipated. However the change is more gradual, almost plotting a straight line. This can be explained by consideration of the observed room-temperature tetrahedral magnetic moment of 4.30 μ_B, compared to the spin-only calculated magnetic moment of 3.87 μ_B. The observed magnetic moment already has some

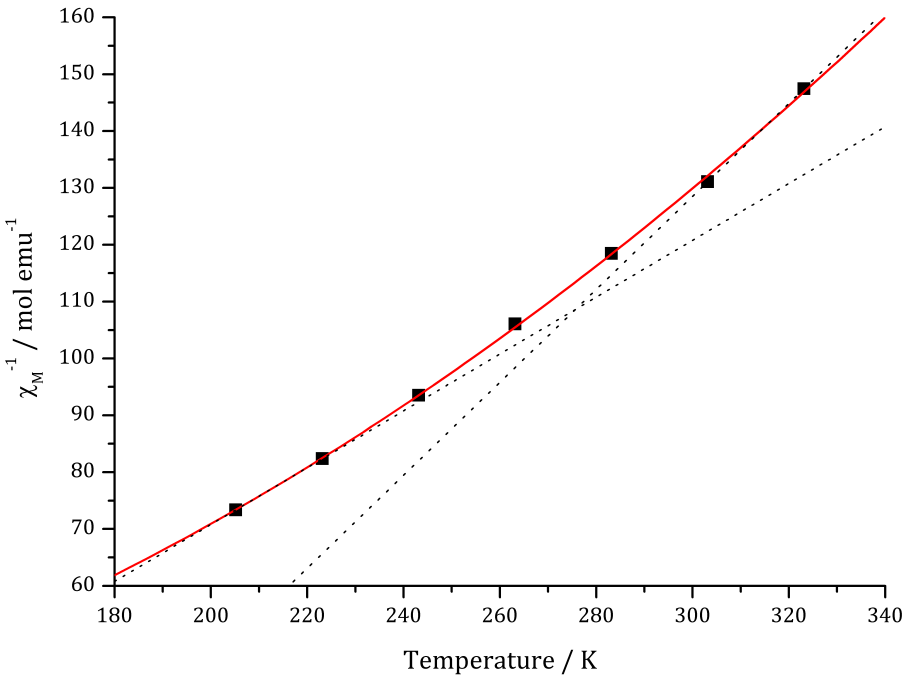

Figure 5.11. Curie-Weiss plot of complex **36**. From the two black dotted lines it can be seen that the data is not linear. The solid red line is a quadratic function. The curve is caused by the coordination of THF to complex **36** at low temperatures, forming complex **37**.

spin-orbit contributions, due to thermal excitation of some electrons from the ground $^4A_2$ state to the $^4T_2$ state. As the temperature of the sample is reduced, less electrons have the energy to occupy the excited T state, and so the spin-orbit contribution is also reduced. This is in contradiction to the increasing fraction of the sample coordinating THF and changing ground state from $^4A_2$ to $^4T_{1g}$, increasing the spin-orbit contribution. It is the combination of these effects which causes the shape of the graph in figure 5.10.

It is expected that the conversion of complex **36** to **37** would prevent the sample from observing Curie behaviour, due to the change in ground state term from $^4A_2$ to $^4T_2$ occurring across the investigated temperature range. From the plot in figure 5.11, it can be seen that this is the case. The dotted black lines indicate that the plot is not linear, by demonstrating the increasing residual as the line continues. While not related to the Curie-Weiss function, the quadratic function, shown as a solid red line, aids in visualising the curve of the plot.

5.4.3 Variable Temperature Studies of Bis(dibutyl Phosphate) Cobalt

It was observed that complex **34** also under went a thermochromic change. This occurred under similar conditions to the phenyl variant; when the compound was solvated in THF and chilled to approximately −60 °C, THF coordinated to the cobalt complex, forming complex **38** as shown in

scheme 5.15. This resulted in a notable colour change from deep blue to light pink.

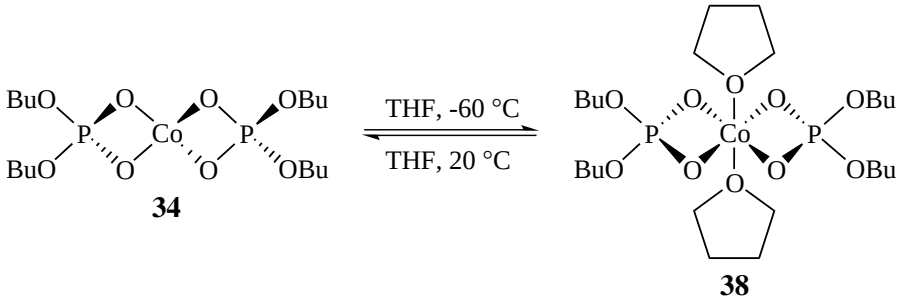

34 **38**

Scheme 5.15. Reversible coordination of THF to complex **34** at low temperatures, leading to formation of complex **38**; of which the *trans* isomer is shown.

This suggested that the identity of the groups on the phosphate ligand are not directly responsible for the thermochromic behaviour. Instead, the unfixed bite angle of the phosphate ligand is likely to play a role. Phosphate ligands have a large degree of flexibility, as observed in the crystal structure previously reported for complex **36**, which allows for the reversible adoption of both tetrahedral and octahedral geometry. This allows the the complex to accommodate the THF ligands. The cobalt metal is also electronically unsaturated, with the tetrahedral complex **34** being a 15 electron species. This allows plenty of electrical and spatial vacancy for the coordination of two THF molecules to the metal centre, forming the 19 electron complex **38**. The electron counting for these two complexes can be seen in tables 5.11 and 5.12. Traditionally complexes tend to prefer arrangements that favour 18 electrons, however it is not uncommon for other electron numbers to be observed.[367,368]

Table 5.11. Electron counting for complex **34**.

Component	Number of Electrons
Cobalt	9
$P(O)(OBu)_2$	3
$P(O)(OBu)_2$	3
Total	15

5.5 Cyclic Voltammetry of Bis(dibutyl Phosphate) Cobalt

As the final target for the cobalt phosphate complexes is a molecular model for the oxygen evolution experiment reported by Kanan and Nocera,[52] the redox chemistry of complex **36** was investigated. Using cyclic voltammetry (CV) it is possible to obtain formal reduction potentials, the number of electrons involved in the redox process, as well as any relevant rate constants.

Table 5.12. Electron counting for complex **38**.

Component	Number of Electrons
Cobalt	9
$P(O)(OBu)_2$	3
$P(O)(OBu)_2$	3
THF	2
THF	2
Total	19

Voltammetry works by monitoring the current flow in a solution as the voltage is varied. Different species have different redox potentials, therefore as the potential is changed different species react. There are many types of voltage scanning patterns, each with different advantages; for CV the triangle wave scanning pattern shown in figure 5.12 is used.

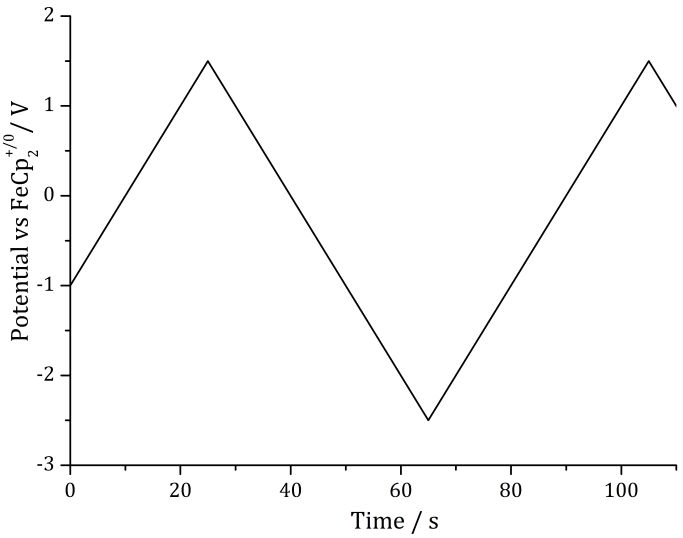

Figure 5.12. Standard voltage scan for a CV experiment.

The experimental set-up, shown in figure 5.13, consists of three electrodes in a solution of the desired complex, at a known molality. The first of the probes is the reference probe, which maintains a constant voltage as a point of reference. The other two probes are the working electrode and the counter electrode. The working electrode is where the chemistry happens, while the counter electrode allows for a current to flow by completing the circuit.

The material of the electrodes is non-trivial. The reference probe is a silver wire, used because it is a well known standard. The counter electrode is a platinum wire, as this minimises any side reactions. The working electrode, in this case, is glassy carbon, a highly chemically-resistant, low-impedance, form of carbon; used here to give a good, well-defined surface area of 7.0 mm^2. Choice of the working electrode can also effect the available potential scanning window, as the

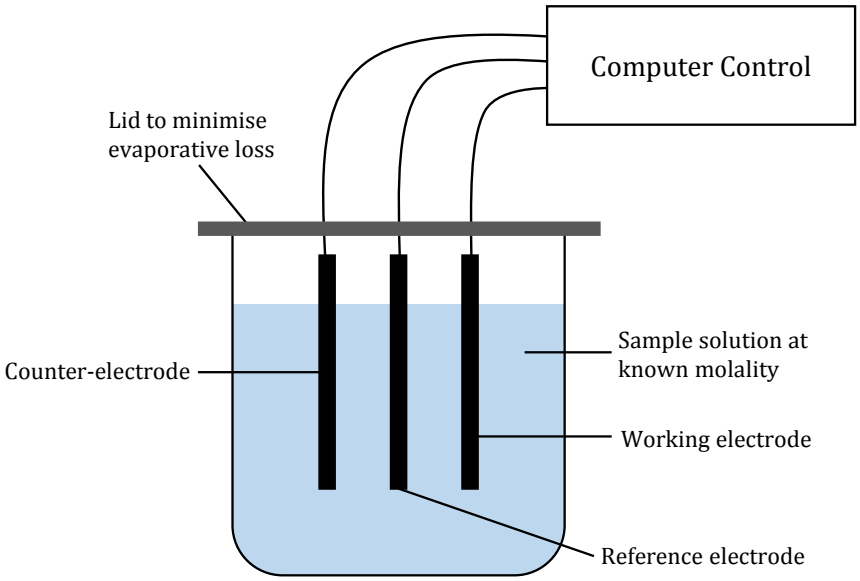

Figure 5.13. Standard set-up for a CV experiment.

known breakdown voltages of specific solvents vary with electrode.

In order to minimise voltage drop between the electrodes, an electrolyte is used to reduce the Ohmic loss (iR drop) of the solvent (deoxygenated THF in this case). The electrolyte needs to be soluble in the solvent, ionic and have minimal interaction with the sample or any formed species. Therefore a variant on the highly non-coordinating ion BAr^F was used, $[^nBu_4N][B(C_6F_5)_4]$.

In much electrochemistry, the reference voltage is taken as the Standard Hydrogen Electrode (SHE). The SHE is based on the reduction of $2\,H^+$ to H_2 at a platinum surface, and defined as 0 V in all cases. This method works well for aqueous solutions, however not for non-aqueous conditions, where the concept of pH is ill-defined. In such cases the use of a quasi-reference electrode is employed, by means of an internal reference. The IUPAC recommended internal reference is the ferrocene +/0 redox couple,[369] which is used throughout this work.

The CV process is diffusion controlled, and so it is important that the solution is not stirred or disturbed in anyway. As the solute is consumed at the working electrode, a concentration gradient is established in the solution, in proximity to the electrodes. It is in this *undisturbed* system that diffusion of unconsumed solute towards the electrodes becomes rate limiting, resulting in a steady current after the initial unsustainable large flux.

The CV of complex **36** was conducted, under the described conditions, with a scan rate of $100\,mV\,s^{-1}$. The resulting voltammogram can be seen in figure 5.14. The mid-peak potential ($\overline{E_{pa} + E_{pc}} = E_{1/2}$) is 0.54 V, which has been assigned to the Co^{II}/Co^{I} redox couple. The feature at ~0.7 V is known to be caused by an impurity in the electrolyte, and played no role in the chem-

istry. The sharp spike in current at either end of the scan is the breakdown voltage — it is at these potentials that the solvent itself begins to become reduced and oxidised.

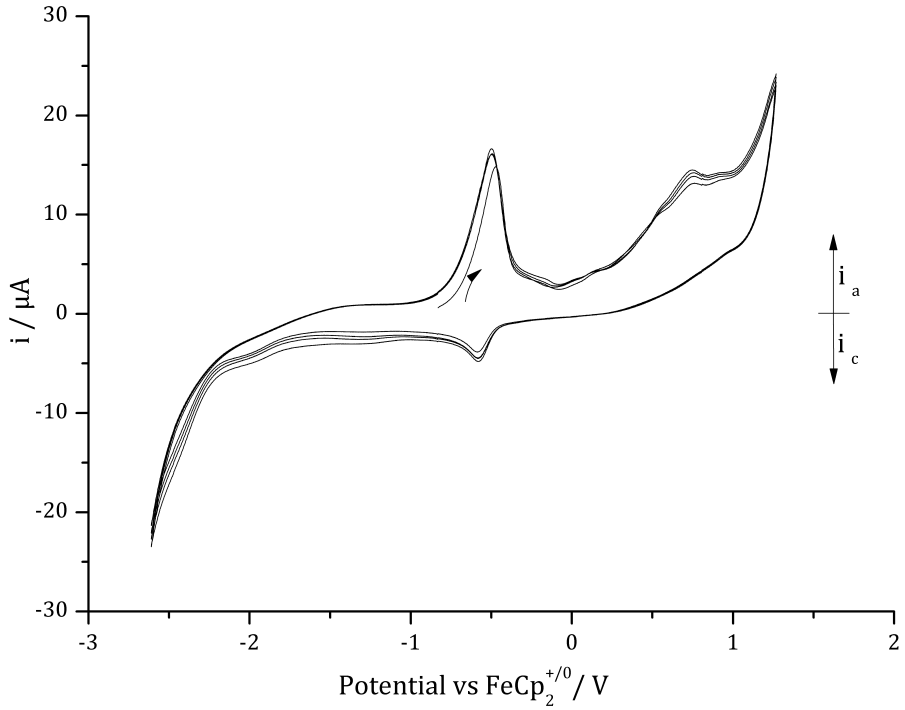

Figure 5.14. The cyclic voltammogram of complex **36**. CV was conducted in 0.05 mol dm^{-3} [^{n}Bu$_4$N][B(C$_6$F$_5$)$_4$] in THF, with a scan rate of 100 mV s^{-1}.

The potential separation between E_{pa} and E_{pc} can be used both to quantify the number of electrons involved in the process, and as a measure of reversibility. For a single electron process, $\Delta E_p = 58$ mV at 25 °C.[370] For the voltammogram of complex **36** in figure 5.14, $\Delta E_p = 86$ mV. This is assigned to a single electron process, with the small increased apportioned to Ohmic losses in THF and sluggish electron transfer kinetics.[371] Due to the diffusion controlled nature of the experiment, a change in scan rate can cause a peak shift if the process is quasi- or ir-reversible. The lack of any change in ΔE_p with scan rate indicates that the electron transfer is fully reversible.

An important feature to note from the voltammogram shown in figure 5.14, is that the peak current is substantially different for the reductive (E_{pa}) and oxidative (E_{pc}) peaks. This implies that complex **36** is being readily reduced to Co^{I} from Co^{II}, but that the resulting oxidation of Co^{I} to Co^{II} is much slower. The likely cause of the slower oxidation step is because the oxidative product is undergoing a non-reversible chemical reaction, consuming the Co^{I} and resulting in a product which is electrochemically inactive under the conditions of the experiment. This consequently leaves a smaller amount of Co^{I} to be oxidised back to Co^{II} by the working electrode.

This reversible electron transfer, followed by a non-reversible chemical reaction is known as

an E_rC_i mechanism.[370] A simplified chemical scheme demonstrating this is shown in scheme 5.16; where Co^{II} is the starting complex **36**; Co^{I} is the resulting reduced species; e^- is an electron; Z is the resulting non-active species; and k is the rate constant.

$$\underset{\mathbf{36}}{Co^{II}} \underset{}{\overset{k_1}{\rightleftharpoons}} Co^{I} \xrightarrow{k_2} Z$$

Scheme 5.16. Reversible redox coupling of complex **36**, followed by an irreversible chemical reaction forming product Z, with a rate constant of k_2.

Theoretically, if the applied voltage is held constant, then the initial reaction can also be considered irreversible, and the reactions considered successive. This allows for the appropriate kinetic considerations made. If the initial concentrations are given by $[Co^{II}]_0$, $[Co^{I}]_0$ and $[Z_0]$ and the concentrations at any time are given by $[Co^{II}]$, $[Co^{I}]$ and [Z], then the following differentials can be used to observe concentration with respect to time.

$$\frac{d[Co^{II}]}{dt} = -k_1[Co^{II}] \tag{5.5}$$

$$\frac{d[Co^{I}]}{dt} = k_1[Co^{II}] - k_2[Co^{I}] \tag{5.6}$$

$$\frac{d[Z]}{dt} = k_2[Co^{I}] \tag{5.7}$$

Integrating the differential in equation (5.5) yields an expression for the concentration of Co^{II} at any point in time, as shown in equations (5.8) and (5.9).

$$\int_{[Co^{II}]_0}^{[Co^{II}]} \frac{d[Co^{II}]}{[Co^{II}]} = \int_0^t -k_1 \tag{5.8}$$

$$[Co^{II}] = [Co^{II}]_0 e^{-k_1 t} \tag{5.9}$$

In order to determine the concentration of Co^{I}, equation (5.9) can be substituted into equation (5.6). This yields equation (5.10), which can in turn be rearranged to give equation (5.11).

$$\frac{d[Co^{I}]}{dt} = k_1[Co^{II}]_0 e^{-k_1 t} - k_2[Co^{I}] \tag{5.10}$$

$$\frac{d[Co^{I}]}{dt} + k_2[Co^{I}] = k_1[Co^{II}]_0 e^{-k_1 t} \tag{5.11}$$

Equation (5.11) is a standard linear first-order differential equation, with a standard solution. The solution is given in equation (5.12).

$$[\mathrm{Co^I}] = \frac{k_1}{\left(k_2 - k_1\right)} \left(e^{-k_1 t} - e^{-k_2 t}\right) [\mathrm{Co^{II}}]_0 \tag{5.12}$$

To calculate the concentration of Z it noted that, for a reaction starting solely with $\mathrm{Co^{II}}$,

$$[\mathrm{Co^{II}}]_0 = [\mathrm{Co^{II}}] + [\mathrm{Co^I}] + [\mathrm{Z}] \tag{5.13}$$

due to the conservation of mass. This can subsequently be rearranged to give equation (5.14). As expressions for the concentrations of $\mathrm{Co^{II}}$ and $\mathrm{Co^I}$ have already been solved in equations (5.9) and (5.12), these can be substituted directly into equation (5.14) to yield equation (5.15).

$$[\mathrm{Z}] = [\mathrm{Co^{II}}]_0 - [\mathrm{Co^{II}}] - [\mathrm{Co^I}]. \tag{5.14}$$

$$[\mathrm{Z}] = [\mathrm{Co^{II}}]_0 - [\mathrm{Co^{II}}]_0 e^{-k_1 t} - \frac{k_1}{\left(k_2 - k_1\right)} \left(e^{-k_1 t} - e^{-k_2 t}\right) [\mathrm{Co^{II}}]_0 \tag{5.15}$$

It is possible to rearrange and simplify equation (5.15). This is done below, with the simplified form shown as equation (5.18).

$$[\mathrm{Z}] = [\mathrm{Co^{II}}]_0 - [\mathrm{Co^{II}}]_0 e^{-k_1 t} - \frac{k_1}{\left(k_2 - k_1\right)} \left(e^{-k_1 t} - e^{-k_2 t}\right) [\mathrm{Co^{II}}]_0 \tag{5.16}$$

$$[\mathrm{Z}] = \left(1 - e^{-k_1 t} - \frac{k_1 e^{-k_1 t} - k_1 e^{-k_2 t}}{\left(k_2 - k_1\right)}\right) [\mathrm{Co^{II}}]_0 \tag{5.17}$$

$$[\mathrm{Z}] = \left(1 + \frac{k_1 e^{-k_2 t} - k_2 e^{-k_1 t}}{\left(k_2 - k_1\right)}\right) [\mathrm{Co^{II}}]_0 \tag{5.18}$$

By taking some arbitrary parameters, a graph of the varying concentrations of the three components with time can be plotted using equations (5.9), (5.12) and (5.18). This is shown in figure 5.15, using the arbitrary values of $[\mathrm{Co^{II}}]_0 = 5\,\mathrm{mol\,dm^{-3}}$, $k_1 = 0.075\,\mathrm{s^{-1}}$, and $k_2 = 0.055\,\mathrm{s^{-1}}$.

For the experimentally observed reaction shown in scheme 5.16, the rate constant k_2 can actually be calculated from the peak current at E_{pa} and E_{pc}, using a method reported by Nicholson and Shain.[372] They discovered that the ratio of peak cathodic current (I_{pc}) to peak anodic current

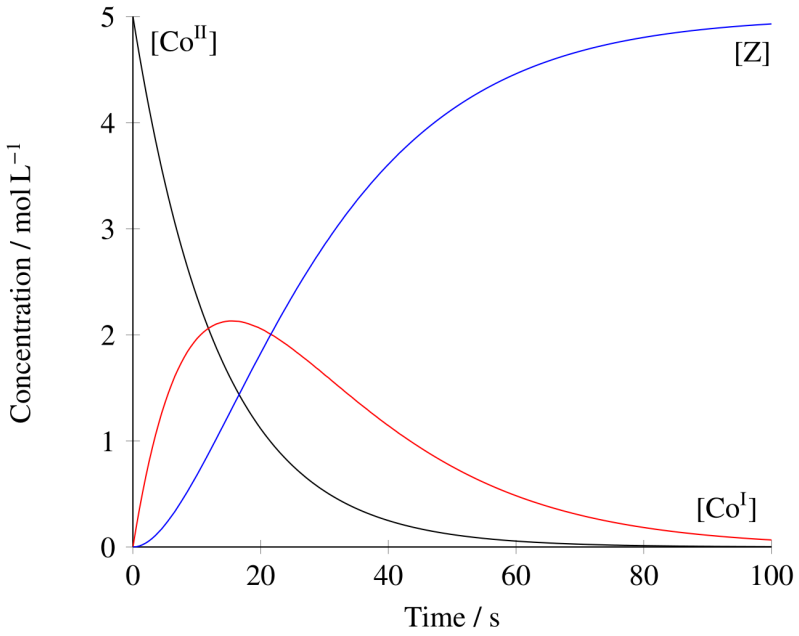

Figure 5.15. Concentrations as a function of time, with parameters $[Co^{II}]_0 = 5$ mol dm^{-3}, $k_1 = 0.075$ s^{-1} and $k_2 = 0.055$ s^{-1}. $[Co^{II}]$ is shown in black, $[Co^{I}]$ in red and [Z] in blue.

(I_{pa}) is constant for a fixed value of $k_2\tau$; where k_2 is the rate constant of the chemically irreversible reaction in scheme 5.16 and τ is the time spent between the redox couple ($E_{1/2}$) and the switching potential ($E_{\lambda 1}$), in seconds. They reported a working curve, from which it is possible to convert a recorded I_{pc}/I_{pa} ratio to $\log(k_2\tau)$ This is demonstrated in equation (5.19).

$$\frac{I_{pc}}{I_{pa}} \propto \log(k_2\tau) \tag{5.19}$$

For the voltammogram shown in figure 5.14, $I_{pc}/I_{pa} = 0.3$. Therefore $k_2\tau = 2.0$. For this experiment $\tau = 18$ s, and so $k_2 = 0.11$ s^{-1}. Theoretical CV traces for an E_rC_i reaction with a rate constant of 0.1 s^{-1} look very similar in shape to the one recorded for complex **36** in figure 5.14, supporting this conclusion.

In order to provide evidence for the reaction shown in scheme 5.16, and to discern the identity of Z, complex **36** was reduced with a more traditional method. The complex was dissolved in THF, to which an equivalent of sodium amalgam was added. The solution was then stirred rapidly until the reaction was seen to have finished (approximately two hours). After work-up, both a precipitate and supernatant were isolated. The precipitate was identified as sodium diphenyl phosphate. The supernatant was reduced and dried *in vacuo*, before analysis by NMR. The ^{1}H NMR spectrum showed paramagnetically shifted phenyl signals. Due to the isolation of an equivalent of the diphenyl phosphate ligand and the paramagnetic NMR shifts of the supernatant, the identity of Z

is tentatively assigned as the binuclear complex **39**, as shown in scheme 5.17.

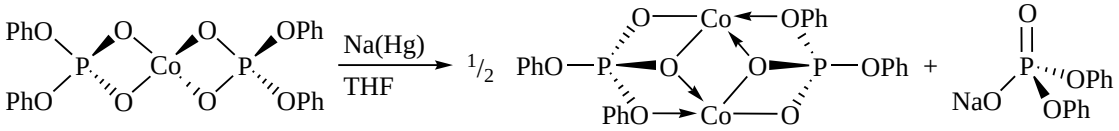

36 **39**

Scheme 5.17. The reduction of **34** by sodium amalgam, yielding the binuclear complex **39**.

In searching for the Co^{II}/Co^{III} redox couple, an equivalent of the phosphate ligand **33** was added to the solution, and the CV experiment repeated. No evidence of this redox couple was observed however. Attempts to oxidise the complex were also made by rapidly stirring the complex with an equivalent of compound **33** over an oxygen atmosphere. However this also resulted in no reaction.

5.6 Conclusions and Future Work

In this chapter the synthesis and characterisation of novel alkyl and aryl phosphate ligands has been reported. The synthesis involved the production of the phosphate, followed by the formation of the relevant potassium salt by reacting with potassium hydride. The potassium salts of the phosphates were then reacted with anhydrous cobalt dichloride in a metathesis reaction. Three cobalt phosphate complexes were produced this way, complexes **34**, **35** and **36**.

Of the three, complex **36** was investigated most fully, due to the inherent idealism of its ^1H NMR spectrum providing a useful handle. Full magnetic investigations were conducted, revealing a tetrahedral complex with three unpaired electrons.

The thermochromic nature of complex **36** was investigated, after noting that a solution of complex **36** in THF changed from a deep royal blue to light pink, on cooling to ~−60 °C. It was discovered that THF was coordinating at lower temperatures, changing the complex from tetrahedral to octahedral, and therefore explaining the colour change.

Attempts were made to follow the change in coordination number by variable-temperature magnetic measurements. Whilst the non-linear Curie plot demonstrated that something was unusual, the magnetic moment did not change as sharply as anticipated. This was due to a reduction in the number of tetrahedral electrons thermally excited to the triplet state, as the temperature was reduced. This coincided with the increase in the octahedral ground state $^4T_{1g}$, ultimately resulting in a gradual change in the amount of orbital-spin contribution to the effective magnetic moment. The high-spin nature of the octahedral complex meant that there was no change in the number of unpaired electrons.

X-ray quality crystals of complex **36** were obtained, and a crystal structure was acquired. This showed that the complex has a polymeric structure as a solid, compared to a mononuclear structure in solution. The cobalt atoms in the solid structure also alternated between coordination numbers of four and six, with tetrahedral and octahedral geometries respectively. Two bound THF molecules provided the additional coordination.

CV experiments have been conducted on complex **36**, in order to probe its redox potential and electrochemisty. Through this, the Co^{II}/Co^{I} redox potential has been recorded as $E_{1/2} = -0.54\,V$, referenced to the ferrocene +/0 redox couple. Once the complex has been reduced, it then chemically reacts ($k = 0.11\,s^{-1}$), ejecting a phosphate ligand and potentially forming the binuclear complex **39**.

Future investigations into this work would focus on generating a Co^{III} analogue of complex **36**, so that attempts can be made to locate the Co^{II}/Co^{III} redox potential. This could be attempted using $[Co(en)_2Cl_2]Cl$, which is readily synthesised from ethylenediamine and cobalt chloride. Treatment with $AgPF_6$ would then form $[Co(en)_2Cl_2]PF_6$, which has a non-coordinating counterion. By reacting this with the phosphate potassium salt (or a silver adduct), then it should be possible to displace the ligands and form $[Co(DPP)_3]PF_6$, which would be an interesting target.

Recrystallisation of complex **36** in a non-coordinating solvent, such as benzene, may provide mononuclear crystals which could be investigated by X-ray crystallography. From this, the solution phase structure could be crystallised.

Superconducting quantum interference device (SQUID) measurements could also be used to measure the magnetic susceptibility across a wide range of temperatures and external magnetic field strengths. From this, precise solid state measurements of magnetism can be made for the sample. This allows for more accurate measurements of Curie and Weiss constants, as well as discovering if the samples magnetism increases linearly with applied magnetic field, as expected for a paramagnetic compound.

Variable temperature UV-visible measurements across a range of temperatures should be able to follow the coordination and geometry change of complex **36**. The use of a spectrometer equipped with a cooling jacket, in combination with a stream of dry air/nitrogen to prevent frosting, would allow the facile observation of the transition. By knowing the temperature and ratios of conversion, it would then be possible to calculate enthalpies of formation.

Use of weaker-field ligands did not allow for access of the cobalt(IV) species. This means that these complexes cannot be used as a molecular model of Nocera's system.

With this additional wealth of knowledge, the application of cobalt phosphates in water splitting can be advanced and enhanced. Potentially with the formation of a new silica-supported cobalt catalyst.

Chapter 6

Experimental

6.1 General Remarks

Unless noted otherwise, all reactions for chapters 4 and 5 were conducted in air and moisture free environments using either standard Schlenk techniques or an MBraun MB 200B glovebox with an MB 20G control system. The glovebox was operated under an argon atmosphere, using a propitiatory catalyst to maintain oxygen and water levels consistently below 0.1 ppm and a solvent scrubber to remove residual solvent vapour. Reactions for chapters 2 and 3 were conducted either on the laboratory bench or in a fume hood.

All solvents were deoxygenated and dried by standing over activated 4 Å molecular sieves, before extended refluxes over the appropriate drying agent, shown in table 6.1, under an argon atmosphere. The solvent required was then distilled off the refluxing still into an ampoule containing either a potassium mirror or activated 4 Å molecular sieves, before freeze-pump-thaw degassing thrice. Before use, all solvents were tested for water and oxygen content using a concentrated potassium benzophenone solution in THF, before storage in the glovebox. Deuterated solvents, for use with NMR samples, were prepared in the same manner, before being vacuum transferred onto the sample in a Youngs NMR tube using an ultra-high vacuum line.

Table 6.1. Appropriate drying agents for use in solvent stills.

Solvent	Drying agent
Benzene	K
Diethyl ether	NaK_3
Hexane	K
Pentane	NaK_3
Tetrahydrofuran	K
Toluene	K

All glassware was thoroughly cleaned using soap, acetone and deionised water, before being

placed sequentially in base and acid baths. After which the glassware was rinsed with deionised water, acetone and dried in an oven at 170 °C. All frits were cleaned using using a solvent and water wash, followed by a rinse with aqua regia, deionised water and acetone. Frits were dried at 200 °C for 36 hours minimum before being cycled into the glovebox under vacuum for 12 hours minimum.

All mass spectrometry was performed at the University of Sussex by Dr A. K. Abdul-Sada. EI-MS was conducted on a VG Autospec Fisons instrument (electron impact ionisation at 70 eV) and ESI-MS was conducted on a Micromass Q-TOF Ultima instrument. Elemental analysis was conducted at London Metropolitan University by Mr Stephen Boyer.

Single crystal X-ray data was collected and solved either by the author, or with help from Dr M. Roe or Miss V. Greenacre, at the University of Sussex. Data was collected at 173 K on an Enraf-Nonius FR590 diffractometer, using either graphite-monochromated Mo K_α radiation ($\lambda = 0.710\,73$ Å) or mirror-monochromated Cu K_α radiation ($\lambda = 1.541\,84$ Å). Data was collected with a 95 mm CCD camera on a κ-goniostat, handled using KappaCCD software. Final cell parameter calculations were performed using the WinGX package and Olex2 program.[373] The data was corrected for absorption using the MULTISCAN program. Refinement was performed using SHELXL-97 and SHELXT.[374,375] Visual representations were generated using Mercury, ORTEP-3 and POV-Ray software.[376,377]

Scanning electron microscopy images were collected on a Jeol JSM-820 scanning microscope equipped with a Jeol 5929 EDX, with images collected with Link ISIS labbook software. Powder X-ray diffraction data was collected on a Siemens Kristalloflex Diffraktometer using Cu K_α radiation ($\lambda = 1.541\,84$ Å), controlled using Diffrac Plus XRD Commander software and analysed using PANalytical X'Pert HighScore Plus software.

Cyclic voltammetry (CV) studies were conducted using a BASi Epsilon-EC potentiostat under computer control. The iR drop was compensated for using the feedback method. CV experiments were performed in an argon glovebox using the three-electrode configuration with a glassy carbon disc (7.0 mm^2) as the working electrode, a platinum wire as the counter-electrode, and a silver wire as the pseudoreference electrode. The solution was prepared by dissolving the sample (5 mmol dm^{-3}) in deoxygenated and dry THF (1.0 mL), followed by addition of the supporting electrolyte, $[^nBu_4N][B(C_6F_5)_4]$. The potentials are referenced internally to the $FeCp_2^{+/0}$ redox couple, by the addition of ferrocene (1 mg) to the solution after all other experiments were concluded.

All GC-MS data was collected on a Perkin Elmer Autosystem XL GC with TurboMass MS. All

GC-FID data was collected on a Perkin Elmer Autosystem GC. All FTIR spectra were collected on a Perkin Elmer Spectrum One FTIR Spectrometer, using either a pass-through cell or an ATR attachment.

Liquid phase UV-Vis spectra were collected on a Varian Cary 50 Bio UV-Visible Spectrophotometer. Diffuse reflectance UV-Vis spectra were collected on an Ocean Optics ISP-REF integrating sphere equipped with a tungsten-halogen illumination source ($300\,\text{nm} \geqslant \lambda \geqslant 1000\,\text{nm}$).

Solid state magnetic measurements were taken using a calibrated Sherwood Scientific Magnetic Susceptibility Balance. All heteronuclear NMR was conducted on a Varian 400/54/ASC operating at 400 MHz, and some ^{1}H & ^{13}C spectra were collected on a Varian 500/54/ASP operating at 500 MHz, both operating with Varian VnmrJ 3.2 software. All NMR samples were referenced to the residual solvent peak and analysed using MestReNova software.

The UV_A light source used in all photocatalytic experiments was a Spectrolinker XL-1500 UV Cross-Linker modified with UV_A tubes. The total UV power output was $4.81\,\text{mW}\,\text{cm}^{-2}$, as measured on a Lutron YK-35UV UV Light Meter.

6.2 Nanomaterial and Metal Oxide Synthesis

6.2.1 Synthesis of Titania Nanofibres

The spinning solution was prepared by dissolving 1.40 g of poly(methyl methacrylate) (PMMA) (with an average molecular weight of $996\,000\,\text{g}\,\text{mol}^{-1}$) in 10 mL of dimethylformamide (DMF) by extended stirring, usually 16 hours. To this was added 1.80 g (6.33 mmol) of titanium tetraisopropoxide (TTiP) and 0.2 g of acetyl acetone with stirring. The solution was then made up to 18 g with DMF, before being loaded into a syringe and extruded through an electrified needle tip (20 kV) at a constant rate of $1\,\text{mL}\,\text{h}^{-1}$. The formed nanofibres were collected on a grounded rotating drum positioned 20 cm horizontally from the syringe needle, before steaming at 80 °C for two hours. The nanofibres were then calcined at 500 °C for 16 hours.

pXRD (Cu K_α) 2θ / ° = 25.35, 37.93, 48.11, 54.10, 55.08, 62.73, 68.89, 70.14, 75.22 and 82.86.

6.2.2 Synthesis of Silver-doped Titania Nanofibres

The synthesis of silver-doped titania nanofibres was conducted using the standard method described in section 6.2.1, with the addition of 10.7 mg (0.063 mmol) of silver nitrate to the solution with the

TTiP. The rest of the procedure is unmodified.

6.2.3 First Synthesis of Tungsten-doped Titania Nanofibres

The synthesis of tungsten-doped titania nanofibres was conducted using the standard method described in section 6.2.1, with the addition of 25 mg (0.063 mmol) of tungsten(VI) chloride to the solution with the TTiP. The rest of the procedure is unmodified.

6.2.4 Second Synthesis of Tungsten-doped Titania Nanofibres

The synthesis of tungsten-doped titania nanofibres was conducted using the standard method described in section 6.2.1, with the addition of 14.6 mg (0.063 mmol) of tungsten(VI) oxide to the solution with the TTiP. The rest of the procedure is unmodified.

6.2.5 Synthesis of Cobalt-doped Titania Nanofibres

The synthesis of cobalt-doped titania nanofibres was conducted using the standard method described in section 6.2.1, with the addition of 30 mg (0.063 mmol) of bis(dibutyl phosphate) cobalt to the solution with the TTiP, whose preparation is described in section 6.5.5. The rest of the procedure is unmodified.

6.2.6 Synthesis of Uranium Dioxide

Uranyl acetate was oxidised to uranium trioxide by calcining in air at 400 °C for four hours. The uranium trioxide was then reduced to uranium dioxide by calcining at 1100 °C either for five hours in an active vacuum of 0.1 mbar, or for 30 hours under argon. All uranium used was isotope ^{238}U, known as depleted uranium.

pXRD (Cu K_α) 2θ / ° = 28.11, 32.59, 46.81, 55.58, 58.30, 68.43, 75.61 and 77.95.

6.3 Photocatalytic Reactions

6.3.1 Degradation of Siloxanes Using Titania Nanofibres

Photocatalytic degradation of hexamethyldisiloxane (L2) was conducted in a static photoreactor with a volume of 134 mL. Synthesised nanofibres (50 mg) were added to the reactor, which was sealed with a suba-seal. Separately, 0.2 mL of L2 was evaporated at 130 °C in a sealed round bottom

flask, from which 10 mL of L2 vapour was taken and injected into the photoreactor. Gaseous GC-FID samples were then taken through the reactor septum periodically. The vessel was illuminated with UV_A radiation from the modified cross-linker.

6.3.2 Activation of Methane with Titania

6.3.2.1 Static Reactor

P25 TiO_2 (0.59 g) was added to a quartz cylinder with a length of 18 cm, an outer diameter of 3.0 cm and wall thickness of 1.5 mm. To this was added deionised water (0.32 g) to make a white paste, which was spread over the bottom half of the vessel. The vessel was then sealed with suba-seals at each end, and purged with 1:1 methane/argon at a combined flow of 20 L min^{-1} for 30 minutes. Afterwards the system was exposed to UV_A radiation using the modified cross-linker. Conversion of methane was monitored using periodic gaseous GC-MS samples by syringe. By conducting the reaction in a gas IR cell, the progress could also be monitored by FTIR.

6.3.2.2 Flow Reactor One

P25 TiO_2 (0.59 g) was added to a quartz cylinder with a length of 18 cm, an outer diameter of 3.0 cm and wall thickness of 1.5 mm. To this was added deionised water (0.32 g) to make a paste, which was spread over the bottom half of the vessel. The vessel was then sealed with suba-seals at each end, and purged with a gas flow of 1:1 methane/argon which had been saturated with moisture by bubbling through deionised water in a Drechsel bottle at a combined flow of 20 L min^{-1} for 30 minutes. After this time the gas flow was permitted to continue, and the UV_A radiation was initiated. The gas out-flow was redirected through an in-line FTIR for continuous monitoring, and periodic gas samples were taken from the out-flow for GC-MS analysis.

6.3.2.3 Flow Reactor Two

P25 TiO_2 (0.59 g) was added to a Drechsel bottle with 40 g of deionised water to form a suspension. The vessel was purged with a gas flow of 1:1 methane/argon, which had been saturated with moisture by bubbling through deionised water in a second Drechsel bottle, at a combined flow of 20 L min^{-1} for 30 minutes. After this time the gas flow was permitted to continue, and the UV_A radiation was initiated. The gas out-flow was redirected through an in-line FTIR for continuous monitoring, and periodic gas samples were taken from the out-flow for GC-MS analysis.

6.3.2.4 Flow Reactor Three

A suspension of P25 TiO_2 (0.59 g) with 40 g of deionised water was added to a quartz cylinder, which was sealed at both ends. The vessel was purged with a gas flow of 1:1 methane/argon, which had been saturated with moisture by bubbling through deionised water in a Drechsel bottle, at a combined flow of 20 L min^{-1} for 30 minutes. With the vessel orientated vertically, gas entered the bottom of the vessel through a sparger, before exiting at the top of the vessel. After the 30 minutes, the gas flow was permitted to continue, and the UV_A radiation was initiated. The gas out-flow was redirected through an in-line FTIR for continuous monitoring, and periodic gas samples were taken from the out-flow for GC-MS analysis.

6.3.3 Activation of Methane with Tungsten Trioxide

Tungsten trioxide (0.67 g) was added to a quartz tube, to which was added 0.19 g of water in order to make a green paste. The paste was spread across the bottom half of the quartz vessel. The vessel was then sealed with suba-seals at each end, and purged with 1:1 methane/argon at a combined flow of 20 L min^{-1} for 30 minutes. Afterwards the system was exposed to UV_A radiation using the modified cross-linker. Conversion of methane was monitored using periodic gaseous GC-MS samples by syringe.

6.3.4 Activation of Methane with Haematite

Haematite, α-Fe_2O_3, (0.31 g) was added to a quartz tube, to which 0.24 g of water was added, forming a dark red paste. The paste was spread across the bottom half of the quartz vessel. The vessel was then sealed with suba-seals at each end, and purged with 1:1 methane/argon at a combined flow of 20 L min^{-1} for 30 minutes. Afterwards the system was exposed to UV_A radiation using the modified cross-linker. Conversion of methane was monitored using periodic gaseous GC-MS samples by syringe.

6.3.5 Activation of Methane with Urania

Urania, UO_2, was first synthesised from uranyl acetate, as described in section 6.2.6. Urania (0.73 g) was then added to a quartz tube, to which was added 0.33 g of water in order to make a viscous dark suspension. This was spread across the bottom of the quartz vessel. The vessel was then sealed with suba-seals at each end, and purged with 1:1 methane/argon at a combined

flow of 20 L min^{-1} for 30 minutes. Afterwards the system was exposed to UV_A radiation using the modified cross-linker. Conversion of methane was monitored using periodic gaseous GC-MS samples by syringe.

6.3.6 Photo-oxidation of Ethanol

P25 TiO_2 (0.59 g) was added to a quartz cylinder with a length of 18 cm, an outer diameter of 3.0 cm and wall thickness of 1.5 mm. To this was added a mixture of deionised water (0.05 g), perfluoromethylcyclohexane (pFMeCy) (0.50 g), and ethanol (0.05 g) to make a white paste. The paste was spread over the bottom half of the vessel. The vessel was then sealed with suba-seals at each end, and purged with argon with a flow of 20 L min^{-1} for 30 minutes. Afterwards the system was exposed to UV_A radiation using the modified cross-linker. Conversion of ethanol was monitored using gaseous GC-MS samples by syringe.

6.4 Ligand Preparation

6.4.1 Synthesis of 9-Bromotriptycene

The synthesis for 9-bromotriptycene was adapted from a literature preparation.[310] Under air, a 1 litre 3-neck round bottom flask was charged with 10.0 mL isopentyl nitrite and 160 mL dichloroethane, to which was added 9-bromoanthracene (13.08 g, 50.9 mmol). Under high stirring and reflux, anthranilic acid (8.20 g, 59.8 mmol) in THF (50 mL) was added dropwise. A further 10.0 mL isopentyl nitrite in THF (50 mL) was then added. Maintaining reflux, maleic anhydride (16.72 g, 170.5 mmol) was added, followed by an addition of 140 mL toluene. Compounds with a boiling point below toluene were then removed by distillation. Activated carbon (0.85 g) was then added, followed by a further reflux for 30 minutes. On cooling, 140 mL dichloromethane was added and the reaction mixture filtered. The solute was washed three times with 15 % aqueous KOH, followed by 10 % aqueous HCl and neutralised with aqueous sodium carbonate. After separation, the organic phase was dried with sodium sulphate, filtered and reduced *in vacuo* at 90 °C. The resulting dark red paste was recrystallised from hot methanol several times, yielding a pale beige powder (4.35 g, 13.1 mmol, 26 %).

^{1}H NMR (400 MHz, $CDCl_3$, 30 °C) δ / ppm = 5.43 (s, 1H, terminal CH), 7.06 (m, *ortho*/*meta* 6H), 7.38 (m, *para*, 3H), 7.80 (m, BrCCC*H*, 3H); ^{13}C NMR (126 MHz, $CDCl_3$, 30 °C) δ / ppm = 53.67 (terminal *C*H), 122.86 (*para*), 123.75 (BrCC*C*), 125.32 (*meta*), 126.16 (*ortho*), 126.65

(Br*C*), 143.56 (BrC*C*), 144.28 (terminal HC*C*). MS (EI) m/z: calcd. for $C_{20}H_{13}{}^{81}Br$: 334, found 334; $C_{20}H_{13}{}^{79}Br$: 332, found: 332; $C_{20}H_{13}$: 253, found: 253.

6.4.2 Synthesis of 9-Lithiotriptycene

A 1:1 mixture of THF and toluene was charged with 9-bromotriptycene (0.658 g, 1.97 mmol) and stirred until fully dissolved; once dissolved the solution was cooled to −40 °C. Pre-chilled ^{n}BuLi (4 mol dm^{-3}, 0.50 mL, 2.00 mmol) was added dropwise to the 9-bromotriptycene solution. The reaction mixture was kept at −40 °C for one hour, before filtering using a chilled frit to yield a solid precipitate. The precipitate was washed with cold toluene (3 × 5 mL), yielding an off-white powder which was stored in the freezer (0.708 g, 1.75 mmol, 89 %).

^{1}H NMR (400 MHz, C_6D_6, 30 °C) δ / ppm = 5.49 (s, 1H, terminal CH), 7.02 (m, *ortho*/*meta* 6H), 7.48 (m, *para*, 3H), 7.94 (m, LiCCC*H*, 3H); ^{7}Li NMR (155 MHz, C_6D_6, 30 °C) δ / ppm = 4.03 (s); ^{13}C NMR (126 MHz, C_6D_6, 30 °C) δ / ppm = 54.18 (terminal *C*H), 123.15 (*para*), 124.19 (LiCC*C*), 126.11 (*meta*), 126.74 (*ortho*), 127.21 (Li*C*), 144.84 (LiC*C*), 144.98 (terminal HC*C*). MS (EI) m/z: calcd. for $C_{20}H_{13}$: 253, found: 253.

6.4.3 Synthesis of Potassium Tris(*tert*-butoxy)silanolate

A round bottom flask was prepared with 2.6443 g (10 mmol) of tris(*tert*-butoxy)silanol in 20 mL of THF. Whilst vigorously stirring, 0.4051 g (10.1 mmol) of potassium hydride was gradually added. Hydrogen gas was observed slowly effervescing. The suspension was left to stir for 16 hours to ensure completion. After which, unreacted KH was removed through vacuum assisted filtration through a number 4 frit. The filtrate was then reduced *in vacuo* to yield a fluffy white powder (2.96 g, 9.78 mmol, 98 %).

^{1}H NMR (500 MHz, C_6D_6, 30 °C) δ / ppm = 1.48 (s, 27H, CCH_3); ^{13}C NMR (126 MHz, C_6D_6, 30 °C) δ / ppm = 32.21 (s, CCH_3), 70.67 (s, *C*CH$_3$); ^{29}Si NMR (80 MHz, C_6D_6, 30 °C) δ / ppm = −88.46 (s).

6.4.4 Attempted Synthesis of Bis(tris(*tert*-butoxy)silyl) Phosphorochloridite

A solution of phosphorous trichloride (0.10 mL, 1.17 mmol) in toluene (7 mL) was prepared and cooled to 0 °C, before a solution of potassium tris(*tert*-butoxy)silanolate (0.7079 g, 2.34 mmol), also cooled to 0 °C, in toluene (15 mL) was added. The addition was done dropwise over approximately 45 minutes. The stirred reaction mixture was allowed to gradually warm to room tempera-

ture over 16 hours. After which the solvent, and any unreacted PCl_3, were removed *in vacuo*. The resulting powder was extracted with benzene and dried under vacuum, yielding a white powder (0.4250 g). The mixture of products was found to be inseparable.

^{1}H NMR (400 MHz, C_6D_6, 30 °C) δ / ppm = 1.39 (s, 1H), 1.42 (s, 15H), 1.44 (s, 39H).

6.4.5 Synthesis of Tris(tris(*tert*-butoxy)silyl) Phosphite

A solution of phosphorous trichloride (0.10 mL, 1.17 mmol) in toluene (7 mL) was prepared, to which a solution of potassium tris(*tert*-butoxy)silanolate (1.0619 g, 3.51 mmol) in toluene (15 mL) was added. The reaction mixture was left to stir for 16 hours, after which the solvent, and any unreacted PCl_3, were removed *in vacuo*. The resulting powder was extracted with benzene and dried under vacuum, yielding an off-white powder (0.6790 g, 0.83 mmol, 71 %).

^{1}H NMR (400 MHz, C_6D_6, 30 °C) δ / ppm = 1.51 (s, 81H, CCH_3); ^{13}C NMR (100 MHz, C_6D_6, 30 °C) δ / ppm = 32.02 (s, CCH_3), 73.53 (s, CCH$_3$); ^{31}P NMR (162 MHz, $CDCl_3$, 30 °C) δ / ppm = −111.66 (s); ^{29}Si NMR (80 MHz, C_6D_6, 30 °C) δ / ppm = −101.03 (s). MS (EI) m/z: calcd. for $C_{36}H_{81}O_{12}PSi_3$: 820, found 820; calcd. for $C_{35}H_{78}O_{12}PSi_3$: 805, found 805.

6.4.6 Synthesis of Bis(tris(*tert*-butoxy)silyl) Phosphorobromidate

A round bottom flask was charged with phosphorus oxybromide (0.252 g, 0.88 mmol) in THF (5 mL). To this, a solution of potassium tris(*tert*-butoxy)silanolate (0.535 g, 1.77 mmol) in THF (20 mL) was added dropwise over four hours, at −78 °C. The reaction was then left to stir at room temperature for a further 12 hours, during which the reaction went cloudy. The solvent was then removed *in vacuo*, leaving an off-white powder. The product was extracted in toluene and dried under vacuum to yield a fluffy white powder (0.537 g, 0.821 mmol, 93 %).

^{1}H NMR (400 MHz, C_6D_6, 30 °C) δ / ppm = 1.41 (s, 54H, CCH_3); ^{13}C NMR (100 MHz, C_6D_6, 30 °C) δ / ppm = 31.44 (s, CCH_3), 74.81 (s, CCH$_3$); ^{31}P NMR (162 MHz, $CDCl_3$, 30 °C) δ / ppm = −43.45 (s); MS (EI) m/z: calcd. for $C_{24}H_{54}BrO_9PSi_2$: 652, found 652; calcd. for $C_{20}H_{45}BrO_8PSi_2$: 579, found 579.

6.4.7 First Attempted Hydrolysis of Bis(tris(*tert*-butoxy)silyl) Phosphorobromidate

An ampoule was charged with 5.5 mg (0.24 mmol) of sodium metal and 10.0 mL of THF. Deionised and degassed water (4.3 µL, 0.24 mmol) was then added. The ampoule was then sealed and heated to 60 °C for 48 hours, creating a 24 mmol dm^{-3} solution of $NaOH_{(THF)}$. Separately, 65.4 mg of

bis(tris(*tert*-butoxy)silyl) phosphorobromidate (0.10 mmol) was prepared in THF (10 mL). The $NaOH_{(THF)}$ solution (4.2 mL, 0.10 mmol) was then added, and the reaction stirred at 55 °C for 16 hours, during which the reaction went cloudy. After which, the reaction was reduced *in vacuo*, yielding a white powder (42 mg). The powder was found to be non-volatile, as well as insoluble in hexane, pentane, toluene, benzene, THF, diethyl ether, pyridine, methanol and water.

FTIR ν / cm^{-1} = 796 (C−H rocking), 1002 (Si−O stretch), 1068 (P−O stretch), 1156 (P=O stretch), 2922 (C−H stretch).

6.4.8 Second Attempted Hydrolysis of Bis(tris(*tert*-butoxy)silyl) Phosphorobromidate

An ampoule was charged with pyridine (7 µL, 0.086 mmol) and 10.0 mL of THF. Deionised and degassed water (1.6 µL, 0.086 mmol) was then added. The ampoule was then sealed and heated to 60 °C for 6 hours in order to fully react the pyridine with the water, creating a 8.6 mmol dm^{-3} solution of $C_5H_5NH \cdot OH_{(THF)}$. Separately, bis(tris(*tert*-butoxy)silyl) phosphorobromidate (45 mg, 0.069 mmol) was prepared in THF (10 mL). The $C_5H_5NH \cdot OH_{(THF)}$ solution (8.0 mL, 0.069 mmol) was then added, and the reaction stirred at 55 °C for 16 hours, during which the reaction went cloudy. After this, the reaction was reduced *in vacuo*, yielding a white powder. The powder was found to be non-volatile, as well as insoluble in hexane, pentane, toluene, benzene, THF, diethyl ether, pyridine, methanol and water.

FTIR ν / cm^{-1} = 796 (C−H rocking), 1002 (Si−O stretch), 1068 (P−O stretch), 1156 (P=O stretch), 2922 (C−H stretch).

6.4.9 General Method to Hydrolyse Bis(tris(*tert*-butoxy)silyl) Phosphorobromidate

An ampoule was charged with either deionised and degassed water (1 eq. or 5 eq.) or pyridine hydroxide (5 eq.), and 10.0 mL of THF. Potassium iodide (0.1 eq.) may be added. This solution was then added dropwise to a prepared solution of bis(tris(*tert*-butoxy)silyl) phosphorobromidate (1 eq.) THF (10 mL), and the reaction stirred at 55 °C for 16 hours. After this, the reaction was reduced *in vacuo*, yielding a white powder. The powder was found to be non-volatile, as well as insoluble in hexane, pentane, toluene, benzene, THF, diethyl ether, pyridine, methanol and water.

FTIR ν / cm^{-1} = 796 (C−H rocking), 1002 (Si−O stretch), 1068 (P−O stretch), 1156 (P=O stretch), 2922 (C−H stretch).

6.4.10 Synthesis of Potassium Dibutylphosphate

A round bottom flask was charged with 1.060 g (5.04 mmol) of dibutylphosphate in hexane (10 mL). Whilst stirring, 0.200 g (5.05 mmol) of potassium hydride was gradually added. Hydrogen gas was observed effervescing. The reaction was left to stir for 16 hours to ensure completion. After which, unreacted KH was removed with vacuum assisted filtration through a number 4 frit. The filtrate was then reduced *in vacuo* to yield a white powder (1.103 g, 4.44 mmol, 88 %).

^{1}H NMR (400 MHz, C_6D_6, 30 °C) δ / ppm = 1.09 (t, 6H, CH_2CH_3), 1.61 (m, 4H), 1.85 (m, 4H), 4.16 (q, 4H); ^{13}C NMR (126 MHz, C_6D_6, 30 °C) δ / ppm = 14.30, 19.73, 33.70, 163.48; ^{31}P NMR (162 MHz, C_6D_6, 30 °C) δ / ppm = 0.17 (s). MS (ESI-) m/z: calcd. for $[C_8H_{18}O_4P]^-$: 209.0943, found 209.0935; $[(C_8H_{18}O_4P)_2K]^-$: 457.1523, found: 457.1495.

6.4.11 Synthesis of Potassium Bis(2-ethylhexyl) Phosphate

A round bottom flask was prepared with 0.965 g (2.99 mmol) of bis(2-ethylhexyl) phosphate in hexane (10 mL). Whilst stirring, 0.120 g (2.99 mmol) of potassium hydride was gradually added. Hydrogen gas was observed effervescing. The reaction was left to stir for 4 hours, yielding a white oil. After filtration, the product was again reduced *in vacuo* to give a sticky solid. To desolvate the product, the compound was frozen with liquid nitrogen, in a Schlenk tube, under a fast flowing stream of argon. Once at temperature, the solid was repeatedly crunched and mixed using a spatula. The Schlenk tube was then sealed and placed under vacuum simultaneously, whilst allowing the vessel to warm to room temperature under active vacuum. This process was repeated three times, yielding a free-flowing white powder (1.01 g, 2.80 mmol, 94 %).

^{1}H NMR (400 MHz, C_6D_6, 30 °C) δ / ppm = 1.02 (d, 12H, CH_3), 1.45 (m, 16H, CH_2), 1.77 (s, 2H, CH), 4.10 (t, 4H, OCH_2); ^{13}C NMR (126 MHz, C_6D_6, 30 °C) δ / ppm = 11.10, 14.27, 23.36, 23.67, 29.27, 30.37, 40.49, 69.72; ^{31}P NMR (162 MHz, C_6D_6, 30 °C) δ / ppm = 0.44 (s). MS (ESI-) m/z: calcd. for $[C_{16}H_{30}O_4P]^-$: 321.2195, found 321.2176; $[(C_{16}H_{30}O_4P)_2K]^-$: 681.4037, found: 681.3978.

6.4.12 Synthesis of Diphenyl Phosphate

Synthesis of diphenyl phosphate was adapted from a literature procedure.[351] Under air, phosphorus oxychloride (0.46 mL, 5 mmol) and phenol (0.988 g, 10.5 mmol) were dissolved in 5 mL of benzene. Under heavy stirring, pyridine (0.89 mL, 10 mmol) was added. The resulting solution was refluxed for 5 hours. After cooling to room temperature, 1 mL of deionised water was added, and

the reaction stirred for 10 minutes. The organic layer was then extracted and reduced *in vacuo*, yielding an oil. The oil was redissolved in 5 mL of acetone and 0.5 mL of deionised water, before refluxing for an additional hour. On cooling, the reaction mixture was reduced *in vacuo*. The resulting solid was redissolved in a saturated aqueous potassium carbonate solution (5 mL) and washed three times with chloroform. Phosphoric acid (5 mL) was then added to the aqueous layer, before extracting the product in dichloromethane (2 x 2 mL). The resulting solution was dried with sodium sulphate, filtered and reduced *in vacuo*, yielding a white solid (0.55 g, 2.20 mmol, 44 %).

^{1}H NMR (400 MHz, D_2O, 30 °C) δ / ppm = 7.28 (m, 6H, *meta*, *para*), 7.46 (t, J = 7.21 Hz, 4H, *ortho*); ^{13}C NMR (126 MHz, D_2O, 30 °C) δ / ppm = 120.32 (*ortho*), 124.57 (*para*), 129.87 (*meta*), 151.65 (*ipso*); ^{31}P NMR (162 MHz, $CDCl_3$, 30 °C) δ / ppm = −9.77 (s). MS (EI) m/z: calcd. for $C_{12}H_{11}O_4P$: 250, found 250.

6.4.13 Synthesis of Potassium Diphenyl Phosphate

A round bottom flask was prepared with 0.550 g (2.20 mmol) of diphenyl phosphate in a mixture of benzene and hexane (5 mL each). Whilst stirring, 0.088 g (2.20 mmol) of potassium hydride was gradually added. Hydrogen gas was observed effervescing. The reaction was left to stir for 16 hours to ensure completion. After which, the reaction mixture was filtered through a number 4 frit. The precipitate was then washed with THF and dried under vacuum to yield a white powder (0.570 g, 1.98 mmol, 90 %).

^{1}H NMR (400 MHz, THF-d_8, 30 °C) δ / ppm = 6.93 (t, J = 6.72 Hz, 2H, *para*), 7.15 (t, J = 7.27 Hz, 4H, *meta*), 7.21 (d, J = 7.94 Hz, 4H, *ortho*); ^{13}C NMR (126 MHz, THF-d_8, 30 °C) δ / ppm = 119.83 (*ortho*), 124.30 (*para*), 128.65 (*meta*), 152.53 (*ipso*); ^{31}P NMR (162 MHz, THF-d_8, 30 °C) δ / ppm = −11.58. FTIR ν / cm^{-1} = 687.47, 891.81, 1098.66, 1212.52, 1489.74, 1590.05. MS (ESI-) m/z: calcd. for $[C_{12}H_{10}O_4P]^-$: 249.0317, found 249.0303.

6.5 Complex Synthesis

6.5.1 Synthesis of Lithium Tritriptycene Tetrahydrofuran Cobaltate

A round bottom flask was charged with 0.0343 g (0.27 mmol) of anhydrous $CoCl_2$. To which was added 10 mL of pre-chilled (−40 °C) benzene, and allowed to stir rapidly for 10 minutes at −40 °C. 9-lithiotriptycene (0.210 g, 0.81 mmol) was then added slowly to the solution over 3 minutes, causing a colour change from light blue to turquoise. The reaction mixture was then placed

back in the freezer for 2 hours, before being filtered through a number 4 frit and washed with a cold toluene/THF mixture to yield an olive powder. This powder was resolvated in THF to yield a bright blue powder (0.070 g, 0.078 mmol, 29 %).

^{1}H NMR (400 MHz, THF-d_8, 30 °C) δ / ppm = 1.72 (THF), 3.58 (THF), 5.49 (s, 1H, terminal CH), 7.02 (m, *ortho*/*meta*/*para*, 9H), 7.94 (m, CoCCC*H*, 3H); ^{7}Li NMR (155 MHz, THF-d_8, 30 °C) δ / ppm = 34.86 (s); ^{13}C NMR (126 MHz, THF-d_8, 30 °C) δ / ppm = 87.38, 124.25, 125.69. FTIR ν / cm^{-1} = 914 (THF C−O), 1450 (C−H bend, C=C stretch), 3000 (C−H stretch). MS (ESI-) m/z: calcd. for $[C_{60}H_{39}Co]^-$: 818.2384, found 818.2200.

6.5.2 Synthesis of Ditriptycene Tetrahydrofuran Iron

A round bottom flask was charged with 0.0289 g (0.18 mmol) of anhydrous $FeCl_3$. To which was added 10 mL of 1:1 THF/toluene, which was allowed to stir rapidly for 15 minutes. 9-lithiotriptycene (0.140 g, 0.54 mmol) was then added slowly to the solution over 3 minutes. The reaction mixture was allowed to stir for 8 hours, during which it changed from a deep red to very dark. It was then filtered through a number 4 frit. The precipitate was washed with cold pentane and dried under vacuum for yield a dark powder (0.062 g, 0.097 mmol, 54 %).

^{1}H NMR (400 MHz, C_6D_6, 30 °C) δ / ppm = 1.42 (THF), 3.59 (THF), 5.20 (s, 1H, terminal CH), 6.85 (m, *ortho*/*meta*/*para*, 9H), 7.29 (m, FeCCC*H*, 3H). MS (EI) m/z: calcd. for $C_{40}H_{26}Fe$: 562, found 562; calcd. for $C_{20}H_{13}$: 253, found 253.

6.5.3 Synthesis of Tritriptycene Tetrahydrofuran Chromium

A round bottom flask was charged with 0.1087 g (0.29 mmol) of anhydrous $CrCl_3(THF)_3$. To which was added 10 mL of benzene, which was allowed to stir rapidly for 15 minutes. 9-lithiotriptycene (0.223 g, 0.86 mmol) was then added slowly to the solution over 3 minutes. The reaction mixture was allowed to stir for 8 hours, before being filtered through a number 4 frit. The filtrate was reduced *in vacuo*, before being taken up in toluene and refiltered. The filtrate was again reduced *in vacuo* to yield a bright green powder (0.194 g, 0.22 mmol, 76 %).

^{1}H NMR (400 MHz, C_6D_6, 30 °C) δ / ppm = 1.40 (THF), 3.55 (THF), 5.18 (s, 1H, terminal CH), 6.82 (m, *para*, 3H), 7.14 (m, *ortho*/*meta*/CrCCC*H*, 9H). MS (EI) m/z: calcd. for $C_{60}H_{39}Cr$: 811, found 811; calcd. for $C_{40}H_{26}$: 506, found 506; calcd. for $C_{20}H_{13}$: 253, found 253.

6.5.4 Synthesis of Dichloro,ditriptycene Zirconium

A round bottom flask was charged with 0.0676 g (0.29 mmol) of anhydrous $ZrCl_4$. To which was added 10 mL of THF, which was allowed to stir rapidly for 15 minutes. 9-lithiotriptycene (0.150 g, 0.579 mmol) was then added slowly to the solution over 3 minutes. The reaction mixture was allowed to stir for 8 hours, before being filtered through a number 4 frit and reduced *in vacuo* to yield a white powder. This powder was taken up in benzene and refiltered before reducing *in vacuo*, yielding a light yellow product, that was washed with hexane (0.119 g, 0.17 mmol, 59 %).

^{1}H NMR (400 MHz, C_6D_6, 30 °C) δ / ppm = 1.40 (THF), 3.59 (THF), 5.21 (s, 1H, terminal CH), 6.84 (m, *para*, 3H), 7.19 (m, *ortho*/*meta*/ZrCCC*H*, 9H); ^{13}C NMR (126 MHz, C_6D_6, 30 °C) δ / ppm = 67.32, 123.90, 125.41, 145.88. MS (EI) m/z: calcd. for $C_{40}H_{26}{}^{37}Cl_2{}^{90}Zr$: 670, found 670; calcd. for $C_{40}H_{26}{}^{35}Cl_2{}^{90}Zr$: 666, found 666; calcd. for $C_{36}H_{22}{}^{35}Cl_2{}^{90}Zr$: 616, found 616; calcd. for $C_{36}H_{22}{}^{35}Cl_2{}^{90}Zr$: 614, found 614.

6.5.5 First Synthesis of Bis(dibutylphosphate) Cobalt

A round bottom flask was prepared with 0.0325 g (0.250 mmol) of anhydrous cobalt chloride in THF (10 mL). Whilst stirring, 0.1440 g (0.50 mmol) of potassium dibutylphosphate in THF was gradually added. The resulting suspension was left to stir for 16 hours to ensure completion. After which, KCl was removed with vacuum assisted filtration through a number 4 frit. The filtrate was then reduced *in vacuo* to yield a sticky blue solid (0.086 g, 0.18 mmol, 73 %).

^{1}H NMR (400 MHz, C_6D_6, 30 °C) δ / ppm = 0.23 (s, brd, 3H), 0.69 (s, brd, 2H), 1.68 (s, brd, 2H), 5.62 (s, v. brd, 2H).

6.5.6 Second Synthesis of Bis(dibutylphosphate) Cobalt

A round bottom flask was prepared with 0.060 g (0.192 mmol) of anhydrous cobalt iodide in THF (10 mL). Whilst stirring, 0.095 g (0.383 mmol) of potassium dibutylphosphate in THF was gradually added. The resulting suspension was left to stir for 16 hours to ensure completion. After which, KI was removed with vacuum assisted filtration through a number 4 frit. The filtrate was then reduced *in vacuo* to yield a sticky blue solid (0.068 g, 0.14 mmol, 75 %).

^{1}H NMR (400 MHz, toluene-d_8, 30 °C) δ / ppm = 0.26 (s, brd, 3H), 0.73 (s, brd, 2H), 1.93 (s, brd, 2H), 5.68 (s, v. brd, 2H).

6.5.7 Synthesis of Bis(bis(2-ethylhexyl) Phosphate) Cobalt

Potassium bis(2-ethylhexyl) phosphate (174 mg, 0.462 mmol) in THF (5 mL) was added dropwise to a stirring solution of $CoCl_2$ (30 mg, 0.231 mmol) also in THF (5 mL), over 5 minutes. The resulting solution was left to stir for 16 hours, before being filtered through a number 4 frit to remove KCl and reduced under vacuum, yielding a blue solid (58 mg, 0.083 mmol, 36 %).

^{1}H NMR (400 MHz, C_6D_6, 30 °C) δ / ppm = 0.88 (v. brd, 22H), 5.62 (brd, 4H).

6.5.8 Synthesis of Bis(diphenyl Phosphate) Cobalt

A round bottom flask was charged with 0.065 g (0.50 mmol) of anhydrous $CoCl_2$. To which was added 10 mL of THF, which was allowed to stir rapidily for 15 minutes. Separately, 0.288 g (1.00 mmol) of compound **33** was dissolved in 10 mL of THF. This solution was then added dropwise to the cobalt chloride solution over 20 minutes. The the reaction was allowed to stir for 16 hours, before being reduced *in vacuo* to form a blue paste. The paste was resolvated in minimal THF and filtered through a number 4 frit, before being reduced *in vacuo* again, yielding a crispy royal blue solid (252 mg, 0.45 mmol, 90 %).

^{1}H NMR (400 MHz, THF-d_8, 30 °C) δ / ppm = 7.32 (brd, *ortho*/*para*, 3H), 9.19 (brd, *meta*, 1H), 11.09 (v. brd, *meta*, 1H). Elemental analysis: calcd. for crystal unit $C_{56}H_{56}Co_2O_{18}P_4 \cdot 4\,KCl \cdot THF$: C = 44.24 %, H = 3.96 %; found: C = 44.70 %, H = 3.07 %. MS (EI) m/z: calcd. for $C_{24}H_{20}CoO_8P_2$: 557, found 557; calcd. for $C_{24}H_{20}CoO_7P_2$: 541, found 541; calcd. for $C_{18}H_{15}CoO_8P_2$: 479, found 479; calcd. for $C_{12}H_{10}CoO_5P$: 324, found 324.

6.5.9 Reduction of Bis(diphenyl Phosphate) Cobalt

Sodium amalgam was prepared by dissolving 0.2290 g of sodium metal into 43.7368 g of mercury, yielding a 0.521 % sodium amalgam. Separately, a round bottom flask was charged with bis(diphenyl phosphate) cobalt (0.1704 g, 0.306 mmol) and THF (20 mL). Once fully dissolved, 1.344 g of the sodium amalgam (Na, 7 mg, 0.306 mmol) was added. The reaction mixture was then stirred rapidly for two hours, during which time a precipitate was observed to form. The precipitate was then isolated from the supernatant by vacuum filtration, and both were dried *in vacuo*.

Filtrate: ^{1}H NMR (400 MHz, THF-d_8, 30 °C) δ / ppm = 6.87 (brd, *para*, 1H), 7.30 (brd, *ortho*, 2H), 8.00 (v. brd, *meta*, 2H).

Precipitate: ^{1}H NMR (400 MHz, THF-d_8, 30 °C) δ / ppm = 6.89 (t, J = 6.78 Hz, *para*, 1H),

7.11 (t, J = 7.40 Hz, *meta*, 2H), 7.24 (d, J = 7.40 Hz, *ortho*, 2H); ^{31}P NMR (162 MHz, THF-d_8, 30 °C) δ / ppm = −9.69.

6.6 Complex Gas Reactions

6.6.1 Standard Method

All complex gas reactions were conducted using the following procedure. Unsuccessful reactions were further heated afterwards to encourage a reaction. The successful reaction is explicitly stated below.

A known quantity of the metal complex was dissolved in a glass ampoule or Youngs NMR tube, degassed using the freeze-vac-thaw technique, and placed on an ultra-high vacuum line (turbomolecular pump backed by a rotary pump, ~10^{-7} mbar). Separately, on the ultra-high vacuum line, a known pressure of the desired gas was transferred to an ampoule of known volume. This gas ampoule was then placed on the same ultra-high vacuum line as the complex solution. After applying an ultra-high vacuum to the adjoining head space, the vessels were isolated from the active vacuum and opened to each other. The transfer of the gas was encouraged by chilling the complex solution with liquid nitrogen. The transfer was allowed to continue for 30 minutes, after which the vessel was resealed and left to warm to room temperature with stirring.

6.6.2 Lithium Tritriptycene Tetrahydrofuran Cobaltate with Oxygen

A Young's NMR tube was charged with lithium tritriptycene tetrahydrofuran cobaltate (5.1 mg, 5.6×10^{-3} mmol) and dissolved in THF-d_8 (2 mL). The solution was then thoroughly degassed using the freeze-vac-thaw method thrice. An ampoule, with a volume of 81 mL, was fully evacuated before being filled with pre-dried oxygen to a pressure of 1.8 mbar (5.6×10^{-3} mmol). The oxygen was vacuum-transferred across to the Young's NMR tube over 30 minutes, encouraged by chilling of the solution with liquid nitrogen. Afterwards the reaction vessel was permitted to warm to room temperature and shaken. After 16 hours the solution had changed from a deep royal blue to an emerald green. The reaction vessel was degassed using the freeze-vac-thaw method thrice, before NMR analysis was conducted. The sample was then analysed with FTIR by evaporating the solution dropwise onto a KBr plate.

^{1}H NMR (400 MHz, THF-d_8, 30 °C) δ / ppm = 5.20 (s, 1H, terminal CH), 6.93-7.25 (m, *meta*/*para* 6H), 7.44 (m, *ortho*, 3H), 7.55-7.80 (m, CoCCC*H*, 3H); ^{7}Li NMR (155 MHz, THF-

d_8, 30 °C) δ / ppm = 13.41 (s); ^{13}C NMR (126 MHz, THF-d_8, 30 °C) δ / ppm = 55.19, 124.37, 125.80, 146.74. FTIR ν / cm^{-1} = 1125 (O−O stretch), 1450 (C−H bend, C=C stretch), 3000 (C−H stretch).

Chapter 7

References

1. J. J. Faust, K. Doudrick, Y. Yang, P. Westerhoff and D. G. Capco, *Cell Biol. Toxicol.*, 2014, **30**, 169–188.
2. E. Keidel, *Farben-Zeitung*, 1929, **34**, 1242.
3. A. Fujishima and K. Honda, *Nature*, 1972, **238**, 37–38.
4. S.-Y. Lee and S.-J. Park, *J. Ind. Eng. Chem.*, 2013, **19**, 1761–1769.
5. E. I. Cedillo-González, R. Riccò, M. Montorsi, M. Montorsi, P. Falcaro and C. Siligardi, *Build. Environ.*, 2014, **71**, 7–14.
6. M. Ni, M. K. Leung, D. Y. Leung and K. Sumathy, *Renew. Sustain. Energy Rev.*, 2007, **11**, 401–425.
7. J. Jeong, K. Sekiguchi, W. Lee and K. Sakamoto, *J. Photochem. Photobiol. A*, 2005, **169**, 279–287.
8. J.-G. Li, T. Ishigaki and X. Sun, *J. Phys. Chem. C*, 2007, **111**, 4969–4976.
9. H. Cheng, J. Ma, Z. Zhao and L. Qi, *Chem. Mater.*, 1995, **7**, 663–671.
10. K. Yanagisawa and J. Ovenstone, *J. Phys. Chem. B*, 1999, **103**, 7781–7787.
11. H. Yin, Y. Wada, T. Kitamura, S. Kambe, S. Murasawa, H. Mori, T. Sakata and S. Yanagida, *J. Mater. Chem.*, 2001, **11**, 1694–1703.
12. D. Reyes-Coronado, G. Rodríguez-Gattorno, M. E. Espinosa-Pesqueira, C. Cab, R. de Coss and G. Oskam, *Nanotechnology*, 2008, **19**, 145605.
13. M. Horn, C. F. Schwerdtfeger and E. P. Meagher, *Zeitschrift für Krist.*, 1972, **136**, 273–281.
14. E. P. Meagher and G. A. Lager, *Can. Mineral.*, 1979, **17**, 77–85.
15. K. Sugiyama and Y. Takéuchi, *Zeitschrift für Krist.*, 1991, **194**, 305–313.
16. H. Zhang and J. F. Banfield, *J. Phys. Chem. B*, 2000, **104**, 3481–3487.
17. Y. Yuan and M. Krüger, *Polymers*, 2011, **4**, 1–19.
18. M. Reed, J. Randall, R. Aggarwal, R. Matyi, T. Moore and A. Wetsel, *Phys. Rev. Lett.*, 1988, **60**, 535–537.

19. G. Schmid and B. Corain, *Eur. J. Inorg. Chem.*, 2003, **17**, 3081–3098.

20. E. Fermi, *Rend. Lincei*, 1926, **3**, 145–149.

21. P. A. M. Dirac, *Proc. R. Soc. A*, 1926, **112**, 661–677.

22. P. Wagner and R. Helbig, *J. Phys. Chem. Solids*, 1974, **35**, 327–335.

23. C. Jacoboni, F. Nava, C. Canali and G. Ottaviani, *Phys. Rev. B*, 1981, **24**, 1014–1026.

24. M. A. Green, *J. Appl. Phys.*, 1990, **67**, 2944–2954.

25. Y. R. Ryu, T. S. Lee and H. W. White, *Appl. Phys. Lett.*, 2003, **83**, 87–89.

26. S. M. Sze and K. K. Ng, *Physics of Semiconductor Devices*, Wiley, Hoboken, NJ, 3rd edn., 2007.

27. S. Vargas, R. Arroyo, E. Haro and R. Rodríguez, *J. Mater. Res.*, 1999, **14**, 3932–3937.

28. R. Zheng, Y. Guo, C. Jin, J. Xie, Y. Zhu and Y. Xie, *J. Mol. Catal. A*, 2010, **319**, 46–51.

29. X. Pan, M.-Q. Yang, X. Fu, N. Zhang and Y.-J. Xu, *Nanoscale*, 2013, **5**, 3601–3614.

30. I. Nakamura, N. Negishi, S. Kutsuna, T. Ihara, S. Sugihara and K. Takeuchi, *J. Mol. Catal. A Chem.*, 2000, **161**, 205–212.

31. T. L. Thompson and J. T. Yates, *Top. Catal.*, 2005, **35**, 197–210.

32. Z. Zhang, O. Bondarchuk, J. M. White, B. D. Kay and Z. Dohnálek, *J. Am. Chem. Soc.*, 2006, **128**, 4198–4199.

33. L. Jing, B. Xin, F. Yuan, L. Xue, B. Wang and H. Fu, *J. Phys. Chem. B*, 2006, **110**, 17860–17865.

34. T. Minato, M. Kawai and Y. Kim, *J. Mater. Res.*, 2012, **27**, 2237–2240.

35. J. M. White, J. Szanyi and M. A. Henderson, *J. Phys. Chem. B*, 2003, **107**, 9029–9033.

36. T. Ihara, M. Miyoshi, Y. Iriyama, O. Matsumoto and S. Sugihara, *Appl. Catal. B*, 2003, **42**, 403–409.

37. F. A. Kröger, *The Chemistry of Imperfect Crystals, Vol. 3*, Elsevier, Amsterdam, 2nd edn., 1974.

38. M. K. Nowotny, T. Bak and J. Nowotny, *J. Phys. Chem. B*, 2006, **110**, 16270–16282.

39. K. Tanaka, M. F. Capule and T. Hisanaga, *Chem. Phys. Lett.*, 1991, **187**, 73–76.

40. S.-D. Mo and W. Y. Ching, *Phys. Rev. B*, 1995, **51**, 13023–13032.

41. M. Xu, Y. Gao, E. M. Moreno, M. Kunst, M. Muhler, Y. Wang, H. Idriss and C. Wöll, *Phys. Rev. Lett.*, 2011, **106**, 138302.

42. Y. Mi and Y. Weng, *Sci. Rep.*, 2015, **5**, 11482.

43. D. Tobaldi, R. Pullar, M. Seabra and J. Labrincha, *Mater. Lett.*, 2014, **122**, 345–347.

44. R. Asahi, T. Morikawa, T. Ohwaki, K. Aoki and Y. Taga, *Science*, 2001, **293**, 269–271.

45. M. W. Kanan, Y. Surendranath and D. G. Nocera, *Chem. Soc. Rev.*, 2009, **38**, 109–114.

46. A. Midilli, M. Ay, I. Dincer and M. Rosen, *Renew. Sustain. Energy Rev.*, 2005, **9**, 255–271.

47. O. Khaselev, *Science*, 1998, **280**, 425–427.

48. J. K. Norskov, J. Rossmeisl, A. Logadottir, L. Lindqvist, J. R. Kitchin, T. Bligaard and H. Jonsson, *J. Phys. Chem. B*, 2004, **108**, 17886–17892.

49. A. Valdes, Z. W. Qu, G. J. Kroes, J. Rossmeisl and J. K. Norskov, *J. Phys. Chem. C*, 2008, **112**, 9872–9879.

50. N. M. Markovic and P. N. Ross, *Cattech*, 2000, **4**, 110–126.

51. R. Eisenberg and H. B. Gray, *Inorg. Chem.*, 2008, **47**, 1697–1699.

52. M. W. Kanan and D. G. Nocera, *Science*, 2008, **321**, 1072–1075.

53. D. A. Lutterman, Y. Surendranath and D. G. Nocera, *J. Am. Chem. Soc.*, 2009, **131**, 3838–3839.

54. Y. Surendranath, M. Dinca and D. G. Nocera, *J. Am. Chem. Soc.*, 2009, **131**, 2615–2620.

55. N. N. Greenwood and A. Earnshaw, *Chemistry of the Elements*, Butterworth-Heinemann, Oxford, 2nd edn., 1998, pp. 1122–1123.

56. Y. Surendranath, M. W. Kanan and D. G. Nocera, *J. Am. Chem. Soc.*, 2010, **132**, 16501–16509.

57. D. K. Bediako, A. M. Ullman and D. G. Nocera, in *Solar Energy for Fuels*, Springer, Cham, 2015, pp. 173–213.

58. J. K. Nørskov, T. Bligaard, B. Hvolbæk, F. Abild-Pedersen, I. Chorkendorff and C. H. Christensen, *Chem. Soc. Rev.*, 2008, **37**, 2163–2171.

59. J. Meeuwissen and J. N. H. Reek, *Nat. Chem.*, 2010, **2**, 615–621.

60. H. I. Karunadasa, E. Montalvo, Y. Sun, M. Majda, J. R. Long and C. J. Chang, *Science*, 2012, **335**, 698–702.

61. E. K. Byrne, D. S. Richeson and K. H. Theopold, *J. Chem. Soc. Chem. Commun.*, 1986, 1491–1492.

62. B. K. Bower and H. G. Tennent, *J. Am. Chem. Soc.*, 1972, **94**, 2512–2514.

63. E. K. Byrne and K. H. Theopold, *J. Am. Chem. Soc.*, 1989, **111**, 3887–3896.

64. L. E. Nicholls, *PhD Thesis*, University of Sussex, 2015.

65. F. Meyer and W. B. Tolman, *Inorg. Chem.*, 2015, **54**, 5039.

66. A. D. McNaught and A. Wilkinson, *IUPAC Compendium of Chemical Terminology*, Blackwell Scientific, Oxford, 2nd edn., 1997, p. 5695.

67. W. P. Schaefer, B. T. Huie, M. G. Kurilla and S. E. Ealick, *Inorg. Chem.*, 1980, **19**, 340–344.

68. D. H. Gibson, *Chem. Rev.*, 1996, **96**, 2063–2096.

69. J. C. Calabrese, T. Herskovitz and J. B. Kinney, *J. Am. Chem. Soc.*, 1983, **105**, 5914–5915.

70. *US Pat.*, 3769329, 1970.

71. L. Guczi, *New Trends in CO Activation*, Elsevier, Amsterdam, 1991.

72. P. van Leeuwen and C. Claver, in *Comprehensive Coordination Chemistry II, Vol 9*, ed. J. A. McCleverty and T. J. Meyer, Elsevier, Oxford, 2005, pp. 142–206.

73. M. J. Baker, M. F. Giles, A. G. Orpen, M. J. Taylor and R. J. Watt, *J. Chem. Soc. Chem. Commun.*, 1995, 197.

74. L. Gonsalvi, H. Adams, G. J. Sunley, E. Ditzel and A. Haynes, *J. Am. Chem. Soc.*, 1999, **121**, 11233–11234.

75. J. M. Berg, J. L. Tymoczko and L. Stryer, *Biochemistry*, W. H. Freeman, New York, 6th edn., 2007, p. 680.

76. M. D. Fryzuk and S. A. Johnson, *Coord. Chem. Rev.*, 2000, **200**, 379–409.

77. A. J. Leal, M. J. Tenorio, M. C. Puerta and P. Valerga, *Organometallics*, 1995, **14**, 3839–3847.

78. M. B. O'Donoghue, W. M. Davis and R. R. Schrock, *Inorg. Chem.*, 1998, **37**, 5149–5158.

79. J. D. Cohen, M. D. Fryzuk, T. M. Loehr, M. Mylvaganam and S. J. Rettig, *Inorg. Chem.*, 1998, **37**, 112–119.

80. P. Berno and S. Gambarotta, *Organometallics*, 1995, **14**, 2159–2161.

81. D. Dvoranová, Z. Barbieriková and V. Brezová, *Molecules*, 2014, **19**, 17279–17304.

82. IEA, *Key World Energy Statistics 2014*, International Energy Agency, Paris, 2014, p. 6.

83. IEA, *World Energy Outlook*, IEA Publications, Paris, 2012, p. 51.

84. F. Berna, P. Goldberg, L. K. Horwitz, J. Brink, S. Holt, M. Bamford and M. Chazan, *Proc. Natl. Acad. Sci.*, 2012, **109**, E1215–E1220.

85. M. K. Hubbert, Spring Meet. South. Dist. Div. Prod., Texas, 1956.

86. P. F. Verhulst, *Nouv. mém. l'Academie R. des Sci. B.-lett. Bruxelles*, 1845, **18**, 1–41.

87. S. Young, *Nature*, 2001, **414**, 487–488.

88. W. Bischof, R. Borchers, P. Fabian and B. C. Krüger, *Nature*, 1985, **316**, 708–710.

89. C. D. Keeling, *Tellus*, 1960, **12**, 200–203.

90. P. Tans, *www.esrl.noaa.gov/gmd/ccgg/trends*, (acccessed January 2016).

91. R. Keeling, *www.scrippsco2.ucsd.edu*, (accessed January 2016).

92. REN21, *Global Status Report*, UNEP, Paris, 2012.

93. M. R. Allen, A. Braithwaite and C. C. Hills, *Environ. Sci. Technol.*, 1997, **31**, 1054–1061.

94. B. Eklund, E. P. Anderson, B. L. Walker and D. B. Burrows, *Environ. Sci. Technol.*, 1998, **32**, 2233–2237.

95. R. Dewil, L. Appels and J. Baeyens, *Energy Convers. Manag.*, 2006, **47**, 1711–1722.

96. R. Huppmann, H. W. Lohoff and H. F. Schroder, *Fresenius J. Anal. Chem.*, 1996, **354**, 66–71.

97. L. Appels, J. Baeyens and R. Dewil, *Energy Convers. Manag.*, 2008, **49**, 2859–2864.

98. A. Molino, M. Migliori, Y. Ding, B. Bikson, G. Giordano and G. Braccio, *Fuel*, 2013, **107**, 585–592.

99. M. Ajhar and T. Melin, *Desalination*, 2006, **200**, 234–235.

100. M. Ajhar, S. Bannwarth, K. H. Stollenwerk, G. Spalding, S. Yuce, M. Wessling and T. Melin, *Sep. Purif. Technol.*, 2012, **89**, 234–244.

101. F. Accettola, G. M. Guebitz and R. Schoeftner, *Clean Technol. Environ. Policy*, 2008, **10**, 211–218.

102. S. C. Popat and M. A. Deshusses, *Environ. Sci. Technol.*, 2008, **42**, 8510–8515.

103. *RU Pat.*, 2093477, 1993.

104. M. Schweigkofler and R. Niessner, *J. Hazard. Mater.*, 2001, **83**, 183–196.

105. A. Albertsen, in *1st die Nachsorgephase Vor dem Hintergrund der Sick. und Deponiegasverwertung ein wirtschaftlich kalkulierbares Risiko*, ed. M. Merten, Klenkes Druck und Verlag, Aachen, 1998.

106. M. Ajhar, M. Travesset, S. Yuce and T. Melin, *Bioresour. Technol.*, 2010, **101**, 2913–2923.

107. B. Wenskowicz, *MSc Thesis*, University of Rhode Island, 2011.

108. D. Schneider, G. Rettenberger and W. Butz, *Entfernung von Silizium- und Halogenverbindungen aus dem Deponiegas - Erfahrungen aus Versuchen an der Deponie Ihlenberg Deponiegas*, Verlag Abfall Aktuell, Berlin, 2001.

109. E. Wheless and J. Pierce, *Siloxanes in Landfill and Digester Gas Update*, 2004.

110. T. Matsui and S. Imamura, *Bioresour. Technol.*, 2010, **101**, S29–S32.

111. K. Oshita, Y. Ishihara, M. Takaoka, N. Takeda, T. Matsumoto, S. Morisawa and A. Kitayama, *Water Sci. Technol.*, 2010, **61**, 2003–2012.

112. N. Khandaker and P. Seto, *Int. J. Green Energy*, 2010, **7**, 38–42.

113. *GB Pat.*, 2440123, 2008.

114. *EP Pat.*, 2244806, 2010.

115. *GB Pat.*, 2530481, 2016.

116. *US Pat.*, 20130137567, 2012.

117. W. Urban, H. Lohmann and J. I. S. Gomez, *J. Power Sources*, 2009, **193**, 359–366.

118. M. Rao, *Air Pollution*, Tata McGraw-Hill, New Delhi, 1989.

119. M. I. Stockman, *Phys. Rev. Lett.*, 2004, **93**, 137404.

120. M. Khorasaninejad, W. T. Chen, R. C. Devlin, J. Oh, A. Y. Zhu and F. Capasso, *Science*, 2016, **352**, 1190–1194.

121. J. S. Bedi, D. W. Lester, Y. X. Fang, J. F. C. Turner, J. Zhou, S. M. Alfadul, C. Perry and Q. Chen, *J. Polym. Eng.*, 2013, **33**, 453–461.

122. D. Aussawasathien, J.-H. Dong and L. Dai, *Synth. Met.*, 2005, **154**, 37–40.

123. J. Moon, J.-A. Park, S.-J. Lee, T. Zyung and I.-D. Kim, *Sensors Actuators B Chem.*, 2010, **149**, 301–305.

124. Z. Ma, M. Kotaki and S. Ramarkishna, *J. Memb. Sci.*, 2005, **265**, 115–123.

125. K.-H. Kim, L. Jeong, H.-N. Park, S.-Y. Shin, W.-H. Park, S.-C. Lee, T.-I. Kim, Y.-J. Park, Y.-J. Seol, Y.-M. Lee, Y. Ku, I.-C. Rhyu, S.-B. Han and C.-P. Chung, *J. Biotechnol.*, 2005, **120**, 327–339.

126. A. Sharma, A. Gupta, G. Rath, A. Goyal, R. B. Mathur and S. R. Dhakate, *J. Mater. Chem. B*, 2013, **1**, 3410–3418.

127. M. Beck-Broichsitter, M. Thieme, J. Nguyen, T. Schmehl, T. Gessler, W. Seeger, S. Agarwal, A. Greiner and T. Kissel, *Macromol. Biosci.*, 2010, **10**, 1527–1535.

128. E. S. Steigerwalt, G. A. Deluga, D. E. Cliffel and C. M. Lukehart, *J. Phys. Chem. B*, 2001, **105**, 8097–8101.

129. M. Zhi, N. Mariani, R. Gemmen, K. Gerdes and N. Wu, *Energy Environ. Sci.*, 2011, **4**, 417–420.

130. G. Zhang, W. Kataphinan, R. Teye-Mensah, P. Katta, L. Khatri, E. A. Evans, G. G. Chase, R. D. Ramsier and D. H. Reneker, *Mater. Sci. Eng. B*, 2005, **116**, 353–358.

131. *US Pat.*, 2010055465, 2008.

132. L. Meitner, *Zeitschrift für Phys.*, 1922, **9**, 131–144.

133. P. Auger, *C.R.A.S.*, 1923, **177**, 169–171.

134. M. A. Cazalilla, N. Lorente, R. D. Muiño, J.-P. Gauyacq, D. Teillet-Billy and P. M. Echenique, *Phys. Rev. B*, 1998, **58**, 13991–14006.

135. J. Tauc, *Mater. Res. Bull.*, 1968, **3**, 37–46.

136. O. Schevciw and W. B. White, *Mater. Res. Bull.*, 1983, **18**, 1059–1068.

137. V. Kumar, S. Kr. Sharma, T. Sharma and V. Singh, *Opt. Mater.*, 1999, **12**, 115–119.

138. D. Menzel and R. Gomer, *J. Chem. Phys.*, 1964, **41**, 3311–3328.

139. P. A. Redhead, *Can. J. Phys.*, 1964, **42**, 886–905.

140. R. O. Adams and E. E. Donaldson, *J. Chem. Phys.*, 1965, **42**, 770–774.

141. J. Franck and E. G. Dymond, *Trans. Faraday Soc.*, 1926, **21**, 536–542.

142. E. Condon, *Phys. Rev.*, 1926, **28**, 1182–1201.

143. H. Aizawa and S. Tsuneyuki, *Surf. Sci.*, 1996, **363**, 223–228.

144. J. I. Gersten, R. Janow and N. Tzoar, *Phys. Rev. B*, 1975, **11**, 1267–1272.

145. H. D. Hagstrum, *Phys. Rev.*, 1954, **96**, 336–365.

146. P. R. Antoniewicz, *Phys. Rev. B*, 1980, **21**, 3811–3815.

147. A. Pedicini and R. J. Farris, *J. Polym. Sci. B Polym. Phys.*, 2004, **42**, 752–757.

148. J. Deitzel, *Polymer*, 2002, **43**, 1025–1029.

149. I. D. Kim and A. Rothschild, *Polym. Adv. Technol.*, 2011, **22**, 318–325.

150. R. Chandrasekar, L. Zhang, J. Y. Howe, N. E. Hedin, Y. Zhang and H. Fong, *J. Mater. Sci.*, 2009, **44**, 1198–1205.

151. D. Li and Y. N. Xia, *Nano Lett.*, 2003, **3**, 555–560.

152. S. Chuangchote, J. Jitputti, T. Sagawa and S. Yoshikawa, *ACS Appl. Mater. Interfaces*, 2009, **1**, 1140–1143.

153. G. Taylor, *Proc. R. Soc. London Ser. a-Mathematical Phys. Sci.*, 1969, **313**, 453–475.

154. N. Bhardwaj and S. C. Kundu, *Biotechnol. Adv.*, 2010, **28**, 325–347.

155. P. Scherrer, *Nachr. Ges. Wiss. Göttingen*, 1918, **26**, 98–100.

156. M. Leoni and P. Scardi, in *Diffraction Analysis of the Microstructure of Materials*, 2004, pp. 413–454.

157. O. Carp, C. Huisman and A. Reller, *Prog. Solid State Chem.*, 2004, **32**, 33–177.

158. P. K. Baumgarten, *J. Colloid Interface Sci.*, 1971, **36**, 71–79.

159. M. Bognitzki, W. Czado, T. Frese, A. Schaper, M. Hellwig, M. Steinhart, A. Greiner and J. H. Wendorff, *Adv. Mater.*, 2001, **13**, 70–72.

160. C. Wessel, R. Ostermann, R. Dersch and B. M. Smarsly, *J. Phys. Chem. C*, 2011, **115**, 362–372.

161. J. A. Bearden, *Rev. Mod. Phys.*, 1967, **39**, 78–124.

162. A. Patri, T. Umbreit, J. Zheng, K. Nagashima, P. Goering, S. Francke-Carroll, E. Gordon, J. Weaver, T. Miller, N. Sadrieh, S. McNeil and M. Stratmeyer, *J. Appl. Toxicol.*, 2009, **29**, 662–672.

163. D. W. Scott, J. F. Messerly, S. S. Todd, G. B. Guthrie, I. A. Hossenlopp, R. T. Moore, A. Osborn, W. T. Berg and J. P. McCullough, *J. Phys. Chem.*, 1961, **65**, 1320–1326.

164. M. Palczewska-Tulińska and P. Oracz, *J. Chem. Eng. Data*, 2005, **50**, 1711–1719.

165. Philips, *Actinic BL TL-D 15W 1SL*, Data Sheet, 2013, p. 2.

166. B. Kaczmarek and A. Radecki, *J. Chem. Eng. Data*, 1989, **34**, 195–197.

167. W. G. Appleby, J. W. Gibson and G. M. Good, *Ind. Eng. Chem. Process Des. Dev.*, 1962, **1**, 102–110.

168. E. E. Wolf and F. Alfani, *Catal. Rev.*, 1982, **24**, 329–371.

169. A. Voorhies, *Ind. Eng. Chem.*, 1945, **37**, 318–322.

170. P. Forzatti, *Catal. Today*, 1999, **52**, 165–181.

171. *GB Pat.*, 1607150.8, 2016.

172. J.-M. Herrmann, J. Disdier and P. Pichat, *Chem. Phys. Lett.*, 1984, **108**, 618–622.

173. *Environmental Photochemistry Part III*, ed. D. W. Bahnemann and P. K. Robertson, Springer, Berlin, 2015, pp. 131–132.

174. *Handbook of Inorganic Compounds*, ed. D. L. Perry and S. L. Phillips, CRC Press, Boca Raton, FL, 1995, p. 354.

175. M. Radecka, M. Wierzbicka, S. Komornicki and M. Rekas, *Phys. B Condens. Matter*, 2004, **348**, 160–168.

176. W. Mu, J.-M. Herrmann and P. Pichat, *Catal. Letters*, 1989, **3**, 73–84.

177. M. V. Dozzi, S. Marzorati, M. Longhi, M. Coduri, L. Artiglia and E. Selli, *Appl. Catal. B*, 2016, **186**, 157–165.

178. T. Li, L. Wang, G. Chen and S. Huang, *Chinese J. Environ. Eng.*, 2016, **10**, 4309–4313.

179. A. A. Ismail, I. Abdelfattah, A. Helal, S. Al-Sayari, L. Robben and D. Bahnemann, *J. Hazard. Mater.*, 2016, **307**, 43–54.

180. G. A. Ozin and S. Ozkar, *J. Phys. Chem.*, 1990, **94**, 7556–7561.

181. Y. Guo, X. Quan, N. Lu, H. Zhao and S. Chen, *Environ. Sci. Technol.*, 2007, **41**, 4422–4427.

182. Y. Fang, *PhD Thesis*, University of Sussex, 2016.

183. C. Yu, J. C. Yu, W. Zhou and K. Yang, *Catal. Letters*, 2010, **140**, 172–183.

184. L. Kavan, M. Grätzel, S. E. Gilbert, C. Klemenz and H. J. Scheel, *J. Am. Chem. Soc.*, 1996, **118**, 6716–6723.

185. G. R. Bamwenda, K. Sayama and H. Arakawa, *J. Photochem. Photobiol. A*, 1999, **122**, 175–183.

186. Y. Matsumoto, *J. Solid State Chem.*, 1996, **126**, 227–234.

187. P. R. Patil and P. S. Patil, *Mater. Res. Bull.*, 2000, **35**, 865–874.

188. K. Ozawa, M. Emori, S. Yamamoto, R. Yukawa, S. Yamamoto, R. Hobara, K. Fujikawa, H. Sakama and I. Matsuda, *J. Phys. Chem. Lett.*, 2014, **5**, 1953–1957.

189. H. Liu, B. Shen, M. Xing, J. Zhang and B. Tian, *Res. Chem. Intermed.*, 2016, **42**, 3459–3471.

190. A. R. Ramadan, N. Yacoub, H. Amin and J. Ragai, *Colloids Surfaces A Physicochem. Eng. Asp.*, 2009, **352**, 118–125.

191. M. J. Frisch, G. W. Trucks, H. B. Schlegel, G. E. Scuseria, M. A. Robb, J. R. Cheeseman, G. Scalmani, V. Barone, B. Mennucci, G. A. Petersson, H. Nakatsuji, M. Caricato, X. Li, H. P. Hratchian, A. F. Izmaylov, J. Bloino, G. Zheng, J. L. Sonnenberg, M. Hada, M. Ehara, K. Toyota, R. Fukuda, J. Hasegawa, M. Ishida, T. Nakajima, Y. Honda, O. Kitao, H. Nakai, T. Vreven, J. A. Montgomery Jr., J. E. Peralta, F. Ogliaro, M. Bearpark, J. J. Heyd, E. Brothers, K. N. Kudin, V. N. Staroverov, R. Kobayashi, J. Normand, K. Raghavachari, A. Rendell, J. C. Burant, S. S. Iyengar, J. Tomasi, M. Cossi, N. Rega, J. M. Millam, M. Klene, J. E. Knox, J. B. Cross, V. Bakken, C. Adamo, J. Jaramillo, R. Gomperts, R. E. Stratmann, O. Yazyev, A. J. Austin, R. Cammi, C. Pomelli, J. W. Ochterski, R. L. Martin, K. Morokuma, V. G. Zakrzewski, G. A. Voth, P. Salvador, J. J. Dannenberg, S. Dapprich, A. D. Daniels, Ö. Farkas, J. B. Foresman, J. V. Ortiz, J. Cioslowski and D. J. Fox, *Gaussian 09, Revision C.01*, 2009.

192. The Royal Dutch Shell Group, *Internal Report*, Shell Research and Technology Centre, Amsterdam, 1999.

193. D. C. Elliott, T. R. Hart, A. J. Schmidt, G. G. Neuenschwander, L. J. Rotness, M. V. Olarte, A. H. Zacher, K. O. Albrecht, R. T. Hallen and J. E. Holladay, *Algal Res.*, 2013, **2**, 445–454.

194. Y. F. Makogon, *J. Nat. Gas Sci. Eng.*, 2010, **2**, 49–59.

195. G. E. Claypool and I. R. Kaplan, in *Natural Gases in Marine Sediments*, Springer, Boston, 1974, pp. 99–139.

196. H. Zimmermann and R. Walzl, in *Ullmann's Encyclopedia of Industrial Chemistry*, Wiley, Weinheim, Germany, 2009, pp. 465–529.

197. J. Lercher, J. Bitter, A. Steghuis, J. Van Ommen and K. Seshan, in *Environmental Catalysis*, Imperial College, London, 1999, pp. 103–126.

198. W. A. Bone and R. V. Wheeler, *J. Chem. Soc. Trans.*, 1903, **83**, 1074.

199. *DE Pat.*, 2807326, 1979.

200. S. Walton, X. He, B. Zigler and M. Wooldridge, *Proc. Combust. Inst.*, 2007, **31**, 3147–3154.

201. J. H. Lunsford, *Catal. Today*, 2000, **63**, 165–174.

202. C. Elmasides, D. I. Kondarides, W. Grünert and X. E. Verykios, *J. Phys. Chem. B*, 1999, **103**, 5227–5239.

203. M. C. J. Bradford and M. A. Vannice, *Catal. Rev.*, 1999, **41**, 1–42.

204. N. F. Gol'dshleger, V. V. Eskova, A. E. Shilov and A. Shteinman, *Zh. Fiz. Khim.*, 1972, 1353–1357.

205. G. A. Luinstra, J. A. Labinger and J. E. Bercaw, *J. Am. Chem. Soc.*, 1993, **115**, 3004–3005.

206. G. A. Luinstra, L. Wang, S. S. Stahl, J. A. Labinger and J. E. Bercaw, *Organometallics*, 1994, **13**, 755–756.

207. S. S. Stahl, J. A. Labinger and J. E. Bercaw, *J. Am. Chem. Soc.*, 1996, **118**, 5961–5976.

208. H. A. Zhong, J. A. Labinger and J. E. Bercaw, *J. Am. Chem. Soc.*, 2002, **124**, 1378–1399.

209. O. A. Mironov, S. M. Bischof, M. M. Konnick, B. G. Hashiguchi, V. R. Ziatdinov, W. A. Goddard, M. Ahlquist and R. A. Periana, *J. Am. Chem. Soc.*, 2013, **135**, 14644–14658.

210. B. J. Wik, M. Lersch and M. Tilset, *J. Am. Chem. Soc.*, 2002, **124**, 12116–12117.

211. J. A. Labinger, A. M. Herring and J. E. Bercaw, *J. Am. Chem. Soc.*, 1990, **112**, 5628–5629.

212. J. Smidt, W. Hafner, R. Jira, J. Sedlmeier, R. Sieber, R. Rüttinger and H. Kojer, *Angew. Chem.*, 1959, **71**, 176–182.

213. J. A. Labinger and J. E. Bercaw, *J. Organomet. Chem.*, 2015, **793**, 47–53.

214. R. A. Periana, D. J. Taube, S. Gamble, H. Taube, T. Satoh and H. Fujii, *Science*, 1998, **280**, 560–564.

215. *WO Pat.*, 1998050333, 1998.

216. R. A. Periana, D. J. Taube, E. R. Evitt, D. G. Loffler, P. R. Wentrcek, G. Voss and T. Masuda, *Science*, 1993, **259**, 340–343.

217. H. Dalton and R. Whittenbury, *Arch. Microbiol.*, 1976, **109**, 147–151.

218. K. Otsuka, I. Yamanaka and Y. Wang, *Stud. Surf. Sci. Catal.*, 1998, 15–24.

219. P. Lens, C. Kennes, P. L. Cloirec and M. Deshusses, *Waste Gas Treatment for Resource Recovery*, IWA, London, 2006, p. 464.

220. R. G. Herman, Q. Sun, C. Shi, K. Klier, C.-B. Wang, H. Hu, I. E. Wachs and M. M. Bhasin, *Catal. Today*, 1997, **37**, 1–14.

221. R. Nedyalkova, D. Niznansky and A.-C. Roger, *Catal. Commun.*, 2009, **10**, 1875–1880.

222. A. de Lucas, J. Valverde, L. Rodriguez, P. Sanchez and M. Garcia, *Appl. Catal. A*, 2000, **203**, 81–90.

223. A. Parmaliana, F. Frusteri, F. Arena, A. Mezzapica and V. Sokolovskii, *Catal. Today*, 1998, **46**, 117–125.

224. G. Reuss, W. Disteldorf, A. O. Gamer and A. Hilt, in *Ullmann's Encyclopedia of Industrial Chemistry*, Wiley, Weinheim, Germany, 2000.

225. G. Keller and M. M. Bhasin, *J. Catal.*, 1982, **73**, 9–19.

226. W. Hinsen and M. Baerns, *Chem. Ztg.*, 1983, **107**, 223–226.

227. R. Horn and R. Schlögl, *Catal. Letters*, 2015, **145**, 23–39.

228. U. Zavyalova, M. Holena, R. Schlögl and M. Baerns, *ChemCatChem*, 2011, **3**, 1935–1947.

229. *US Pat.*, 4443644, 1984.

230. B. Warren, *Catal. Today*, 1992, **13**, 311–320.

231. M. Stoukides, *Catal. Rev.*, 2000, **42**, 1–70.

232. A. I. Bostan, Y. I. Pyatnitskii, L. N. Raevskaya, V. G. Pryanikova, S. A. Nedil'ko, A. G. Dzyaz'ko and E. G. Zen'kovich, *Theor. Exp. Chem.*, 2005, **41**, 32–36.

233. Y. Zeng, F. Akin and Y. Lin, *Appl. Catal. A*, 2001, **213**, 33–45.

234. *WO Pat.*, 2005005042, 2005.

235. K. Machida and M. Enyo, *J. Chem. Soc. Chem. Commun.*, 1987, 1639.

236. A. H. Tullo, *Chem. Eng. News*, 2014, **92**, 20.

237. A. Blume, *Hydrocarb. Process.*, 2016, **2**, 1.

238. E. V. Kondratenko and M. Baerns, in *Handbook of Heterogeneous Catalysis*, Wiley, Weinheim, Germany, 2008, pp. 3010–3023.

239. J. X. Wang and J. H. Lunsford, *J. Phys. Chem.*, 1986, **90**, 5883–5887.

240. J. H. Lunsford, *Angew. Chem. Int. Edit. Engl.*, 1995, **34**, 970–980.

241. H. Schwarz, *Angew. Chem. Int. Edit.*, 2011, **50**, 10096–10115.

242. L. Luo, X. Tang, W. Wang, Y. Wang, S. Sun, F. Qi and W. Huang, *Sci. Rep.*, 2013, **3**, 1625.

243. P. Mars and D. van Krevelen, *Chem. Eng. Sci.*, 1954, **3**, 41–59.

244. H. Yoshida, N. Matsushita, Y. Kato and T. Hattori, *J. Phys. Chem. B*, 2003, **107**, 8355–8362.

245. D. Schröder and H. Schwarz, *Angew. Chem. Int. Edit. Engl.*, 1995, **34**, 1973–1995.

246. K. A. Zemski, D. R. Justes and A. W. Castleman, *J. Phys. Chem. B*, 2002, **106**, 6136–6148.

247. S. Feyel, J. Döbler, D. Schröder, J. Sauer and H. Schwarz, *Angew. Chem. Int. Edit.*, 2006, **45**, 4681–4685.

248. D. Schröder and J. Roithová, *Angew. Chem. Int. Edit.*, 2006, **45**, 5705–5708.

249. C. H. Lin, K. D. Campbell, J. X. Wang and J. H. Lunsford, *J. Phys. Chem.*, 1986, **90**, 534–537.

250. A. Anshits, N. Kirik, V. Roguleva, A. Shigapov and G. Selyutin, *Catal. Today*, 1989, **4**, 399–407.

251. M. Sinev, *J. Catal.*, 2003, **216**, 468–476.

252. E. M. Kennedy and N. W. Cant, *Appl. Catal. A*, 1992, **87**, 171–183.

253. J. A. Labinger, *Catal. Letters*, 1988, **1**, 371–375.

254. *US Pat.*, 4754091, 1988.

255. A. H. Laufer and J. R. McNesby, *Can. J. Chem.*, 1965, **43**, 3487–3490.

256. B. A. Younglove and J. F. Ely, *J. Phys. Chem. Ref. Data*, 1987, **16**, 577–798.

257. P. A. Cook, M. N. R. Ashfold, Y.-J. Jee, K.-H. Jung, S. Harich and X. Yang, *Phys. Chem. Chem. Phys.*, 2001, **3**, 1848–1860.

258. K. Okabe, K. Sayama, H. Kusama and H. Arakawa, *Chem. Lett.*, 1997, 457–458.

259. K. Wada, H. Yamada, Y. Watanabe and T. Mitsudo, *J. Chem. Soc. Faraday Trans.*, 1998, **94**, 1771–1778.

260. H. Berndt, A. Martin, A. Brückner, E. Schreier, D. Müller, H. Kosslick, G.-U. Wolf and B. Lücke, *J. Catal.*, 2000, **191**, 384–400.

261. L. Nguyen, S. Loridant, H. Launay, A. Pigamo, J. Dubois and J. Millet, *J. Catal.*, 2006, **237**, 38–48.

262. L. Yuliati and H. Yoshida, *Chem. Soc. Rev.*, 2008, **37**, 1592–1602.

263. C. E. Taylor, *Catal. Today*, 2003, **84**, 9–15.

264. H. Yoshida, K. Hirao, J. Nishimoto, K. Shimura, S. Kato, H. Itoh and T. Hattori, *J. Phys. Chem. C*, 2008, **112**, 5542–5551.

265. D. Shi, Y. Feng and S. Zhong, *Catal. Today*, 2004, **98**, 505–509.

266. A. Fujishima, X. Zhang and D. Tryk, *Surf. Sci. Rep.*, 2008, **63**, 515–582.

267. D. M. Stanbury, in *Advances in Inorganic Chemistry*, Elsevier, Amsterdam, 1989, pp. 69–138.

268. R. C. Nelson, E. K. Plyler and W. S. Benedict, *J. Res. Natl. Bur. Stand.*, 1948, **41**, 615–621.

269. G. Herzberg and L. Herzberg, *J. Opt. Soc. Am.*, 1953, **43**, 1037–1044.

270. L.-B. Xiong, J.-L. Li, B. Yang and Y. Yu, *J. Nanomater.*, 2012, **2012**, 831524.

271. S. Andersson, B. Collén, U. Kuylenstierna and A. Magnéli, *Acta Chem. Scand.*, 1957, **11**, 1641–1652.

272. C. R. A. Catlow, *AIP Conf. Proc.*, 1979, **53**, 149–161.

273. F. M. Pesci, G. Wang, D. R. Klug, Y. Li and A. J. Cowan, *J. Phys. Chem. C*, 2013, **117**, 25837–25844.

274. K. L. Feilberg, S. R. Sellevåg, C. J. Nielsen, D. W. T. Griffith and M. S. Johnson, *Phys. Chem. Chem. Phys.*, 2002, **4**, 4687–4693.

275. J. Sun, J. W. Thybaut and G. B. Marin, *Catal. Today*, 2008, **137**, 90–102.

276. J. Zhang and Y. Nosaka, *J. Phys. Chem. C*, 2014, **118**, 10824–10832.

277. W. D. Moor, *Oil Gas J.*, 1977, **75**, 159–177.

278. G. G. Stokes, *Mathematical and Physical Papers, Vol. 1*, University Press, Cambridge, 1880.

279. P. P. Gonzalez-Borrero, F. Sato, A. N. Medina, M. L. Baesso, A. C. Bento, G. Baldissera, C. Persson, G. A. Niklasson, C. G. Granqvist and A. Ferreira da Silva, *Appl. Phys. Lett.*, 2010, **96**, 061909.

280. Y. Zhang, S. Jiang, W. Song, P. Zhou, H. Ji, W. Ma, W. Hao, C. Chen and J. Zhao, *Energy Environ. Sci.*, 2015, **8**, 1231–1236.

281. G. Samasonov, *The Oxide Handbook*, Springer, Boston, MA, 2nd edn., 1982.

282. A. Hagfeldt and M. Graetzel, *Chem. Rev.*, 1995, **95**, 49–68.

283. S. D. Tilley, M. Cornuz, K. Sivula and M. Grätzel, *Angew. Chem. Int. Edit.*, 2010, **49**, 6405–6408.

284. K. Sivula, F. Le Formal and M. Grätzel, *ChemSusChem*, 2011, **4**, 432–449.

285. P. S. Bassi, Gurudayal, L. H. Wong and J. Barber, *Phys. Chem. Chem. Phys.*, 2014, **16**, 11834.

286. C. Kormann, D. W. Bahnemann and M. R. Hoffmann, *J. Photochem. Photobiol. A*, 1989, **48**, 161–169.

287. M. Barroso, S. R. Pendlebury, A. J. Cowan and J. R. Durrant, *Chem. Sci.*, 2013, **4**, 2724–2734.

288. P. A. Kolinko, T. N. Filippov, D. V. Kozlov and V. N. Parmon, *J. Photochem. Photobiol. A*, 2012, **250**, 72–77.

289. S. H. Taylor, C. S. Heneghan, G. J. Hutchings and I. D. Hudson, *Catal. Today*, 2000, **59**, 249–259.

290. S. D. Pollington, A. F. Lee, T. L. Overton, P. J. Sears, P. B. Wells, S. E. Hawley, I. D. Hudson, D. F. Lee and V. Ruddock, *Chem. Commun.*, 1999, 725–726.

291. O. Anderson, C. R. Ottermann, R. Kuschnereit, P. Hess and K. Bange, *Fresenius. J. Anal. Chem.*, 1997, **358**, 315–318.

292. G. G. Popov, J. J. Carbajo, V. K. Ivanov and G. L. Yoder, *Thermophysical Properties of MOX and UO2 Fuels Including the Effects of Irradiation, ORNL/TM-2000/351*, Oak Ridge National Laboratory, Tennessee, 2000.

293. H. L. Clever and C. L. Young, *IUPAC Solubility Data Series, Vol. 27/28*, Pergamon, Oxford, 1987.

294. R. Battino, T. R. Rettich and T. Tominaga, *J. Phys. Chem. Ref. Data*, 1984, **13**, 563.

295. G. V. Buxton, C. L. Greenstock, W. P. Helman and A. B. Ross, *J. Phys. Chem. Ref. Data*, 1988, **17**, 513–886.

296. W. C. Lee, Y. Fang, J. F. Turner, J. S. Bedi, C. C. Perry, H. He, R. Qian and Q. Chen, *Sensors Actuators B Chem.*, 2016, in press.

297. W. C. Lee, G. E. Canciani, B. O. Alwhshe and Q. Chen, *Int. J. Hydrogen Energy*, 2016, **41**, 123–131.

298. M. R. Alenezi, S. J. Henley and S. R. P. Silva, *Sci. Rep.*, 2015, **5**, 8516.

299. Y. Fang, J. Tong, Q. Zhong, Q. Chen, J. Zhou, Q. Luo, Y. Zhou, Z. Wang and B. Hu, *Nano Energy*, 2015, **16**, 301–309.

300. Y. Fang, W. C. Lee, G. E. Canciani, T. C. Draper, Z. F. Al-Bawi, J. S. Bedi, C. C. Perry and Q. Chen, *Mater. Sci. Eng. B*, 2015, **202**, 39–45.

301. W. C. Lee, Y. Fang, R. Kler, G. E. Canciani, T. C. Draper, Z. T. Al-Abdullah, S. M. Alfadul, C. C. Perry, H. He and Q. Chen, *Mater. Chem. Phys.*, 2015, **149**, 12–16.

302. P. D. Bartlett, M. J. Ryan and S. G. Cohen, *J. Am. Chem. Soc.*, 1942, **64**, 2649–2653.

303. B. H. Klanderman and J. W. H. Faber, *J. Polym. Sci. A Polym. Chem.*, 1968, **6**, 2955–2965.

304. R. L. Pohl and B. R. Willeford, *J. Organomet. Chem.*, 1970, **23**, C45–C46.

305. J. M. Chance, J. H. Geiger and K. Mislow, *J. Am. Chem. Soc.*, 1989, **111**, 2326–2327.

306. G. Yamamoto, S. Ohta, M. Kaneko, K. Mouri, M. Ohkuma, R. Mikami, Y. Uchiyama and M. Minoura, *Bull. Chem. Soc. Jpn.*, 2005, **78**, 487–497.

307. T. M. Long and T. M. Swager, *Adv. Mater.*, 2001, **13**, 601–604.

308. C. A. Tolman, *Chem. Rev.*, 1977, **77**, 313–348.

309. C. A. Tolman, *J. Am. Chem. Soc.*, 1970, **92**, 2956–2965.

310. G. Molle, P. Bauer and J. E. Dubois, *J. Org. Chem.*, 1983, **48**, 2975–2981.

311. H. Hsieh and R. P. Quirk, *Anionic Polymerization: Principles and Practical Applications*, Marcel Dekker, New York, 1996, p. 41.

312. E. Weiss and G. Hencken, *J. Organomet. Chem.*, 1970, **21**, 265–268.

313. T. Kottke and D. Stalke, *Angew. Chem. Int. Edit. Engl.*, 1993, **32**, 580–582.

314. A. D. Becke, *J. Chem. Phys.*, 1993, **98**, 5648–5652.

315. C. Lee, W. Yang and R. G. Parr, *Phys. Rev. B*, 1988, **37**, 785–789.

316. K. J. Palmer and D. H. Templeton, *Acta Crystallogr. B*, 1968, **24**, 1048–1052.

317. W. F. Sanjuan-Szklarz, A. A. Hoser, M. Gutmann, A. Ø. Madsen and K. Woźniak, *IUCrJ*, 2016, **3**, 61–70.

318. Y. Tanabe and S. Sugano, *J. Phys. Soc. Japan*, 1954, **9**, 753–766.

319. Y. Tanabe and S. Sugano, *J. Phys. Soc. Japan*, 1954, **9**, 766–779.

320. B. N. Figgis and M. A. Hitchman, *Ligand Field Theory and Its Applications*, Wiley, New York, 2000.

321. D. F. Evans, *J. Chem. Soc.*, 1959, 2003–2005.

322. D. H. Grant, *J. Chem. Educ.*, 1995, **72**, 39–40.

323. C. Piguet, *J. Chem. Educ.*, 1997, **74**, 815–816.

324. P. Pascal, *Ann. Chim. Phys.*, 1910, **19**, 5.

325. P. Pascal, *Ann. Chim. Phys.*, 1912, **25**, 289.

326. P. Pascal, *Ann. Chim. Phys.*, 1913, **28**, 218.

327. G. A. Bain and J. F. Berry, *J. Chem. Educ.*, 2008, **85**, 532–536.

328. J. I. Hoppe, *J. Chem. Educ.*, 1972, **49**, 505.

329. T. M. Dunn, *Trans. Faraday Soc.*, 1961, **57**, 1441–1444.

330. P. Curie, *J. Phys.*, 1894, **3**, 393–415.

331. P. Weiss, *C.r. hebd. Séanc, Acad. Sci.*, 1906, **143**, 1136–1139.

332. J. M. Zadrozny, D. J. Xiao, M. Atanasov, G. J. Long, F. Grandjean, F. Neese and J. R. Long, *Nat. Chem.*, 2013, **5**, 577–581.

333. E. A. K. V. Gustorf, F.-W. Grevels and I. Fischler, *The Organic Chemistry of Iron*, Academic Press, New York, 1st edn., 1978, p. 3.

334. D. M. Jenkins, A. J. Di Bilio, M. J. Allen, T. A. Betley and J. C. Peters, *J. Am. Chem. Soc.*, 2002, **124**, 15336–15350.

335. M. Mantina, R. Valero, C. J. Cramer and D. G. Truhlar, in *Handbook of Chemistry and Physics*, ed. W. M. Haynes, CRC Press, London, 94th edn., 2013, pp. 49–50.

336. J. R. de Laeter, J. K. Böhlke, P. De Bièvre, H. Hidaka, H. S. Peiser, K. J. R. Rosman and P. D. P. Taylor, *Pure Appl. Chem.*, 2003, **75**, 683–800.

337. G. Wilkinson, J. A. McCleverty and R. D. Gillard, *Comprehensive Coordination Chemistry, Vol 2*, Pergamon, Oxford, 1987, pp. 318–333.

338. P. Doppelt, J. Fischer, L. Ricard and R. Weiss, *New J. Chem.*, 1987, **11**, 357–364.

339. J. Li, B. C. Noll, A. G. Oliver and W. R. Scheidt, *J. Am. Chem. Soc.*, 2012, **134**, 10595–10606.

340. P. M. Wood, *Biochem. J.*, 1988, **253**, 287–289.

341. A. Yamamoto, S. Kitazume, L. S. Pu and S. Ikeda, *Chem. Commun.*, 1967, **2**, 79–80.

342. R. Imayoshi, H. Tanaka, Y. Matsuo, M. Yuki, K. Nakajima, K. Yoshizawa and Y. Nishibayashi, *Chem. Eur. J.*, 2015, **21**, 8905–8909.

343. P. L. Pauson, J. P. Stambuli, T.-C. Chou and B.-C. Hong, in *Encyclopedia of Reagents for Organic Synthesis*, Wiley, Chichester, 2014, pp. 1–26.

344. R. Beck, S. Camadanli, U. Flörke and H.-F. Klein, *Eur. J. Inorg. Chem.*, 2015, **2015**, 2543–2559.

345. G. Fachinetti, C. Floriani and P. F. Zanazzi, *J. Am. Chem. Soc.*, 1978, **100**, 7405–7407.

346. D. J. Darensbourg and S. J. Wilson, *Macromolecules*, 2013, **46**, 5929–5934.

347. P. K. Kipkemboi, P. C. Kiprono and J. J. Sanga, *Bull. Chem. Soc. Ethiop.*, 2003, **17**, 221–218.

348. I. Boustani and A. W. Allaf, *Vib. Spectrosc.*, 1998, **16**, 157–162.

349. N. J. Clayden, P. Pernice and A. Aronne, *J. Non. Cryst. Solids*, 2005, **351**, 195–202.

350. R. Chen, H. Wagner, A. Dastgheib-Shirazi, M. Kessler, Z. Zhu, V. Shutthanandan, P. P. Altermatt and S. T. Dunham, *J. Appl. Phys.*, 2012, **112**, 124912.

351. I. E. Nifant'ev, A. N. Tavtorkin, S. A. Korchagina, I. F. Gavrilenko, N. N. Glebova, N. N. Kostitsyna, V. A. Yakovlev, G. N. Bondarenko and M. P. Filatova, *Appl. Catal. A*, 2014, **478**, 219–227.

352. Z. Hnatejko, S. Lis and Z. Stryła, *J. Therm. Anal. Calorim.*, 2010, **100**, 253–260.

353. A. N. Kantacha and S. Wongnawa, *Inorganica Chim. Acta*, 1987, **134**, 135–137.

354. I. Bertini, C. Luchinat and G. Parigi, in *Solution NMR of Paramagnetic Molecules Applications to Metallobiomolecules and Models*, Elsevier, Amsterdam, 2001, pp. 143–203.

355. I. Marshall, S. D. Bruce, J. Higinbotham, A. MacLullich, J. M. Wardlaw, K. J. Ferguson and J. Seckl, *Magn. Reson. Med.*, 2000, **44**, 646–649.

356. D. D. Schmidt and J. T. Yoke, *Inorg. Chem.*, 1970, **9**, 1176–1178.

357. S. Lenzer, *J. Chem. Soc.*, 1964, 5768–5774.

358. A. B. P. Lever, *Inorganic Electronic Spectroscopy*, Elsevier, Amsterdam, 2nd edn., 1984, pp. 480–505.

359. A. Müller, P. Christophliemk and I. Tossidiss, *J. Mol. Struct.*, 1973, **15**, 289–299.

360. J. S. Maass, M. Zeller, T. M. Breault, B. M. Bartlett, H. Sakiyama and R. L. Luck, *Inorg. Chem.*, 2012, **51**, 4903–4905.

361. J. B. Anderson, E. Kostiner, M. C. Miller and J. R. Rea, *J. Solid State Chem.*, 1975, **14**, 372–377.

362. D. F. Evans, *J. Phys. E.*, 1974, **7**, 247–249.

363. M. De Bolster, I. Kortram and W. Groeneveld, *J. Inorg. Nucl. Chem.*, 1973, **35**, 1843–1853.

364. R. A. Palmer and C. R. Taylor, *Inorg. Chem.*, 1971, **10**, 2546–2552.

365. V. Murthy and S. Lakshman, *Solid State Commun.*, 1981, **38**, 651–652.

366. S. Koide, *Philos. Mag.*, 1959, **4**, 243–252.

367. W. Herwig and H. Zeiss, *J. Org. Chem.*, 1958, **23**, 1404.

368. M. L. H. Green, L. Pratt and G. Wilkinson, *J. Chem. Soc.*, 1959, 3753–3767.

369. G. Gritzner and J. Kuta, *Pure Appl. Chem.*, 1984, **56**, 461–466.

370. G. A. Mabbott, *J. Chem. Educ.*, 1983, **60**, 697–702.

371. J. J. Van Benschoten, J. Y. Lewis, W. R. Heineman, D. A. Roston and P. T. Kissinger, *J. Chem. Educ.*, 1983, **60**, 772–776.

372. R. S. Nicholson and I. Shain, *Anal. Chem.*, 1964, **36**, 706–723.

373. O. V. Dolomanov, L. J. Bourhis, R. J. Gildea, J. A. K. Howard and H. Puschmann, *J. Appl. Crystallogr.*, 2009, **42**, 339–341.

374. G. M. Sheldrick, *Acta Crystallogr. Sect. A Found. Crystallogr.*, 2008, **64**, 112–122.

375. G. M. Sheldrick, *Acta Crystallogr. Sect. A Found. Adv.*, 2015, **71**, 3–8.

376. C. F. Macrae, P. R. Edgington, P. McCabe, E. Pidcock, G. P. Shields, R. Taylor, M. Towler and J. van de Streek, *J. Appl. Crystallogr.*, 2006, **39**, 453–457.

377. L. J. Farrugia, *J. Appl. Crystallogr.*, 2012, **45**, 849–854.